

AD-A186 610

DTIC FILE COPY

Bulletin 52  
(Part 4 of 5 Parts)

2

# THE SHOCK AND VIBRATION BULLETIN

Part 4  
Fatigue and Random Loading  
Control, Isolation and Damping

MAY 1982

A Publication of  
THE SHOCK AND VIBRATION  
INFORMATION CENTER  
Naval Research Laboratory Washington, D.C.

DTIC  
ELECTE  
NOV 19 1987  
S  
CED



Office of  
The Under Secretary of Defense  
for Research and Engineering

Approved for public release; distribution unlimited.

87 10 28 019

## **SYMPOSIUM MANAGEMENT**

### **THE SHOCK AND VIBRATION INFORMATION CENTER**

Henry C. Pusey, Director

Rudolph H. Volin

J. Gordan Showalter

Jessica Hileman

Elizabeth A. McLaughlin

#### **Bulletin Production**

Publications Branch, Technical Information Division.

Naval Research Laboratory

Bulletin 52  
(Part 4 of 5 Parts)

# THE SHOCK AND VIBRATION BULLETIN

MAY 1982

A Publication of  
THE SHOCK AND VIBRATION  
INFORMATION CENTER  
Naval Research Laboratory, Washington, D.C.

Accession For	
NTIS GRA&I	<input checked="checked" type="checkbox"/>
DTIC TAB	<input type="checkbox"/>
Unannounced	<input type="checkbox"/>
Justification	
By	
In	
Availability Codes	
DAI	Avail or 1, or Unavail
A-1	

The 52nd Symposium on Shock and Vibration was held at the Monteleone Hotel, New Orleans, LA on October 26-28, 1981. The Defense Nuclear Agency, Washington, D.C. and the U.S. Army Waterways Experiment Station, Vicksburg, MS were Co-Hosts.

Office of  
The Under Secretary of Defense  
for Research and Engineering

## CONTENTS

### PAPERS APPEARING IN PART 4

#### Fatigue and Random Loading

FATIGUE LIFE PREDICTION FOR VARIOUS RANDOM STRESS PEAK DISTRIBUTIONS R. G. Lambert, General Electric Company, Aircraft Equipment Division, Utica, NY	1
FATIGUE LIFE EVALUATION, STOCHASTIC LOADING AND MODIFIED LIFE CURVES M. El Menoufy, H. H. E. Leipholz and T. H. Topper, University of Waterloo, Waterloo, Ontario, Canada	11
THE EFFECTS OF ENDURANCE LIMIT AND CREST FACTOR ON TIME TO FAILURE UNDER RANDOM LOADING A. J. Curtis and S. M. Moite, Hughes Aircraft Company, Culver City, CA	21
SINGLE POINT RANDOM MODAL TEST TECHNOLOGY APPLICATION TO FAILURE DETECTION W. M. West, Jr., NASA, Johnson Space Center, Houston, TX	25
FORCED VIBRATIONS OF A LARGE DAMPED MECHANICAL SYSTEM D. W. Nicholson, Naval Surface Weapons Center, White Oak, Silver Spring, MD	33
INDIRECT FOURIER TRANSFORM (IFT) AND SHOCK RESPONSE — A DETAILED PRESENTATION OF BASIC THEORY C. T. Morrow, Encinitas, CA	37

#### Control, Isolation and Damping

ACTIVE VIBRATION CONTROL OF LARGE FLEXIBLE STRUCTURES T. T. Soong and J. C. H. Chang, State University of New York at Buffalo, Buffalo, NY	47
FORCE OPTIMIZED RECOIL CONTROL SYSTEM P. E. Townsend, U.S. Army Armament Research and Development Command, Dover, NJ, R. J. Radkiewicz, U.S. Army Armament Research and Development Command, Rock Island, IL and R. F. Gartner, Honeywell, Inc., Edina, MN	55
PERFORMANCE ANALYSIS OF HIGH-SPEED HYDRAULIC SUSPENSION SYSTEMS IN MULTIPLE WHEELED LAND TRANSPORTERS P. Woods, Martin Marietta Corporation, Denver, CO	73
NONLINEAR ANALYSIS OF PNEUMATIC FORCE GENERATORS USED FOR VIBRATION CONTROL S. Sankar, Concordia University, Montreal, Quebec, Canada, R. R. Guntur, Union College, Schenectady, NY, and S. G. Kalumbar, Electronic Associates, Inc., West Long Branch, NJ	87
REDUCTION OF HYDRAULIC LINE OSCILLATING PRESSURES INDUCED BY PUMP CAVITATION G. Druhak, P. Marino and M. Bernstein, Grumman Aerospace Corporation, Bethpage, NY	103
RUBBER ISOLATORS FOR THE ADATS MISSILE J. Frottier, Oerlikon-Buehler Werkzeugmaschinenfabrik, Zurich, CH and C. F. O'Hearne, Martin Marietta Orlando Aerospace, Orlando, FL	123
TIME AND TEMPERATURE EFFECTS ON CUSHIONS G. S. Mustin, Naval Sea Systems Command, Washington, DC	131
EXTRANEEOUS EFFECTS IN DAMPING MEASUREMENT R. J. Hooker, University of Queensland, Queensland, Australia and S. Prasertsan, Prince of Songkla University, Hat-yai, Thailand	141
DYNAMIC ANALYSIS OF A LARGE STRUCTURE WITH ARTIFICIAL DAMPING Q. L. Tian, D. K. Liu, Y. P. Li and D. F. Wang, Institute of Mechanics, The Chinese Academy of Sciences, Beijing, China	147



AN EXPERIMENTAL STUDY OF THE NONLINEAR BEHAVIOUR OF A STRANDED CABLE AND DRY FRICTION DAMPER .....	155
C. S. Chang and Q. Tian, Institute of Mechanics, The Chinese Academy of Sciences, Beijing, China	
RESPONSE OF PNEUMATIC ISOLATOR TO STANDARD PULSE SHAPES .....	161
M. S. Hundal, The University of Vermont, Burlington, VT	

## PAPERS APPEARING IN PART 1

### Welcome

#### WELCOME

Colonel Tilford Creel, Commander/Director, U.S. Army Waterways Experiment Station, Vicksburg, MS

### Keynote Address

#### KEYNOTE ADDRESS

Marvin Atkins, Director, Offensive and Space Systems, Office of the Under Secretary of Defense  
Research Engineering, Department of Defense, Washington, DC

### Invited Papers

#### EQUIPMENT SURVIVABILITY ON THE INTEGRATED BATTLEFIELD

Charles N. Davidson, Technical Director, U.S. Army Nuclear and Chemical Agency, Springfield, VA

#### NAVAL OPERATIONS IN A NUCLEAR ENVIRONMENT

Captain Donald Alderson, U.S.N., Acting Chief, Tactical Nuclear Weapons Project Office (PM-23)  
Department of the Navy, Washington, DC

#### SURVIVABILITY REQUIREMENTS FOR FUTURE AIR FORCE SYSTEMS

Henry F. Cooper, Deputy for Strategic and Space Systems, Assistant Secretary of the Air Force  
(Research, Development and Logistics), Washington, DC

#### NUCLEAR HARDNESS VALIDATION TESTING

Edward Conrad, Deputy Director (Science and Technology), Defense Nuclear Agency, Washington, DC

#### ELIAS KLEIN MEMORIAL LECTURE — THE CHANGING DIMENSIONS OF QUALIFICATION TESTING

H. Norman Abramson, Vice-President, Engineering Sciences, Southwest Research Institute, San Antonio, TX

#### REQUIRED DEVELOPMENTS IN STRUCTURAL DYNAMICS

Ben K. Wada, Jet Propulsion Laboratory, Pasadena, CA

#### EFFECT OF SEALS ON ROTOR SYSTEMS

David P. Fleming, NASA, Lewis Research Center, Cleveland, OH

#### MACHINERY VIBRATION EVALUATION TECHNIQUES

R. L. Eshleman, The Vibration Institute, Clarendon Hills, IL

#### SHAFT VIBRATION MEASUREMENT AND ANALYSIS TECHNIQUES

Donald E. Bently, President, Bently Nevada Corporation, Minden, NV

### Rotor Dynamics and Machinery Vibration

#### SPIN TEST VIBRATIONS OF PENDULOUSLY SUPPORTED DISC/CYLINDRICAL ROTORS

F. H. Wolff and A. J. Molnar, Westinghouse Research and Development Center, Pittsburgh, PA

#### MODAL ANALYSIS AS A TOOL IN THE EVALUATION OF A TURBINE WHEEL FAILURE

A. L. Moffa and R. L. Leon, Franklin Research Center, Philadelphia, PA

#### CONTRIBUTION TO THE DYNAMIC BEHAVIOUR OF FLEXIBLE MECHANISMS

E. Imam, T. Der Hagopian and M. Lalanne, Institut National des Sciences Appliquées, Villeurbanne, France

#### SELF-EXCITED VIBRATION OF A NONLINEAR SYSTEM WITH RANDOM PARAMETERS

R. A. Ibrahim, Texas Tech University, Lubbock, TX

## PAPERS APPEARING IN PART 2

### Invited Papers

#### Space Shuttle Loads and Dynamics

##### SPACE SHUTTLE MAIN ENGINE (SSME) POGO TESTING AND RESULTS

J. R. Fenwick, Rockwell International, Rocketdyne Division, Canoga Park, CA and  
J. H. Jones and R. E. Jewell, NASA, Marshall Space Flight Center, Huntsville, AL

##### SPACE SHUTTLE SOLID ROCKET BOOSTER WATER ENTRY CAVITY COLLAPSE LOADS

R. T. Keefe and E. A. Rawls, Chrysler Corporation, Slidell, LA and  
D. A. Kross, NASA, Marshall Space Flight Center, Huntsville, AL

##### SPACE SHUTTLE SOLID ROCKET BOOSTER REENTRY AND DECELERATOR SYSTEM LOADS AND DYNAMICS

R. Moog, Martin Marietta/Denver Division, Denver, CO and D. Kross, NASA,  
Marshall Space Flight Center, Huntsville, AL

##### INVESTIGATION OF SIDE FORCE OSCILLATIONS DURING STATIC FIRING OF THE SPACE SHUTTLE SOLID ROCKET MOTOR

M. A. Behring, Thiokol Corporation/Wasatch Division, Brigham City, UT

#### Space Shuttle Data Systems

##### DEVELOPMENT OF AN AUTOMATED PROCESSING AND SCREENING SYSTEM FOR THE SPACE SHUTTLE ORBITER FLIGHT TEST DATA

D. K. McCutchen, NASA, Johnson Space Center, Houston, TX, J. F. Brose, Lockheed Engineering and  
Management Services Company, Inc., Houston, TX and W. E. Palm, McDonnell Douglas Corp., Houston, TX

##### DEVELOPMENT OF A VIBROACOUSTIC DATA BASE MANAGEMENT AND PREDICTION SYSTEM FOR PAYLOADS

F. J. On, NASA, Goddard Space Flight Center, Greenbelt, MD and  
W. Hendricks, Lockheed Missiles and Space Company, Sunnyvale, CA

##### AUTOMATION OF VIBROACOUSTIC DATA BANK FOR RANDOM VIBRATION CRITERIA DEVELOPMENT

R. C. Ferebee, NASA, Marshall Space Flight Center, Huntsville, AL

##### THE DEVELOPMENT AND VERIFICATION OF SHUTTLE ORBITER RANDOM VIBRATION TEST REQUIREMENTS

M. C. Coody, NASA, Johnson Space Center, Houston, TX, H. K. Pratt, Rockwell International Corporation,  
Downey, CA and D. E. Newbrough, Management and Technical Services Corporation, Houston, TX

##### SPACE SHUTTLE ORBITER ACOUSTIC FATIGUE CERTIFICATION TESTING

R. A. Stevens, Rockwell International, Downey, CA

#### Space Shuttle Thermal Protection Systems

##### STRUCTURAL CHARACTERISTICS OF THE SHUTTLE ORBITER CERAMIC THERMAL PROTECTION SYSTEM

P. A. Cooper, NASA, Langley Research Center, Hampton, VA

##### SHUTTLE TILE ENVIRONMENTS AND LOADS

R. J. Muraca, NASA, Langley Research Center, Hampton, VA

##### DYNAMIC AND STATIC MODELING OF THE SHUTTLE ORBITER'S THERMAL PROTECTION SYSTEM

J. M. Housner, G. L. Giles and M. Vallas, NASA, Langley Research Center, Hampton, VA

##### BUFFET LOADS ON SHUTTLE THERMAL-PROTECTION-SYSTEM TILES

C. F. Coe, NASA, Ames Research Center, Moffett Field, CA

##### UNSTEADY ENVIRONMENTS AND RESPONSES OF THE SHUTTLE COMBINED LOADS ORBITER TEST

P. H. Schuetz, Rockwell International, Downey, CA and  
L. D. Pinson and H. T. Thornton, Jr., NASA, Langley Research Center, Hampton, VA

#### Space Shuttle Main Engine Dynamics

##### VIBRATION MATURITY OF THE SPACE SHUTTLE MAIN ENGINES

E. W. Larson and E. Mogil, Rockwell International/Rocketdyne Division, Canoga Park, CA

STRUCTURAL RESPONSE OF THE SSME FUEL FEEDLINE TO UNSTEADY SHOCK OSCILLATIONS  
E. W. Larson, G. H. Ratekin and G. M. O'Connor, Rockwell International/Rocketdyne Division, Canoga Park, CA

### PAPERS APPEARING IN PART 3

#### Environmental Testing and Simulation

DIGITAL CONTROL OF A SHAKER TO A SPECIFIED SHOCK SPECTRUM

J. F. Unruh, Southwest Research Institute, San Antonio, TX

GUNFIRE VIBRATION SIMULATION ON A DIGITAL VIBRATION CONTROL SYSTEM

J. Cies, Hewlett-Packard Company, Paramus, NJ

MEASUREMENT OF ALL COMPONENTS OF STRAIN BY A 3-D FIBER OPTIC STRAIN GAGE

S. Edelman and C. M. Davis, Jr., Dynamic Systems, Inc., McLean, VA

REGISTRATION OF THREE SOIL STRESS GAGES AT 0 THROUGH 28 MPa (4000 psi)

C. R. Welch, U.S. Army Engineer Waterways Experiment Station, Corps of Engineers, Vicksburg, MS

CABLE PROTECTION FOR GROUND SHOCK INSTRUMENTATION IN SEVERE ENVIRONMENTS —  
RESULTS OF AN EVALUATION TEST

C. R. Welch, U.S. Army Engineer Waterways Experiment Station, Corps of Engineers, Vicksburg, MS

STRUCTURAL RESPONSE OF HEPA FILTERS TO SHOCK WAVES

P. R. Smith, New Mexico State University, Las Cruces, NM and W. S. Gregory, Los Alamos National Laboratory, Los Alamos, NM

A TECHNIQUE COMBINING HEATING AND IMPACT FOR TESTING REENTRY VEHICLE IMPACT  
FUZES AT HIGH VELOCITIES

R. A. Benham, Sandia National Laboratories, Albuquerque, NM

USE OF A DROPPED WEIGHT TO SIMULATE A NUCLEAR SURFACE BURST

C. R. Welch and S. A. Kiger, U.S. Army Engineer Waterways Experiment Station, Corps of Engineers, Vicksburg, MS

ANALYSIS AND TESTING OF A NONLINEAR MISSILE AND CANISTER SYSTEM

R. G. Benson, A. C. Deerhake and G. C. McKinnis, General Dynamics/Convair Division, San Diego, CA

BIO-DYNAMIC RESPONSE OF HUMAN HEAD DURING WHOLE-BODY VIBRATION CONDITIONS

B. K. N. Rao, Birmingham Polytechnic, Perry Barr, England

#### Flight Environments

YC-15 EXTERNALLY BLOWN FLAP NOISE

Capt. L. G. Peck, Flight Dynamics Laboratory, Air Force Wright Aeronautical Laboratories, Wright-Patterson AFB, OH

DETERMINATION OF THE DYNAMIC ENVIRONMENT OF THE F/FB-111 TAIL POD ASSEMBLY

J. Chinn and P. Bolds, Air Force Wright Aeronautical Laboratories, Wright-Patterson AFB, OH

AN ASSESSMENT OF THE A-10's CAPABILITY TO OPERATE ON ROUGH SURFACES

T. G. Gerardi and D. L. Morris, Air Force Wright Aeronautical Laboratories, Wright-Patterson AFB, OH

SUBCRITICAL FLUTTER TESTING USING THE FEEDBACK SYSTEM APPROACH

C. D. Turner, North Carolina State University, Raleigh, NC

TOMAHAWK CRUISE MISSILE FLIGHT ENVIRONMENTAL MEASUREMENT PROGRAM

E. S. Rosenbaum and F. L. Gloyne, General Dynamics/Convair Division, San Diego, CA

TEST PROGRAM TO DEVELOP VIBROACOUSTICS TEST CRITERIA FOR THE GALILEO BUS

D. L. Kern and C. D. Hayes, Jet Propulsion Laboratory, California Institute of Technology, Pasadena, CA

SLV-3 FLIGHT VIBRATION ENVIRONMENT

S. A. Palaniswami, G. Muthuraman and P. Balachandran, Aerospace Structures Division, Vikram Sarabhai Space Centre, Trivandrum, India

## PAPERS APPEARING IN PART 5

### Mathematical Modeling

#### DAMPED STRUCTURE DESIGN USING FINITE ELEMENT ANALYSIS

M. F. Kluesener and M. L. Drake, University of Dayton Research Institute, Dayton, OH

#### DETERMINATION OF NORMAL MODES FROM MEASURED COMPLEX MODES

S. R. Ibrahim, Old Dominion University, Norfolk, VA

#### THE EFFECT OF JOINT PROPERTIES ON THE VIBRATIONS OF TIMOSHENKO FRAMES

I. Yaghmai, Sharif University of Technology, Tehran, Iran and

D. A. Frohrib, University of Minnesota, Minneapolis, MN

#### SOIL STRUCTURE INTERACTION AND SOIL MODELS

J. M. Ferritto, Naval Civil Engineering Laboratory, Port Hueneme, CA

#### FINITE ELEMENTS FOR INITIAL VALUE PROBLEMS IN DYNAMICS

T. E. Simkins, U.S. Army Armament Research and Development Command, Watervliet, NY

### Structural Dynamics

#### A PROCEDURE FOR DESIGNING OVERDAMPED LUMPED PARAMETER SYSTEMS

D. J. Inman, State University of New York at Buffalo, Buffalo, NY and

A. N. Andry, Jr., Lockheed California Company, Burbank, CA

#### ON THE OPTIMAL LOCATION OF VIBRATION SUPPORTS

B. P. Wang and W. D. Pilkey, University of Virginia, Charlottesville, VA

#### DYNAMIC BUCKLING OF PINNED COLUMNS

J. M. Ready, David W. Taylor Naval Ship Research and Development Center, Bethesda, MD

#### LARGE DEFLECTION RANDOM RESPONSE OF SYMMETRIC LAMINATED COMPOSITE PLATES

K. R. Wentz and D. B. Paul, Air Force Wright Aeronautical Laboratories, Wright-Patterson AFB, OH and

C. Mei, Old Dominion University, Norfolk, VA

#### DYNAMIC CHARACTERISTICS OF A NON-UNIFORM TORPEDO-LIKE HULL STRUCTURE

A. Harari, Naval Underwater Systems Center, Newport, RI

#### VIBRATION AND ACOUSTIC RADIATION FROM POINT EXCITED SPHERICAL SHELLS

E. H. Wong, Naval Ocean Systems Center, San Diego, CA and

S. I. Hayek, The Pennsylvania State University, University Park, PA

#### DAMPING OF SHALLOW-BURIED STRUCTURES DUE TO SOIL-STRUCTURE INTERACTION

F. S. Wong and P. Weidlinger, Weidlinger Associates, Menlo Park, CA and New York, NY

## TITLES AND AUTHORS OF PAPERS PRESENTED IN THE SHORT DISCUSSION TOPICS SESSION

NOTE: These papers were only presented at the Symposium. They are not published in the Bulletin and are only listed here as a convenience.

#### TRANSFER FUNCTION ANALYSIS OF LARGE STRUCTURES

H. J. Weaver, Lawrence Livermore National Laboratory, Livermore, CA

#### SHOCK HARDENED STRUCTURAL ATTACHMENTS FOR HONEYCOMB BULKHEADS

P. W. Buermann, Gibbs & Cox, Inc., New York, NY

#### DISCOVERING THE THIRD (AND SECOND) DIMENSION

B. Meeker, Pacific Missile Test Center, Point Mugu, CA

#### A MICROPROCESSOR BASED ADAPTIVE ISOLATION AND DAMPING OF A VIBRATING STRUCTURE

A. S. R. Murty, Indian Institute of Technology, Kharagpur, India

- HARMONIC RESPONSE OF A STRUCTURE INCLUDING A DRY FRICTION DAMPER**  
J. Der Hagopian and M. LaLanne, Institut National des Sciences Appliquees, Villeurbanne, France
- RATIONALE FOR VIBRATION TESTING IN MIL-STD-810D (DRAFT)**  
H. J. Caruso, Westinghouse Electric Corporation, Baltimore, MD
- VIBRATION ISOLATION OF SENSITIVE IUS COMPONENTS REQUIRING THERMAL CONDUCTION**  
F. W. Spann, Boeing Aerospace Company, Seattle, WA
- FINITE ELEMENT ANALYSIS OF SHOCK AND VIBRATION FIXTURES**  
L. G. Smith, Hughes Aircraft Company, Fullerton, CA
- A UNIQUE METHOD FOR VIBRATION TESTING FAR BELOW THE NORMAL AMBIENT NOISE LEVEL OF ELECTRODYNAMIC SHAKERS**  
H. D. Camp, Jr., U.S. Army; ERADCOM, Fort Monmouth, NJ
- BOLTS AND FASTENER TIGHTENING TO BROCHURE IDEALNESS THROUGH VIBRATION SIGNATURES**  
A. S. R. Murty, Indian Institute of Technology, Kharagpur, India
- COST EFFECTIVE METHODS OF INCREASING DATA RECORDING CAPACITY**  
M. Dowling, Franklin Research Center, Philadelphia, PA
- PIEZOELECTRIC FORCE GAUGE WITH HIGH SENSITIVITY**  
R. R. Bouche, Bouche Laboratories, Sun Valley, CA
- PYROTECHNIC SHOCK ENVIRONMENTS MEASURED ON INERTIAL UPPER STAGE (IUS)**  
C. J. Beck, Jr., Boeing Aerospace Company, Seattle, WA
- USE OF BAND-SELECTABLE HANNING SMOOTHING TO IMPROVE TRANSIENT WAVEFORM REPRODUCTION ON SHAKERS**  
D. O. Smallwood and D. L. Gregory, Sandia National Laboratories, Albuquerque, NM
- SHAKER SHOCK TEST DATA — BASED ON OPTIMIZED PRE AND POST PULSES**  
R. T. Fandrich, Harris Corporation, Melbourne, FL
- PROGRESS ON THE EDESS MACHINES**  
F. J. Sazama, Naval Surface Weapons Center, Silver Spring, MD
- MULTI-AXIS RANDOM VIBRATION TESTER FOR AVIONICS**  
D. Everett, Pacific Missile Test Center, Point Mugu, CA and G. Greanias, UCLA, Los Angeles, CA
- ACOUSTIC FACILITY FOR CRUISE MISSILE TESTING**  
O. H. Moore, Jr., General Dynamics/Convair, San Diego, CA
- EFFECT OF FRICTION AND MISTUNING ON THE RESPONSE OF A BLADED DISK DISCRETE MODEL**  
A. Muszynska, University of Dayton and Bently Nevada Corp., Minden, NV
- CURRENT DEVELOPMENTS IN HUMAN VIBRATION RESEARCH**  
J. C. Guignard, Naval Biodynamics Laboratory, New Orleans, LA

## FATIGUE AND RANDOM LOADING

### FATIGUE LIFE PREDICTION FOR VARIOUS RANDOM STRESS PEAK DISTRIBUTIONS

Ronald G. Lambert  
General Electric Company  
Aircraft Equipment Division, Utica, NY 13503

Closed form analytical expressions have been derived to predict the fatigue life for various random stress peak distributions. These distributions include the Rayleigh, exponential, truncated exponential, skewed Rayleigh, and finite sample size Rayleigh. Numerical examples of all expressions are worked out for a common structural aluminum alloy 7075-T6. The slopes of the resulting fatigue curves have application to accelerated random vibration test criteria.

#### INTRODUCTION

The stress peak envelope probability density function (pdf) used in conjunction with Miner's Linear Cumulative Damage Rule has previously been shown to accurately predict fatigue life for narrowband Gaussian random stress situations which are typical of single-degree-of-freedom (SDF) vibration systems subjected to wideband Gaussian random forcing functions. [1] In these cases the stress peak envelope is represented by a Rayleigh mathematical function. Additionally, it was previously shown [2] that the same analytical technique can be used to accurately predict the fatigue life of several two-degree-of-freedom (2DF) systems which were experimentally evaluated. The reason given for such accuracy in extending the analytical approach to systems with widely different stress-time profiles was that the stress peak envelope pdf's of the SDF and 2DF systems were identical in the important stress region above the root-mean-square stress level. Thus, the hypothesis that the stress peak envelope pdf is useful to accurately predict fatigue life is considered reasonable.

This paper extends the above-mentioned analytical approach for various non-Rayleigh random stress peak envelope distributions which were chosen for their practical value.

#### APPLICATION

The exponential pdf arises due to aerodynamic gust and certain sea state loading conditions. The truncated exponential pdf occurs as a result of a limited

stress peak sample size. The large valued stress peaks of an exponential pdf are considered to be nonexistent in a finite duration test or service environment exposure due to their low probability of occurrence (Chauvenet's criterion). [3] Truncation of the large valued stress peaks can also occur if any blunting or softening at higher amplitudes takes place in the force generating system or in the response of the structural elements themselves. Such truncation extends fatigue life by a calculable amount. The skewed Rayleigh envelope arises from certain types of vibration exciter system forcing functions or as a result of nonlinear damping. The skewing process is represented in this paper by the power law transformation  $y = z^n$  of the nonskewed Rayleigh envelope pdf because of the mathematical simplicity and close approximation to measured data. Coulomb friction damping which is representative of riveted or bolted structural assemblies is characterized by  $n > 1.0$ . Viscoelastic damping or internal stress-strain hysteresis damping is characterized by  $n < 1.0$ . The latter damping mechanism is representative of dip-brazed or adhesive bonded structural assemblies. Values of 1.07 and 0.93 respectively were used as examples. The fatigue lives are significantly different for those structural elements whose stress response is controlled by these nonlinear damping mechanisms even though the skewing is slight (i.e.,  $n \approx 1.0$ , linear) in the examples evaluated. Coulomb friction accentuates the stress peaks (i.e., more damaging) whereas the viscoelastic and hysteresis damping deemphasizes stress peaks (i.e., less damaging) compared to the linear

nonskewed case. The finite sample size Rayleigh pdf also results from a finite duration test or service environment exposure.

#### SINUSOIDAL FATIGUE CURVE

A material's sinusoidal (i.e., cyclic) fatigue S-N curve is used in all of the developed expressions and is as follows:

$$S = \bar{A} N_s^{-1/\beta} \quad (1)$$

where

$S$  = applied sinusoidal stress cyclic amplitude

$\bar{A}$  = material constant; true cyclic ultimate stress

$$\bar{A} = 2^{-1/\beta} \sigma'_f \text{ (stress units)} \quad (2)$$

$$\beta = 1/b = \text{slope parameter} \quad (3)$$

$\sigma'_f$  = fatigue strength coefficient

$b$  = fatigue strength exponent

Values of  $\sigma'_f$  and  $b$  are tabulated in reference 4 for various materials. Table 1 lists typical fatigue curve constants.

#### CLASSICAL RANDOM FATIGUE CURVE

The classical random stress case involves a narrowband Gaussian process of zero mean value and standard deviation (i.e., rms) value of  $\sigma$  to represent the instantaneous stress. The positive envelope of this Gaussian process is represented by a Rayleigh pdf. Using Miner's Cumulative Damage Rule, it was shown [1] that the Classic Random Fatigue Curve is as follows:

$$\sigma = \bar{C} \tilde{N}_f^{-1/\beta} \text{ (stress units)} \quad (4)$$

where

$\sigma$  = rms stress value

$\bar{C}$  = material constant

$\tilde{N}_f$  = median number of random stress cycles to failure

$\beta$  = slope parameter from material's S-N curve

$$\bar{C} = \left[ \frac{\bar{A}}{\sqrt{2}} \right] \left[ \Gamma\left(\frac{\beta}{2} + 1\right) \right]^{-1/\beta} \text{ (stress units)} \quad (5)$$

$\Gamma(\alpha)$  = Gamma Function [5]

Typically  $\beta \approx 9$  for ductile materials and  $\beta \approx 20$  for brittle materials.

#### APPROACH SUMMARY

Miner's Cumulative Fatigue Damage Law can be expressed [1] as follows:

$$\tilde{N}_f = \frac{1}{\int_0^\infty G(S) dS} \quad (6)$$

$$G(S) = \frac{P(S)}{N_s} \quad (7)$$

where

$\tilde{N}_f$  = median number of random stress cycles to failure

$S$  = applied stress amplitude

$P(S)$  = stress envelope pdf

$N_s$  = number of sinusoidal stress cycles to failure at stress level  $S$  (see equation (1))

$G(S)$  = scaled damage pdf

TABLE 1. TYPICAL FATIGUE CURVE CONSTANTS

Material	$\bar{A}$		$\beta$	$\bar{C}$	
	(MPa)	(ksi)		(MPa)	(ksi)
Aluminum Alloy (7075-T6)	1238	179.5	9.65	551	79.9
Copper Wire	565	82	9.28	254	37
Soft Solder (37% Lead, 63% Tin)	105	15	9.85	47	7
Magnesium Alloy (AZ31B)	299	43	22.4	94	14

Each of the various pdf's  $P(S)$  being evaluated is described mathematically and used in equation (7) to calculate  $G(S)$ .  $G(S)$  is used in equation (6) to calculate  $\bar{N}_f$ . It should be noted that the solution of equation (6) usually involves solving either the Complete or Incomplete Gamma Functions [5]. There then exists a relationship between  $\bar{N}_f$  and  $\sigma$ , which is the fatigue curve for the particular envelope  $P(S)$ . This random fatigue curve can be plotted and compared with the Classical Random Fatigue Curve (Rayleigh  $P(S)$ ) of equation (4) or other fatigue curves.

Appendices A and B show typical derivations for the exponential and skewed Rayleigh stress peak envelopes.

Truncations and finite sample size results in the absence of stress peaks above a stress level  $L$ . The integration limits of equation (6) are broken from zero to  $L$  and from  $L$  to  $\infty$ . The latter integral has a value of zero. The first integral requires evaluation of the incomplete Gamma Function  $\gamma(\alpha)$ .

Both  $\Gamma(\alpha)$  and  $\gamma(\alpha)$  are easily computed. [5] Truncation stress level  $L$  values can be estimated as shown in Appendix C.

Expressions for  $P(S)$  and  $G(S)$  along with their statistical parameters are shown in Appendix D.

#### DERIVED EXPRESSIONS

The derived fatigue curve expressions are shown in Table 2. All of these expressions are of the same power law form as the sinusoidal S-N curve. All of the  $\bar{C}$  terms are constants except  $\bar{C}_{FSS}$  which is a function of  $\bar{N}_f$ . All of the slope parameters are the same as for the sinusoidal S-N curve,  $\beta$ , except for the skewed Rayleigh envelope. Its slope parameter is  $n\beta$ .

Example:

Given: Material 7075-T6 Aluminum Alloy

$\bar{A} = 1238 \text{ MPa (179.5 ksi)}$

$L/\sigma = \infty, 4, 2$

TABLE 2. DERIVED RANDOM FATIGUE CURVE EXPRESSIONS

Rayleigh	$\sigma = \bar{C} \bar{N}_f^{-1/\beta} \quad (4)$	$\bar{C} = \left[ \frac{\bar{A}}{\sqrt{2}} \right] \left[ \Gamma\left(\frac{\beta}{2} + 1\right) \right]^{-1/\beta} \quad (5)$
Exponential	$\sigma = \bar{C}_E \bar{N}_f^{-1/\beta} \quad (8)$	$\bar{C}_E = \bar{A} \left[ \Gamma(\beta + 1) \right]^{-1/\beta} \quad (9)$
Truncated Exponential	$\sigma = \bar{C}_{TE} \bar{N}_f^{-1/\beta} \quad (10)$	$\bar{C}_{TE} = \left[ \frac{\bar{A}}{(1 - a_T)} \right] \left[ \gamma(\beta + 1, L/\sigma) \right]^{-1/\beta} \quad (11)$ $a_T = e^{-L/\sigma}$
Skewed Rayleigh	$\sigma = \bar{C}_{skew} \bar{N}_f^{-1/n\beta} \quad (12)$	$\bar{C}_{skew} = \left[ \frac{\bar{A}^{1/n}}{\sqrt{2}} \right] \left[ \Gamma\left(\frac{n\beta}{2} + 1\right) \right]^{-1/n\beta} \quad (13)$
Truncated Rayleigh	$\sigma = \bar{C}_{TR} \bar{N}_f^{-1/\beta} \quad (14)$	$\bar{C}_{TR} = \left[ \frac{\bar{A}}{\sqrt{2}} \right] \left[ \frac{1 - e^{-T}}{\gamma(x, T)} \right]^{1/\beta} \quad (15)$ $x = \frac{\beta + 2}{2} \quad ; \quad T = \frac{L^2}{2\sigma^2}$
Finite Sample Size Rayleigh	$\sigma = \bar{C}_{FSS} \bar{N}_f^{-1/\beta} \quad (16)$	$\bar{C}_{FSS} = \left[ \frac{\bar{A}}{\sqrt{2}} \right] \left[ \gamma(x, \ln \bar{N}_f) \right]^{-1/\beta} \quad (17)$



$$\beta = 9.65$$

$$n = 0.93, 1, 1.07$$

Find: Fatigue curve expressions and plots

Solution: The fatigue curve expressions are shown in Table 3 using the equations in Table 2. The corresponding plots are in Figures 1 through 5.

Example:

Given: Material 7075-T6 Aluminum Alloy

$$\sigma = 48 \text{ MPa (7 ksi)}$$

$$n = 0.93, 1, 1.07$$

Find: Plot G(S) and calculate the mode  $S_0$  for the exponential and skewed Rayleigh envelopes.

Solution: Plots of G(S) are shown in Figures 6 through 9 using the expressions in Appendix D.

Example:

Given: Material 7075-T6 Aluminum Alloy

$$\sigma = 48 \text{ MPa (7 ksi)}$$

Find: The nonlinear damping transformation and the P(S) curves for the skewed Rayleigh envelope case for  $n = 0.93, 1, 1.07$

Solution: Using the equation in Appendices B and D, the above curves are shown in Figures 10 and 11.

Example:

$$\text{Given: } \sigma = 7 \text{ MPa (1 ksi)}$$

Find: Plot P(S) for the Rayleigh and exponential envelopes.

Solution: Using the expressions in Appendix D, the curves for P(S) are shown in Figure 12.

TABLE 3. 7075-T6 FATIGUE CURVE EXPRESSIONS

Curve Type	Fatigue Expression	
	(MPa)	(ksi)
Sinusoidal	$S = 1238\tilde{N}_f^{-0.104}$	$S = 179.5\tilde{N}_f^{-0.104}$
Rayleigh	$\sigma = 551\tilde{N}_f^{-0.104}$	$\sigma = 79.9\tilde{N}_f^{-0.104}$
Exponential	$\sigma = 280\tilde{N}_f^{-0.104}$	$\sigma = 40.6\tilde{N}_f^{-0.104}$
Truncated Exponential		
$L/\sigma = \infty$	$\sigma = 280\tilde{N}_f^{-0.104}$	$\sigma = 40.6\tilde{N}_f^{-0.104}$
$L/\sigma = 4$	$\sigma = 505\tilde{N}_f^{-0.104}$	$\sigma = 73.2\tilde{N}_f^{-0.104}$
$L/\sigma = 2$	$\sigma = 1026\tilde{N}_f^{-0.104}$	$\sigma = 148.8\tilde{N}_f^{-0.104}$
Skewed Rayleigh		
$n = 0.93$	$\sigma = 833\tilde{N}_f^{-0.1118}$	$\sigma = 120.8\tilde{N}_f^{-0.1118}$
$n = 1$	$\sigma = 551\tilde{N}_f^{-0.104}$	$\sigma = 79.7\tilde{N}_f^{-0.104}$
$n = 1.07$	$\sigma = 381\tilde{N}_f^{-0.0972}$	$\sigma = 55.2\tilde{N}_f^{-0.0972}$
Truncated Rayleigh		
$L/\sigma = \infty$	$\sigma = 551\tilde{N}_f^{-0.104}$	$\sigma = 79.9\tilde{N}_f^{-0.104}$
$L/\sigma = 3$	$\sigma = 617\tilde{N}_f^{-0.104}$	$\sigma = 89.5\tilde{N}_f^{-0.104}$
$L/\sigma = 2$	$\sigma = 862\tilde{N}_f^{-0.104}$	$\sigma = 125\tilde{N}_f^{-0.104}$

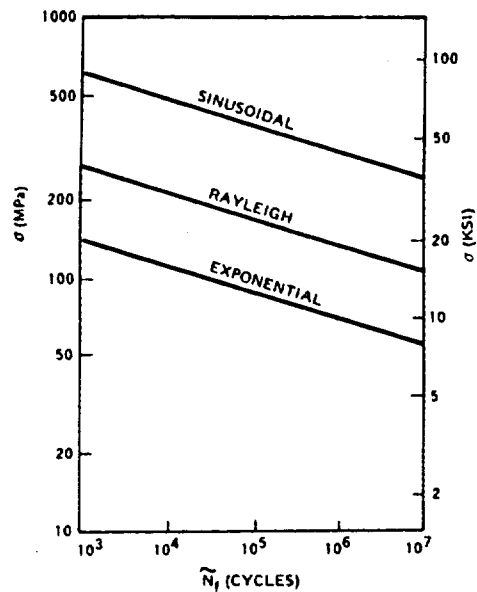


Fig. 1 - Fatigue Curves for Several Envelope pdf's

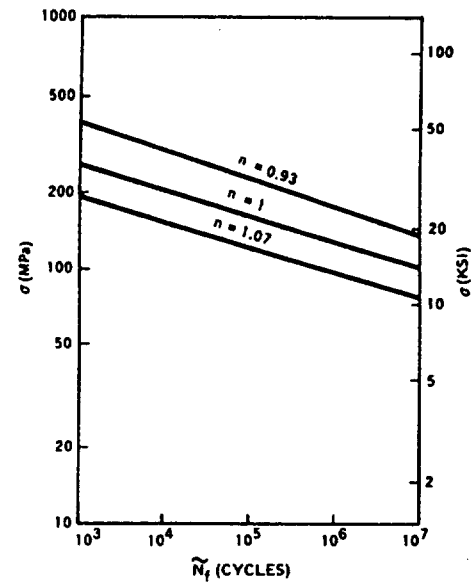


Fig. 3 - Fatigue Curves for Skewed Rayleigh Envelope pdf's

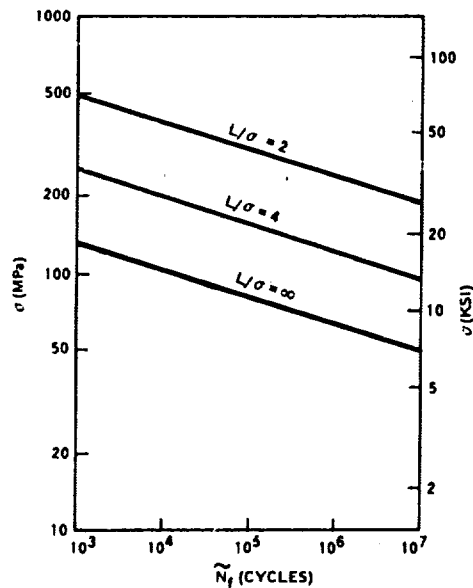


Fig. 2 - Fatigue Curves for Truncated Exponential Envelope pdf's

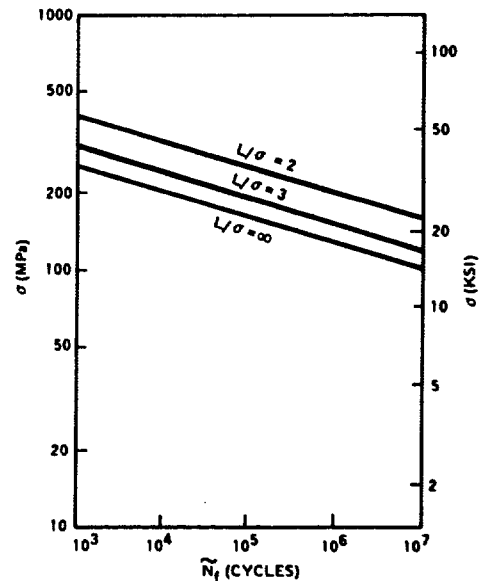


Fig. 4 - Fatigue Curves for Truncated Rayleigh Envelope pdf's

#### EXAMPLE RESULTS DISCUSSION

1. Most of the cumulative fatigue damage is done by stress peaks above  $2\sigma$  (see Figures 6 - 9). For the Rayleigh ( $n=1$ ) most damage is done by stress peaks between  $2\sigma$  and  $4\sigma$ . Truncation extends fatigue life. See Figure 4. The skewing constant  $n$  alters this

range somewhat. For the exponential, the most damaging peaks are between  $5\sigma$  and  $15\sigma$ . If these peaks were truncated, the fatigue life would be increased. See Figure 2.

2. The value for the  $G(S)$  mode  $S_0$  is dependent only upon  $\sigma$ ,  $\beta$ , and  $n$ . See Table 5 in Appendix D.

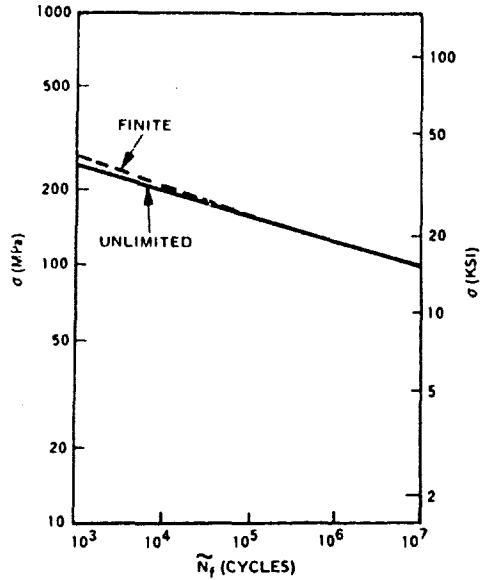


Fig. 5 - Fatigue Curves for Finite and Unlimited Sample Size

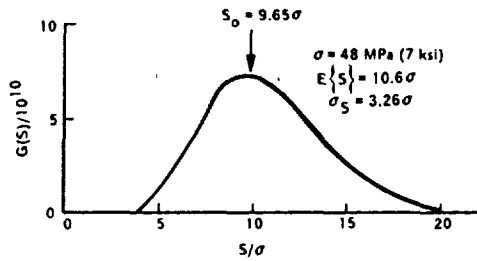


Fig. 6 - G(S) for Exponential Envelope

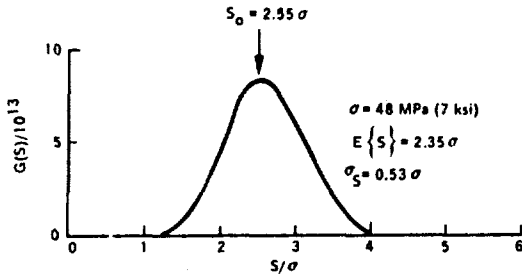


Fig. 7 - G(S) for Skewed Rayleigh Envelope;  $n = 0.93$

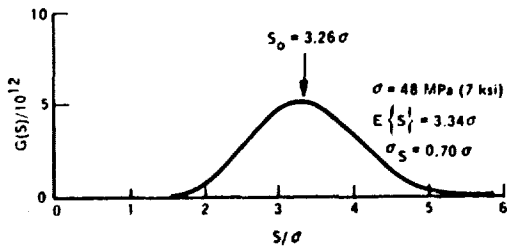


Fig. 8 - G(S) for Skewed Rayleigh Envelope;  $n = 1$

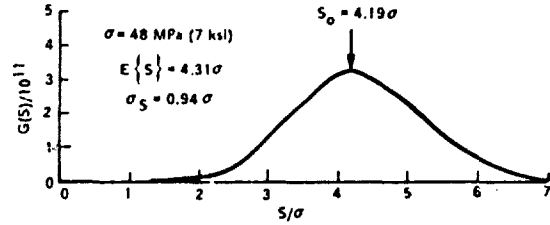


Fig. 9 - G(S) for Skewed Rayleigh Envelope;  $n = 1.07$

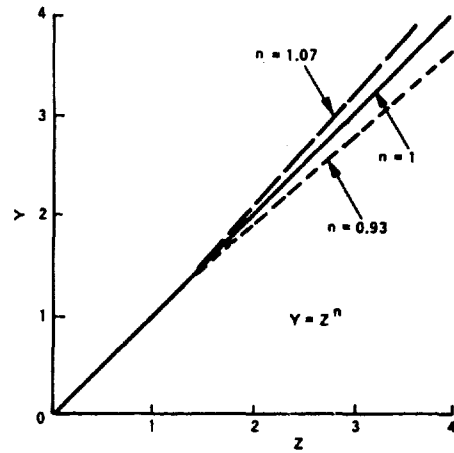


Fig. 10 - Nonlinear Damping Transformation Plot

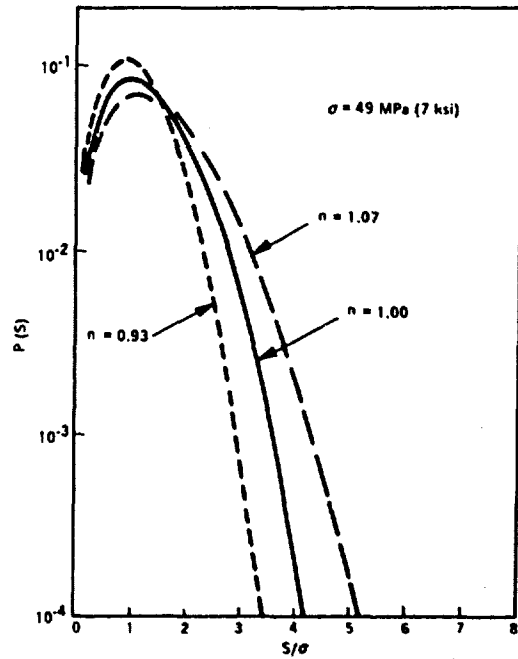


Fig. 11 - P(S) for Skewed Rayleigh;  $\sigma = 48 \text{ MPa (7 ksi)}$

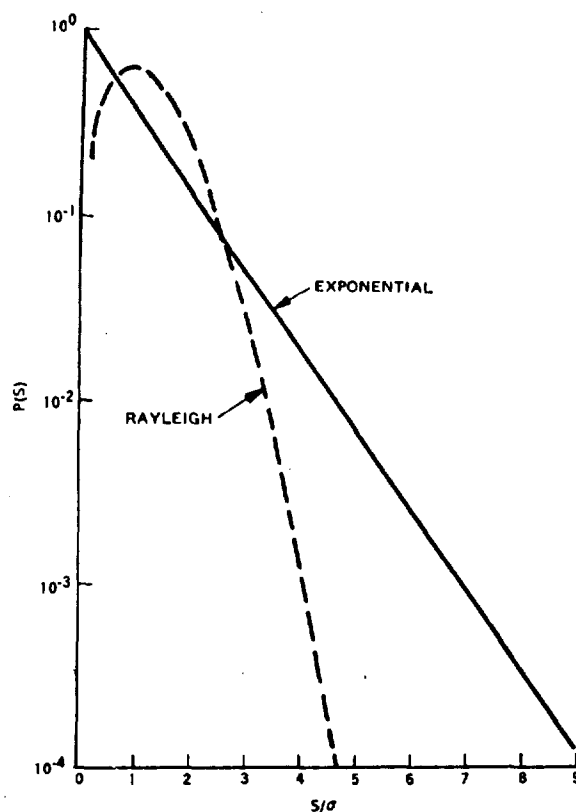


Fig. 12 -  $P(S)$  for Rayleigh and Exponential Envelopes;  
 $\sigma = 7 \text{ MPa (1 ksi)}$

3. The exponential envelope is more damaging than the Rayleigh envelope due to more frequent occurrence of damaging stress peaks. See Figures 1, 6, 8, and 12.
4. Even slight nonlinear damping significantly affects fatigue life. See Figure 3. The most damaging case is  $n > 1$  compared to the linear case of  $n = 1$ . The least damaging case is  $n < 1$ . Refer to Figures 10 and 11 which show that stress peaks are exaggerated for  $n > 1$  and deemphasized for  $n < 1$ .
5. The finite sample size Rayleigh has an insignificant effect on the fatigue life. See Figure 5.
6. The slopes of all the fatigue curves are the same except for the nonlinear skewed Rayleigh where  $n \neq 1$ . See Tables 2 and 3. The slope parameter  $n\beta = 8.97$  for  $n = 0.93$  and  $n\beta = 10.3$  for  $n = 1.07$  compared to 9.65 for  $n = 1$ . This affects the accelerated test criteria. [1] Based upon measured values of nonlinear damping in various electronic equipment structures,

the above values used for  $n$  in the examples are considered to be of practical value.

7. The slope of a random fatigue curve can be hypothesized to be significantly different from any calculated in this paper if the stress peak envelope  $P(S)$  changed from one type to another (e.g., from Rayleigh to exponential), if the truncation level  $L$  or if  $n$  changes as a function of rms stress level  $\sigma$ . It is not known if this happens in real structures.

#### CONCLUDING REMARKS

All of the developed closed form expressions are considered to be practical, accurate, and simple to use. Most of the needed parameter data can be obtained from a material's sinusoidal fatigue curve constants. Computations can be done on contemporary programmable calculators.

#### SYMBOLS

$\bar{A}$	material constant; true ultimate stress
$a_T$	truncated area
$\bar{C}$ , $\bar{C}_E$ , $\bar{C}_{FSS}$	random fatigue curve constant
$\bar{C}_{TE}$ , $\bar{C}_{TR}$	
$\bar{C}_{skew}$	
$E\{\sigma\}$	expected or mean value of $\sigma$
$E^2\{\sigma\}$	mean square value of $\sigma$
$G(S)$	scaled damage probability damage function
ksi	thousands of pounds per square inch
$L$	truncation stress value
$n$	skewed stress envelope constant
$N_s$	number of sinusoidal stress cycles to failure at stress level 3
$\tilde{N}_f$	median number of random stress cycles to failure
pdf	probability density function
$p(\alpha)$	probability density function of $\alpha$
$P(S)$	stress envelope pdf

rms	root mean square
S	applied stress amplitude
$S_o$	mode of G(S)
$S_p$	mode of P(S)
T	parameter of stress limiting
x	truncation parameter
z	general variable
$\alpha$	general variable
$\beta$	fatigue curve slope parameter
$\Gamma(\alpha)$	Gamma Function of argument $\alpha$
$\gamma(\alpha)$	Incomplete Gamma Function of argument $\alpha$
$\sigma$	random rms stress value
$\sigma_S$	standard deviation of S for G(S)
$\sigma'_f$	material fatigue strength coefficient
MPa	mega-Pascals
6.895	MPa/ksi

#### REFERENCES

1. R.G. Lambert, "Analysis of Fatigue under Random Vibration," The Shock and Vibration Bulletin No. 46, Naval Research Laboratory, Washington, DC, August 1976.
2. R.G. Lambert, "Fatigue Analysis of Multi-Degree-of-Freedom Systems under Random Vibration," The Shock and Vibration Bulletin No. 47, Naval Research Laboratory, Washington, DC, September 1977.
3. Y. Beers, Introduction to the Theory of Error, Addison-Wesley Publishing Co., Inc., Cambridge, Mass., 1953.
4. Technical Report on Fatigue Properties - SAE J1099, Society of Automotive Engineers, Inc., February 1975.
5. R.G. Lambert, "Computation Methods," Navy Contract N00019-78-C-0407, March 1980.
6. A. Papoulis, Probability, Random Variables, and Stochastic Processes, McGraw-Hill Book Co., New York, 1965.

7. R.G. Lambert, "Criteria for Accelerated Random Vibration Tests," Proc. of Institute of Environmental Sciences Symposium, May 1980.

#### APPENDIX A DERIVATION OF EXPONENTIAL RANDOM FATIGUE CURVE

$$\tilde{N}_f = \frac{1}{\int_0^{\infty} G(S) dS} = \frac{1}{\frac{1}{\sigma \bar{A}^{\beta}} \int_0^{\infty} S^{\beta} e^{-S/\sigma} dS}$$

Substitute  $x = \beta + 1$ ;  $z = S/\sigma$

$$\tilde{N}_f = \frac{1}{\left[\frac{\sigma}{\bar{A}}\right]^{\beta} \int_0^{\infty} z^{x-1} e^{-z} dz} = \frac{1}{\left[\frac{\sigma}{\bar{A}}\right]^{\beta} \Gamma(\beta + 1)}$$

or

$$\sigma = \frac{\bar{A}}{[\Gamma(\beta + 1)]^{1/\beta}} \tilde{N}_f^{-1/\beta} = \bar{C}_E \tilde{N}_f^{-1/\beta}$$

where

$$\bar{C}_E = \frac{\bar{A}}{[\Gamma(\beta + 1)]^{1/\beta}}$$

#### APPENDIX B DERIVATION OF RANDOM FATIGUE CURVE FOR SKEWED RAYLEIGH STRESS PEAK ENVELOPE

P(S) transformation:  $y = x^n$

$x \equiv$  Rayleigh pdf

$y \equiv$  skewed Rayleigh pdf

$n \equiv$  transformation constant

$$x_1 = y^{1/n} ; g'(x_1) = nx_1^{n-1}$$

$$P_y(y) = \frac{P_x(x_1)}{|g'(x_1)|} = \frac{P_x(x_1)}{n|y^{1-1/n}|}$$

$$P_x(x) = \frac{x}{\sigma^2} \exp \left[ -\frac{x^2}{2\sigma^2} \right]$$

$$P_y(y) = \frac{\frac{2}{n} - 1}{n\sigma^2} \exp \left[ -\frac{\frac{2}{n}}{2\sigma^2} \right]$$

Therefore, for the skewed Rayleigh

$$P(S) = \frac{\frac{2}{n} - 1}{n\sigma^2} \exp \left[ -\frac{\frac{2}{n}}{2\sigma^2} \right]$$

$$\tilde{N}_f = \frac{1}{\int_0^\infty G(S) dS}$$

$$= \frac{1}{\frac{1}{n\sigma^2 \bar{A}^\beta} \int_0^\infty S^{2/n + \beta - 1} e^{-\frac{S^{2/n}}{2\sigma^2}} dS}$$

Substitute

$$z = \frac{S^{2/n}}{2\sigma^2} \quad ; \quad x - 1 = \frac{n\beta}{2}$$

$$\begin{aligned} \tilde{N}_f &= \frac{1}{\frac{(2\sigma^2)^{\frac{n\beta}{2}}}{\bar{A}^\beta} \int_0^\infty z^{x-1} e^{-z} dz} \\ &= \frac{\bar{A}^\beta}{(2\sigma^2)^{\frac{n\beta}{2}} \Gamma(\frac{n\beta}{2} + 1)} \end{aligned}$$

or

$$\sigma = \left[ \frac{\bar{A}^{1/n}}{\sqrt{2}} \right] \left[ \frac{1}{\Gamma(\frac{n\beta}{2} + 1)} \right]^{\frac{1}{n\beta}} \tilde{N}_f^{-\frac{1}{n\beta}}$$

$$\sigma = \bar{C}_{skew} \tilde{N}_f^{-\frac{1}{n\beta}}$$

where

$$\bar{C}_{skew} = \left[ \frac{\bar{A}^{1/n}}{\sqrt{2}} \right] \left[ \frac{1}{\Gamma(\frac{n\beta}{2} + 1)} \right]^{\frac{1}{n\beta}} \text{ ksi}$$

#### APPENDIX C STRESS PEAK OCCURRENCE ESTIMATION

It can be shown [3, 6] that stress peaks of normalized magnitude  $L/\sigma$  will occur in a test of finite duration  $\bar{T}$  for a Gaussian random process of bandwidth  $B$

$$L/\sigma = \sqrt{2 \ln \bar{T} + 2 \ln B + 8.189}$$

where

$\bar{T}$  = test duration (minutes)

$B$  = stress bandwidth (Hz)

$L$  = stress level of largest peak

$\sigma$  = rms stress level

For  $B = 15$  Hz

$\bar{T}$ (min)	$L/\sigma$
5	4.10
10	4.26
30	4.52
60	4.67
1440 (24 hr)	5.31
28800 (20 days)	5.84

Thus, a 30-minute test will produce on the average one stress peak at a level of 4.52 times the rms stress value  $\sigma$ .

#### APPENDIX D P(S) AND G(S) EXPRESSIONS

TABLE 4. P(S) AND G(S) FUNCTIONS

Envelope Type	P(S)	G(S)
Rayleigh	$\frac{S}{\sigma^2} e^{-\frac{S^2}{2\sigma^2}}$	$\left[ \frac{1}{\sigma^2 \bar{A}^\beta} \right] S^{1+\beta} e^{-S^2/2\sigma^2}$
Exponential	$\frac{1}{\sigma} e^{-S/\sigma}$	$\left[ \frac{1}{\sigma \bar{A}^\beta} \right] S^\beta e^{-S/\sigma}$
Skewed Rayleigh	$\frac{2}{n\sigma^2} e^{-\frac{S^{2/n}}{2\sigma^2}}$	$\left[ \frac{1}{n\sigma^2 \bar{A}^\beta} \right] S^{\beta + \frac{2}{n} - 1} e^{-\frac{S^{2/n}}{2\sigma^2}}$

TABLE 5. MODE FUNCTIONS

Envelope Type	P(S) Mode, $S_p$	G(S) Mode, $S_o$
Rayleigh	$\sigma$	$\sigma\sqrt{\beta + 1}$
Skewed Rayleigh	$\left[ n\sigma^2 \left( \frac{2}{n} - 1 \right) \right]^{n/2}$	$\left[ n\sigma^2 \left( \beta + \frac{2}{n} - 1 \right) \right]^{n/2}$
Exponential	-	$\beta \sigma$

TABLE 6. DAMAGE FUNCTION G(S) STATISTICAL PROPERTIES

Envelope pdf Type	$E\{S\}$	$E\{S^2\}$
Raleigh	$\sigma\sqrt{\beta + 1.5}$	$\sigma^2(\beta + 2)$
Skewed Rayleigh	$(2\sigma^2)^{n/2} \left[ \frac{\Gamma\left\{\frac{n\beta}{2} + 1 + \frac{n}{2}\right\}}{\Gamma\left\{\frac{n\beta}{2} + 1\right\}} \right]$	$(2\sigma^2)^n \left[ \frac{\Gamma\left\{\frac{n\beta}{2} + 1 + n\right\}}{\Gamma\left\{\frac{n\beta}{2} + 1\right\}} \right]$
Exponential	$\sigma \left[ \frac{\Gamma(\beta + 2)}{\Gamma(\beta + 1)} \right]$	$\sigma^2 \left[ \frac{\Gamma(\beta + 3)}{\Gamma(\beta + 1)} \right]$
$\sigma_S = \text{Standard Deviation of } S \text{ for } G(S)$ $\sigma_S = \sqrt{E\{S^2\} - E^2\{S\}}$		

# FATIGUE LIFE EVALUATION, STOCHASTIC LOADING, AND MODIFIED LIFE CURVES

M. El Menoufy, H.H.E. Leipholz and T.H. Topper  
Department of Civil Engineering, University of Waterloo  
Waterloo, Ontario, Canada.

In this paper modified life curves have been introduced to facilitate the fatigue life predictions with sufficient accuracy for a material - (Van-80 steel) - subjected to stochastic loading programmes with a finite number of strain levels.

It is assumed that the material is elastic-plastic in the ideal sense and subjected to a loading programme with well defined strain peaks. It is also assumed that the material returns after each reversal to the zero-strain state. Such assumption is not restricting generality in a severe way. Any other strain level could have been chosen as the state of rest in place of the zero-strain level which has only a normalizing function. Keeping in so far the features of the loading programme very regular, and restricting the stochastic nature of the programme to the random sequence in which the possible strain peaks are distributed over time, makes it possible to rigorously evaluate the probability distribution of the hysteresis loops over the entire history, collected in classes of equal damaging events. This is achieved using combinatorics.

The Monte Carlo technique has been used to reproduce the load programmes, and a number of tests have been performed. Also, for these tests, knowing the actual fatigue life, the probability distribution of the closed hysteresis loops over the entire history can then be easily obtained.

For each test a straight line, tangent to the strain-life curve or the Smith Parameter-life curve, is constructed to satisfy Miner's theory, i.e.  $\sum n_i/N_i = 1.0$ . A family of lines is obtained, out of which an "average" line has been chosen for fatigue life predictions. It is of great importance to mention here that if the usual life curves before modification had been used for fatigue life evaluation, they would have resulted in large non-conservative errors.

Axially loaded smooth specimens of Van-80 steel have been tested to failure using 2-strain levels and 4-strain levels histories with different strain amplitudes and different probabilities. Life predictions were made using the proposed modified strain-life curve and modified Smith Parameter-life curve prior to testing a number of specimens. The actual lives are within a range of 0.81 to 1.68 of the predicted lives when using the modified strain-life curve and within a range of 0.89 to 1.40 when using the modified Smith Parameter-life curve.

During the course of this investigation, it has come to light that the loading programmes considered may not only in themselves have merit (as they may be appropriate models for practical situations of some significance) but that in addition they have great pedagogical value for any one concerned with the development of a sound theory of stochastic fatigue.

## NOMENCLATURE

$\Delta \epsilon$  Strain range for the closed hysteresis loop.  
 $\sigma_{\max}$  Max positive stress for the closed hysteresis loop.

E Modulus of elasticity.  
 $\pi_i$  Probability assigned for the  $i$ th strain level.  
k Length of the loading programme in terms of strain peaks.



N The expected number of strain peaks the material can resist under the stochastic loading programme.

D/A Digital to analog converter.

A/D Analog to digital converter.

$\sigma_F$  Fatigue strength coefficient.

b Fatigue strength exponent.

$\epsilon_F$  Fatigue ductility coefficient.

c Fatigue ductility exponent.

#### MATERIAL AND SPECIMENS

For this study, a Van-80 steel\* was used. The monotonic and cyclic stress-strain curves are shown in Fig. 1. Figs. 2 and 3 show the fatigue life behaviour of smooth specimens. Fig. 4 shows the shape and dimensions of the used smooth, unnotched, plate-specimens.

#### TEST EQUIPMENT AND CONTROL

All tests have been performed in the Fatigue Laboratory of the University of Waterloo using an MTS electro-hydraulic servo controlled machine. For random histories or experiments using variable amplitude load or strain waveforms, tests have been controlled by a digital process control computer, operating in conjunction with an analog computer. The computer programme which reconstructs the stochastic histories has been stored in the digital computer. The series of strain peaks are sent one at a time through the D/A converter to the analog computer's ramp generation circuit.

Upon completion of the ramp (the strain peak), the computer can read a strain response into the memory prior to the transmission of the next peak to the D/A converter.

Test environment consisted of room temperature of a relative humidity between 50 and 70 per cent.

#### MODELS FOR THE DISTRIBUTION OF THE HYSTERESIS LOOPS AND LIFE PREDICTION FOR A MATERIAL WITH IDEAL ELASTO-PLASTIC BEHAVIOUR, SUBJECTED TO A STOCHASTIC LOADING PROGRAMME WITH A FINITE NUMBER OF STRAIN LEVELS

##### A Model for Two-Strain Levels

For this model a material is considered which is subjected to a sequence of  $k$  strain peaks randomly chosen from two possible values,  $\epsilon_1 < 0 < \epsilon_2$ , with corresponding probabilities  $\pi_1, \pi_2$ ;  $\pi_1 + \pi_2 = 1$ . The values of  $|\epsilon_i|$  ( $i=1,2$ ) are taken, in this model, to be large enough to lay in the plastic domain of the material, Fig. 5. In this case, three different kinds of closed loops  $h_1, h_2, h_3$  are observed as indicated in Fig. 6, where  $h_3$  may be generated in two different ways as shown. It is to be noted, that

\* Product of Midland Steel Company.

the state of zero strain is here considered as a certain event occurring after every strain peak. This is only a slight restriction of generality as any other prescribed value between  $\epsilon_1$  and  $\epsilon_2$  could have been chosen as the "rest state" without any change in the following derivation. However, if no "rest state" would be defined, an uncountable set of possible closed loops would have been obtained. Therefore, such a situation will be ruled out henceforth.

Let  $P_k(R_0), P_k(R_1), P_k(R_2)$  denote the probabilities that after  $k$  strain peaks, the material is left in the "rest states"  $R_0, R_1, R_2$  respectively.

These probabilities are given by the following equations:

$$P_k(R_0) = 0, \quad (1)$$

$$P_k(R_1) = \pi_1, \quad (2)$$

$$P_k(R_2) = \pi_2. \quad (3)$$

For the  $2^k$  possible loading programmes with  $k$  peaks, the expected number of those programmes leading the material into the "rest state"  $R_i$  has been denoted by  $N_k(R_i)$ , which is given by:

$$N_k(R_1) = 2^k P_k(R_1) = 2^k \pi_1, \quad (4)$$

$$N_k(R_2) = 2^k P_k(R_2) = 2^k \pi_2.$$

Let  $H_k(h_i)$ , ( $i = 1, 2, 3$ ), denote the expected number of programmes of length  $k$  finishing with an  $h_i$ -loop.  $H_k(h_i)$  may be obtained by

$$H_k(h_1) = 2 \pi_1 N_{k-1}(R_1), \quad (6)$$

$$H_k(h_2) = 2 \pi_2 N_{k-2}(R_2), \quad k = 1, 2, 3, \dots \quad (7)$$

A relationship involving  $H_k(h_3)$  is not easily derived. For this reason the  $h_3$ -loops will be split into their two positive and negative reversals denoted by  $h_3^+$  and  $h_3^-$ . Instead of counting events corresponding to  $h_3$ , this will be done with respect to  $h_3^+$  and  $h_3^-$ :

$$H_k(h_3^+) = 2 \pi_2 N_{k-1}(R_1), \quad (8)$$

$$H_k(h_3^-) = 2 \pi_1 N_{k-1}(R_2), \quad k = 1, 2, 3, \dots \quad (9)$$

Substituting from (4) and (5) into (6) through (9) yields

$$H_k(h_1) = 2^k (\pi_1)^2, \quad (10)$$

$$H_k(h_2) = 2^k (\pi_2)^2, \quad (11)$$

$$H_k(h_3^+) = 2^k \pi_1 \pi_2, \quad (12)$$

$$H_k(h_3^-) = 2^k \pi_1 \pi_2, \quad k = 1, 2, 3, \dots \quad (13)$$

$H_k(h_3^+)$  is the expected number of programmes of length  $k$  finishing with the half of an  $h_3$ -loop, and must not be confounded with  $H_k(h_3)$ .

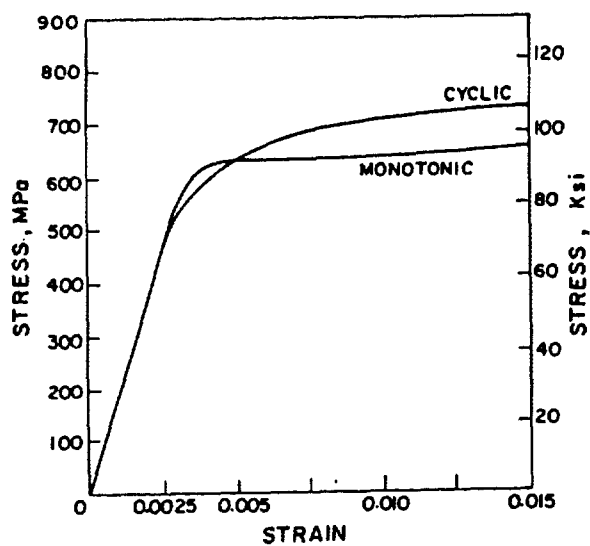


Fig. 1 - Monotonic and Cyclic Stress-Strain Curves of Van-80 Steel

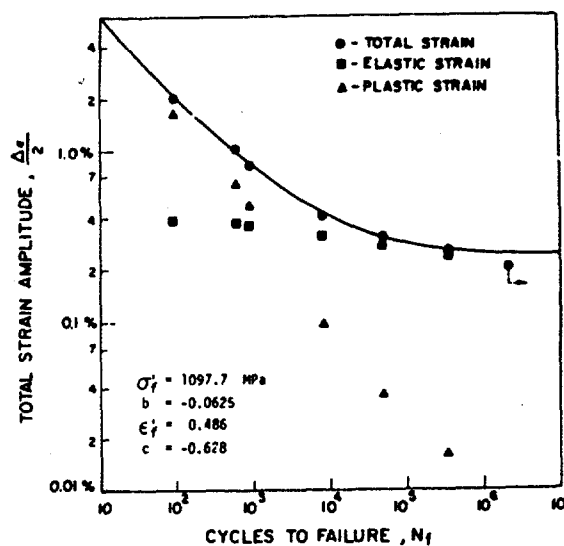


Fig. 2 - Strain-Life Curve (Van-80 Steel)

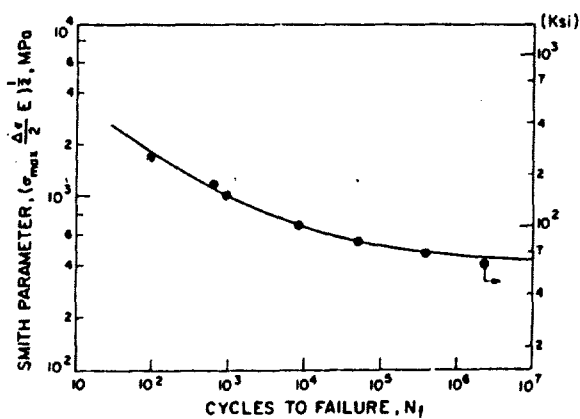


Fig. 3 - Smith Parameter-Life Curve (Van-80 Steel)

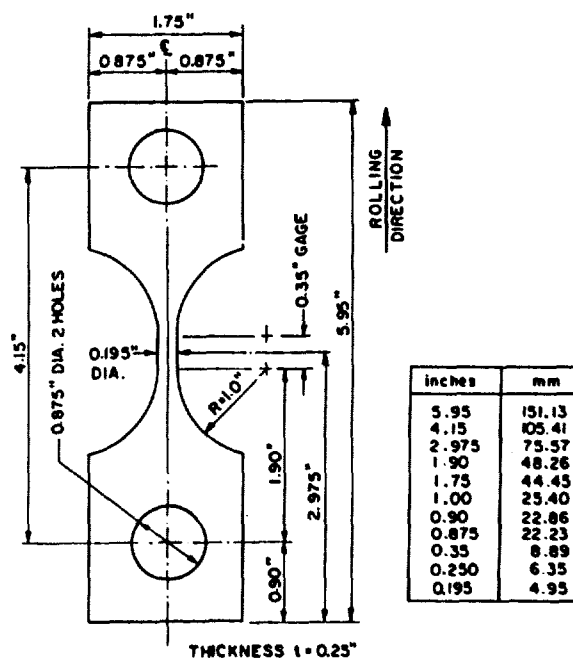


Fig. 4 - Shape and Dimensions of Specimen

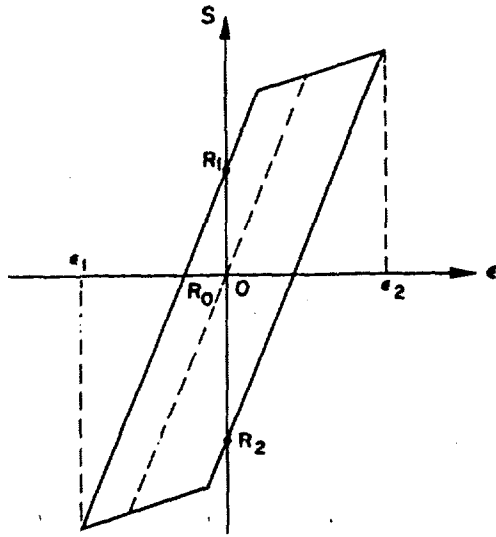
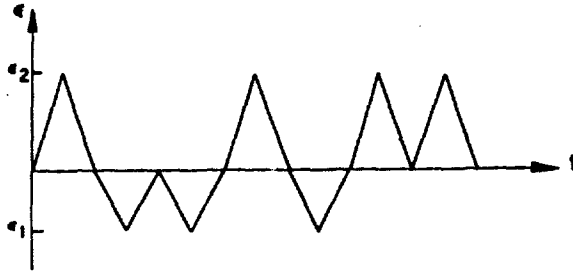


Fig. 5 - A Model for Two Strain Levels

$H_k(h_3^+)$  is given by:

$$\begin{aligned} H_k(h_3^+) &= H_k(h_3^+) + H_k(h_3^-) \\ &= 2^{k+1} \pi_1 \pi_2, \quad k = 1, 2, 3, \dots \end{aligned} \quad (14)$$

Let  $N_k(h_3^+)$  be the expected number of half  $h_3$ -loops contained in  $2^k$  possible loading programmes of length  $k$ .  $N_k(h_3^+)$  is determined by the following recursion formula:

$$N_k(h_3^+) = 2 N_{k-1}(h_3^+) + H_k(h_3^+), \quad k = 1, 2, 3, \dots, \quad (15)$$

with the initial condition

$$N_1(h_3^+) = 0. \quad (16)$$

The solution of (15), (16) is

$$N_k(h_3^+) = \sum_{u=2}^k 2^{k-u} H_u(h_3^+), \quad (17)$$

or, with the aid of (14),

$$N_k(h_3^+) = 2^{k+1} \pi_1 \pi_2 (k-1), \quad k = 1, 2, 3, \dots \quad (18)$$

Let  $n_k(h_3^+)$  be the expected number of half  $h_3$ -loops contained in one loading programme of length  $k$ . The expected number  $n_k(h_3)$  of  $h_3$ -loops

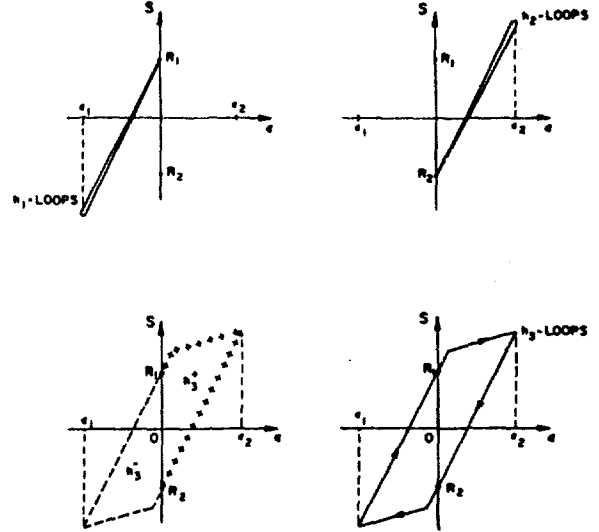


Fig. 6 - The Three Possible Kinds of Closed Loops

contained in such a programme is then

$$\begin{aligned} n_k(h_3) &= \frac{1}{2} \cdot n_k(h_3^+) = \frac{1}{2} \frac{N_k(h_3^+)}{2^k} \\ &= \pi_1 \pi_2 (k-1), \quad k = 1, 2, 3, \dots \end{aligned} \quad (19)$$

Let  $N_k(h_i)$ ,  $i = 1, 2$ , be the expected numbers of  $h_i$ -loops contained in  $2^k$  possible loading programmes of length  $k$  peaks. These two quantities satisfy the same recursion formula which already has been used for the computation of  $N_k(h_3^+)$ ,

$$\begin{aligned} N_k(h_i) &= 2 N_{k-1}(h_i) + H_k(h_i), \quad i = 1, 2 \\ & \quad k = 1, 2, 3, \dots, \end{aligned} \quad (20)$$

with the same initial condition:

$$N_1(h_i) = 0, \quad i = 1, 2. \quad (21)$$

Solving (20), (21) yields

$$\begin{aligned} N_k(h_i) &= 2^k (k-1) (\pi_i), \quad i = 1, 2 \\ & \quad k = 1, 2, 3, \dots \end{aligned} \quad (22)$$

Again, the expected numbers  $n_k(h_i)$ ,  $i = 1, 2$ , of the  $h_i$ -loops contained in a loading programme of length  $k$  peak are

$$n_k(h_i) = (k-1)(\pi_i)^2, \quad i = 1, 2$$

$$k = 1, 2, 3, \dots \quad (23)$$

The quantities obtained by equations (19) and (23) are not stationary. However, the small non-stationary effect which tends to zero when  $k \rightarrow \infty$  can be neglected, and the following asymptotic formulas may be obtained:

$$\left. \begin{aligned} n_k(h_1) &= k(\pi_1)^2, \\ n_k(h_2) &= k(\pi_2)^2, \\ n_k(h_3) &= k\pi_1\pi_2, \quad k = 1, 2, 3, \dots \end{aligned} \right\} \quad (24)$$

Recall  $n_k(h_i)$ ,  $i = 1, 2, 3$ , is the expected number of  $h_i$ -loops contained in a loading programme of length  $k$  strain peaks.

If the evaluation of the damage is based upon the assumption that all hysteresis loops with the same characteristics will cause the same amount of damage, Miner's theory, [1], can be used to predict the mean life  $N$  associated with the prescribed loading programme. It is of great value to emphasize here that Miner's rule is only a mathematical tool which is recognized to be valid from a probabilistic point of view, [2], and it is not responsible for the damage evaluation but it only adds up the accumulated damage that has been estimated according to any chosen damage parameter.

According to Miner's theory,

$$\sum_{i=1}^3 \frac{n_i(h_i)}{N_i} = 1 \quad (25)$$

from which together with (24) follows

$$N = \left[ \frac{\pi_1^2}{N_1} + \frac{\pi_2^2}{N_2} + \frac{\pi_1\pi_2}{N_3} \right]^{-1}, \quad (26)$$

where  $N_i$ , ( $i = 1, 2, 3$ ), denotes the mean life corresponding to a loading programme containing only  $h_i$ -loops.  $N_i$  has to be determined experimentally which proved to be extremely difficult due to the mean stress relaxation especially for hysteresis loops with some plasticity and this will lead to other methods for finding  $N_i$ .

#### A Model for Four-Strain Levels

This model has been studied by Philippin and Leipholz [3] and by Philippin, Topper and Leipholz [4] for which an ideal elasto-plastic material has been considered subjected to a stochastic loading programming consisting of a sequence of strain peaks, randomly chosen from four possible values  $\epsilon_{-2} < \epsilon_{-1} < 0 < \epsilon_1 < \epsilon_2$  with corresponding probabilities  $\pi_i$ ,

$$\sum_{i=-2}^{+2} \pi_i = 1, \quad i \neq 0 \quad (27)$$

In this model, the strain level zero is consid-

ered to be a certain event occurring after every strain peak of the loading programme. The material under consideration is supposed to be initially in the state of rest  $R_0$ , Fig. 7. The only condition to be satisfied with respect to the values of the possible strain levels  $\epsilon_i$  is that the different kinds of possible closed hysteresis loops registered in a stress-strain diagram of the material are consistent with the map in Fig. 7.

In this situation, five states of rest denoted by  $R_i$ ,  $i = -2, \dots, +2$ , are observed. The number of different kinds of possible closed hysteresis loops is 16, as shown in Fig. 8. Among these different kinds, 13 are degenerated, i.e., their corresponding surface areas are zero. They will be denoted by  $h(i, j)$  or by  $h(i, j, -j)$ ,  $i, j = -2, \dots, +2$ , where  $i$  indicates that they are born from the state of rest  $R_i$ , indices  $j$ ,  $-j$  indicate the strain peaks  $\epsilon_j$ ,  $\epsilon_{-j}$  responsible for their creation. The three remaining loops containing a non-zero surface area will be denoted by  $h(\alpha)$ ,  $\alpha = 0, \pm 2$ . The values  $\alpha = \pm 1$  will be used to designate the two positive and negative reversals which built the  $h(0)$ -loops. If the same kind of loops can be generated in two different ways, that is the case for  $h(i, i)$ ,  $i = \pm 1$ , one of them will be marked by a star. Fig. 8 shows the location of these loops in a stress strain diagram.

A similar procedure to that used previously, makes it possible for the authors to rigorously evaluate the probability distribution of hysteresis loops collected in classes of equal damaging events. The so obtained probability densities have then been used in Miner's theory yielding the mean life  $N$  of a specimen subjected to the described stochastic loading programme as

$$N = \left[ \sum_{i=1}^{16} \frac{E_i}{N_i} \right]^{-1}, \quad (28)$$

where the  $E_i$ ,  $i = 1, \dots, 16$ , are given in Table 1.

Recall that  $N$  is defined as the expected number of strain peaks the material can resist under the stochastic loading programme, while the mean life  $N_i$  is the expected number of  $h_i$ -loops the material can resist under application of the loading programme containing only  $h_i$ -loops.

#### LOAD PROGRAMME SIMULATION USING THE MONTE CARLO TECHNIQUE

The Monte Carlo technique has been used to reproduce the described stochastic loading programmes with two-strain and four-strain levels. For the sake of illustration, consider a stochastic loading programme of  $k$  strain peaks randomly chosen from the four possible values  $\epsilon_{-2} < \epsilon_{-1} < 0 < \epsilon_1 < \epsilon_2$  with corresponding probabilities  $\pi_i$ , where

$$\sum_{i=-2}^{+2} \pi_i = 1.$$

(29)

Let  $\epsilon$  be a discrete random variable having the probability and cumulative distributions as shown in Table 2.

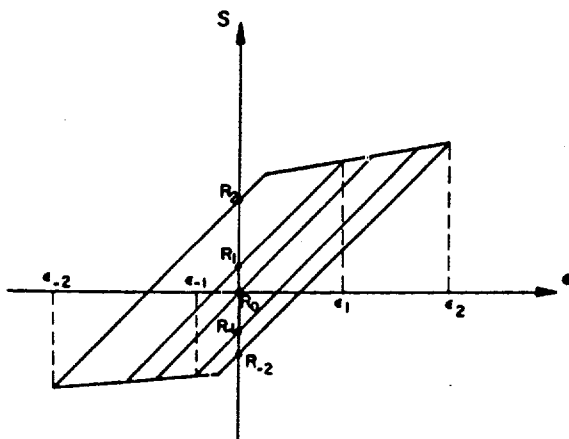


Fig. 7 - A Model for Four Strain Levels

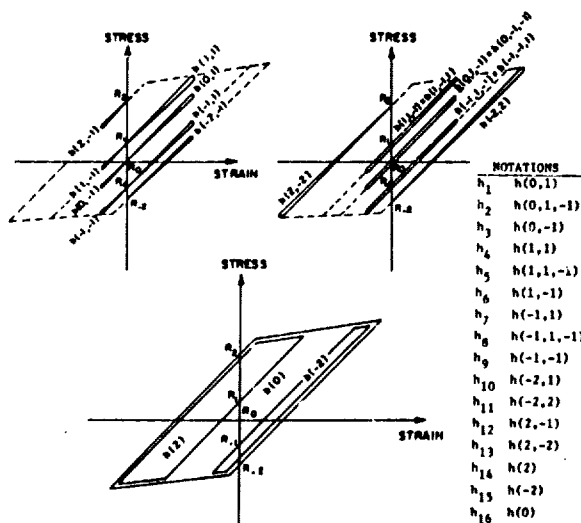


Fig. 8 - The Sixteen Different Kinds of Closed Loops

$\epsilon$	$\pi_i$	$F(\epsilon)$	$\pi_i$
1	0	0.20	0.00 - 0.20
2	0	0.60	>0.20 - 0.60
3	0	0.75	>0.60 - 0.75
4	0	1.00	>0.75 - 1.00
5	0		
6	0		
7	0		
8	0		
9	0		
10	0		
11	0		
12	0		
13	0		
14	0		
15	0		
16	0		

$$v = (v_1 + v_2)$$

$$n_k(h_1) = k \pi_1$$

where  $n_k(h_1)$  is the number of  $h_1$ -loops contained in a loading programme of length  $k$  strain peaks.

Table 1

$\epsilon$	$p(\epsilon)$	$F(\epsilon)$	Simulation Numbers
$\epsilon_{-2}$	0.20	0.20	0.00 - 0.20
$\epsilon_{-1}$	0.40	0.60	>0.20 - 0.60
$\epsilon_1$	0.15	0.75	>0.60 - 0.75
$\epsilon_2$	0.25	1.00	>0.75 - 1.00

Table 2

A Monte Carlo simulation of this distribution can be performed by comparing a sequence of random numbers to the simulation numbers in the last column of the table above. The mechanics of this technique is demonstrated in Fig. 9. Notice that the proportion of simulation numbers for each  $\epsilon$  value corresponds to the probability associated with that  $\epsilon$  value. Fig. 10 shows samples of the reproduced load programmes. For this simulation, as many random numbers as the desired size of the simulated sample are needed. A computer routine has been used to generate the required number of random numbers. Several such generators have been developed and described in [5]. The generated RN's should be uniformly distributed over the interval 0.0 + 1.0. The goodness-of-fit of this uniform distribution has been checked and accepted using the chi-squared test.

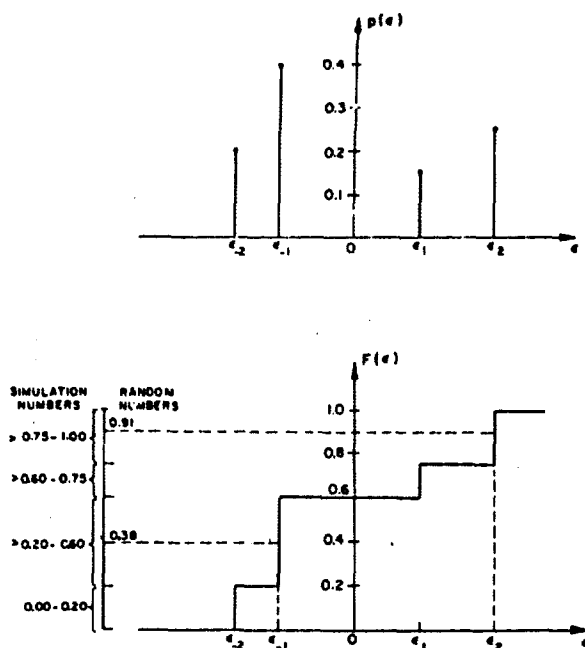


Fig. 9 - Relationships of  $\epsilon, p(\epsilon), F(\epsilon)$ , Simulation Numbers and Random Numbers

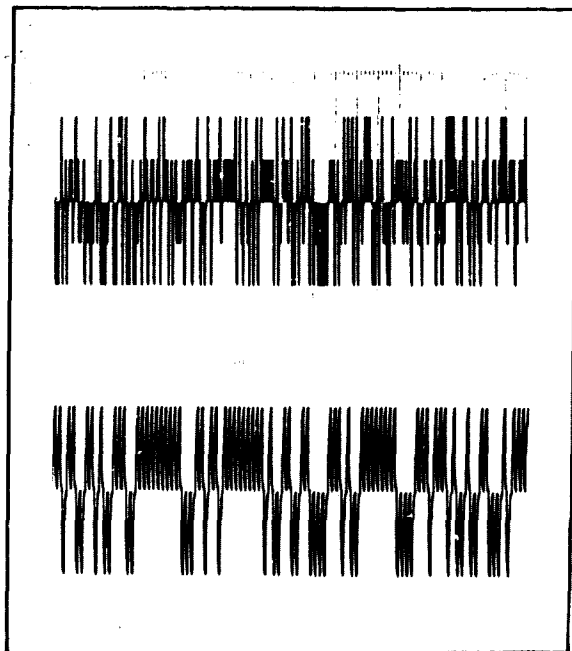


Fig. 10 - Sample of the Reproduced 2-Levels and 4-Levels Histories

#### MODIFIED LIFE CURVES

As mentioned before, it was difficult, if not impossible, to determine the  $N_1$  values (Equations 26 and 28) experimentally due to the effect of mean stress relaxation.

Several attempts were made to predict fatigue lives using the strain range,  $\Delta\epsilon$ , as the damage parameter and the strain-life curve to determine the corresponding  $N_1$  values, but large non-conservative errors did occur. Other attempts for fatigue life predictions were made using the Smith Parameter-life curve, [6], which accounts for the mean stress effects but which still yielded large non-conservative errors of magnitude up to three times that of the actual life. These large errors are due to the sequence and interaction effects.

The preceding discussion suggests therefore the introduction of so called modified life curves from which the  $N_1$  values can be obtained more accurately so that the subsequent life prediction can be carried out in a more realistic way.

Eight tests have been performed with two and four-strain levels. For these tests, the actual lives are known, and the probability distribution of the closed hysteresis loops over the entire history could easily be obtained using equation (24) and the values of Table 1. For each test, a straight line tangent to the strain-life curve or to the Smith Parameter-life curve was constructed as to satisfy Miner's rule, i.e.  $\sum n_i/N_i = 1$ . A family of lines was obtained in this way out of which an "average" line was chosen for fatigue life predictions. Fig. 11 and Fig. 12 show this family of lines as well as the average lines used for life prediction.

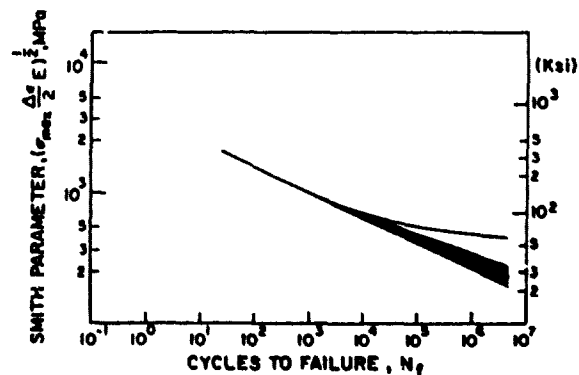
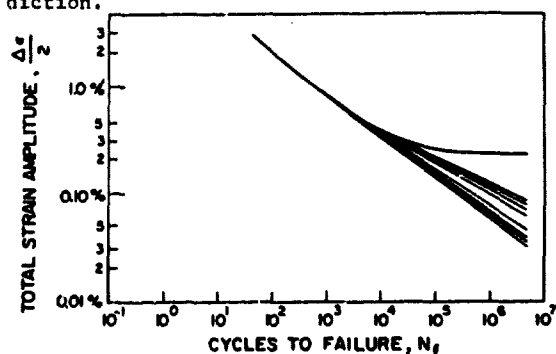


Fig. 11 - Family of Lines Satisfying Miner's Rule

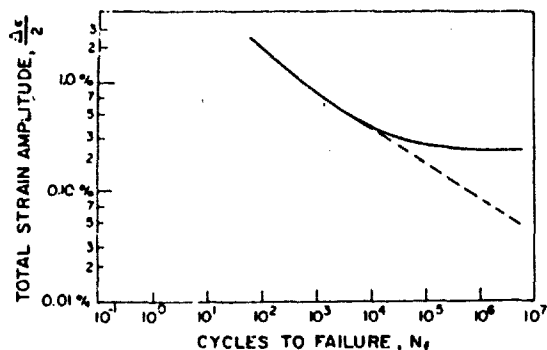


Fig. 12(a) - Modified Strain-Life Curve

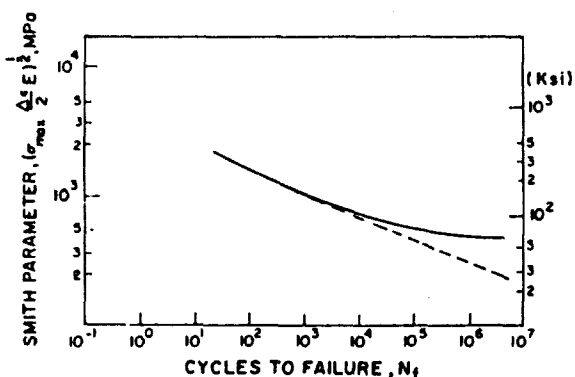


Fig. 12(b) - Modified Smith Parameter-Life Curve

#### LIFE PREDICTIONS AND RESULTS

Axially loaded smooth specimens of Van-80 steel have been tested to failure under strain-control conditions. Seventeen tests were performed using two-strain levels and four-strain levels histories with different strain amplitudes and different probability distributions. The data and results of these tests are shown in Tables 3 and 4, and in Fig. 13 and 14. Life predictions were made prior to these tests using the proposed modified strain-life curve and the modified Smith Parameter-life curve. The actual lives from these tests are within a range of 0.81 to 1.68 of the predicted lives when using the modified strain-life curve and within a range of 0.89 to 1.40 when using the modified Smith Parameter-life curve.

#### CONCLUDING REMARKS

The main idea of this investigation was, firstly, to choose degenerated random load histories which, simple as they are, have made it possible to rigorously predict the distribution of the closed hysteresis loops over the entire history. These load histories have been reproduced using the Monte Carlo technique, and the probability distributions have been checked for the goodness-of-fit using the chi-squared test.

#### RESULTS FOR 2-STRAIN LEVELS HISTORIES

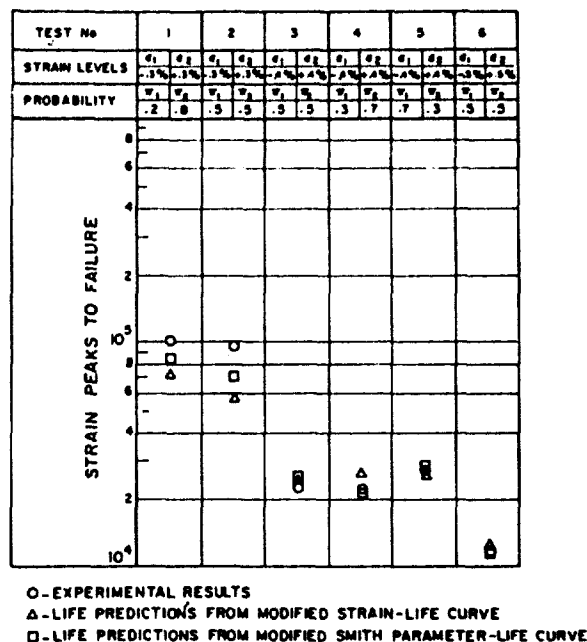


Fig. 13

#### RESULTS FOR 4-STRAIN LEVELS HISTORIES

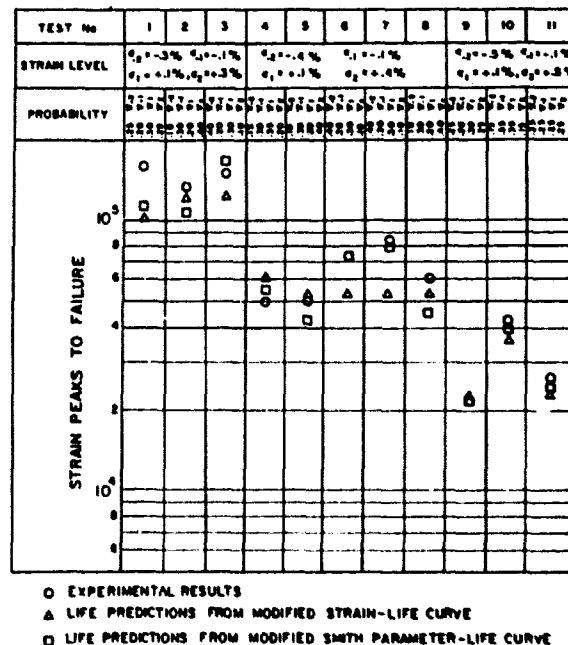


Fig. 14

Test #	Probability Distribution		N experiment (strain peaks)	N predicted from Mod. S-N Curve (strain peaks)	N predicted from Mod. Smith-life Curve (strain peaks)
	$\epsilon_1$	$\epsilon_2$			
Strain Levels $\epsilon_1 = -0.3\%$ , $\epsilon_2 = +0.3\%$					
1	0.20	0.80	100,792	72,748	84,178
2	0.50	0.50	96,492	57,273	71,029
Strain Levels $\epsilon_1 = -0.4\%$ , $\epsilon_2 = +0.4\%$					
3	0.50	0.50	22,482	23,743	24,920
4	0.30	0.70	21,304	26,284	22,260
5	0.70	0.30	36,845	26,284	27,703
Strain Levels $\epsilon_1 = -0.5\%$ , $\epsilon_2 = +0.5\%$					
6	0.50	0.50	11,646	12,014	11,726

Table 3

Test #	Probability Distribution				N experiment (strain peaks)	N predicted from Mod. S-N Curve (strain peaks)	N predicted from Mod. Smith-life Curve (strain peaks)
	$\epsilon_2$	$\epsilon_1$	$\epsilon_1$	$\epsilon_2$			
Strain Levels $\epsilon_2 = -0.3\%$ , $\epsilon_1 = -0.1\%$ $\epsilon_1 = +0.1\%$ , $\epsilon_2 = +0.3\%$							
1	0.25	0.20	0.30	0.25	157,476	103,576	112,353
2	0.10	0.30	0.20	0.40	131,500	121,994	106,798
3	0.40	0.20	0.30	0.10	148,989	121,994	163,492
Strain Levels $\epsilon_2 = -0.4\%$ , $\epsilon_1 = -0.1\%$ $\epsilon_1 = +0.1\%$ , $\epsilon_2 = +0.4\%$							
4	0.15	0.30	0.35	0.20	49,486	61,747	55,834
5	0.10	0.30	0.20	0.40	50,648	53,475	42,550
6	0.40	0.20	0.30	0.10	73,209	53,475	73,795
7	0.40	0.20	0.30	0.10	83,728	53,475	80,315
8	0.10	0.30	0.20	0.40	59,839	53,475	46,365
Strain Levels $\epsilon_2 = -0.5\%$ , $\epsilon_1 = -0.1\%$ $\epsilon_1 = +0.1\%$ , $\epsilon_2 = +0.5\%$							
9	0.25	0.20	0.30	0.25	21,803	22,903	21,978
10	0.15	0.35	0.35	0.15	42,860	36,867	39,580
11	0.25	0.25	0.25	0.25	25,960	22,772	23,630

Table 4

Secondly, it was of great importance to try to find an adequate means of evaluating the damage and to choose a proper damage parameter to collect in classes of equally damaging events. For this investigation, two different damage parameters, the strain range and the Smith Parameter,  $[(\sigma_{\max} \cdot \Delta \epsilon / 2 \cdot E)^{1/2}]$ , have been used together with modified life curves for an appropriate evaluation of the damage.

If these two, above mentioned points, are observed, Miner's rule, which is only a mathematical tool, [2], can then safely be applied to predict life.

The modified life curves have proved to be very helpful in getting sufficiently accurate life predictions. It seems to be the case that the modified curves can be obtained from the common life curves by constructing the tangent to these curves at the "transition life". But this assertion has to be confirmed through further investigations and using different materials.

During the course of this research, it has become very clear that the damage process should not be categorized as an interaction-free-process. In other words, the assumption, that the damage caused by any group of cycles does not depend on the previously acquired damage, is certainly not a valid one.

Finally, one should not try to modify Miner's rule, which is only a mathematical tool, but one should better try to find an appropriate means of evaluating the damage during the process of random fatigue.

#### ACKNOWLEDGEMENT

This research was carried out under support of the National Research Council of Canada under Grants No. A7297 and A1694.

#### REFERENCES

- [1] Miner, M.A., "Cumulative Damage in Fatigue", Journal of Appl. Mech., Vol. 12, 1945, pp. A159-A164.
- [2] Philippin, G.A., Topper, T.H. and Leipholz, H.H.E., "Mean Life Evaluation for a Stochastic Loading Programme with a Finite Number of Strain Levels Using Miner's Rule", 46th Symposium on Shock and Vibration, 1975, San Diego, California.
- [3] Philippin, G.A. and Leipholz, H.H.E., "On the Distribution of the Stress States of a Material with Ideal Elasto-plastic Behaviour, Subjected to a Finite Number of Strain Levels", Mech. Res. Comm., Vol. 2, 1975, pp. 215-220.
- [4] Philippin, G.A., Topper, T.H. and Leipholz, H.H.E., "On Mean Life Evaluation of a Material with Ideal Elasto-Plastic Behaviour, Subjected to a Stochastic Loading Programme with a Finite Number of Strain Levels", Bulletin 47, The Shock and Vibration Information Center, Naval Research Laboratory, Washington, D.C., 1977.
- [5] Hull, T.E., and Dobel, A.R., "Random Number Generators", SIAM Review, 4:3, July 1962.
- [6] Smith, K.N., Watson, P., and Topper, T.H., "A Stress-Strain Function for the Fatigue of Metals", Journal of Materials, JMLSA, Vol. 5, No. 4, pp. 767-778, Dec. 1970.



# THE EFFECTS OF ENDURANCE LIMIT AND CREST FACTOR ON TIME TO FAILURE UNDER RANDOM LOADING

Allen J. Curtis, Sally M. Moite

Hughes Aircraft Company  
Culver City, California

## ABSTRACT

Customary calculations of time to failure under random loading have been based on three concepts: (1) Miner's Cumulative Damage Theory; (2) the loading is narrowband random giving complete stress reversals between successive extrema which are Rayleigh distributed; and (3) the  $\sigma$ -N curve may be defined by  $N\sigma^b = c$ .

This paper is an extension of previous analyses by Miles, and by Curtis, Tinling and Abstein to determine the increase in average time to failure which may be expected due to: (1) the absence of stresses in excess of  $\pm 3\bar{\sigma}$  and (2) the lack of fatigue damage for stress reversals less than the endurance limit. The increase due to the latter factor is given as a function of the ratio of the endurance limit,  $\sigma_e$ , to the RMS stress,  $\bar{\sigma}$ , for three typical values of the slope,  $b$ , of the  $\sigma$ -N curve. The increase in time is presented as the dimensionless ratio of the time without consideration of these effects to the time with them included.

## INTRODUCTION

Customary calculations of time to failure under random loading have been based on three concepts:

1. Miner's Cumulative Damage Theory;
2. the loading is narrowband random giving complete stress reversals between successive extrema which are Rayleigh distributed; and
3. the  $\sigma$ -N curve may be defined by  $N\sigma^b = c$ .

The second concept permits, mathematically, an infinite crest factor while the third factor implies that no stress amplitude is too small to not cause cumulative damage, i.e., the endurance limit is zero. Both these concepts lead to pessimistic estimates of the average time to failure. First, analysis and test are generally based on a crest-factor of three or, in more common terms, the distribution of peaks is limited to no more than  $\pm 3\bar{\sigma}$ . Secondly, certain materials, particularly ferrous metals, do exhibit distinct endurance limits under sinusoidal loading.

This paper is an extension of previous analyses by Miles [Ref. 1], and by Curtis, Tinling and Abstein [Ref. 2] to determine the increase in average time to failure which may be expected due to: (1) the absence of stresses in excess of  $\pm 3\bar{\sigma}$  and (2) the lack of fatigue damage for stress reversals less than the endurance limit.

## MATHEMATICAL DERIVATION

The average time to failure under random loading can be calculated from the following three fundamental relationships:

1. *Miner's Rule for Cumulative Damage.* This rule postulates that failure will occur when the sum of the cycle ratios equals a constant  $D$ , i.e.

$$\sum \frac{n_i}{N_i} = D \quad (1)$$

where:

$n_i$  = number of cycles at stress amplitude  $\sigma_i$

$N_i$  = number of cycles to failure at stress amplitude  $\sigma_i$

$D_s$  = constant for constant amplitude sinusoidal stress,  $0.3 < D_s < 3.0$ , average = 1.0

$D_r$  = constant for random stress,  $0.2 < D_r < 0.67$ , average = 0.5

2. *The random loading has a narrowband spectrum.* This implies complete stress reversals between successive extrema (for zero average stress). Further, the extrema, i.e., peak stresses, are Rayleigh distributed (as shown in Figure 1) defined by the probability density function:

$$p(\sigma/\bar{\sigma}) = \frac{\sigma}{\bar{\sigma}} e^{-\frac{1}{2} \left(\frac{\sigma}{\bar{\sigma}}\right)^2} \quad (2)$$

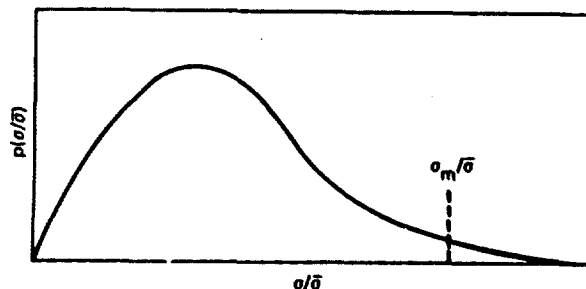


Figure 1. Rayleigh distribution of stress amplitudes.

3. The fatigue curve of the material may be expressed as:

$$N\sigma^b = c, \sigma \geq \sigma_e \quad (3)$$

where:

$N$  = number of cycles to failure at sinusoidal stress amplitude  $\sigma$

$\sigma$  = stress amplitude (peak stress)

$\sigma_e$  = endurance limit

$c, b$  = constants,  $3 \leq b \leq 25$ , average  $b = 9$

This expression is plotted in Figure 2.

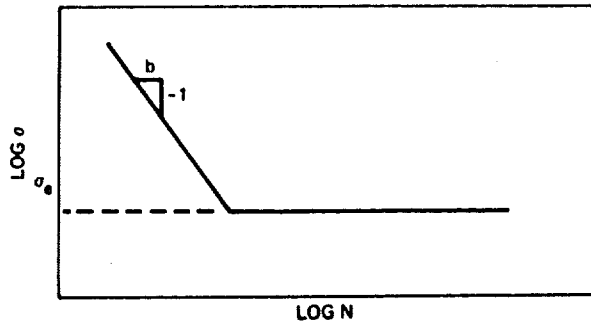


Figure 2. Typical  $\sigma$ - $N$  fatigue curve with endurance limit  $\sigma_e$  and slope  $-1/b$ .

A modified expression of Miner's Rule for narrow-band random loading is:

$$D_r = \sum_i \frac{n_i}{N_i} = \sum_i \frac{\sigma_i^b n_i}{\sigma_e^b N_i} = \frac{1}{c} \int_{\sigma_e}^{\sigma_m} \sigma^b p\left(\frac{\sigma}{\bar{\sigma}}\right) d\left(\frac{\sigma}{\bar{\sigma}}\right) \quad (4)$$

$$= \frac{f_c T}{c} \int_{\sigma_e}^{\sigma_m} \sigma^b p\left(\frac{\sigma}{\bar{\sigma}}\right) d\left(\frac{\sigma}{\bar{\sigma}}\right) / \int_{\sigma_e}^{\sigma_m} \sigma^b p\left(\frac{\sigma}{\bar{\sigma}}\right) d\left(\frac{\sigma}{\bar{\sigma}}\right)$$

where:

$\sigma_m$  = the maximum stress amplitude

$f_c$  = the center frequency of narrowband spectrum

$T$  = cumulative time of loading.

It is assumed that the random loading is limited ("clipped") to a maximum value  $\sigma_m/\bar{\sigma}$ , typically  $\pm 3$ , and that stress cycles below the endurance limit do not contribute to cumulative damage.

Previous analyses [References 1 and 2] have been performed for  $\sigma_m \rightarrow \infty$  and  $\sigma_e \rightarrow 0$ , i.e., no limiting of the Rayleigh distribution and zero endurance limit. The following analysis does not employ these restrictions.

If an equivalent cyclic stress amplitude  $\sigma^*$  is defined such that the damage accumulated in any number of cycles by  $\sigma^*$  is the same as for the random stress,

$$1 = D_r = \sum_i \frac{n_i}{N_i} = \sum_i \frac{(\sigma^*)^b n_i}{c} = \frac{(\sigma^*)^b f_c T}{c} \quad (5)$$

then,

$$\frac{(\sigma^*)^b f_c T}{c} = \frac{f_c T}{c} \int_{\sigma_e}^{\sigma_m} \sigma^b p\left(\frac{\sigma}{\bar{\sigma}}\right) d\left(\frac{\sigma}{\bar{\sigma}}\right) / \int_{\sigma_e}^{\sigma_m} \sigma^b p\left(\frac{\sigma}{\bar{\sigma}}\right) d\left(\frac{\sigma}{\bar{\sigma}}\right)$$

or

$$\sigma^* = \frac{1}{(D_r)^{1/b}} \left( \frac{\int_{\sigma_e}^{\sigma_m} \sigma^b p\left(\frac{\sigma}{\bar{\sigma}}\right) d\left(\frac{\sigma}{\bar{\sigma}}\right)}{\int_{\sigma_e}^{\sigma_m} \sigma^b p\left(\frac{\sigma}{\bar{\sigma}}\right) d\left(\frac{\sigma}{\bar{\sigma}}\right)} \right)^{1/b} \quad (6)$$

Let

$$u = \frac{\sigma}{\bar{\sigma}}, \alpha = \frac{\sigma_m}{\bar{\sigma}}, \tau = \frac{\sigma_e}{\bar{\sigma}}$$

Then

$$\sigma^* = \frac{1}{(D_r)^{1/b}} \left[ \frac{\int_{\tau}^{\alpha} u^b e^{-u^2/2} du}{\int_{\tau}^{\alpha} u e^{-u^2/2} du} \right]^{1/b} \quad (7)$$

$$\sigma^* = \frac{\bar{\sigma}}{(D_r)^{1/b}} \left( \frac{\int_{\tau}^{\alpha} u^{b+1} e^{-u^2/2} du}{\int_{\tau}^{\alpha} u e^{-u^2/2} du} \right)^{1/b}$$

$$\sigma^* = \frac{\bar{\sigma}}{(D_r)^{1/b}} \frac{1}{(1 - e^{-\alpha^2/2})^{1/b}} \left( \int_{\tau}^{\alpha} u^{b+1} e^{-u^2/2} du \right)^{1/b} \quad (8)$$

Substituting  $z = u^2/2$  transforms the integral to the incomplete  $\Gamma$  function,  $\Gamma_s(p) = \int_0^s z^{p-1} e^{-z} dz$ . Let  $z = u^2/2$ ,  $dz = u du$ , then if  $u = \alpha$ ,  $z = \alpha^2/2$ ; if  $u = \tau$ ,  $z = \tau^2/2$  and  $u = \sqrt{2z}$ .

$$\sigma^* = \frac{\bar{\sigma}}{(D_r)^{1/b}} \frac{\sqrt{2}}{(1 - e^{-\alpha^2/2})^{1/b}} \left( \int_{\tau^2/2}^{\alpha^2/2} z^{b/2} e^{-z} dz \right)^{1/b} \quad (9)$$

$$= \frac{\bar{\sigma} \sqrt{2}}{(D_r)^{1/b} (1 - e^{-\alpha^2/2})^{1/b}} \left( \Gamma_{\alpha^2/2} \left( \frac{b}{2} + 1 \right) - \Gamma_{\tau^2/2} \left( \frac{b}{2} + 1 \right) \right)^{1/b}$$

When  $\tau = 0$  and  $\alpha \rightarrow \infty$ , this equation for  $\sigma^*$  is the same as Equation 3-37 in Reference [1], except that in that equation, Stirling's formula was used to evaluate the gamma function.

The time to failure is determined from:

$$T = \frac{N}{f_c} = \frac{c}{f_c (\sigma^*)^b}$$

or

$$T = \frac{c D_r (1 - e^{-\alpha^2/2})}{f_c (\bar{\sigma} \sqrt{2})^b \left( \Gamma_{\alpha^2/2} \left( \frac{b}{2} + 1 \right) - \Gamma_{\tau^2/2} \left( \frac{b}{2} + 1 \right) \right)} \quad (10)$$

Table 1 lists  $\Gamma_{1/2}((b/2) + 1)$  for  $b = 3, 6.5, 9, 25$  together with values of  $(1 - e^{-r^2/2})$  for  $0.10 \leq r \leq 4.0$  in 0.1 increments.

TABLE 1

$r$	$\Gamma_{1/2}(\frac{b}{2} + 1)$				$1 - e^{-r^2/2}$
	$b = 3.0$	$b = 6.5$	$b = 9.0$	$b = 25.0$	
0.10	0.0000	0.0	0.0	0.	0.005
0.20	0.0000	0.0	0.0	0.	0.020
0.30	0.0002	0.000	0.0	0.	0.044
0.40	0.0007	0.000	0.0	0.	0.077
0.50	0.0020	0.000	0.000	0.	0.118
0.60	0.0048	0.000	0.000	0.	0.165
0.70	0.0100	0.000	0.000	0.	0.217
0.80	0.0185	0.001	0.000	0.	0.274
0.90	0.0314	0.004	0.001	0.	0.333
1.00	0.0498	0.008	0.003	0.	0.393
1.10	0.0746	0.017	0.007	0.	0.454
1.20	0.1065	0.033	0.016	0.	0.513
1.30	0.1460	0.059	0.035	0.	0.570
1.40	0.1932	0.099	0.072	0.	0.625
1.50	0.2478	0.159	0.136	0.	0.675
1.60	0.3092	0.244	0.243	0.	0.722
1.70	0.3763	0.359	0.413	0.	0.764
1.80	0.4479	0.510	0.672	0.	0.802
1.90	0.5227	0.702	1.048	256.	0.836
2.00	0.5990	0.937	1.575	256.	0.865
2.10	0.6753	1.217	2.284	512.	0.890
2.20	0.7501	1.542	3.210	1280.	0.911
2.30	0.8222	1.908	4.380	3328.	0.929
2.40	0.8903	2.310	5.816	8448.	0.944
2.50	0.9536	2.744	7.528	19968.	0.956
2.60	1.0115	3.199	9.517	45312.	0.966
2.70	1.0635	3.667	11.770	98304.	0.974
2.80	1.1096	4.140	14.260	204288.	0.980
2.90	1.1498	4.606	16.950	406528.	0.985
3.00	1.1844	5.058	19.791	776448.	0.989
3.10	1.2136	5.488	22.729	1427456.	0.992
3.20	1.2380	5.890	25.704	2530560.	0.994
3.30	1.2581	6.259	28.656	4333056.	0.996
3.40	1.2744	6.592	31.531	7179264.	0.997
3.50	1.2874	6.888	34.277	11527168.	0.998
3.60	1.2978	7.146	36.852	17960704.	0.998
3.70	1.3058	7.368	39.224	27195392.	0.999
3.80	1.3120	7.556	41.372	40066816.	0.999
3.90	1.3167	7.712	43.283	57502976.	1.000
4.00	1.3202	7.841	44.956	80484608.	1.000

$\Gamma(b/2 + 1)$			
$b = 3.0$	$b = 6.5$	$b = 9.0$	$b = 25.0$
1.3293	8.285	52.343	1710540800.

#### ADJUSTED TIME TO FAILURE

Let  $T_1$  be the average time to failure for the case when  $r = \sigma_e/\bar{\sigma} = 0$ , and  $\alpha = \sigma_m/\bar{\sigma} = \infty$ , that is, for a zero endurance limit and no limiting of the maximum stress.

Then

$$T_1 = \frac{c D_r}{f_s (\pi \sqrt{2})^b \Gamma((b/2) + 1)} \quad (11)$$

The ratio of this time to failure to the time to failure with a non-zero endurance limit and a peak stress cut-off of  $\alpha = \sigma_m/\bar{\sigma} = 3$  is

$$\frac{T_1}{T} = \frac{\Gamma_{1/2}((b/2) + 1) - \Gamma_{1/2}((b/2) + 1)}{(1 - e^{-4.5}) \Gamma((b/2) + 1)} \quad 0 \leq r \leq 3 \quad (12)$$

This adjustment to the time to failure is plotted in Figure 3 for  $b = 3, 6.5$ , and  $9$  and is tabulated in Table 2.

It should be noted that  $T_1/T$  is independent of  $D_r$ ,  $D_s$ ,  $c$  and  $f_s$ .

#### EFFECTS OF CREST FACTOR

The effects on fatigue life of limiting the crest factor can be inferred from Figure 3. The intercept of the curves with the ordinate axis, i.e., for  $\sigma_e/\bar{\sigma} = 0$ , provides the change in fatigue life for a typical crest factor of 3 compared to the theoretical infinite value. As the slope of the  $\sigma$ - $N$  curve becomes steeper (larger  $b$ ), the limiting effect becomes more pronounced. For a typical value,  $b = 6.5$ , fatigue life increases to  $1/0.63 - 1 = 0.59$ , i.e., 59 percent.

#### EFFECTS OF ENDURANCE LIMIT

The effects on fatigue life as a function of endurance limit are shown in Figure 3, for  $\sigma_m/\bar{\sigma} = 3$  and  $b = 3.0, 6.5$  and  $9.0$ . When  $\sigma_e/\bar{\sigma} = 3.0$ , infinite life is achieved since no stresses exceed the fatigue limit. For small values of

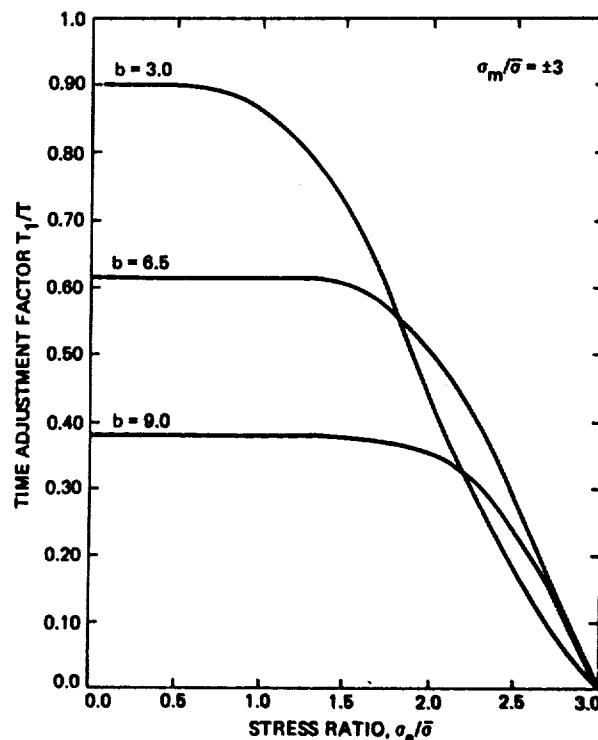


Figure 3. Time-to-failure adjustment factor

TABLE 2.

Time To Failure Adjustment Factor  $T_1/T$   
 $T_1/T \sigma_m/\bar{\sigma} = 3$

$\sigma_c/\bar{\sigma}$	b = 3.0	b = 6.5	b = 9.0
0.0	0.9009	0.6174	0.3824
0.10	0.9009	0.6174	0.3824
0.20	0.9009	0.6174	0.3824
0.30	0.9008	0.6174	0.3824
0.40	0.9001	0.6174	0.3824
0.50	0.8994	0.6174	0.3824
0.60	0.8973	0.6174	0.3824
0.70	0.8933	0.6173	0.3824
0.80	0.8869	0.6172	0.3823
0.90	0.8771	0.6169	0.3823
1.00	0.8631	0.6164	0.3823
1.10	0.8442	0.6153	0.3822
1.20	0.8199	0.6134	0.3820
1.30	0.7899	0.6102	0.3817
1.40	0.7540	0.6053	0.3810
1.50	0.7124	0.5980	0.3797
1.60	0.6658	0.5877	0.3777
1.70	0.6147	0.5736	0.3744
1.80	0.5602	0.5551	0.3694
1.90	0.5033	0.5317	0.3621
2.00	0.4455	0.5030	0.3519
2.10	0.3873	0.4688	0.3382
2.20	0.3303	0.4292	0.3203
2.30	0.2755	0.3846	0.2977
2.40	0.2237	0.3354	0.2700
2.50	0.1755	0.2825	0.2369
2.60	0.1315	0.2269	0.1985
2.70	0.0919	0.1698	0.1550
2.80	0.0568	0.1121	0.1069
2.90	0.0263	0.0552	0.0549
3.00	0.0	0.0	0.0

$\sigma_c/\bar{\sigma}$ , little change in fatigue life is observed since the cumulative damage at small amplitudes is relatively insignificant. As  $\sigma_c/\bar{\sigma}$  increases, a point is reached where the effect rapidly increases and the curves in Figure 3 "nose over". It is apparent that for smaller slopes of the  $\sigma$ -N curve, the effect of discounting the smaller cycles becomes significant at much smaller values of  $\sigma_c/\bar{\sigma}$ .

A representative value of  $b = 6.5$  is often used to estimate the effects of vibration level on time to failure and to derive accelerated tests. The rule of thumb, "3 dB equals ten in time" is based on this value. For  $b = 6.5$ , limiting the stress to  $3\bar{\sigma}$  increases the time to failure by 59 percent for values of  $\sigma_c/\bar{\sigma}$  up to approximately 1.5. As  $\sigma_c/\bar{\sigma}$  increases beyond 1.5, the time to failure increases rapidly, becoming infinite for  $\sigma_c/\bar{\sigma} = 3.0$ , since no stresses now exceed the endurance limit. Thus, if there is a known endurance limit, the above rule of thumb should be modified by use of Figure 3. Unfortunately, stresses are seldom known and an endurance vibration level, e.g., endurance ASD, is also infrequently available. Thus it is difficult to obtain the value of  $\sigma_c/\bar{\sigma}$  or an acceleration equivalent to use Figure 3 quantitatively. However, it is evident that the rule-of-thumb, which assumes  $\sigma_c = 0$ , underestimates the time ratio for a given acceleration level. In other words, "3 dB in level often equals more than ten in time."

#### REFERENCES

- [1] J.M. Miles, "On Structural Fatigue Under Random Loading" J. Aero Sci. 21, 753-762 (1954)
- [2] A.J. Curtis, N. G. Tinling, H. T. Abstein, Jr., "Selection and Performance of Vibration Tests" SVM-8, SVIC, 1971.

#### DISCUSSION

Voice: Did you clip the input signal?

Mr. Curtis: No.

## SINGLE POINT RANDOM MODAL TEST TECHNOLOGY APPLICATION

### TO FAILURE DETECTION

Walter M. West, Jr.  
Lyndon B. Johnson Space Center  
Houston, Texas

The information contained in this paper demonstrates that frequency response function data, normally acquired as a data base for use in development of empirically based mode shapes, has additional utility. Comparison and analysis of frequency response function data sets obtained prior to and after environmental tests of an Orbiter body flap have enabled identification of structural damage that had not been detected by conventional visual, X-ray, and ultrasonic inspections. The analyses and conclusions reported in this paper demonstrate that specific damaged areas within a relatively complex structure can be identified on a timely basis.

### INTRODUCTION

Selected segments of the Shuttle Orbiter structure have undergone acoustic fatigue testing in the Vibration and Acoustic Test Facility (VATF) at the Lyndon B. Johnson Space Center. Some of the external surfaces of these test specimens have been completely covered with Orbiter Thermal Protective System (TPS) tiles and access to the internal structure has been very limited. Schedule motivation has prevented rigorous inspection of some test specimens during the course of acoustic fatigue testing. As part of this fatigue test program, single point random modal tests were conducted using a minicomputer-based system to determine critical areas of structure prior to beginning acoustic tests and changes in structural characteristics caused by the acoustic tests.

The use of minicomputer-based modal analysis systems employing modern analog-to-digital converters and fast fourier transforms provides a tool that can be used to rapidly develop engineering information. This paper illustrates a practical application of the utility of such a system, which may not be generally recognized. The information contained in this paper demonstrates that frequency response function data, normally acquired as a data base for use in development of empirically based mode shapes, has additional utility. Comparison and analysis of frequency response function data sets obtained prior to and after acoustic tests of an Orbiter body flap and rapid development of mode shapes enables identification of otherwise undetected structural changes. These changes were observed even though the frequency response function data sets were obtained with acceleration

measurements made directly on tile surfaces, not on structure surfaces. Analyses and conclusions reported in this paper demonstrate that specific damaged areas within a relatively complex structure can be identified on a timely basis.

The specific testing, which provides the basis for this paper, was performed on a one-half span segment of the Orbiter body flap and its associated forward fuselage stub assembly. Test-based modal data is presented for each of two configurations before and after exposure to the acoustic environment. This paper compares these data and identifies the conclusions derived from the comparisons.

As a result of these conclusions, additional detailed inspections were conducted. Tiles were removed from the external surfaces and visual and ultrasonic inspections were conducted, but no failures were identified. Based on interpretation of modal test results, three possible causes of an observed frequency shift were identified in a report issued prior to disassembly of the test specimen. Subsequent disassembly disclosed significant structural damage and substantiated two of the three causes previously identified.

### TEST SPECIMEN DESCRIPTION

The specimen tested consisted of a one-half span segment of an Orbiter body flap approximately 3.4 meters wide, a fuselage stub assembly, and interfacing actuators. The test specimen is shown in Fig. 1. The trailing edge assembly is joined to the forward box assembly via piano hinge joints and by shear clips attaching

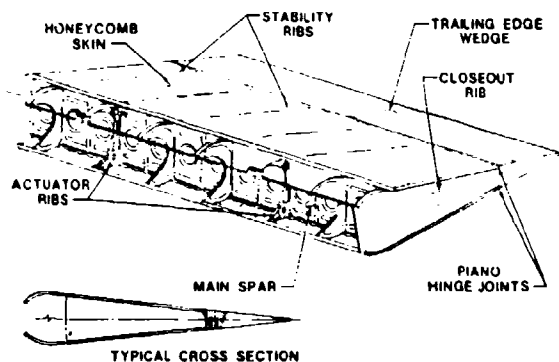


Fig. 1 - Orbiter body flap assembly

the actuator rib webs and stability rib webs to the rear spar. Components of the flap assembly are illustrated in Figs. 2, 3, 4, and 5. The fuselage stub section was bolted to a massive steel billet having dimensions of 241 x 114 x 30 centimeters, which was resting on the facility floor. Initially, the test specimen was fitted with steel nonflight-like actuators bridging the flap assembly to the fuselage stub assembly. In the final test configuration, the steel actuators were replaced with flight-type actuators having the full planetary gear system normally used to control the body flap position. All exterior surfaces were composed of aluminum honeycomb and covered with TPS tile. Interior structural elements could not be inspected without special apparatus.

#### OPERATIONAL SEQUENCE

Environmental acoustic and modal tests were conducted on each of the two configurations. Prior to the acoustic tests, a modal test was conducted from which frequency response function data were obtained at the numbered locations shown in Figs. 6 and 7. Three working days were required to acquire approximately 370 frequency response functions. Data acquisition conditions

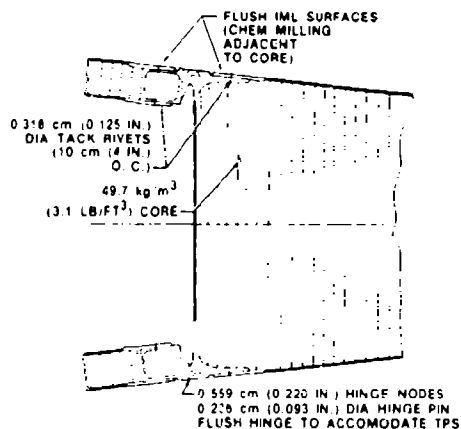


Fig. 2 - Trailing edge wedge/forward skin assembly

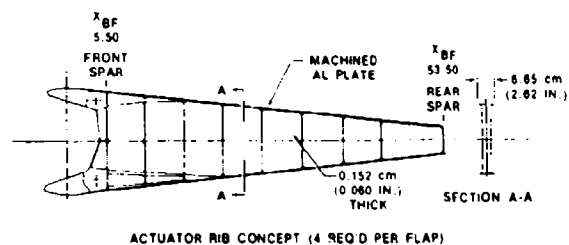


Fig. 3 - Actuator rib construction

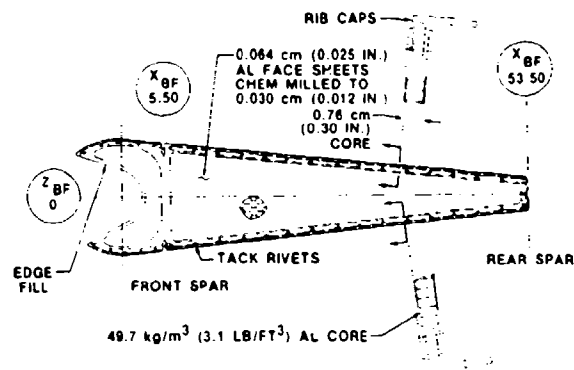


Fig. 4 - Stability rib construction

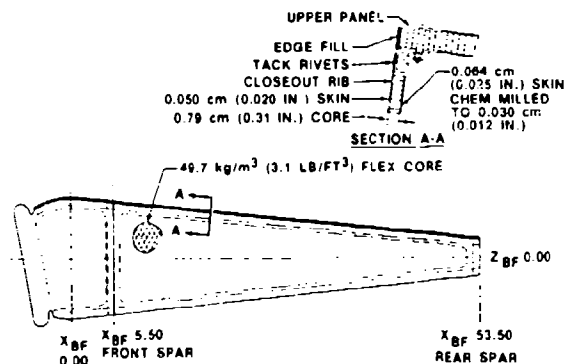


Fig. 5 - Closeout rib

used in obtaining the frequency response functions were

Alias filter setting - 150 hertz  
Sample rate - 500 samples/second  
Number of ensembles - 40  
Windowing function - Hanning

A random force having an overall value of 2.81 newtons rms was input in the Z direction at grid point location 25. The force spectrum was flat from approximately 7 to 150 hertz with no significant peaks or valleys in the spectrum. With the system used, acquisition of frequency response functions yields a function having 300 spectral lines distributed from 0 to 150 hertz.

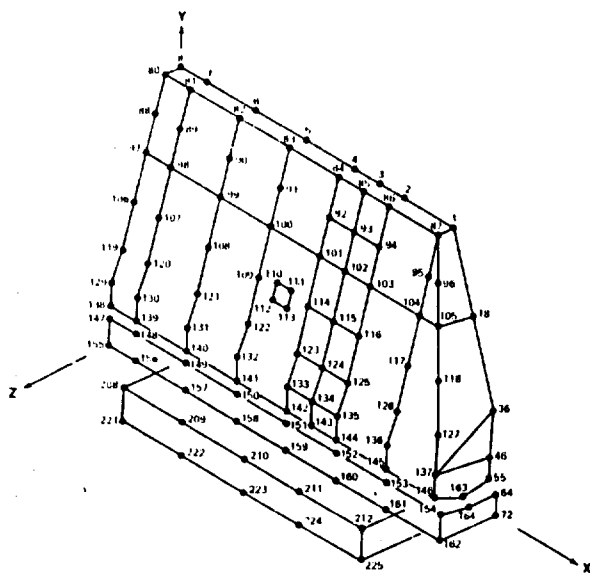


Fig. 6 - Body flap modal model (upper surface)

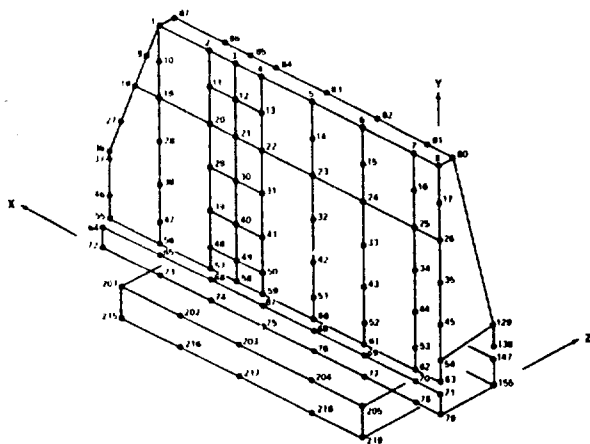


Fig. 7 - Body flap modal model (lower surface)

At arbitrary times during the data acquisition operation, frequency response function measurements were repeated and compared to those originally acquired to check acquisition system performance and stability of test specimen characteristics. Overlays of originally measured and repeated functions with original functions plotted as a solid line and repeated functions plotted as dots are shown in Figs. 8 and 9. The repeatability shown in these Bode plots is typical. Subsequent to identification of resonance frequencies, mode shapes were generated by extraction and storage of the quadrature component of the measured frequency response function at the resonance frequencies. Other methods of modal coefficient derivation are available to reduce residual contribution of one mode on another, but they are time consuming and experience has shown that simple quadrature component extraction produces results compatible with test program objectives. Analyses of these

data were completed during preparation of acoustic tests without any effect on test schedules. One sequence of acoustic tests was then completed and an abbreviated set of modal data was obtained for analysis and comparison to the preceding data set. Subsequently, testing of the configuration having dummy actuators was terminated and the specimen was returned to the manufacturer where it was partially disassembled, inspected, and fitted with flight actuators. The TPS tile installation on the specimen surfaces was modified and the test specimen returned to the VATF for additional testing. A complete modal test was conducted followed by a complete sequence of acoustic tests and an abbreviated set of modal data was again obtained.

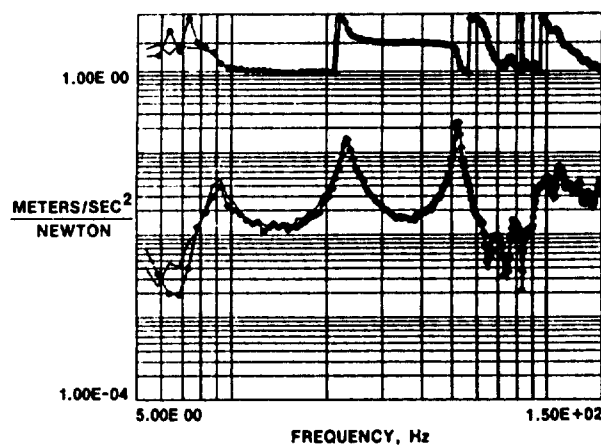


Fig. 8 - Frequency response function measurement repeatability location 18Z-

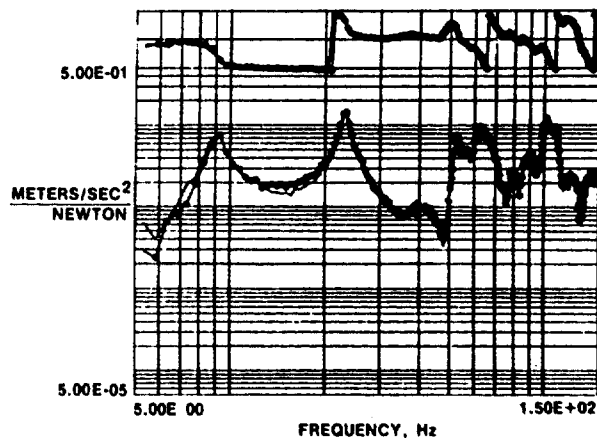


Fig. 9 - Frequency response function repeatability, location 2Z-

#### MODE SHAPE DESCRIPTION

The first three modes of the body flap test specimen are described as follows.

Mode 1 - The body flap has a cantilever motion with the flap assembly pivoting on a center

line through the two actuators. All elements of the flap assembly are in phase with one another and moving as a rigid body with little or no evidence of elastic body deformation in the flap structure. Moments associated with this motion are reacted by the actuators that bridge the flap and fuselage billet.

**Mode 2** - The flap assembly is in torsion with a node line running chordwise approximately midway between the two actuator ribs.

**Mode 3** - The first spanwise bending of the body flap section has the outboard and inboard ends in phase with one another and the center of the specimen out of phase with the ends. Two chordwise node lines lie on the actuator ribs.

Undeformed views of the modal model are shown in Figs. 6 and 7. Modes 1, 2, and 3 are shown in Figs. 10, 11, and 12.

In these mode-shape illustrations, the dashed lines represent undeformed structure and the solid lines represent the deformed shape. Note that of the three modes discussed previously only one (the third) does not involve motion of the actuator ribs. The first and second modes involve actuator rib motion and their resonance frequencies are obviously dependent on the stiffness of the load path between the flap and the fuselage stub. The third mode does not involve actuator rib motion and its frequency is obviously dependent on spanwise stiffness of the flap assembly. The mode shapes shown by graphs in Figs. 10, 11, and 12 are those derived from data measured in the configuration having flight-type actuators.

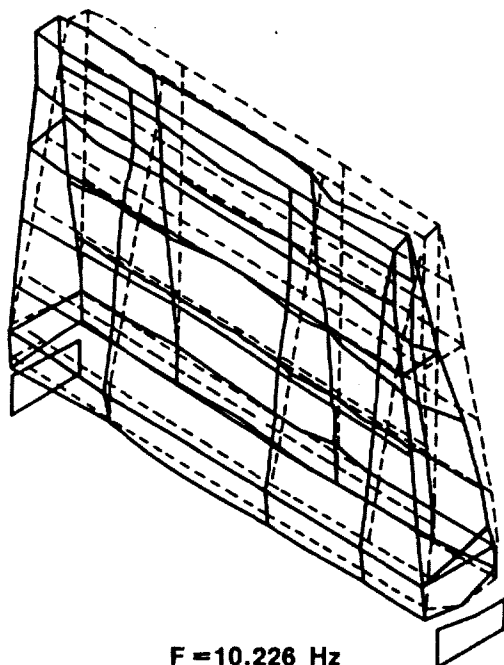


Fig. 10 - First mode - cantilever

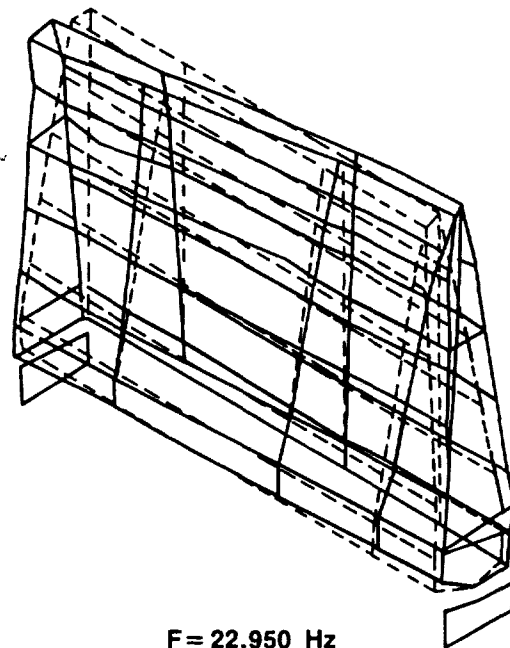


Fig. 11 - Second mode - torsion of assembly

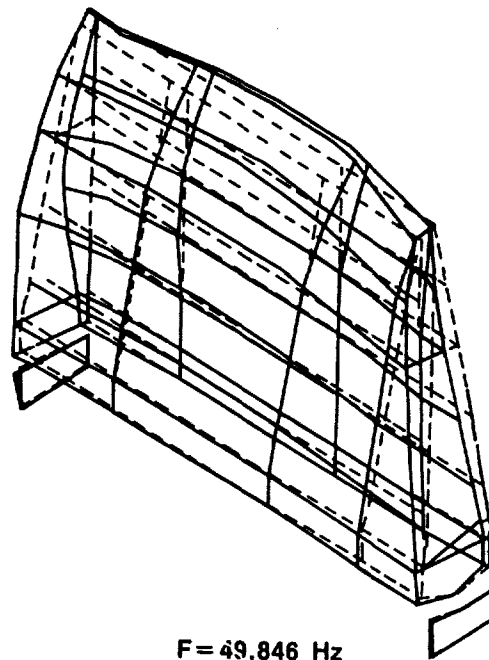


Fig. 12 - Third mode - spanwise bending

#### PRE-POSTACOUSTIC TEST MODAL DATA EVALUATION

Comparisons of the first three modal frequencies of the test specimen, given in Table 1, are based on data obtained at the following times: 1) preceding the first acoustic test sequence with dummy actuators, 2) after the first acoustic test sequence, 3) preceding acoustic tests with flight-type actuators, and



TABLE 1  
Modal Frequency Comparison

Mode No.	Mode Description	Configuration/Test Phase			
		Dummy Actuators		Flight Actuators	
		Preacoustic Frequency (Hz)	Postacoustic Frequency (Hz)	Preacoustic Frequency (Hz)	Postacoustic Frequency (Hz)
1	Cantilever	8.98	5.81	10.23	10.15
2	Torsion	23.29	21.54	22.95	22.04
3	Spanwise bending	52.25	50.73	49.85	43.11

4) after the final acoustic test sequence with flight-type actuators.

During the first acoustic test, a significant reduction of the first bending mode frequency occurred, which was attributed to exposure of the specimen to the acoustic environment. A smaller change occurred for the third mode frequency. The shift in first mode frequency was attributed to a change in stiffness of the load path between the flap assembly and the fuselage stub because the mode shapes indicated that elastic body deformation of the flap assembly was not significant in either pre- or post-acoustic test modes. Because the mass of the test specimen had not changed, an estimate of the change in modal stiffness was obtained using the simple spring/mass single-degree-of-freedom relationship. The observed frequency shift was reported as equivalent to a reduction in effective modal stiffness to a value equal to approximately 40 percent of that which existed preceding exposure of the test specimen to the acoustic environment. Imaginary parts of typical frequency response functions measured prior to and after acoustic tests of the configuration having nonflight-like actuators are shown in Figs. 13 and 14. Resonance fre-

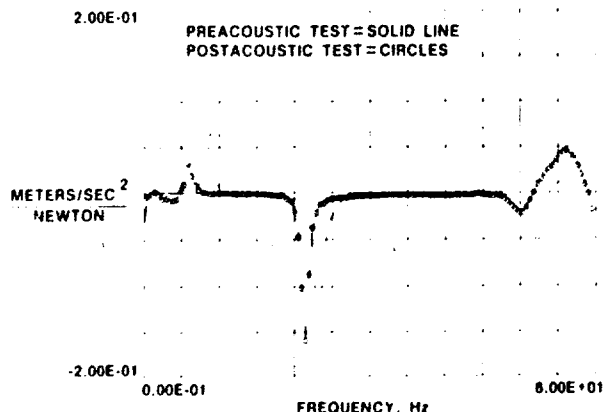


Fig. 13 - Comparison of frequency response functions location 22

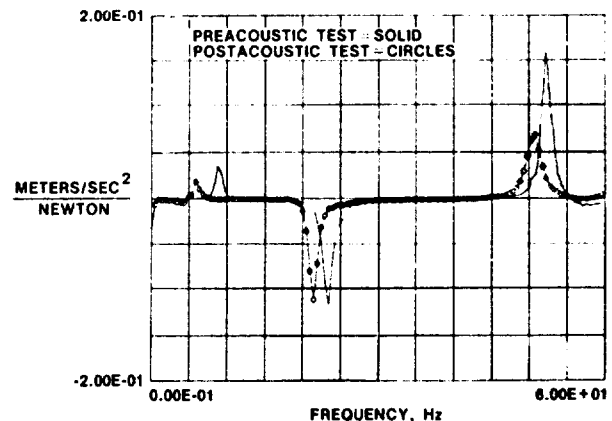


Fig. 14 - Comparison of frequency response functions prior to and following acoustic tests, location 19Z

quencies for each of the first three modes can be readily identified.

Subsequent to the return of the specimen to the manufacturer and disassembly and inspection, there was an indication that galling of spherical bearings at the actuator rib interfaces had occurred. The conclusion that there had been a significant reduction in stiffness of the load path between the flap assembly and fuselage stub is supported by the observation that an increase in the first mode frequency was brought about by installation of flight-type actuators as shown in Table 1.

Prior to beginning the second acoustic test series, it was reported that a slight reduction in the third mode frequency had not been recovered after installation of the flight-type actuators and that a decrease in bending stiffness across the span of the specimen may have occurred during the initial acoustic tests. Data obtained after the final acoustic test sequence show that the third mode frequency was

even further reduced by the additional exposure time as shown in Table 1. During acoustic tests of the flight-type actuator configuration, little change in modal frequencies occurred for modes involving bending of the actuator/rib and a significant change occurred in the third mode frequency, which involves spanwise bending. Based on these observations, the conclusion was that the third mode frequency shift was caused by a reduction in spanwise bending stiffness. Possible causes were reported as 1) core/skin separation at the trailing edge and/or forward box, 2) failure of trailing edge/forward box interfacing structure, and 3) failure of spanwise spars.

Approximately one-fourth of the tiles were removed from the external surface and visual, ultrasonic, and X-ray inspections were conducted. The only damage reported consisted of two small dents in the upper surface of the skin.

After the test article was returned to the manufacturer, it was disassembled and additional inspections disclosed significant damage. Four shear clips, which attach the trailing edge wedge forward spar to the stability ribs, were cracked and the shear clip attaching the trailing edge wedge to the closeout rib was also cracked. Note that the two clips, which attach the spar to the actuator ribs, were not damaged and these clips lie on node lines for the third mode. The hinge pins on both upper and lower surfaces were each broken in two places and faceplate core separation was found in local areas of the trailing edge forward spar. Some of the damage described above is shown in Figs. 15 and 16.

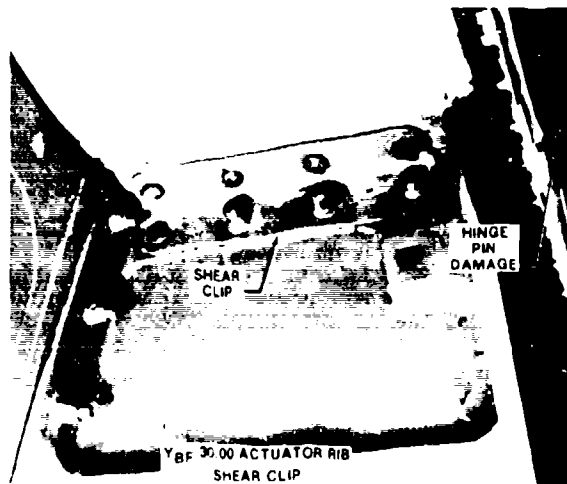


Fig. 15 - Typical hinge pin damage

#### CONCLUSIONS

This paper presents conclusions drawn from comparison of modal data obtained prior to and

succeeding acoustic environment testing. Comparison of animated mode shape displays based on data obtained after environmental tests enabled a determination that pre- and postenvironmental test shapes were generally the same. These same data identified changes in resonant frequencies that could only have been caused by significant structural damage. Study of the animated displays along with cognizance of the shift in resonance frequencies allowed three possible

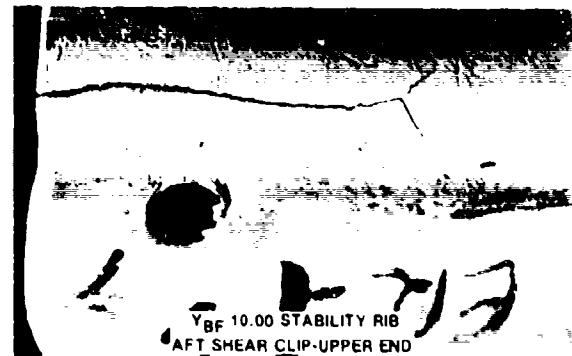


Fig. 16 - Typical shear clip damage

causes of an observed shift in resonance frequency to be identified and reported even though visual, X-ray, and ultrasonic inspections had not disclosed any significant damage. Subsequent disassembly of the test specimen verified two of the three identified possible causes.

The utility and speed inherent in modern analog-to-digital processors, discrete fourier transforms, and single point random frequency response function-based modal test methodology provide a powerful tool for understanding the dynamic behavior of complex structures and an efficient method of detecting changes in their dynamic characteristics.

#### ACKNOWLEDGEMENTS

The author wishes to acknowledge the support of the Structural Dynamics Research Corporation personnel who participated in modal data acquisition and analysis of the original test specimen. Special thanks go to Mr. Charles Mitchell and other Northrup Services personnel who bore the brunt of the data acquisition and analysis tasks.

#### DISCUSSION

Mr. Zurnaciyen (Northrop Electronics): I think your procedure is very commendable in identifying that failure in a structure. Were you able to determine the cause of the failure? How can you relate the test data to the cause of the failure itself?

Mr. West: The cause of the failure? This is the rationale that we used. First we look for a frequency shift, and then we go back and look at the mode shape. If you go back and look at these mode shapes on an animated display, the parts of the structure that are getting worked become very apparent. For instance, the first mode is a simple cantilever going back and forth. When you look at that on the animated display, you can see everything moves together; no bending takes place. So you can conclude that the part that is getting worked is that load path in between the body flap and the fuselage stub. The same thing applies to the third mode. If you study it carefully, you can ask yourself if the elements of the thing that is getting worked contribute to the spanwise and bending stiffness. That is the rationale that was used. We identified in writing prior to the disassembly, which elements in general would probably fail. I think we made a statement like, "The interfacing structure between trailing edge wedge and the forward box assembly was a likely culprit".

# FORCED VIBRATIONS OF A LARGE DAMPED MECHANICAL SYSTEM

David W. Nicholson  
Naval Surface Weapons Center  
White Oak, Silver Spring, Maryland 20910

Recently, the author extended a theorem of Strang to derive a function whose extreme values give bounds on the forced response of a damped mechanical system. Here the derivation is briefly reviewed, the numerical algorithm for its computation is presented, and some computational results are given which show the expected trend

## INTRODUCTION

We consider the forced vibrations of a large damped mechanical system, governed by

$$M_0 \ddot{x} + D_0 \dot{x} + K_0 x = g_0 \exp(i\omega t) \quad (1)$$

Here  $M_0$ ,  $D_0$  and  $K_0$  are the mass, damping and stiffness matrices, assumed constant, real,  $n$  by  $n$ , symmetric and positive definite. Also,  $g_0$  is a constant vector of force amplitudes,  $x$  is the response (displacement) vector and  $i = \sqrt{-1}$ .

In this work, using some recent results of the author [1], we obtain a response bound holding for all  $\omega$ : i.e. a quantity  $B_n$  is derived such that

$$\max_{\omega} [|x|/|g_0|] \leq B_n,$$

where  $|x| = x^H x$  is the Euclidean vector norm [2] and  $x^H$  is the Hermitian transpose of  $x$ . The actual evaluation of  $B_n$  requires some elementary calculations which are described and illustrated in the subsequent paragraphs.

The bounds are particularly simple, depending only on the extreme eigenvalues of the modal damping and stiffness matrices. They are expected to be useful in the design and analysis of large systems for which accurate direct integration of (1) may be difficult.

We first illustrate the analysis using simple systems, and then we treat the general problem.

## ONE DEGREE-OF-FREEDOM SYSTEM

For a simple one degree-of-freedom system with a sinusoidal force input, represented by

$$m\ddot{x} + d\dot{x} + kx = f_0 \sin \omega t, \quad (2)$$

the displacement is given by

$$x = f_0 \sin(\omega t - \theta) / [(k - \omega^2 m)^2 + \omega^2 d^2]^{1/2}$$

where

$$\theta = \tan^{-1}(\omega d / (k - \omega^2 m)).$$

Neglecting  $\sin(\omega t - \theta)$ , the magnitude of  $x$  obeys

$$\frac{|x|}{|f_0|} = ((k - \omega^2 m)^2 + \omega^2 d^2)^{-1/2}.$$

Elementary calculus serves to show that

$$B_1 = \max_{\omega > 0} [|x|/|f_0|] = \begin{cases} \frac{1}{k}, & \frac{k}{m} < \frac{d^2}{2m^2} \\ \frac{1}{d\sqrt{k/m}}, & \text{otherwise.} \end{cases} \quad (3)$$

Clearly, if  $d = 0$  the bound becomes infinite, corresponding to the natural frequency  $\omega = \sqrt{k/m}$ .

## DECOMPOSABLE SYSTEMS

As shown in Reference 3, if

$$DM^{-1}K = KM^{-1}D, \quad (4)$$

the system represented by (1) can be "decoupled" to furnish  $n$  independent modes governed by

$$m_i \ddot{x}_i + d_i \dot{x}_i + k_i x_i = g_i \exp(i\omega t)$$

where  $m_i$ ,  $d_i$  and  $k_i$  are the eigenvalues of  $M_0$ ,  $D_0$  and  $K_0$ . The analysis of the last section applies to each mode to yield

$$B_n = \max_{\omega} [|x|/|g_0|] = \max_i \left( \frac{1}{k_i}, \frac{k_i}{m_i} \leq \frac{d_i^2}{2m_i^2} \right) \quad (5)$$

$$\cdot \frac{1}{d_i \sqrt{\frac{k_i}{m_i}}}, \text{ otherwise}$$

## GENERAL SYSTEMS

Large systems in which (4) does not hold are now treated using the author's recent results [1], which involve a simple extension of a theorem due to Strang [4]. The relations of interest are summarized below.

Equation (1) is rewritten as

$$I\ddot{x}_1 + D\dot{x}_1 + Kx_1 = f_1 \exp(i\omega t) \quad (6)$$

$$x_1 = U^T M_0^{-1/2} x \quad f_1 = U^T M_0^{-1/2} g_0$$

$$D = U^T M_0^{-1/2} D_0 M_0^{-1/2} U \quad K = \text{diag}(k_j)$$

$$k_j = \lambda_j (M_0^{-1/2} K_0 M_0^{-1/2})$$

and  $U$  is a proper orthogonal matrix

which "diagonalizes"  $M_0^{-1/2} K_0 M_0^{-1/2}$ . Also,  $D$  and  $K$  may be called modal damping and stiffness matrices since they are referred to a basis formed by the eigenvectors of the undamped system:

$$(K_0 - \omega^2 M_0) y = 0.$$

For later convenience, let  $\Sigma$  denote the set of quantities  $\{\rho_k, \rho_d, \cos\theta, \cos\phi\}$ , subject to the constraints

$$0 \leq \rho_k \leq 1 \quad -1 \leq \cos\theta \leq 1$$

$$0 \leq \rho_d \leq 1 \quad -1 \leq \cos\phi \leq 1$$

It is shown in [1] that

$$\frac{x_1^H x_1}{f_1^H f_1} \leq \left[ \min_{\Sigma} \left[ \min_{\omega > 0} [q] \right] \right]^{-1} \equiv B_n^2$$

where

$$q = (k_n - \omega^2)^2 + 2\rho_k (k_n - \omega^2) (k_1 - k_n) \cos^2\theta$$

$$+ \rho_k^2 (k_1 - k_n)^2 \cos^2\theta + \omega^2 d_n^2$$

$$+ 2\rho_d \omega^2 d_n (d_1 - d_n) \cos^2\phi$$

$$+ \rho_d^2 \omega^2 (d_1 - d_n)^2 \cos^2\phi$$

$$+ 2\omega\rho_d\rho_k (k_1 - k_n) (d_1 - d_n) \cos\theta \cos\phi \sin\theta \sin\phi.$$

The quantity  $q$  is always nonnegative. As discussed in Reference 1, the bound represented (7) is mathematically the best possible.

## NUMERICAL TREATMENT

It is extremely tedious, if not impossible, to determine analytically the values of  $\rho_k$ ,  $\rho_d$ ,  $\cos\theta$ ,  $\cos\phi$  and  $\omega$  which minimize  $q$  under the constraints represented by (7). However, an efficient numerical method can be used, involving three straightforward steps:

1. Choose the trial values  $\Omega_{ijkl}$

$$= \{\rho_k^{(i)}, \rho_d^{(j)}, \cos\theta^{(k)}, \cos\phi^{(l)}\}$$

where  $1 \leq i \leq N_k$ ,  $1 \leq j \leq N_d$ ,

$$1 \leq k \leq N_\theta, 1 \leq l \leq N_\phi.$$

2. For each  $\Omega_{ijkl}$ , determine the value of  $\omega$ , say  $\omega_{ijkl}$ , which minimizes  $q(\Omega_{ijkl}, \omega)$ .

3. Search the values  $q(\Omega_{ijkl}, \omega_{ijkl})$  for the minimum value  $B_n$ .

In regard to Step 2, note that

$$\frac{\partial q}{\partial \omega} = 0$$

is a cubic equation in  $\omega$  and its roots can be calculated using simple formulae. Its positive real roots, together with  $\omega = 0$ , may be substituted into  $q(\Omega_{ijkl}, \omega)$  to determine the minimizing value of  $\omega$ , namely  $\omega_{ijkl}$ .

## RESULTS

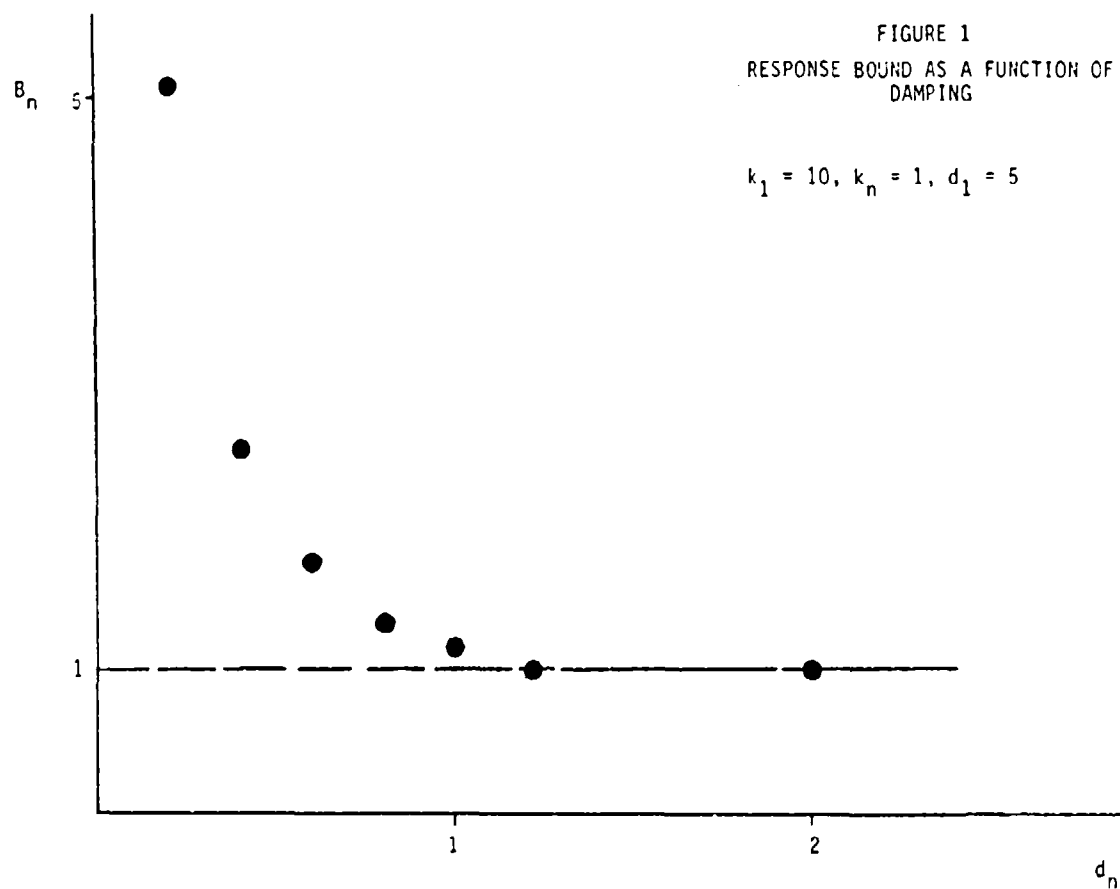
Figure 1 displays the quantity  $B_n$  as a function of  $d_n$  with  $k_1 = 10$ ,  $k_n = 1$  and  $d_1 = 5$ . As expected, as  $d_n$  approaches zero the response bound becomes infinite, but it decreases strongly as  $d_n$  increases.

## DISCUSSION

Simple computations serve to bound the forced response of a damped mechanical system. The bound depends on only four quantities, the maximum and minimum eigenvalues of the modal stiffness and modal damping matrices. The first two are known directly since the modal stiffness matrix is diagonal. The computational results show the expected trend.

## REFERENCES

1. Nicholson, D. W., "Response Bounds for Asymptotically Stable Time Invariant Linear Dynamical Systems", submitted for publication.
2. Young, D. M. Iterative Solution of Large Linear Systems, Academic Press, New York, 1971.
3. Coughy, T. K. and Kelley, M. E. J., "Classical Normal Modes in Damped Linear Systems", J. Appl. Mech., Trans ASME 32 (2), pp. 583-588, 1965.
4. Strang, G., "Eigenvalues of Jordan Products", Amer Math. Monthly, 1962.



INDIRECT FOURIER TRANSFORM (IFT) AND SHOCK RESPONSE  
--a Detailed Presentation of Basic Theory

Charles T. Morrow  
Consultant  
Encinitas, California

An algorithm, based in part on early work by O'Hara, is capable of yielding undamped residual shock spectra and indirect Fourier transforms, with minimal calculator or computer data-memory requirements, and with about the same computation time as with the fast Fourier transform (FFT). For the same number of frequencies in the spectrum, computation is slower than with the FFT algorithm, but the latter fundamentally requires many more frequencies than are otherwise necessary for spectral analysis of shock. With minor alteration, the IFT algorithm can yield quite simply the instantaneous responses of undamped or damped linear and some nonlinear mechanical systems. A preliminary adaptation of this algorithm, for both spectral and response computation, to the Radio Shack TRS-80 personal computer, with 16 kilobytes of memory for program and data, was demonstrated at the 51st Shock and Vibration Symposium, in San Diego, 21-23 October 1980. The algorithm is presented here essentially as originally developed for the HP-97 card-programmable calculator, whose memory limitations are more obvious.

## INTRODUCTION

The most fundamental spectral description of shock, with the most appeal to theoreticians, is the Fourier transform, expressed by magnitude and phase (or alternately cosine and sine terms) as functions of frequency. (1) It is uniquely defined for any one excitation time-history and vice versa. By an inverse transformation -- an integration similar to that used in the definition of the transform, the excitation time-history can in fact be reconstructed from the transform. An inverse transformation after multiplication of the transform of the excitation by the transfer function of any linear mechanical system yields the response time-history for that system.

Among shock and vibration engineers, the most common spectral criterion of shock severity is the shock spectrum -- the peak acceleration response of a simple linear mechanical resonator as a function of frequency of resonance. (1) Originally conceived for earthquake applications, in terms of an

undamped resonator, (2) it has commonly been computed (usually by an analog shock spectrum computer) in recent years for resonators of finite Q in an attempt to make it a more realistic representation of possible internal responses of equipment to be shock tested.

In 1962, by expressing the instantaneous response of a simple linear mechanical resonator as a Duhamel integral and comparing mathematical forms, O'Hara showed that the undamped residual shock spectrum is proportional to the magnitude of the Fourier transform of the instantaneous velocity time-history of a shock excitation. (3) He showed further that shock response could be computed by digital integration and that the same methods could yield a Fourier analysis. In 1963, Morrow provided a shortened derivation of the proportionality property in terms of the excitation acceleration time-history. (4) These developments have suggested there may be virtues in making the undamped residual spectrum, with phase information incorporated,



the basic computation and obtaining the Fourier transform, as needed, indirectly -- hence the name indirect Fourier transform (IFT) for the present algorithm.

The shock spectrum commonly in use today in shock and vibration engineering is not an undamped residual but a damped maximum, used both as a spectral description and an indication of the possible responses of equipment subject to shock excitation -- simulation of equipment dynamics is seldom carried out in more detail than that of commercially available shock spectrum computers. Partly to revert to fundamentals and partly to provide a healthier conservatism in test requirements, the author has recommended that the undamped residual become the standard spectral description for shock. (5) Furthermore, to facilitate development for greater reliability in the shock environment, the author has recommended that the shock and vibration engineer be able to explore the effect of design changes on response -- in other words that he have available a dynamical simulator with stored subroutines for an arbitrary number of degrees of freedom, to be chosen at will. (5) No instrument manufacturer would market an instrument for either recommendation unless it is mentioned in a specification. Conversely, specification writers are extremely reluctant to require or favor a measurement unless a capability for it already exists and is generally available. The IFT algorithm provides a potential solution to this dilemma in the form of spectral and response programs that require only a minimal expenditure for computer hardware.

#### STRATEGY

The algorithm as it now exists arose out of the author's interest, several years ago, in making programmable calculators accomplish something useful in shock analysis. Initially, most of his effort was expended in dealing with the extremely limited data and program memories of the Hewlett Packard HP-65 card-programmable calculator, using whatever programming tricks he could devise, such as storing two numbers in the same register. (6) The result was successful -- just barely. The more recent HP-97 (printing) and HP-67 calculators began to be partners rather than adversaries to the programmer for the shock analysis challenge and permitted more programming features out of choice rather than necessity.

Minimizing the data memory requirements, however, remained the dominant consideration. The strategy was to approximate the shock excitation time-history by a succession of straight lines, devise a general response equation with arbitrary coefficients, and update these coefficients after each discontinuity of slope or acceleration so that not even the input data needed to be retained. From the beginning, the algorithm was developed in terms of data inputs from the keyboard -- once its merit was determined, analog-digital converter inputs could be provided for later. With the user able to decide whether adding a RAMP or STEP would provide a better approximation to the excitation in the interval between updates, both types of input, by choice of key, were provided for in all programs, once the effort was no longer limited by the memory capabilities of the HP-65. With analog-digital converter inputs, probably only the RAMP subroutine will be used.

#### FUNDAMENTAL EQUATIONS

Once the transfer function for any linear mechanical system has been determined, it becomes possible to establish RAMP and STEP responses, set up a general updatable equation for any succession of RAMPs and STEPs, and apply the algorithm. This will now be illustrated for a simple resonator shown in Figure 1, which has a unique significance because, for zero damping, it leads very simply to a residual spectrum. However, it is a very limited approximation to equipment dynamics. The differential equation is

$$m d^2x/dt^2 + c dx/dt + k(x - x_b) = 0, \quad (1)$$

where  $m$  is the mass,  $c$  is the damping coefficient,  $k$  is the stiffness,  $x$  is the absolute displacement of the base of the resonator, and  $x$  is the absolute response displacement of the mass. Differentiating this twice and rearranging yields

$$m d^2a/dt^2 + c da/dt + ka = ka_b + c da_b/dt. \quad (2)$$

Replacing the derivative by  $s$  and rearranging further yields the transfer function

$$\begin{aligned} L(s) &= (2\alpha s + \omega^2) / (s^2 + 2\alpha s + \omega^2) \\ &= 1 - s^2 / (s^2 + 2\alpha s + \omega^2) \\ &= 1 - s^2 / [(s + \alpha)^2 + \omega'^2], \end{aligned} \quad (3)$$

where

$$\omega = 2\pi f = \sqrt{k/m}, \quad (4)$$

$$\alpha = c/2m = \pi f/Q = \omega/2Q \text{ and} \quad (5)$$

$$\omega'^2 = \omega^2 - \alpha^2 \quad (6)$$

are parameters readily obtained by measurement of response in the region of resonance, without necessarily looking deeper into the mechanical details.

The Laplace transformation of the response to a unit RAMP excitation is obtained by multiplying Equation (3) by  $1/s^2$ , the Laplace transform of the RAMP, to yield

$$L(s) = 1/s^2 - 1/[(s+\alpha)^2 + \omega'^2], \quad (7)$$

from which an inverse transformation yields the RAMP response

$$a(t) = t - (1/\omega')e^{-\alpha t} \sin \omega' t. \quad (8)$$

The Laplace transformation of the response to a unit STEP excitation is obtained by multiplying Equation (3) by  $1/s$  to yield

$$L(s) = 1/s - s/[(s+\alpha)^2 + \omega'^2], \quad (9)$$

from which an inverse transformation yields the STEP response

$$a(t) = 1 - e^{-\alpha t} \cos \omega' t + e^{-\alpha t} (\alpha/\omega') \sin \omega' t. \quad (10)$$

Examination of Equations (8) and (10) suggests an updatable equation sufficiently general for the total response after any sequence of RAMPs and STEPs

$$a(t \geq t_k) = B_k + C_k t + e^{-\alpha t} (D_k \cos \omega' t + E_k \sin \omega' t), \quad (11)$$

where  $t_k$  is shown here as the time of the last discontinuity of slope or acceleration.

In actual data inputs  $t_k$  may be used instead, for convenience, as the time corresponding to the latest acceleration input a whether it determines a RAMP or STEP, so that each RAMP will actually begin at  $t_{k-1}$ . Thus, each acceleration input will result in a new slope

$$\gamma_k = (a_k - a_{k-1}) / (t_k - t_{k-1}) \quad (12)$$

and corresponding slope change

$$\Delta \gamma = \gamma_k - \gamma_{k-1}, \quad (13)$$

or an acceleration discontinuity  $\Delta a_k$ .

From Equation (8), the added response after a RAMP input is

$$\Delta a(t \geq t_{k-1}) = \Delta \gamma_k [t - (1/\omega')e^{-\alpha(t-t_{k-1})} \sin \omega'(t-t_{k-1})]. \quad (14)$$

From Equation (10), the added response after a STEP input, with as yet no alteration in slope, is

$$\Delta a(t \geq t_k) = \Delta a_k [1 - e^{-\alpha(t-t_k)} \cos \omega'(t-t_k) + e^{-\alpha(t-t_k)} (\alpha/\omega') \sin \omega'(t-t_k)]. \quad (15)$$

Thus, Equations (11), (14) and (15) become the foundation for the IFT algorithm applied to the simple linear mechanical resonator. It would be nice if after each data input the cosine and sine coefficients could merely be increased by the corresponding multiplying factors of Equation (14) or (15). There is one complication -- after the initial data inputs the arguments of the trigonometric functions of Equation (11) will not be the same as that of the functions in Equation (14) and (15). Therefore either Equation (14) or (15) must undergo a time shift in connection with coefficient updating (Method 1), or Equation (11) must be ratcheted along in time (Method 2). It will be found that Method 2 is dramatically improved in computation time if a constant time increment is used. In both methods, the time shifts will be accomplished by using the identities

$$\cos(x \pm y) = \cos x \cos y \mp \sin x \sin y \text{ and} \quad (16)$$

$$\sin(x \pm y) = \sin x \cos y \pm \cos x \sin y. \quad (17)$$

In practical application of the algorithm, the excitation slope will arbitrarily be set to zero by the calculator or computer after each STEP data input. Since STEP inputs will be infrequent, there can be no serious penalty in computation time, but this will permit setting the terminal slope of the excitation to zero without any necessity for inputting a zero acceleration for a time  $t_k$  after shock termination. A terminal STEP in the data inputs will automatically leave the excitation slope at zero. After a terminal RAMP in the data inputs, a STEP to the same final acceleration at the same final  $t_k$  will set the slope to zero.

If the actual slope of the excitation following the STEP is not zero, this will be adjusted by the next RAMP input.

#### METHOD 1 SPECTRAL COMPUTATION

The first method permits variable time increments, with the user inputting both time and acceleration data. Because it requires the computation of sines and cosines after every data in-

put and each updating of coefficients is therefore slow, it is practical only for simple pulses, such as the terminal-peak sawtooth, that can be defined by a few data inputs. However, it is of fundamental interest because, as applied to an undamped simple resonator, it leads directly and simply to a spectrum.

General updatable Equation (11), for an undamped simple resonator, becomes

$$a(t-t_{K-1}) = B_K + C_K t + D_K \cos \omega t + E_K \sin \omega t \quad (18)$$

after a RAMP input or

$$a(t-t_K) = B_K + C_K t + D_K \cos \omega t + E_K \sin \omega t \quad (19)$$

after a STEP input.

For a RAMP data input, Equation (14), simplified for an undamped resonator, before addition of  $\cos \omega t$  and  $\sin \omega t$  multipliers to the existing coefficients  $D_{K-1}$  and  $E_{K-1}$  for updating, is shifted by Equations (16) and (17) to yield trigonometric functions of  $t$  and  $t$ . The new trigonometric coefficients are

$$D_K = D_{K-1} + (\Delta Y_K / 2\pi f) \sin 2\pi f t \quad \text{and} \quad (20)$$

$$E = E_{K-1} - (\Delta Y_K / 2\pi f) \cos 2\pi f t \quad (21)$$

For a STEP data input, Equation (15) is processed in the same way to provide for updating additions, but the excitation slope is set to zero after the STEP, which requires the the calculator or computer to add also a RAMP type correction for a  $-Y_{K-1}$  change of slope. Finally, the new trigonometric coefficients are

$$D_K = D_{K-1} - \Delta a_K \cos 2\pi f t - (Y_{K-1} / 2\pi f) \sin 2\pi f t \quad \text{and} \quad (22)$$

$$E = E_{K-1} - \Delta a_K \sin 2\pi f t + (Y_{K-1} / 2\pi f) \cos 2\pi f t \quad (23)$$

If there is no intent but a spectrum, coefficients  $B$  and  $C$  need not be updated, and no actual response computations need be carried out. It is merely necessary for the calculator or computer to apply Equations (20) and (21) or Equations (22) and (23) as appropriate after each data input, for each assigned spectral frequency, until all data inputs are complete. The final trigonometric coefficients  $D$  and  $E$  are respectively the cosine and sine coefficients (with time measured from

the origin) of the undamped sinusoid persisting after the shock -- in other words, they may be interpreted as the cosine and sine coefficients of the undamped residual spectrum, from which magnitude and angle may be obtained by a shift to polar coordinates.

Should the program user prefer a Fourier transform, it is shown in Appendix 1 that the cosine and sine transforms are given respectively by

$$F_C(f) = E_K / 2\pi f \quad \text{and} \quad (24)$$

$$F_S(f) = D_K / 2\pi f, \quad (25)$$

from which magnitude and angle may be obtained by a shift to polar coordinates.

For practical purposes, the undamped residual shock spectrum contains in slightly different form the same information as the Fourier transform. Its magnitude is expressed in terms of acceleration instead of velocity, which makes it more intuitively meaningful to the shock and vibration engineer, who likes as direct a relationship as possible to measures of failure. It will be shown in a later paper that the frequency derivative of the angle defined by the undamped residual spectrum can be interpreted as the APPARENT STARTING TIME of the undamped residual sinusoid. This is a well-behaved function of frequency and more suitable than the angle itself for plotting, or, in specification writing, for possible application of tolerances so as to approach a greater degree of uniqueness in a test shock.

## METHOD 2 SPECTRA AND RESPONSES

The second method utilizes a constant time increment, declared by the user near the beginning, after which only acceleration inputs are necessary. This time increment must be short enough to permit defining the wave shape, and, if instantaneous responses are desired, short enough to provide the user sufficient detail at the highest response frequency of interest. After each acceleration input, time shifts are applied to the existing response (the same amount each time) rather than to new terms generated by a RAMP or STEP. As trigonometric functions are computed only once, it is faster than the first method for complicated wave shapes. It is more directly suitable for the computation of response. Like Method 1, it can provide a spectrum by its final trigonometric coefficients, but these require an accumulated time-shift correction in or-

der to yield the correct phase angles.

Method 2 will be illustrated primarily in terms of the undamped resonator. Instead of Equation (11), the general updatable equation is

$$a(t > t_{K-1}) = E_K + C_K(t - t_{K-1}) + D_K \cos 2\pi f(t - t_{K-1}) + E_K \sin 2\pi f(t - t_{K-1}) \quad (26)$$

after a RAMP input or

$$a(t > t_K) = B_K + C_K(t - t_K) + D_K \cos 2\pi f(t - t_K) + D_K \sin 2\pi f(t - t_K) \quad (27)$$

after a STEP input.

Note that

$$t - t_{K-1} = t - t_K + t_K - t_{K-1} = t - t_K + \Delta t, \quad (28)$$

where

$$\Delta t = t_K - t_{K-1} \quad (29)$$

is the constant time increment, by which the updatable equation will be ratcheted along in time for RAMP and for STEP after STEP (as in a square wave) but not STEP after RAMP. This requires a combination of Equations (16), (17) and (28) applied to Equation (26) or (27).

To put it simply, the subscript  $K$  is incremented by the calculator or computer after every RAMP input and after every STEP after STEP. Each time  $K$  is incremented, the updatable equation is ratcheted along one more time increment by equations

$$\cos 2\pi f(t - t_K) = \cos 2\pi f \Delta t \cos 2\pi f(t - t_{K-1}) + \sin 2\pi f \Delta t \sin 2\pi f(t - t_{K-1}) \quad \text{and} \quad (30)$$

$$\sin 2\pi f(t - t_K) = \sin 2\pi f \Delta t \cos 2\pi f(t - t_{K-1}) - \cos 2\pi f \Delta t \sin 2\pi f(t - t_{K-1}), \quad (31)$$

or in other words, the coefficients are given by the calculator or computer a transformation

$$D_K = D_{K-1} \cos 2\pi f \Delta t + E_{K-1} \sin 2\pi f \Delta t \quad \text{and} \quad (32)$$

$$E_K = D_{K-1} \sin 2\pi f \Delta t - E_{K-1} \cos 2\pi f \Delta t. \quad (33)$$

Before this transformation, the RAMP addition is made in accordance with Equation (14) with the exponential set to unity. The STEP addition, preceded by this transformation unless the previous input was a RAMP, is made in accordance with Equation (15) with the exponential set to unity, and a RAMP term for  $\Delta \gamma_K = -\gamma_{K-1}$  is added.

After all data inputs are complete, the first time spectral phase information is required, the stored  $t$  is replaced by  $-n t$ , and the subroutine for Equations (32) and (33) is utilized to make a one-time correcting time shift. Testing for a negative sign prevents the operation from being erroneously repeated.

If the immediate intent is not one or more points in a spectrum but a sequence of instantaneous responses versus time, the operations are the same except that the general equation is evaluated after updating of coefficients every time  $k$  is incremented. Setting  $t=t$  in Equation (27) reduces it to the very simple

$$a(t_K) = E_K + D_K, \quad \text{where} \quad (34)$$

$$B_K = a_K. \quad (35)$$

In the more general case of a damped resonator, the updating and response operations remain exactly the same, except that the cosines and sines of Equations (26) and (27) are multiplied by  $\text{Exp}(-\alpha(t - t_{K-1}))$  or  $\text{Exp}(-\alpha(t - t_K))$  and consequently Equations (32) and (33) are replaced by

$$D_K = D_{K-1} e^{-\alpha \Delta t} \cos 2\pi f \Delta t + E_{K-1} e^{-\alpha \Delta t} \sin 2\pi f \Delta t \quad \text{and} \quad (36)$$

$$E_K = D_{K-1} e^{-\alpha \Delta t} \sin 2\pi f \Delta t - E_{K-1} e^{-\alpha \Delta t} \cos 2\pi f \Delta t. \quad (37)$$

After selection of  $\Delta t$  by the user, the calculator or computer computes exponential-trigonometric products once for each frequency, rather than merely trigonometric functions, and stores them for use in the updating time-shift operations.

On the HP-97 or HP-67 card-programmable calculator, Method 1 permits computation of spectra for six frequencies at a time. Method 2, requiring more memory registers per frequency, permits spectral computation for four frequencies at a time but is faster for a shock requiring many data inputs. Method 2 also permits computation of instantaneous responses for two frequencies of interest at a time, with whatever damping the user wishes.

#### HYBRID METHOD

Method 1 is satisfactory for computation of spectra of simple pulses and Method 2 permits computation of both spectra and responses for more complicated shock excitations. A problem remains if the user wants to obtain

responses to a simple pulse without more data inputs than are necessary to define the pulse. Several hybrid methods are possible for which the data inputs are as in Method 1 but the response computations are more like those of Method 2. According to the method selected for the programmable calculator, after each time-acceleration input, except for an initial STEP or STEP after RAMP, the user inputs a selected integer  $m$  large enough to provide sufficient detail at the highest response frequency of interest. The calculator divides the interval from the previous data input into  $m$  time segments, carries out suitable trigonometric and exponential computations for each frequency and stores the products, and then carries out updating and response computations as in Method 2 for that interval.

#### MULTIPLE-DEGREE-OF-FREEDOM RESONATORS

The general response equation can be generalized for a multiple-degree-of-freedom system while retaining essentially the same form. The primary difference is that there are terms for every frequency of the system, so that coefficient updating must be performed for each of these.

However, the HP-97 and HP-67 do not have sufficient memory capability for this straightforward approach. A variation on the two-resonator response program permitted computation of the response of a two-degree-of-freedom system in which the second resonator does not load the first (i.e.  $m/m = 0$ ). The computed response of the first resonator is used by the calculator as the RAMP input for the second resonator. After completion of excitation data inputs, the user can input zeros until the response of the first resonator is zero, or as long as he wishes, and observe the second resonator instantaneous response computations.

It is natural for a mechanical designer to design equipment so that successively smaller parts are attached to larger parts. This is favorable for withstanding static loads. However, when dynamic loads are propagated through successively smaller masses, any coincidence of successive resonance frequencies can result in violent whipping at the end of the transmission path. Therefore the calculator program for zero loading can at least illustrate a worst case that should be avoided.

#### COMPARISON TO FFT ALGORITHM

The indirect Fourier transform algorithm is by far superior to the fast Fourier transform algorithm in respect to relative memory requirement, whether the user's intent is spectral analysis or response computation. In respect to computation time the IFT is for practical purposes about comparable to the FFT for spectral analysis and again superior for response computation.

The development of the FFT algorithm (7,8,9,10) starts from an approximating summation for each frequency, known as the discrete Fourier transform (DFT) -- a set of  $N$  simultaneous equations (one for each frequency) each involving  $N$  data points from the shock excitation time-history. This is expressed as a matrix equation with an  $N \times N$  square matrix representing coefficients in quantity totalling to  $N$  squared, all of which would have to be computed and stored in memory. The number  $N$  of data points must be at least twice the maximum frequency of the set. The frequencies must be linearly spaced and equal to the number of data points. There can be no compromise on these matters, even if the excitation could be defined by fewer data inputs or only one or two frequencies are of interest.

The number of coefficients to be computed and stored is decreased by taking advantage of a potential redundancy. This is maximized and made most explicit by making  $N$  an integral power of 2:

$$N = 2^p, \quad (38)$$

where, by definition,

$$p = \log_2 N. \quad (39)$$

This changes the number of coefficients to be computed and stored from  $N$  squared to the much smaller  $N \log_2 N$ . The practical benefit may be slightly less, since  $N$  must be increased beyond twice the maximum frequency, even if this involves data inputs beyond the time for which the excitation has become negligible. This summarizes the FFT algorithm.

The IFT algorithm places no constraint on the number of frequencies in a spectral computation or on their numerical relationships. The HP-97/HP-67 spectral programs are for six or less -- clearly the FFT would be completely

out of the question for any practical shock computation on these calculators. IFT programs under continuing development for the Radio Shack TRS-80 personal computer are for 301 frequencies logarithmically spaced from 2 to 2000 Hz, or 100 per decade -- far less than required by FFT, yet more realistically what the shock and vibration engineer needs for adequate resolution over the frequency range.

IFT Method 1 requires computation of trigonometric functions for every frequency for each time-acceleration data input, but no more data inputs than are necessary to define the excitation pulse. IFT Method 2 requires a number N of acceleration data inputs comparable to that of FFT but like FFT permits computation of all trigonometric functions at the beginning, after which the multiply-add-on operations that consume most of the computation time are of essentially the same type for both algorithms.

First, consider IFT Method 2 versus FFT in respect to memory requirements for spectral analysis. Both algorithms require storage of trigonometric functions for every frequency, but the number M of frequencies chosen for IFT may be much smaller or even trivial in comparison to N, the number required by FFT. More important, IFT requires the storage of only 4M coefficients at any one time, compared to  $N \log N$  for FFT, and therefore has a major advantage in respect to memory requirements.

Second, consider IFT Method 2 versus FFT in respect to computation time for spectral analysis. IFT requires NM multiply-add-on operations versus  $N \log N$  for FFT. There is no general quantitative relationship between M and log N, but both are usually much less than N, so the two algorithms can be considered crudely comparable.

The number of frequencies required for acceptable resolution in spectral analysis is less for shock than for random vibration, because the problem is less immediately statistical. A finite sample of random vibration must be analyzed in such a way that the results are representative of an assumed infinite-duration stationary signal from which the sample was taken or, in the case of continuous control of a vibration test system, so that they will be representative of the next sample and no more adjustment of the system will take place than necessary. In either case, averaging in frequency is necessary to achieve statistical significance in the power spectra. A shock

time-history is not a sample of an infinite stationary signal but a complete record from initiation to negligibility -- the challenge of spectral analysis is merely to describe that one shock deterministically and accurately. If the shock should blend into a random vibration while becoming negligible, spectral analysis procedure is the same, except that there is a statistical error that can be estimated independently. Any one shock can be considered to be a member of a large non-ergodic ensemble or process, but this involves in principle a different kind of statistical analysis that is in practice impractical to carry out. In practical shock and vibration engineering, only one or two or at most a few records of a given type of shock at the same location and direction will be available, and these are best compared directly rather than analyzed statistically.

Finally, consider IFT Method 2 versus FFT for response computation. IFT is essentially the same as for spectral analysis except that the number of resonance frequencies of interest in a practical equipment item is usually much less than the number of frequencies required by FFT spectral analysis or even that desired for IFT spectral analysis. On the other hand, for any one set of resonance frequencies and any one shock excitation, FFT requires the computation of the Fourier transform of the excitation, multiplication by the transfer function of the equipment, and computation of an inverse transform. Therefore IFT is superior in respect to both memory requirement and computation time for equipment response computation, starting from excitation time-history data.

#### APPENDIX 1 -- O'HARA'S RELATIONSHIP

Previous authors (3,4) have derived a relationship between the residual shock spectrum and the Fourier transform by expressing a succession of velocity STEPs as a Duhamel integral. The present derivation will start from a succession of acceleration STEPs beginning at  $t=0$ . From Equation (10), the IFT summation that represents the response of an undamped simple resonator can be expressed as

$$a_r(t \geq t_k) = \sum_{k=0}^{\infty} (1 - \cos 2\pi f(t - t_k)) \Delta a, \quad (40)$$

which in the limit yields the integral

$$a_r(t \geq 0)$$

$$\begin{aligned}
&= \int_{u=-\infty}^{u=1} (1 - \cos 2\pi f(t-u)) da \\
&= \int_{u=0}^{\infty} (1 - \cos 2\pi f(t-u)) da, \quad (41)
\end{aligned}$$

because there is no error in changing the limits on the integral if they remain outside the shock duration. When this expression is integrated by parts, the first term generated will disappear because  $a(0)=0$  and  $a(\infty)=0$ :

$$\begin{aligned}
a_r(t) &= (1 - \cos 2\pi f(t-u)) a(u) \Big|_{u=0}^{\infty} \\
&+ 2\pi f \int_0^{\infty} a(u) \sin 2\pi f(t-u) du \\
&= -2\pi f \cos 2\pi f t \int_0^{\infty} a(u) \sin 2\pi f u du \\
&+ 2\pi f \sin 2\pi f t \int_0^{\infty} a(u) \cos 2\pi f u du \\
&= 2\pi f F_c(f) \cos 2\pi f t + 2\pi f F_s(f) \sin 2\pi f t, \quad (42)
\end{aligned}$$

where  $F_c(f)$  and  $F_s(f)$  are respectively the cosine and sine Fourier transforms of  $a(t)$ . The latter involves a minus sign because in the exponential version of the transform the exponent is negative. Equation (42) is the equation for the undamped sinusoid, or in other words the residual response, at the frequency of the resonator, that persists after shock termination. Inasmuch as the cosine and sine are functions of  $t$  as in IFT Method 1, this leads directly to the relationship expressed by Equations (24) and (25).

For the typical shock excitation, a sequence of RAMPs is preferable in practical spectral analysis because, without increasing the computation time significantly, it maintains a slope that is a good approximation to that of the excitation. Derivation of O'Hara's relationship from a succession of RAMPs is quite feasible but would require more integrations by parts. In any event, the derivation given above should be sufficient.

#### APPENDIX 2 -- HP97/67 PROGRAMS

There are ten programs, utilizing nine magnetic cards in various combinations. After each data input, the format of the printout (on HP-97) and display allow the user to keep his place in the data bank even in the event of distractions or interruptions.

##### PROGRAMS

##### CARDS

1 IFT and undamped residual 1  
magnitudes and phases, up to six  
frequencies, variable time incre-  
ments.

2 IFT and undamped residual 2,3  
magnitudes and phases, up to four  
frequencies, constant time incre-  
ment initially and acceleration  
time inputs only thereafter

3 Undamped single resonator 4,5,9  
responses after each acceleration  
input, constant time increment, up  
to two frequencies, IFT and residual

4 Undamped coupled resonator 4,6  
response after each acceleration  
input, constant time increment, two  
frequencies, second mass negligible  
compared to the first.

5 Responses and spectrum 4,6,9  
modified by a damped by a damped reso-  
nator, constant time increment, two  
frequencies, one Q.

6 Damped single resonator 4,5  
responses, up to two frequencies and  
Q's, residual magnitudes only.

7 Damped coupled resonator 4,6  
responses, constant time incre-  
ment, two frequencies and Q's.

8 Responses and spectrum 4,8,9  
modified by a damped resonator, hy-  
brid time increments, two frequen-  
cies, one Q, responses for  $m$  equal  
increments between acceleration-  
time increments.

9 Damped single-resonator 4,7  
responses, hybrid time incre-  
ments, up to two frequencies  
and Q's.

10 Damped coupled resonator 4,8  
responses, hybrid time incre-  
ments, two frequencies and Q's.

The individual magnetic program  
cards function as follows:

1 IFT and undamped residual, up to  
six frequency inputs, successive va-  
riable time inputs, and corresponding  
acceleration inputs until shock termi-  
nation, spectral printout.

2 IFT and undamped residual, up to  
four frequencies, constant time incre-  
ment, acceleration inputs to shock  
termination.

3 Four-frequency spectral printout.

4 Up to two frequency inputs and up  
to two Q inputs.

5 Single-resonator responses for up

to two frequencies and Q's, constant time increment and successive acceleration inputs to shock termination, response printouts.

6 Coupled-resonator responses for two frequencies and Q's, second mass negligible compared to first, constant time increment and successive acceleration inputs to shock termination, response printouts.

7 Single-resonator responses for up to two frequencies and Q's, hybrid, successive variable time inputs, number of subsegments inputs and acceleration inputs to shock termination, response printouts.

8 Coupled-resonator responses for two frequencies and Q's, second mass negligible compared to first, hybrid, successive variable time inputs, number of subsegments inputs and acceleration inputs to shock termination, response printouts.

9 Two-frequency spectral printouts.

#### BIBLIOGRAPHY

- 1 C. M. Harris and C. E. Crede, SHOCK AND VIBRATION HANDBOOK, Chapter 21, McGraw-Hill, 1976.
- 2 M. A. Biot, "Analytical and Experimental Methods in Engineering Seismology", Transactions of the ASCE, No. 18, pp. 365-385, 1943.
- 3 B. J. O'Hara, "A Numerical Procedure for Shock and Fourier Analysis", NRL Report 5772, June 5, 1962.
- 4 C. T. Morrow, SHOCK AND VIBRATION ENGINEERING, Chapter 9, Wiley, 1963.
- 5 C. T. Morrow, THE ENVIRONMENTAL SPECIFICATION AS A TECHNICAL MANAGEMENT TOOL, 59-62, The Shock and Vibration Information Center, November 1981.
- 6 C. T. Morrow, "Shock Spectra and Responses by Pocket Calculator", SHOCK AND VIBRATION BULLETIN 47, Part 1, 49-76, The Shock and Vibration Information Center, 1977.
- 7 L. D. Enochson and R. K. Otnes, PROGRAMMING AND ANALYSIS FOR DIGITAL TIME SERIES DATA, CHAPTER 4, The Shock and Vibration Information Center, 1968.
- 8 J. W. Cooley and J. W. Tukey, "An Algorithm for the Machine Calculation of Complex Fourier Series", Math. Comput., 19, 297, April 1965.

9 W. M. Gentleman and G. Sande, "Fast Fourier Transforms for Fun and Profit", AFIPS Conference Proc., 29, 563-578, 1966, Spartan Books, Washington, D.C.

10 E. O. Brigham and R. E. Morrow, "The fast Fourier transform", IEEE SPECTRUM, 63-70, December 1967.



## CONTROL, ISOLATION AND DAMPING

### ACTIVE VIBRATION CONTROL OF LARGE FLEXIBLE STRUCTURES

T.T. Soong and J.C.H. Chang  
Department of Civil Engineering  
State University of New York at Buffalo  
Amherst Campus, Buffalo, New York 14260

This paper is concerned with active vibration control of large and complex structures. An important problem of actively controlling large flexible structures is one of compensating for control and observation spillover when a large-dimensional system must be controlled by a much smaller dimensional controller. A modal control design procedure is developed in this paper which not only insures that the controlled structural modes stay close to the designed values but also preserves stability in the uncontrolled modes. The sensitivity of spillover compensation to the placement of controllers and sensors is also studied.

#### INTRODUCTION

The application of modern control theory to the control of flexible structures has produced some notable successes in the past. Aircraft flutter control and motion control of rockets and aerospace vehicles are two prime examples in which control is applied in order to reduce excessive vibration and to insure structural integrity. In recent years, however, interest in the study of structural control has been extended to control problems associated with very large and complicated structures. Two of the important areas are:

(a) Large Space Structures (LSS). The development of space systems has led to the consideration of very large spacecrafts and satellites which could be assembled and deployed in space. These structures conceptually can span literally miles in size with large flexible appendages. Stringent pointing and motion requirements immediately suggests the use of active control concepts whereby sensors and actuators are located about the structure to perform required functions via on board computers.

(b) Civil Engineering Structures (CES). The idea of actively controlling the motion of tall buildings and long bridges subject to environmental loads also has a recent origin. With the trend toward taller, longer, and more flexible structures, control concepts are advanced for the purpose of increasing structural integrity, enhancing human comfort and safety, and reducing potential damages by means of modifying a structure's response to

environmental loads induced by wind, earthquake, and other disturbances.

The development of control methodology for flexible structures of sizes and complexities as encountered in LSS and CES gives rise to a number of unique and important problems from both theoretical and practical points of view. These include (1) the necessity of using low-order discretized systems to approximate flexible structures which are basically distributed-parameter systems, (2) the problem of control and observation spillovers when control is designed based on the discretized system but is applied to the actual system, (3) the problem of placement of limited number of sensors and controllers in some optimal fashion, and (4) control design under practical constraints such as external energy supply.

This paper is primarily concerned with active modal control design which compensates for control and observation spillover. Since control and observation spillover leads to potential instabilities in the uncontrolled modes, one of the fundamental problems in active control of complex structures is that of spillover compensation and preservation of stability in all modes. In this paper, a design procedure is developed which not only insures that the controlled modes of the structures stay close to the designed values but also preserves stability in the uncontrolled modes. It is shown that the appropriate control methodology obtained based upon this approach is in general different from conventional control design.

The sensitivity of spillover compensation to the placement of controllers and sensors is also studied. Given the available number of controllers and sensors and under controllability and observability conditions, optimal controller and sensor configurations can also be determined with respect to spillover minimization.

#### MODEL REDUCTION AND CONTROL-OBSERVATION SPILLOVER

Complex structures are continua whose dynamic behavior is generally described by distributed-parameter systems. In the design of active control for such systems using known state variable methods, a lumped-parameter approximation is usually applied which possesses very large or infinite dimension in its state space. However, due to limitations on the number of implementable controllers and sensors as well as limited on-board computation capacity, it is impractical or impossible to carry out control design based upon full-order discretized systems. Hence, reduced-order models are necessary for the purpose of control design, resulting in control and observation spillover into the vibrational modes ignored in the reduced-order model.

In order to see this spillover effect, let us start with the full-order discretized system (FOS) represented by the vector-matrix equation

$$\dot{x} = Ax + Bu \quad (1)$$

with the observation equation

$$y = Cx \quad (2)$$

where  $x$  is an  $n$ -dimensional state vector of the structural system ( $n$  large),  $A$  is the system matrix,  $u$  is a  $p$ -dimensional control vector, and  $B$  is the control location matrix. In Eq. (2),  $y$  is the  $k$ -dimensional output or observation vector and  $C$  is the observation matrix.

A reduced-order model (ROM) can be generated through aggregation or modal eigenfunction expansion techniques by retaining only the controlled modes of the system, giving

$$\dot{x}_c = A_c x_c + B_c u + E_c \quad (3)$$

with the observation equation

$$y = C_c x_c + R_c \quad (4)$$

In the above, the dimension of  $x_c$  is in general much smaller than that of  $x$ .  $E_c$  and  $R_c$  are error terms introduced through the truncation process; they can be represented by

$$E_c = A_{cr} x_r \quad \text{and} \quad R_c = C_r x_r \quad (5)$$

where  $x_r$  is the state vector associated with the residual (or uncontrolled) modes of the FOS. It is governed by

$$\dot{x}_r = A_r x_r + B_r u + E_r \quad (6)$$

The error term  $E_r$  in the residue equation has the form

$$E_r = A_{rc} x_c \quad (7)$$

The error term  $E_c$  in Eq. (3) represents the modelling error due to the model reduction process. The term  $B_r u$  in Eq. (6) shows the effect of control  $u(t)$  entering the residue subsystem, or control spillover to the residue modes. The contamination of observations in Eq. (4) with residue information  $R_c$  produces observation spillover. Thus, the  $C_c$  controller imparts energy to the residual modes through the interaction term  $B_r u$  and the resulting residual mode excitation is in turn detected by the sensors through the term  $R_c$  for control design, resulting in an escalating performance degradation. These interactions are graphically shown in Fig. 1. It can be shown that spillovers can reduce stability margins of the actual structure and are at the heart of the control problem based upon reduced-order models [1].

Clearly, the magnitude of control and observation spillover is a function of the model reduction process. It is also a function of controller and sensor locations and their effects on the residue modes. Our interest here is, however, not with the derivation of reduced-order models but with the interaction of spillover and control design, together with the problem of controller and sensor placement from the point of view of spillover minimization. This is developed in the next section.

#### CONTROL DESIGN AND EFFECT OF SPILLOVER

In this section, we begin by developing the feedback control  $u(t)$  based upon the reduced-order system given by Eqs. (3) and (4) with  $E_c = 0$  and  $R_c = 0$ . It is assumed that the system  $C(A_c, B_c, C_c)$  is controllable and observable [2].

The active controller consists of (a) a state estimator which accepts the sensor measurement  $y(t)$  and produces an estimate  $\hat{x}_c(t)$  of the state  $x_c(t)$  and (b) a linear state feedback control law which gives control  $u(t)$  as

$$u(t) = K \hat{x}_c(t) \quad (8)$$

where the constant gain  $K$  is determined as though the true state  $x_c(t)$  were available

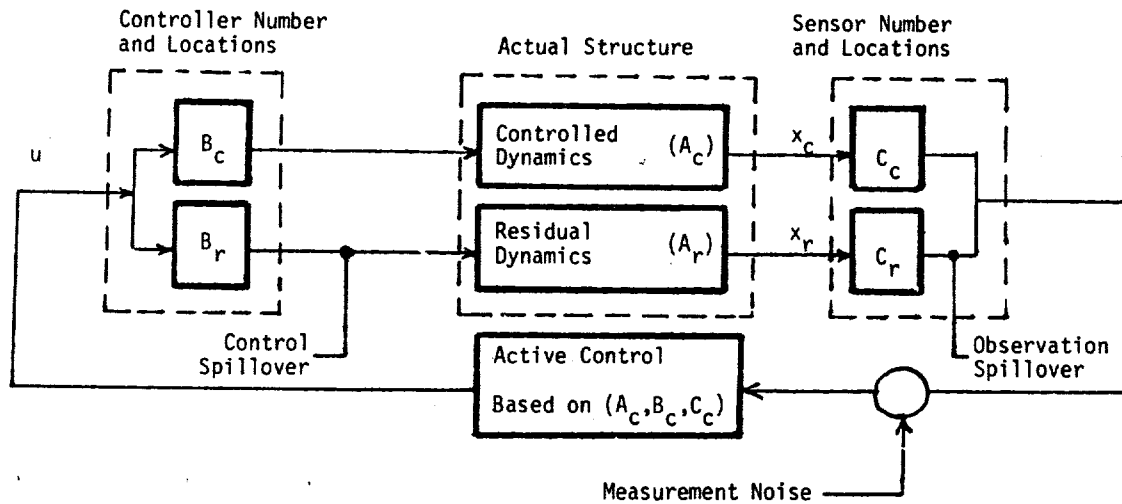


Fig. 1. - Interaction Among Model Reduction, Spillover, and Sensor and Controller Placement.

instead of  $\hat{x}_c(t)$  and is obtained using either modal control or optimal control methods. In the modal control approach, for example, the gain  $K$  is found in such a way that the eigenvalues of the matrix  $A_c + B_c K$  are appropriately placed and this can always be accomplished when  $(A_c, B_c, C_c)$  is controllable and observable.

The state estimator can be designed as a Luenberger observer when the signal-to-noise ratio for the output is sufficiently high and as a Kalman filter otherwise. It has the form

$$\dot{\hat{x}}_c(t) = A_c \hat{x}_c(t) + B_c u(t) + G[y(t) - \hat{y}(t)] \quad (9)$$

$$\hat{x}_c(0) = 0; \quad \hat{y}(t) = C_c \hat{x}_c(t)$$

that is, it has an internal model of the system  $(A_c, B_c, C_c)$  being estimated and it corrects the model by a linear feedback of the difference between the measured output  $y(t)$  and the computed output  $\hat{y}(t)$ . In the Luenberger version, the estimator gain  $G$  is chosen so that the estimator error  $\hat{x}_c(t) - x_c(t)$  decays exponentially at a prescribed rate.

Consider now the effect of spillover when the controller, designed based on the reduced-order system, is applied to the full-order system given by Eqs. (1) and (2). The substitution of Eq. (8) into Eq. (1) yields

$$\begin{aligned} \dot{x} &= Ax + BK\hat{x}_c \\ &= Ax + BKx_c + BK[\hat{x}_c - x_c] \end{aligned} \quad (10)$$

Let

$$e(t) = \hat{x}_c(t) - x_c(t) \text{ and } x_c = Dx \quad (11)$$

we then have

$$\dot{x} = (A + BKD)x + BKe \quad (12)$$

For the error term  $e(t)$ , the first of Eqs. (11) leads to

$$\dot{e} = G(C - C_c D)x + (A_c - GC_c)e \quad (13)$$

Define the composite closed-loop system state by

$$w(t) = \begin{bmatrix} x(t) \\ e(t) \end{bmatrix} \quad (14)$$

Then,

$$\dot{w}(t) = Qw(t) = \begin{bmatrix} Q_{11} & Q_{12} \\ Q_{21} & Q_{22} \end{bmatrix} w(t) \quad (15)$$

with

$$\begin{aligned} Q_{11} &= A + BKD \\ Q_{12} &= BK \\ Q_{21} &= G(C - C_c D) \\ Q_{22} &= A_c - GC_c \end{aligned} \quad (16)$$

It is seen that the sensor output is contaminated by the residue modes through the term  $(C - C_D)x(t)$ , which can be identified as  $C_r x_r$ , the observation spillover. Thus, while the poles of  $A + BKD$  and  $A_c - GC_c$  can be designed with substantial stability margin, the presence of observation spillover can lead to instabilities in the residue modes. This is especially true in the lightly damped system. The theorem stated below helps to quantify this pole shifting effect due to the observation spillover; its proof can be found in [3].

**Theorem.** Let the  $j$ th eigenvalue and its corresponding eigenvector of  $Q$  in the absence of observation spillover be denoted by  $\lambda_j$  and  $u_j$ , respectively, and assume that the  $\lambda_j$  eigenvalues are distinct without loss of generality. Then the amounts of change in  $\lambda_j$  and  $u_j$  due to the presence of  $Q_{21}$  are given by

$$\delta\lambda_j = \frac{[\delta Q u_j]^T v_j}{u_j^T v_j} \quad (17)$$

$$\delta u_j = \sum_{i \neq j} \frac{[\delta Q u_j]^T v_i u_i}{(\lambda_j - \lambda_i) u_i^T v_i} \quad (18)$$

where

$$\delta Q = \begin{bmatrix} 0 & I & 0 \\ - & - & - \\ Q_{21} & I & 0 \end{bmatrix} \quad (19)$$

and  $v_j$  is the  $j$ th eigenvector associated with  $\lambda_j^*$ , the complex conjugate of the spillover-free matrix  $Q$ .

#### ACTIVE CONTROL DESIGN WITH SPILLOVER COMPENSATION

In view of the fact that spillover can cause serious system performance degradation, it is important that conventional design procedure be modified in order to eliminate or minimize spillover effects. The most obvious method of spillover reduction is to locate the controllers and sensors at or very near the zeros of the affected modes. However, this is difficult, if not impossible, to do as the freedom of locating sensors and controllers is rarely available to the control designer. Other attempts include the introduction of a "comb" filter between the sensor output and state estimator for the purpose of "combing out" the residue modes [4], implementation of an orthogonal filter in an attempt to counteract spillover as an unmodelled disturbance [5,6], and addition

of measurements for more complete state feedback [7]. However, these procedures are indirect and can become ineffective when the residue modes are closely spaced or when it becomes impractical to add required number of sensors.

The control design procedure proposed in this paper is a direct modification of the spillover-free control law as indicated in Sec. III by requiring that the controlled modes of the system stay close to the designed values and that the stability of the uncontrolled modes be preserved.

Let the dimensions of  $x$  in Eq. (1) and  $x_c$  in Eq. (3) be  $n$  and  $m$ , respectively, and consider the  $(n+m) \times (n+m)$  matrix  $Q$  defined in Eqs. (15) and (16). For structural systems, the eigenvalues of  $Q$  consist of complex conjugate pairs  $(\lambda_1, \lambda_1^*), (\lambda_2, \lambda_2^*), \dots, (\lambda_{n+m}, \lambda_{n+m}^*)$  and, for convenience, we shall assume that they are distinct at least in the controlled modes. In modal control, the control objective is to affect changes in the controlled modes so that they take prescribed eigenvalue pairs  $(\rho_1, \rho_1^*), (\rho_2, \rho_2^*), \dots, (\rho_m, \rho_m^*)$ .

In the absence of spillover, it is straightforward to determine the control gain  $K$  as indicated in Sec. IV. With the presence of spillover, the proposed procedure calls for a modification in the value of  $K$  by minimizing the cost function

$$J = \sum_{j=1}^m r_j |\lambda_j - \rho_j|^2 = \omega_c^T R \omega_c^* \quad (20)$$

where

$$\omega_c = \begin{bmatrix} \lambda_1 - \rho_1 \\ \vdots \\ \lambda_m - \rho_m \end{bmatrix} \quad (21)$$

and

$$R = \text{diag}[r_1 \dots r_m] \quad (22)$$

while a set of inequality constraints is satisfied. These inequality constraints arise from stability requirements in the uncontrolled modes and can be written in the form

$$\text{Re}(\lambda_j) + \epsilon_j \leq 0, \quad j = m+1, \dots, n \quad (23)$$

where  $\epsilon_j$  are some prescribed small positive numbers.

The optimization problem with the cost function defined by Eq. (20) and inequality constraints given by Eq. (23), although highly

nonlinear, can be numerically carried out using the method of Lagrange multipliers with the help of carefully defined slack variables. It can be shown that the problem reduces to that of finding the solution of a set of  $(r+n-m)$  simultaneous nonlinear equations, where  $r$  is the number of unknown parameters in the optimization problem. While the dimension  $(r+n-m)$  is in general large due to large  $n$ ; the procedure can be facilitated by seeking the control gain  $K$  sequentially by incorporating into the solution procedure the inequality constraints given by Eq. (23) sequentially. Numerical experimentations show that the solution for control gain stabilizes at a rate proportional to the number of inequality constraints considered at each stage.

It is noted that, in addition to  $K$ , the optimization process can also be carried out with respect to  $B$  and  $C$ , leading to optimal locations for sensors and controllers. In these cases, we see that the value of  $r$  increases and a more difficult numerical problem is encountered.

#### A NUMERICAL EXAMPLE

For the purpose of numerical comparison, it is instructive to illustrate the results with a simple example in which all modal data are readily obtained. Consider a structural system whose FOS is described by Eqs. (1) and (2) with  $n = 10$ ,  $p = 1$ ,  $k = 1$  and

$$A = \begin{bmatrix} 0 & \vdots & I \\ \vdots & \ddots & \vdots \\ A_{21} & \vdots & A_{22} \end{bmatrix} \quad (24)$$

$$B^T = [0 \ 0 \ 0 \ 0 \ 0 \ 0 \ 0 \ 0 \ 0 \ 1.0] \quad (25)$$

$$C = [0 \ 0 \ 0 \ 0 \ 1 \ 0 \ 0 \ 0 \ 0 \ 20.0] \quad (26)$$

in which the matrices  $A_{21}$  and  $A_{22}$  take values so that FOS represents a lightly damped five-degree-of-freedom mass-spring-damper system. Eq. (25) indicates that a single controller is applied at the fifth mass and Eq. (26) shows that a single sensor is located at the same mass with its displacement and velocity observed. The eigenvalues of  $A$  are

$$\begin{aligned} \lambda_1, \lambda_1^* &= -0.0036 \pm 12.679i \\ \lambda_2, \lambda_2^* &= -0.0055 \pm 37.011i \\ \lambda_3, \lambda_3^* &= -0.0012 \pm 58.344i \\ \lambda_4, \lambda_4^* &= -0.0458 \pm 74.950i \\ \lambda_5, \lambda_5^* &= -0.0941 \pm 85.484i \end{aligned} \quad (27)$$

In this example, the critical modes are taken to be the first three structural modes (the first three pairs of eigenvalues) and the fourth and fifth modes are the residue modes. Thus, the reduced-order system is one of order six ( $m = 6$ ) with

$$B_c^T = [0 \ 0 \ 0 \ 0.12 \ -0.16 \ 0.86] \quad (28)$$

$$C_c = [0 \ 0 \ 1 \ 0 \ 0 \ 20.0] \quad (29)$$

The control objective is to apply active control to the uncontrolled system so that the three controlled modes take the following desired values:

$$\begin{aligned} \rho_1, \rho_1^* &= -1.370 \pm 16.679i \\ \rho_2, \rho_2^* &= -1.888 \pm 40.011i \\ \rho_3, \rho_3^* &= -2.583 \pm 61.344i \end{aligned} \quad (30)$$

In the control design, the following cases are of interest:

- Case A. The conventional modal control design based upon the ROM while ignoring the uncontrolled modes.
- Case B. The modified modal control design where the control gain is determined by minimizing the cost function given by Eq. (20) with inequality constraints given by Eq. (23). The matrix  $R$  in Eq. (20) is taken to be  $I$  and  $\epsilon_1 = \epsilon_2 = 0.00001$  in Eq. (23).
- Case C. The same as Case B but with  $\epsilon_1 = \epsilon_2 = 0.1$ .

The pole shifting characteristics for all three cases are summarized in Tables I-III. It is shown that conventional modal control design (Case A) can lead to instabilities in the residue modes in the presence of spillover. On the other hand, the modified procedure (Cases B and C) insures stability in the residue modes while the controlled modes are kept close to their desired values. Results for Cases B and C also show that varied stability margins in the residue modes can be achieved but modal accuracy in the controlled modes is somewhat sacrificed.

A more dramatic difference in results between Cases A and B is shown in Figs. 2 and 3 when the system is subjected to a somewhat arbitrary forcing function. Fig. 2 shows  $x_5$ , the displacement of the fifth mass, as a function of time under uncontrolled condition and under conventional control (Case A). While a reduction of displacement magnitude is affected by Case A control, instabilities in the residue modes cause oscillation with increasing magnitude. In contrast, Case B

TABLE I  
Pole Shifting Characteristics (Case A)

Mode	Uncontrolled	Controlled without Spillover	Controlled with Spillover
1	$-0.0036 \pm 12.68i$	$-1.370 \pm 16.68i$	$-1.376 \pm 16.67i$
2	$-0.0055 \pm 37.01i$	$-1.888 \pm 40.01i$	$-1.876 \pm 39.93i$
3	$-0.0012 \pm 58.34i$	$-2.583 \pm 61.34i$	$-2.107 \pm 60.91i$
4	$-0.0458 \pm 74.95i$	$-0.0458 \pm 74.95i$	$+0.189 \pm 75.61i$
5	$-0.0941 \pm 85.48i$	$-0.0941 \pm 85.48i$	$-0.033 \pm 85.59i$

TABLE II  
Pole Shifting Characteristics (Case B)

Mode	Uncontrolled	Controlled without Spillover	Controlled with Spillover
1	Same as Case A	$-1.404 \pm 16.68i$	$-1.410 \pm 16.67i$
2		$-1.974 \pm 40.05i$	$-1.971 \pm 39.97i$
3		$-4.118 \pm 61.27i$	$-3.038 \pm 60.79i$
4		$-0.046 \pm 74.95i$	$-0.00001 \pm 75.81i$
5		$-0.094 \pm 85.48i$	$-0.054 \pm 85.64i$

TABLE III  
Pole Shifting Characteristics (Case C)

Mode	Uncontrolled	Controlled without Spillover	Controlled with Spillover
1	Same as Case A	$-2.105 \pm 16.32i$	$-2.109 \pm 16.29i$
2		$-3.143 \pm 38.24i$	$-2.937 \pm 38.26i$
3		$-0.807 \pm 58.84i$	$-0.778 \pm 58.85i$
4		$-0.046 \pm 74.95i$	$-0.100 \pm 75.26i$
5		$-0.094 \pm 85.48i$	$-0.100 \pm 85.55i$

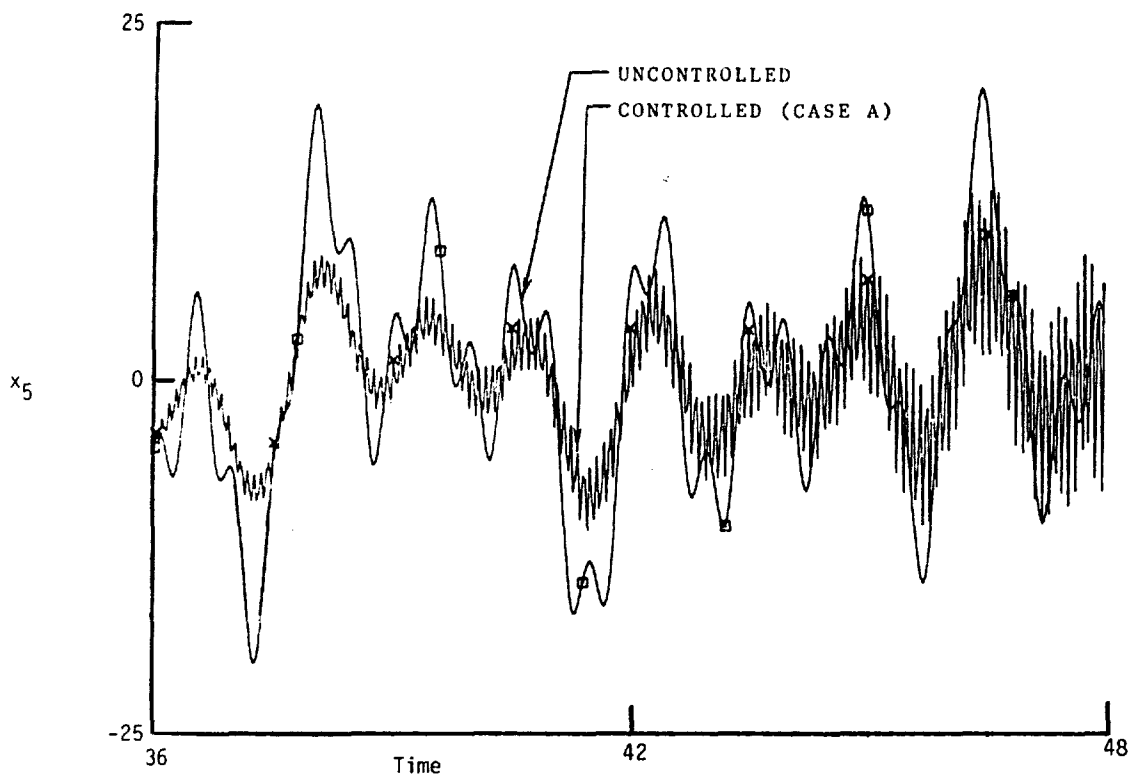


Fig. 2 - Displacement  $x_5$  - Uncontrolled and Controlled (Case A)

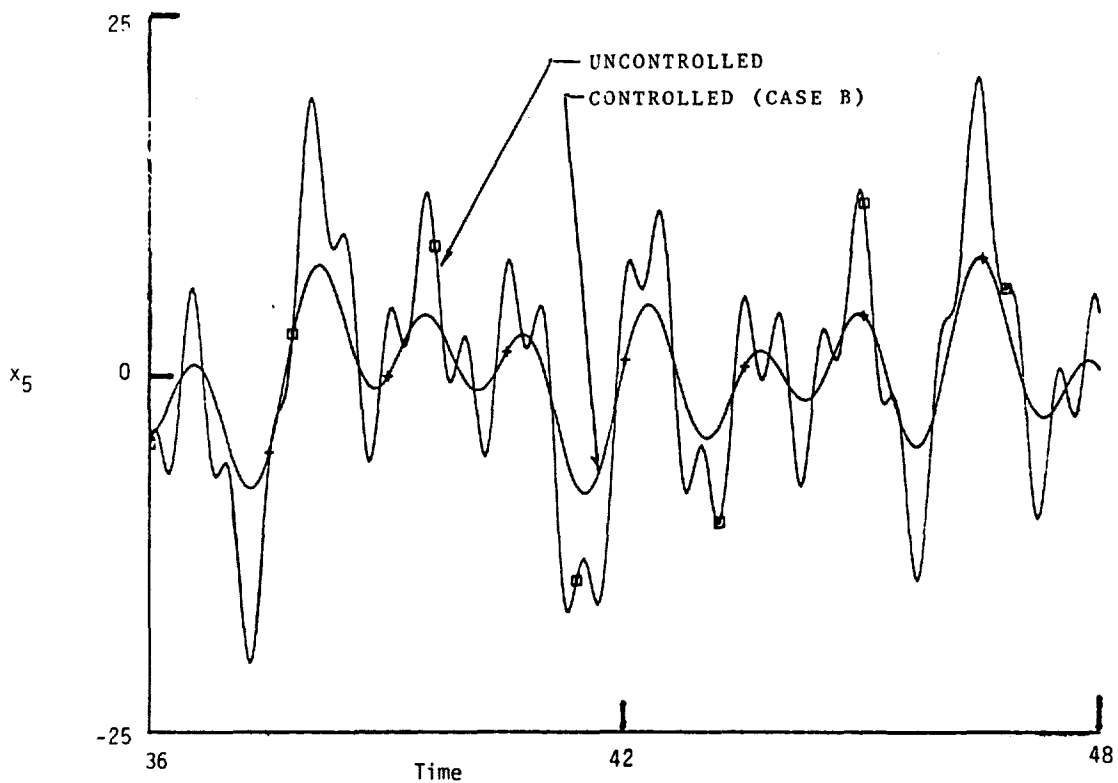


Fig. 3 - Displacement  $x_5$  - Uncontrolled and Controlled (Case B)

control leads to stable results as shown in Fig. 3.

#### CONCLUDING REMARKS

Since reduced-order systems are generally needed for control design for control of complex structural systems, it is shown that serious system performance degradation can result due to control and observation spillover. In particular, possible instability in the residue modes due to observation spillover is quantified.

In this paper, a procedure is proposed which modifies the conventional control design in order to remove undesirable spillover effects from the residue modes. The proposed procedure also permits a study of the sensitivity of sensor and controller placement to spillover compensation.

#### REFERENCES

1. M.J. Balas, "Modal Control of Certain Flexible Dynamic Systems," SIAM J. Control and Optimization, 16, pp. 450-462, 1978
2. H. Kwakernaak and R. Sivan, Linear Optimal Control Systems, Wiley-Interscience, New York, 1972
3. J.N. Franklin, Matrix Theory, Prentice-Hall, New York, 1968
4. D.E. Gustafson and J.L. Speyer, "Linear Minimum Variance Filters Applied to Carrier Tracking," IEEE Trans. Auto. Cont., AC-21, pp. 65-73, 1976
5. R.E. Skelton and P.W. Likins, "Orthogonal Filters for Model Error Compensation in the Control of Nonrigid Spacecrafts," J. Guidance and Cont., 1, pp. 41-49, 1978
6. R.E. Skelton, "Adaptive Orthogonal Filters for Compensation of Truncated Modes and Other Modal Data Uncertainty in Spacecraft," Proc. AIAA 17th Aerospace Science Meeting, New Orleans, 1979
7. Y.W. Wu, R.B. Rice, and J.H. Juang, "Sensor and Actuator Placement for Large Flexible Space Structures," Preprint JACC, 1979

#### ACKNOWLEDGMENT

This work was partially supported by the National Science Foundation under Grant No. CEE 8010291.



## FORCE OPTIMIZED RECOIL CONTROL SYSTEM

PHILIP E. TOWNSEND  
US ARMY ARMAMENT RESEARCH AND DEVELOPMENT COMMAND  
DOVER, NEW JERSEY

and

ROBERT J. RANKIEWICZ  
US ARMY ARMAMENT RESEARCH AND DEVELOPMENT COMMAND  
ROCK ISLAND, ILLINOIS

and

ROBERT F. GARTNER  
HONEYWELL, INC.  
EDINA, MINNESOTA

### INTRODUCTION

1.0 In the era of the MX missile and the neutron bomb, the basic tool of the military is still the gun. Whether its form is the rifle for a footsoldier, an automatic cannon on an aircraft, or howitzer in an artillery battalion, the gun is effective, reliable, and economical. The inherent wide mission versatility of the gun allows the quick response employment of gun-type weapons in the broadest range of battle scenarios.

Today heavy emphasis is placed on the ability to provide global response with minimum time lapse by the airlift of troops and materiel. In the battle zone, high combat fluidity is produced with helicopter dispatched movement of troops and materiel under coordinated command and control of the combined arms team concept.

The need to airlift materiel requires the armament engineer to design systems that are lightweight, yet retain or increase the firepower previously provided. When gun systems were first employed on helicopter gunships during the early 1960's, low impulse 7.62mm machine guns and grenade launchers were employed. Today the threat posed by the Sino-Soviet military machine requires that automatic cannons replace the low impulse weapons to provide greater standoff range and greater terminal effects.

The gun is a classical demonstration of Newton's first law. The action of a gun is the release of a large amount of energy in a few milliseconds. The dissipation of this energy is one of the key design factors in

the integration of the gun into its system application. Typically, a spring damper unit is imposed between the gun and its mount to absorb the energy. The spring system lowers the peak force generated by the gun and lengthens the action time. The actual force level is a function of the propellant impulse, the masses of the projectile and recoiling weapon, friction and the spring system design. The spring system design presents a tradeoff between the tolerable force level, the distance the gun is allowed to recoil, and the period between firings.

While the design problem is essentially the same for any gun system integration, the helicopter gunship offers some unique challenges to the designer. First, weight is a critical consideration in helicopter design so the basic airframe is a skeletal structure that is very sensitive to vibration loading such as produced by a rapidly firing gun. The lightweight structure also requires the peak recoil force transferred to it to be held at a minimum level to preclude damage through immediate stresses or longer term fatigue effects. The gun is employed primarily as a suppressive weapon and is turret mounted to provide the widest volume of coverage possible. This restricts the length of recoil within the turret envelope and causes the direction of the loading to vary widely as it is transferred through the surrounding structure. These design considerations coupled with the need to provide greater firepower, are approaching the limits of what can be accomplished with passive spring damper systems on the current helicopter airframes. As

the peak recoil force increases, the sensitivity of other system components, such as optical sighting systems, to firing rate frequency increases because the lightweight structure transmits the vibrations throughout the structure.

Continuing to increase the firepower, yet retain the other desired or required armament system features demands a departure from the current mounting philosophy. Replacing the passive spring-damper unit with a microprocessor controlled electro-hydraulic cylinder allows a maximum reduction in the peak recoil load, indeed changing the nature of the loading from a vibration generating pulse to a constant force that reacts with the local structure as if it were a static load during the firing period.

This paper will discuss a fire-out-of-battery concept for reducing gun peak recoil loads and test results obtained from two significantly different automatic, rapid fire guns. This Force Optimized Recoil Controller (FORC) system reduced the transmitted recoil loads from the firing guns by over 70% when compared to recoil loads measured when using conventional recoil adapters.

The theory of the FORC system will be discussed in Section 2.0 along with the control algorithm used to adjust changes in the recoil displacement and velocity of the system during firing due to variations in system parameters. Section 3.0 will discuss the hardware used to implement the FORC system and the guns and ammunition that were used in testing the system. Test results for two different guns are provided in Section 4.0, with comparison made between recoil loads measured with standard adapters and with the FORC system. Finally, a summary of results is presented in Section 5.0.

## 2.0 FORC CONCEPT

The FORC concept is to average the impulse of a fired round of ammunition over the total time between rounds. The average force is then much lower than the large impulse force of the round, reducing shock loads throughout the structure to which the gun is mounted.

Consider a round of ammunition with an impulse,  $I$ , causing a recoil force,  $F(t)$ . Then, if no other dissipative forces such as friction are present, we know that

$$I = \int_0^T f(t) dt \quad (1)$$

where  $T$  is the time between rounds. If the recoil system can provide a constant force transmitted from the gun to the mount between rounds equivalent to the impulsive force, then

$$I = F_{AV} \cdot T \quad (2)$$

$F_{AV}$  is the minimum recoil force that can then be achieved by the gun system with no other energy dissipative system present.

## 2.1 Fire-Out-Of Battery Principle

The fire-out-of-battery principle uses the initial momentum of the gun's dynamic components to absorb a portion of the ammunition's energy. The recoil system provides a constant force to the gun before it fires and ideally the gun fires when its forward momentum is equal to one half the round impulse. Consider Eqn. (2) rewritten in terms of the constant acceleration of the system. Then

$$\dot{x} = \frac{I}{T \cdot M} \quad (3)$$

where  $M$  is the mass of the recoiling components of the gun system. Integrating this equation with the system initially at rest and with the gun firing at time  $T/2$ , half the time between rounds, the velocity is then given by

$$\dot{x}_F = \frac{I}{2M} \quad (4)$$

The momentum of the moving system at the time of fire is then one half the round momentum as stated previously. The impulse of the round then causes the velocity of the system to reverse and it is equal to  $-\dot{x}_F$ . This is shown in Figure 1, which is a graph of the constant acceleration, velocity, and displacement for an ideal recoil system.

The constant forward acceleration causes the velocity to increase linearly to zero at time  $T$ , the time between rounds. At this time, the displacement is also again zero and the cycle repeats.

## 2.2 Hydropneumatic Spring

The constant forward acceleration for the FORC system is provided by a hydropneumatic spring. To maintain nearly constant acceleration requires that the force-displacement curve for the spring be flat, i.e., a large preload on a low spring rate. This was achieved by means of a hydraulic piston with an integral nitrogen accumulator to act as the spring. The hydraulic fluid provided the preload for the spring and its compressibility can be neglected when compared to that of the nitrogen.

For an ideal system the average force required for the FORC system can be determined from Eqn. (2). This force is then equal to

$$F_{AV} = \left( \frac{P_I + P_F}{2} \right) \cdot A_p \quad (5)$$

where  $P_I$  is the initial nitrogen pressure,  $P_F$  is the nitrogen pressure at the time of firing, and  $A_p$  is the piston area. Due to the small volume change adiabatic expansion of the

nitrogen is assumed and we have

$$P_I V_I^{1.4} = P_F V_F^{1.4} \quad (6)$$

where  $V_I$  is the initial nitrogen volume and  $V_F$  is the nitrogen volume at the time of firing.

With the gun displacement at the time of firing,  $x_F$ , known, the two nitrogen volumes can be related by

$$V_F = V_I + x_F A_p \quad (7)$$

Substituting Eqns (6) and (7) into Eqn (5) and solving for  $P_I$ , we obtain

$$P_I = \frac{2F_{AV}}{A_p} \frac{1}{\left(1 + \left(\frac{V_I}{V_I + A_p x_F}\right)^{1.4}\right)} \quad (8)$$

By including friction,  $F_c$ , and back pressure in the hydraulic system,  $P_{B2}$  Eqn (8) becomes

$$P_I = \frac{2F_{AV} + F_c + P_{B2} A_B}{A_p \left(1 + \left(\frac{V_I}{V_I + A_p x_F}\right)^{1.4}\right)} \quad (9)$$

$A_B$  is the area of the piston opposite the working side (see next section). This equation can be used to size the piston, accumulator volumes, and to determine system working pressure. However, since all values are not known exactly the system was designed so that the preload of the hydropneumatic spring could be adjusted by the addition and subtraction of oil from the hydraulic side of the spring. The system, therefore, was designed as a closed loop system capable of handling a variety of parameter variations.

### 2.3 FORC Control Algorithm

Control of the recoiling gun system is maintained by monitoring key system parameters with a microprocessor and then solving a control algorithm to vary the preload on the hydropneumatic spring. The preload is controlled by a servovalve which adds or subtracts hydraulic fluid from the recoil piston.

Parameters which are used by the control algorithm include piston pressure, recoil travel, and recoil velocity. These were measured by standard transducers and their output was fed to an A/D converter. From the A/D converter, the data was transferred to a 6802 microprocessor, which performed all calculations, and then commands were sent to the servovalve.

The control algorithm was designed to adjust the constant force applied by the hydropneumatic spring to maintain the velocity at the time of fire to one half the round momentum and to insure that maximum counterrecoil

distance for the gun occurs at the initial equilibrium position (see Figure 1). The algorithm provides corrections at two points in time during each firing cycle; the first, immediately after firing and the second, when the velocity passes through zero from the negative to the positive side.

The explanation of the algorithm that follows will be somewhat simplified since in actual implementation adjustments were made to account for time delays in the system, to account for wait times built into the system to allow noise to reduce immediately after firing, and because all calculations were performed in the microprocessor in integer arithmetic to speed solution of the algorithm.

Figure 1 will be used to discuss the algorithm and parameters will be referred to the points annotated on the velocity curve. For instance,  $T_{12}$  refers to the time from point 1 to 2 on the velocity curve and  $V_2$  refers to the velocity at point 2. The calculated values which refer to events that occurred previously will be unprimed, while calculated values for events to occur in the future will be primed.

At the time of fire of the first round, the microprocessor calculates the average pressure of the recoil cylinder as given below

$$P_{12} = \frac{V_2}{T_{12}} \cdot \frac{M}{A_p} + \frac{F_c}{A_p} \quad (10)$$

where  $P_{12}$  is the average pressure and the remaining values were explained above or in Eqn (9).

The time expected for the system to reach zero velocity,  $T'_{45}$ , is then calculated by

$$T'_{45} = (T - T_{12}) - \frac{D_G X_2}{V_4} \quad (11)$$

where  $T$  is the time between rounds,  $X_2$  is the distance the system displacement was from equilibrium at zero velocity for the previous round ( $X_2 = 0$  after the first round) and  $D_G$  is a gain factor arrived at from digital computer simulations of the system when using realistic friction forces. This expected time is then used to estimate the average pressure required to reach zero velocity at point 5.

$$P'_{45} = \frac{V_4}{T'_{45}} \cdot \frac{M}{A_p} - \frac{F_c}{A_p} \quad (12)$$

Note that the sign of the friction is opposite that of Eqn (13) since the friction now assists the spring in resisting motion of the piston.

\*Due to the cylinder design, a change in volume within it causes an equivalent to a change in volume of the nitrogen accumulator.

The change in pressure for the preload can now be calculated as

$$\Delta P = P'_{45} - P_{12} \quad (13)$$

This pressure increment is achieved by opening the system servovalve for a length of time calculated from empirical results. The command is given to the servovalve to open fully for the calculated time, either adding or subtracting oil. The times are dependent on the pressure-drop across the servovalve and the empirical equations were determined separately for adding or subtracting oil.

A second preload correction is made at point 5 on the velocity curve. The average pressure of the recoil cylinder is calculated as

$$P_{45} = \frac{V_4}{T_{45}} \cdot \frac{M}{A} - \frac{F_c}{A_p} \quad (14)$$

The desired velocity at point 6, the next time of fire, is determined from

$$V'_6 = V_G (V_2 - V_4) - \frac{D_G \cdot X_z}{T} \quad (15)$$

where  $V$  is a velocity gain constant based on the average impulse of the round and for an ideal system is given by  $\frac{V_2}{V_2 - V_4} = \frac{1}{2}$

The time to fire the next round is given by

$$T'_{56} = T - T_{54} \quad (16)$$

From Eqns (15) and (16) the average recoil pressure required is then found.

$$P'_{56} = \frac{V'_6}{T'} \cdot \frac{M}{A_p} + \frac{F_c}{A_p} \quad (17)$$

The change in pressure required at time 5 on the velocity curve is then

$$\Delta P = P'_{56} - P_{45} \quad (18)$$

The servovalve command is determined from the same empirical formulas discussed previously.

This completes one cycle through the control algorithm and for each successive round the system loops back to Eqn (10) until the number of rounds requested is fired or in an operational system when the trigger is released. At that time, the system transfers to an algorithm to return the gun to its equilibrium position so it is ready to fire another burst.

Throughout the firing cycle the micro-processor also checks system parameters to determine if any are maintained within preset bounds. If any parameter falls outside the bounds or the gun misfires, the cycle is aborted and the system is prepared to begin another burst.

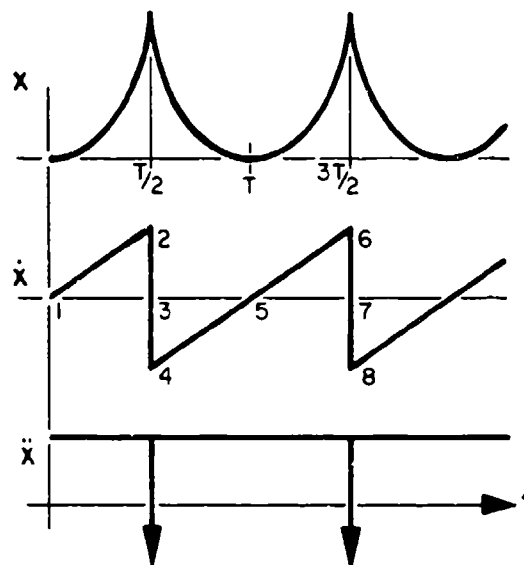


FIGURE 1. CURVES FOR IDEAL FIRE-OUT-OF-BATTERY GUN

### 3.0 HARDWARE DESCRIPTION

Two different gun systems were tested using the FORC system. Due to the wide variations between the guns, different recoil cylinders were designed for each gun, however, other components such as servovalves, sensors, and the microprocessor were identical for both systems. The hardware description of the FORC system will therefore be given for one system since the differences between the two are only in the sizing of recoil cylinders and the nitrogen accumulators and in the construction of the hydraulic manifold.

#### 3.1 FORC Hardware

A general diagram of the hydropneumatic system for FORC is shown in Figure 2. Recoil cylinders are mounted on each side of the gun so all fluid flow occurs in parallel. Lengths of hydraulic lines were kept equal to insure symmetry of the system.

A double sided piston is used to maintain the system at the equilibrium position prior to firing. Servo valves A and B of Figure 2 are adjusted during the prefire stage to maintain the equilibrium position and to maintain the proper preload on the nitrogen spring. At the initiation of the firing sequence the dump valve and servo valve B are opened to the return line. (The dump valve was only required for the largest gun system due to its increased flow requirements.) The nitrogen spring then applied a force to move the recoil cylinders and gun forward. Servo valve A is then used to adjust the system preload as described in Section 2.4. The back pressure used in Eqn. (9) is due to the return line pressure and during testing did vary as the piston moved back and forth.

The sensors used in the system were off the shelf transducers including an LVDT for displacement, an LVT for velocity and a pressure transducer. Care was needed in the mounting of the transducers to reduce system noise during firing, but otherwise no unique requirements were necessary for the transducers.

The microprocessor system used to control the FORC system was a Honeywell H100 system. It consists of a Motorola 6802 microprocessor, A/D and D/A boards, real time clock and a RS232 interface. All programming of the system was performed in assembly language to insure timely solution of the control algorithm.

The final hardware required to insure proper operation of the FORC system was the sliders which contained the gun motion. Unless these sliders were low friction, too much power would be required to operate the system effectively. Two different methods of eliminating friction were used and both worked effectively. The first system consisted of cylindrical rods attached to the gun which rode in self aligning ball bushings. In the second system, wheels

were attached to the gun which then rode in a channel attached to the gun cradle.

#### 3.2 Guns and Ammunition

Two different guns, with round impulse varying by over a factor of two, have been tested using the FORC concept. These were a prototype model of the 30mm XM230 chain gun developed by Hughes Helicopter and the 30mm GAU-13/A gun developed by General Electric.

The XM230 chain gun is a single barrel, externally powered weapon which incorporates a rotating bolt mechanism driven by a chain drive. The production model of this weapon will be used on the Advanced Attack Helicopter (AAH) in a secondary armament role. At the time of testing only a prototype model was available, however, the operation of this weapon is identical to the production model. A reduced rate of fire from the production model was used due to the gear ratio of the drive system (500 SPM vs 625 SPM).

A feed system was not available for the gun so only five rounds could be loaded for each test. This was considered sufficient to effectively test the FORC concept since it was estimated the system would have reached steady state operation within five rounds.

The ammunition fired from the XM230 was the XM788 Target Practice (TP) round.

The characteristics of the gun/ammunition system of primary interest for recoil control are given below:

Rate of fire	500 SPM
Muzzle Velocity	800 m/sec
Impulse w/o muzzle brake	245 N-sec
Impulse w/muzzle brake	209 N-sec
Mass of gun	54.4 kg
Mass of gun and FORC system	70.3 kg

The second weapon tested using the FORC system, the GAU-13/A gun, is a four-barrel, externally powered, Gatling-type weapon. This weapon, in a pod mount, has been extensively tested on several high performance aircraft including the F-15. A circular feeder was fabricated by GE for the FORC testing that could store a maximum of 15 rounds. The FORC testing was limited to 10 round bursts since recoil control operation could be effectively determined over this period.

The gun fired the GAU-8/A target practice round during the testing. Characteristics for this gun/ammunition system are listed below:

Rate of fire	360 SPM
Muzzle velocity	1036 m/sec
Impulse	600 N-sec
Mass of gun	214 kg
Mass of gun and FORC system	259 kg

The two different gun/ammunition systems, therefore, provided an ideal test of the adaptability of the FORC concept. Between the two systems there were significant variations in size, mass, round impulse, and rate of fire. However, the design of the FORC system was similar for both guns with the most significant difference being the size of the recoil cylinders and the nitrogen accumulators.

#### 4.0 TEST RESULTS

Results obtained from testing the two weapon systems will be presented in this section and will be compared to ideal results. General results discovered during testing of both systems are: (1) Friction between the gun and mount must be minimized to reduce system power requirements and maintain constant system acceleration; (2) Maximum flow rates occur at system start-up and are significantly lower (less than 10% of maximum rate) during firing; (3) System back pressure must be minimized to insure proper operation; (4) The system servo valve operated effectively in the high shock environment of the gun mount; (5) The system microprocessor can solve the control algorithm for even higher rates of fire (estimated limit is 800 SPM).

Both weapons were initially fired from hard stands using conventional recoil adapters and then tested using the hydraulically controlled recoil system for comparison purposes.

##### 4.1 XM230 Test Firings

Original testing of the FORC system was performed with the XM230 gun. The recoil loads and recoil displacement obtained from a 5 shot firing burst from the XM230 using the standard recoil adapters that were supplied with the prototype weapon are shown in Figure 3. The peak recoil load for this test was 19.1kN.

From this displacement curve for the recoil adapters, it can be seen that they were not fully tuned to the firing rate of 500 SPM since the recoil piston did not return to zero between shots. However, with proper tuning, the minimum recoil force that could be expected would still be at least as great as obtained from the first round, 11.3kN. The shape of the recoil curve is consistent with that obtained using standard spring-damper recoil adapters. The maximum recoil travel was 3.5cm.

The test fixture for testing the XM230 with the FORC system is shown in Figure 4. The hydraulic manifold which also contains the nitrogen spring and control servovalves is attached to the barrel of the gun. One of the two ring springs used to measure the recoil force is seen attached to the triangular mounting fixture in the center of the picture. The Honeywell microprocessor system used to solve the control algorithm is setting on the table next to the gun. During firing tests the microprocessor was located in a remote room to shield it from the shock and blast overpressure that occur during firing tests.

Test results obtained from a 5 round firing burst with the FORC system are shown in Figures 5 and 6. The scale for the recoil force is the same as that for the hard stand firings to effectively reveal the recoil force reduction. Peak recoil force for the burst was 4.8kN, four times less than the peak force measured with standard recoil adapters.

The recoil displacement, shown in Figure 5, varies considerably from the ideal in that the recoil distance is not consistent from round to round and does not reach zero velocity at zero displacement. As mentioned above, this was caused by binding in the recoil cylinder and this was corrected in the design of the cylinder for the GAU-13/A gun. The maximum recoil travel, minimum displacement to maximum displacement, was 5.5cm while the maximum travel for a single round was 4.8cm. This distance is larger than that of the spring-damper system and is a penalty obtained when reducing the recoil loads.

Velocity and trim hydraulic oil pressure (equal to the nitrogen accumulator pressure) are shown in Figure 6. The slope of the velocity curve between rounds is expected to remain constant, however, variations in slope can be seen particularly at the zero velocity point. The control algorithm is programmed to make corrections in trim pressure approximately 6msec after firing and when the velocity reaches zero. The changes in pressure commanded by the control algorithm can readily be seen with maximum pressure changes approaching 1.8MPa.

The results from the XM230 revealed that the FORC concept was viable but that extreme care was required in both piston and mount design to minimize friction. Based on these results a second recoil system was designed for the GAU-13/A gun using many of the components from the XM230 FORC system.

##### 4.2 GAU-13/A Test Firings

Test results obtained from firing a 10 round burst from the GAU-13/A gun with a conventional spring-damper recoil adapter is shown in Figure 7. The firing rate was 360 SPM and the recoil adapter was tuned for this firing rate. The adapter was designed to take a

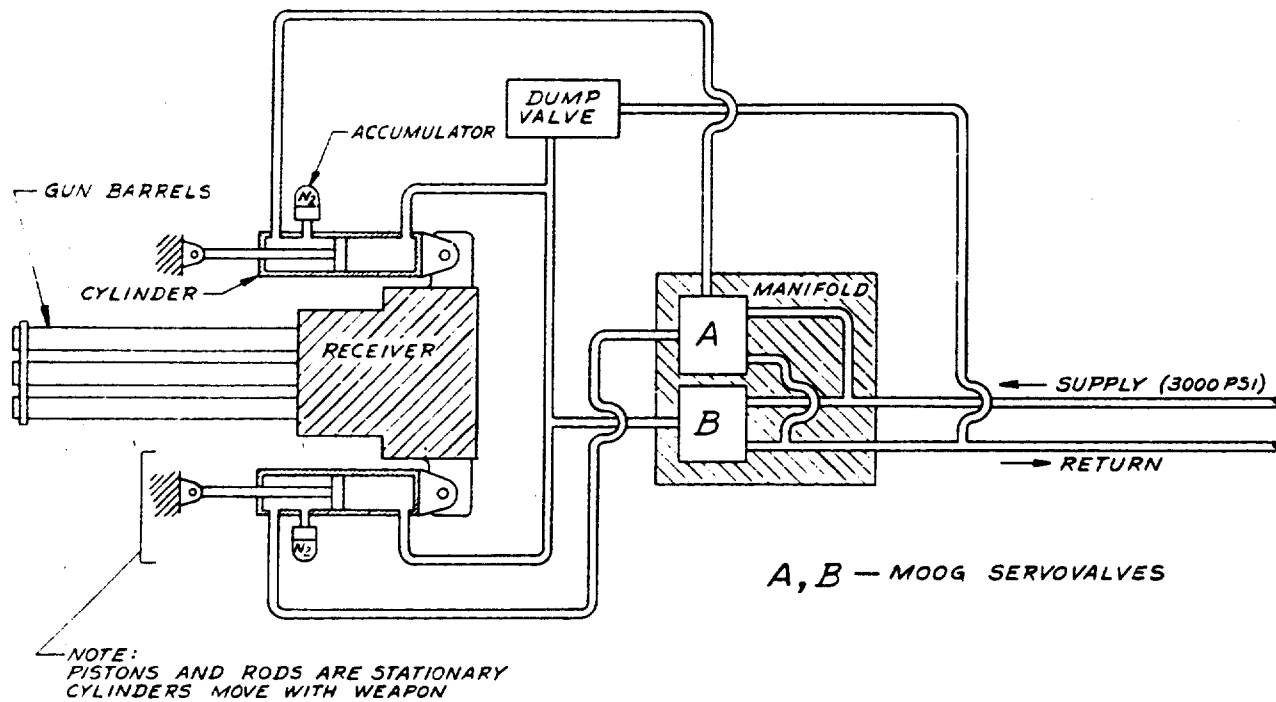


FIGURE 2. FORC HYDROPNEUMATIC SYSTEM

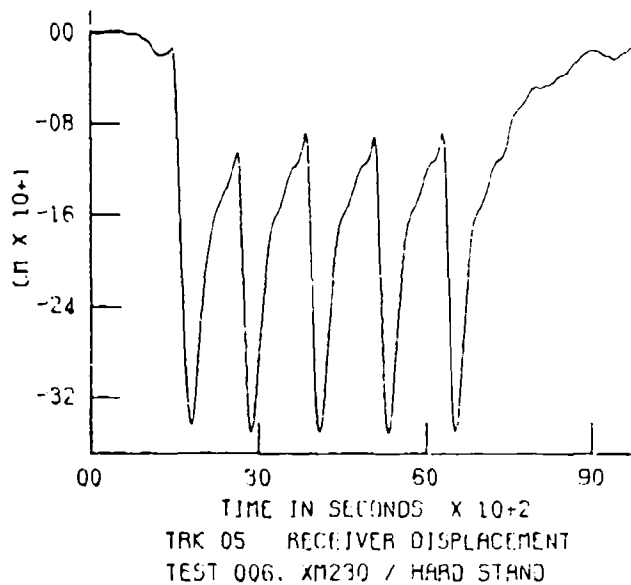
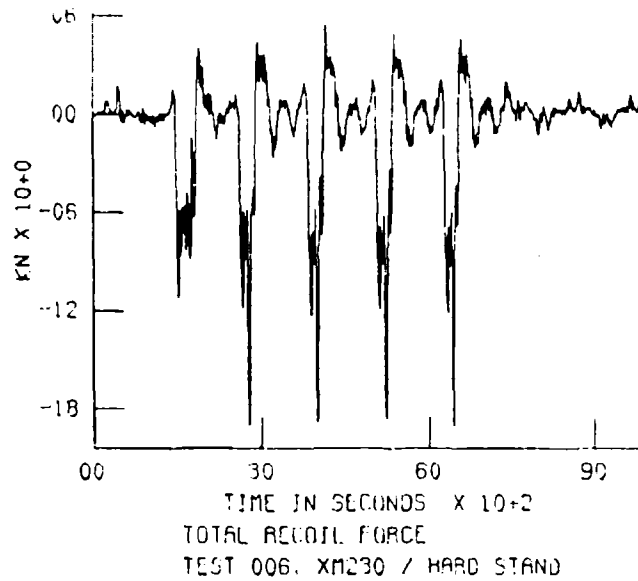


FIGURE 3. RECOIL FORCE AND DISPLACEMENT FOR  
 XM230 WITH CONVENTIONAL RECOIL ADAPTERS



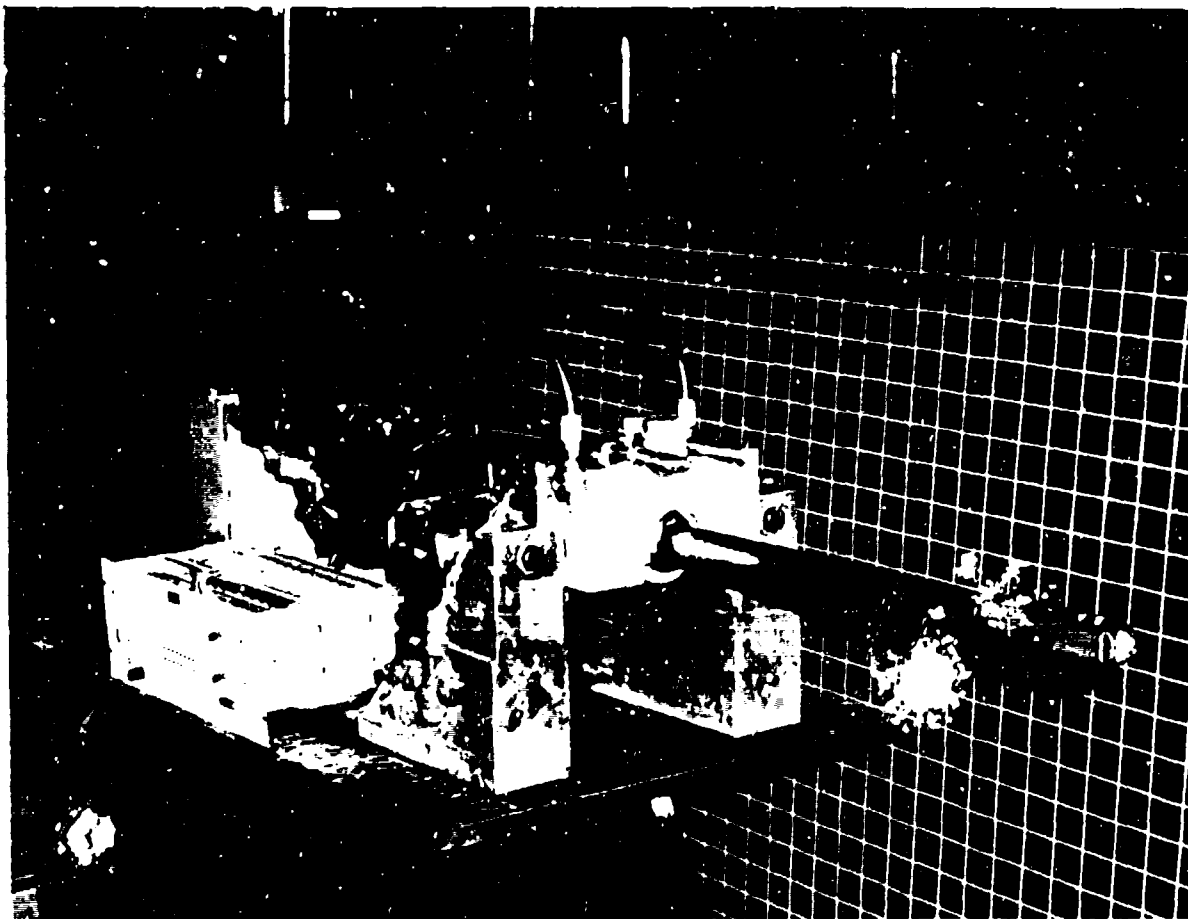


FIGURE 4.  
XM230 MOUNTED IN FORC TEST FIXTURE

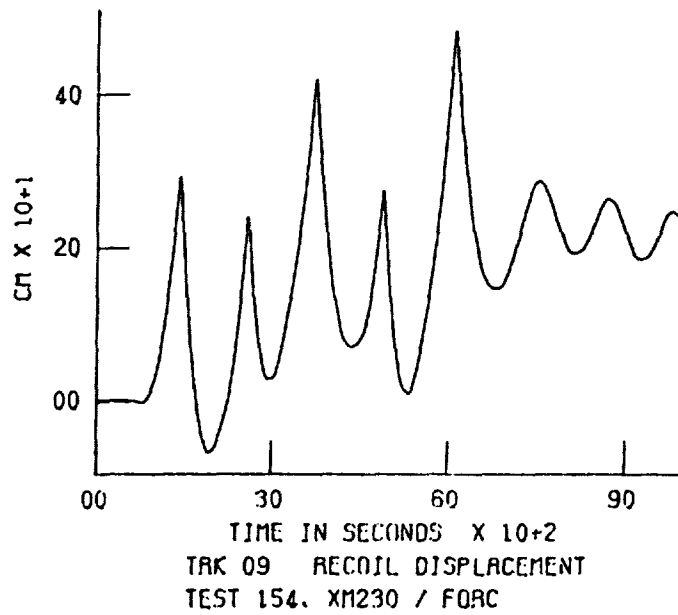
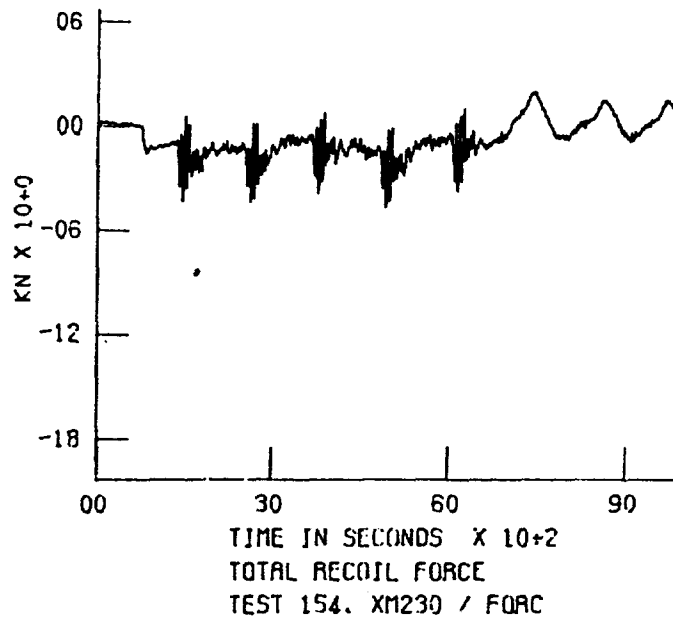


FIGURE 5. RECOIL FORCE AND DISPLACEMENT FOR XM230 WITH FORC SYSTEM

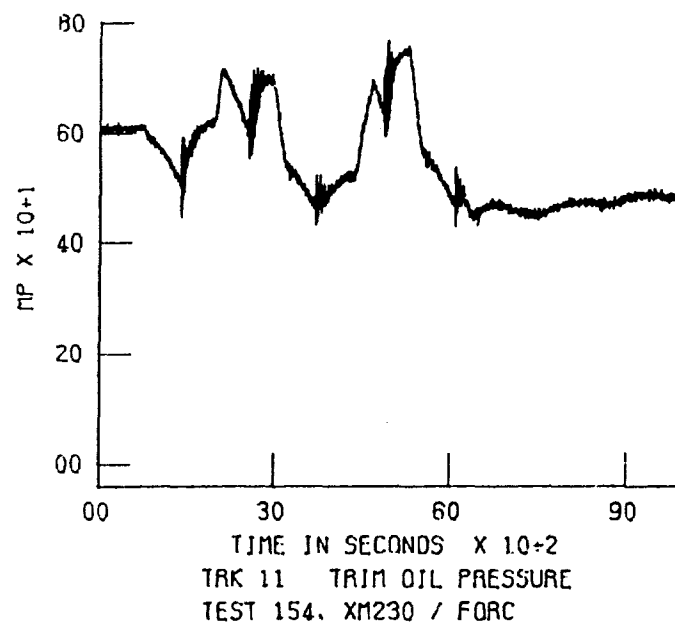
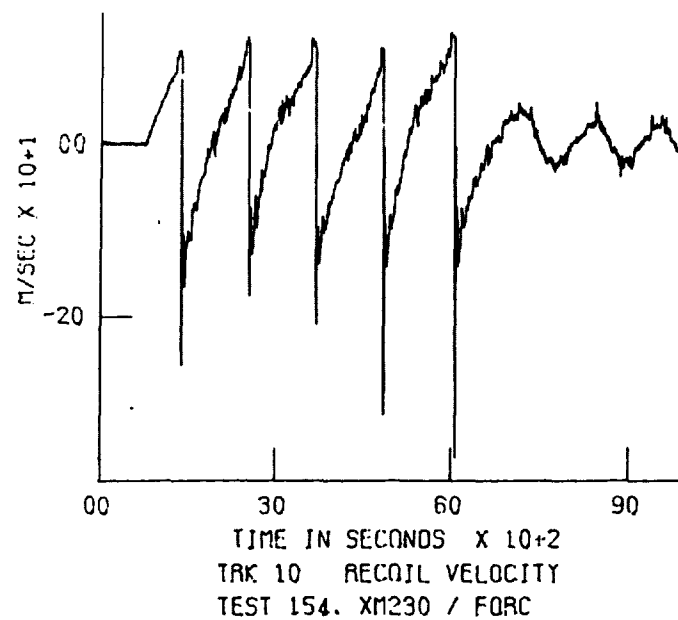


FIGURE 6. VELOCITY AND PRESSURE FOR XM230 WITH FORC SYSTEM

set back displacement on the first round and then dither around this displacement. Comparing Figure 7 with Figure 3, it can be seen that the shape of the recoil force curves and recoil displacement curves are very similar for the standard recoil adapter even though gun characteristics vary significantly.

The peak recoil force obtained from this test was 27.9kN and the maximum displacement was 6.0cm.

The GAU-13/A gun mounted in the FORC test fixture is shown in Figure 8. The gun was attached to wheels which were allowed to move freely along tracks in the gun cradle. The hydropneumatic recoil cylinders were located inside the cradle and were attached to the cradle and the gun receiver. The cradle was supported by front and rear legs and was attached to the legs by taper bearings. The recoil forces were measured by force washers on each side of the gun that were attached to the cradle and to the stiff triangular structure bolted to the gun mount table.

Tests results obtained from a 10 round burst using the FORC system are shown in Figures 9 and 10. The maximum recoil force was 7.6kN, a reduction in peak recoil force of greater than 20kN. The range of the recoil displacement was only 6.4cm, slightly larger than that obtained with conventional recoil adapters. Operation of the control algorithm can be seen throughout the firing test as the zero displacement position is adjusted during the burst. There is some delay in obtaining displacement corrections for two reasons: (1) The control algorithm is dependent on system velocity as well as displacement; (2) The nitrogen volume is larger for the GAU-13/A than for the XM230 and therefore, the maximum pressure corrections that could be achieved each round were less than for the XM230. The trim oil pressure, shown in Figure 10, changes by a maximum of 0.4MPa during servo valve commands as compared to the 1.8MPa change achieved during the XM230 testing. This was not unexpected, but did slow system response in some cases.

The velocity curves shown in Figure 10 are approximately as expected. Small variations in peak velocity (velocity at the time of firing) were obtained. The velocity measured immediately after firing was noisy and therefore the measurement of recoil velocity was not made until 6msec after firing.

These results show improved system performance over that obtained with the XM230. This was due to improved piston design reducing internal friction in the system. One problem that did affect performance with the GAU-13/A was system back pressure. As the system recoiled after firing, back pressures as high as 1.0MPa were measured and slowed system recoil velocity. Since back pressure was not measured by the microprocessor, it was treated as an increased friction term in the recoil direction by the control algorithm.

## 5.0 SUMMARY

The FORC concept for reducing the recoil force of high rate of fire automatic guns has been tested and proven effective. Reductions in the total recoil force for the two weapons tested are shown in the table below:

TABLE I

### RECOIL LOAD (kN)

GUN	CONVEN.ADAPTER	FORC SYS	% RED
XM230	19.1	4.8	75
GAU-13/A	27.9	7.6	73

This system will allow consideration of more powerful guns for use in both helicopter and armored personnel carrier applications. By substituting the large shock loads of firing guns with a nearly constant force, both vibration and fatigue problems that prevent mounting of powerful automatic guns can be eliminated.

Continued study of the FORC system is underway in the Army and concepts for field applications are being considered.

#### DISCUSSION

Mr. Sutherland (Wyle Labs): You briefly mentioned the weight penalty. Could you elaborate on that just a bit more?

Mr. Townsend: The passive recoil adapters are just mechanical spring type systems. Normally they weigh about 8-10 pounds, depending on the size of the system you're working with. We figure the hydraulic system weighs about 18-25 pounds, depending on the design and the nature of the integration. So there is a weight penalty, but we may have to pay that penalty in order to mount the higher impulse weapons.

Mr. Sutherland: Is the hydraulic system supply self-contained?

Mr. Townsend: It depends again on the system. There is a system hydraulic supply on the Cobra helicopter and the Advance Tech helicopter, so I wasn't attributing any weight to that. We could build an independent hydraulic supply, and we looked briefly at that to power the system. It would be electrically powered or powered by an accumulator, depending on the mission length.

Mr. Silver (Westinghouse Electric Corporation): I'm curious about the change in the frequency spectrum one can attain in a forcing function with or without the damping. Could you change the frequency spectrum of the forcing function?

Mr. Townsend: No. In this case we are using an externally powered gun, and it would depend on the nature of the basic design.

Voice: If you are talking about the energy transmitted into the helicopter, yes, we did. We have the curves that were done early in the cycle, and we have smoothed them out quite a bit, so we have a much smoother constant forcing level now. When you apply energy at the harmonics of the gunfiring rate to the helicopter, you have a very sharp energy input to the mount. With this system you get some ringing due to friction in the system; you don't get rid of it entirely.

Mr. Silver: How much of the energy goes into the blast itself, and how much energy goes into

recoil?

Mr. Townsend: We really aren't changing the amount of energy that goes into the structure. We are just averaging it out over the firing cycle. So there is just as much energy, and we are just taking away the peak forces.

Mr. Silver: I just wondered about the different influences on the dynamic environment for equipment on helicopters.

Mr. Townsend: Again, it depends on the particular system. The basic vibration frequency won't change, but its magnitude will be lower. The frequency doesn't change because the basic frequency is associated with the firing rate.

Mr. Frydman (Harry Diamond Labs): Has your control system reduced the vibrations in the direction other than the firing direction?

Mr. Townsend: We really didn't measure it appreciably throughout the aircraft structure in this particular series of tests. It probably would not. Most of the recoil load is directed fore and aft, and we were only interested in the fore and aft peak recoil forces. It wouldn't change in another direction.

Mr. Moran (Argonne National Laboratory): You apparently chose to optimize on the peak force of that impulse. Did you look at any other parameters of that impulse?

Mr. Townsend: Yes. We also looked at position control of the gun and the control algorithm. That is the beauty of being able to use the micro-processor for control. You can optimize on the parameter that you want to. You can also trade off peak recoil force versus displacement, recoil distance, if you want to.

Mr. Moran: You decided that peak force indeed is the most important parameter for this purpose?

Mr. Townsend: The primary problem was to get rid of the vibration and minimize the force on the helicopter structure. So that is what we looked at initially.

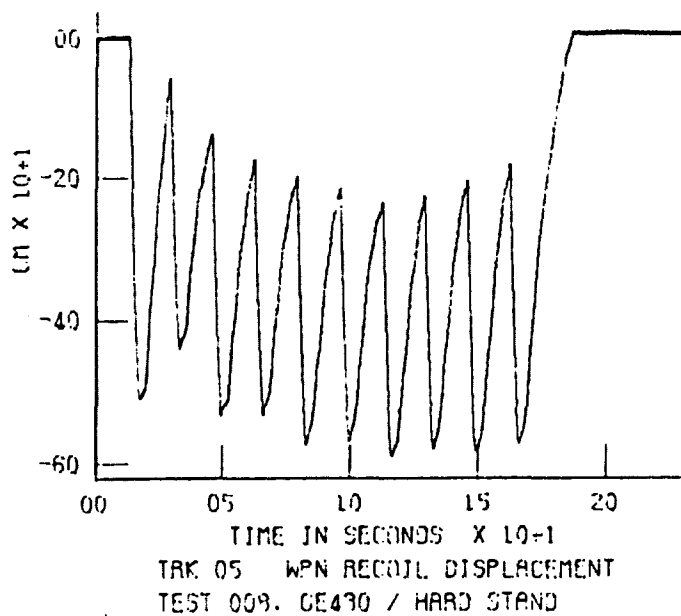
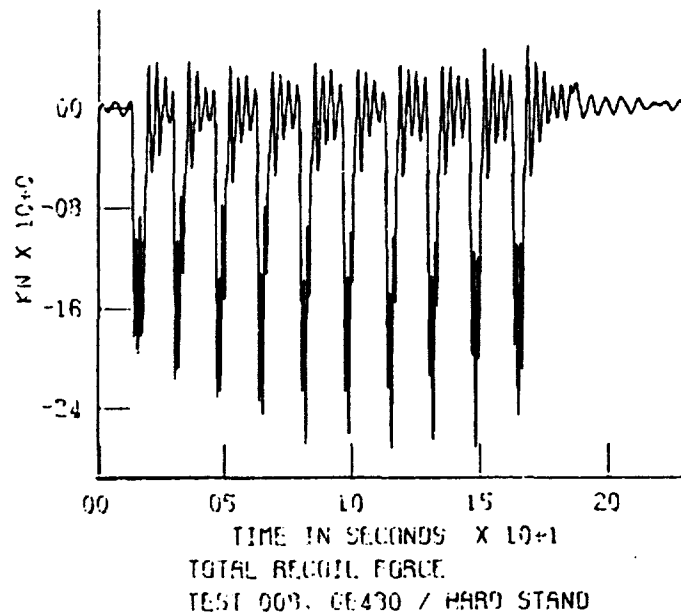


FIGURE 7. RECOIL FORCE AND DISPLACEMENT FOR  
GAU-13/A WITH CONVENTIONAL RECOIL ADAPTERS

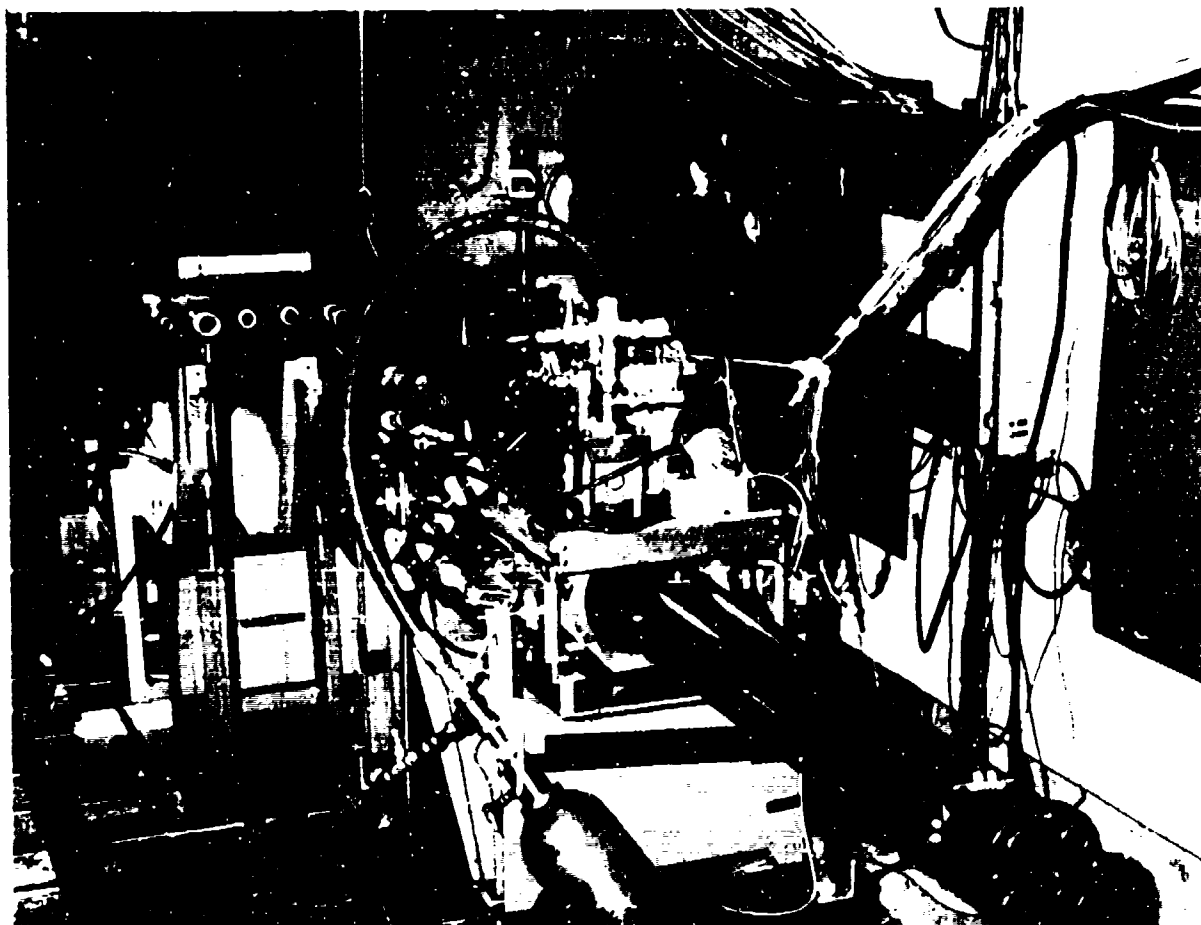


FIGURE 8.

GAU-13/A MOUNTED IN FORC TEST FIXTURE

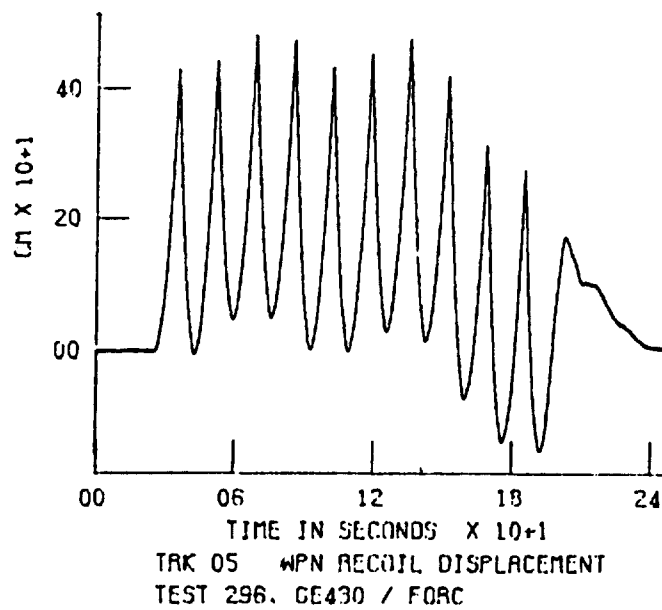
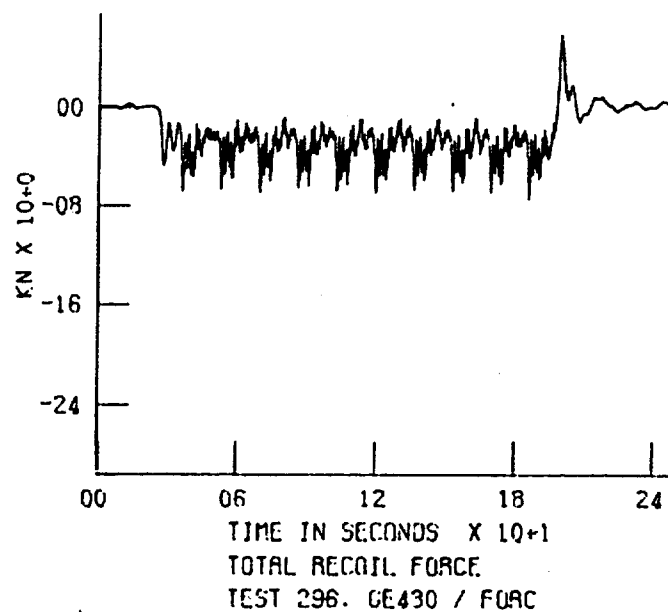


FIGURE 9. RECOIL FORCE AND DISPLACEMENT FOR GAU-13/A WITH FORC SYSTEM



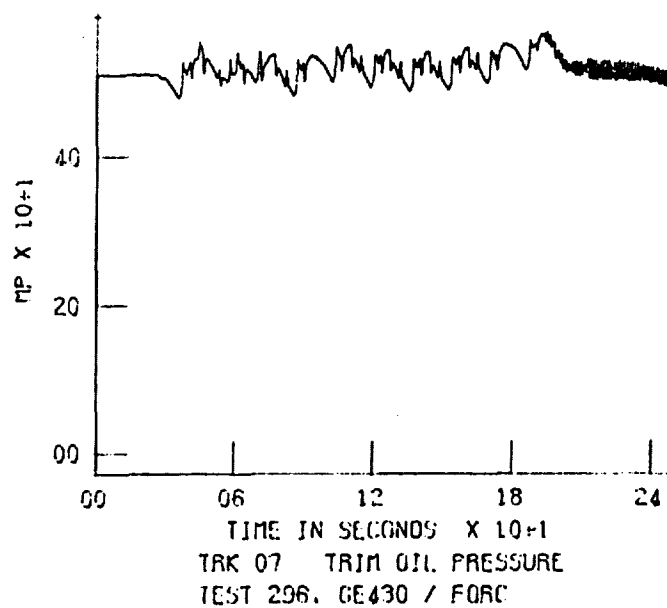
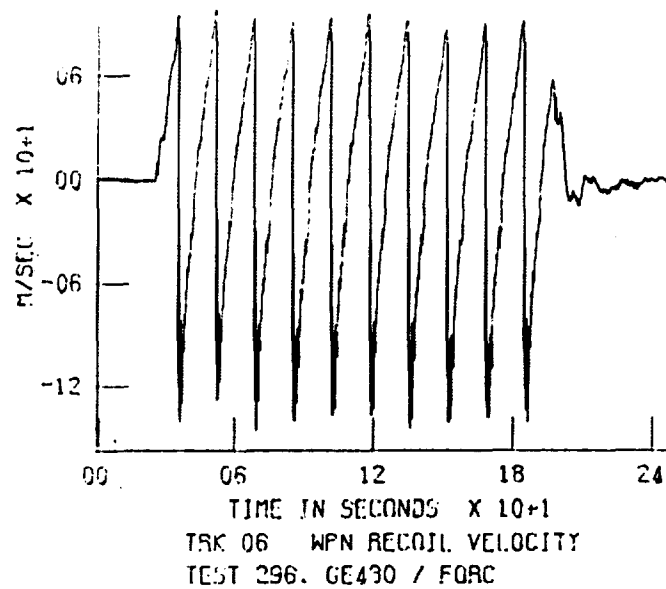


FIGURE 10. VELOCITY AND PRESSURE FOR GAU-13/A WITH FORC SYSTEM

PERFORMANCE ANALYSIS OF HIGH-SPEED HYDRAULIC SUSPENSION SYSTEMS  
IN MULTIPLE WHEELED LAND TRANSPORTERS

Phineas Woods  
Martin Marietta Corporation  
Denver, Colorado

Fluid/Structure interaction is developed for a hydraulic suspension system. Finite element models of the fluid are developed in a manner identical to structural elements. After imposing continuity, the fluid system is coupled to the structural system by Rayleigh-Ritz assumed modes which satisfy boundary conditions. Damping in the combined system is built up from discrete constant coefficients for the tires, from laminar flow resistance in the fluid and from modal damping assumed for the structure. Input disturbances at the roadway surface are expressed as functions of time or random acceleration spectra. Response of the transporter system is expressed in time or frequency domains. Good agreement is obtained with a limited amount of test data.

NOTATION

$A_i$ = Cross sectional area of $i$ th element, $m^2$	$K_A$ = Stiffness of accumulator, $N/m$
$c$ = Damping coefficient in structure, $Ns/m$	$K_t$ = Radial tire stiffness, $N/m$
$c_c$ = Critical damping coefficient in structure	$m$ = Mass of structural element, $Ns^2/m$
$C_i$ = Compliance of $i$ th fluid element, $m/N$	$p_i$ = Pressure head on $i$ th fluid element, $m$
$C_f$ = Compliance matrix	$\bar{p}$ = Fluid system pressure head, $m$
$D$ = Inside diameter of hydraulic line, $m$	$q$ = Generalized coordinate
$E$ = Modulus of elasticity in structure, $N/m^2$	$2R_i$ = Resistance of $i$ th fluid element, $ms/N$
$E_b$ = Bulk modulus of hydraulic fluid, $N/m^2$	$R_f$ = Resistance matrix
$E_{eff}$ = Effective modulus of elasticity, $N/m^2$	$\left(\frac{r}{R}\right)$ = Ratio of piston stroke to axle stroke
$f$ = Frequency or friction factor, $hz$ or non-dim.	$S_u^u(f)$ = Power spectral density of base drive acceleration, $g^2/hz$ .
$g$ = Gravity constant, $m/s^2$	$t$ = Wall Thickness, $m$
$\Delta h$ = Stroke of hydraulic piston, $m$	$T$ = Static or Guyan reduction matrix
$2I_i$ = Inertance of $i$ th fluid element, $ms^2/N$	$T_F$ = Transformation matrix from fluid to structure
$I_f$ = Inertance matrix	$V$ = Velocity, $m/s$
$I$ = Unit matrix	$W_i$ = Flow of $i$ th fluid element, $N$
$\tilde{I}$ = Relative coordinate transformation matrix	$\bar{W}$ = Total flow degree of freedom, $N$
$k$ = Stiffness of structural element, $N/m$	

$\tilde{W}$  = Relative flow degree of freedom, N  
 $x$  = Displacement of structural degree of freedom, m  
 $\Gamma$  = Modal participation factor  
 $\nu$  = Kinematic viscosity of hydraulic fluid,  $m^2/s$   
 $\phi_r$  =  $r$ th system mode

$\Phi$  = Mode matrix  
 $\omega$  = System modal frequency, Rad/s.  
 $\Psi$  = Strain matrix  
 $\zeta$  = Damping ratio,  $\frac{c}{c_c}$   
 $\bar{\rho}$  = Weight density of hydraulic fluid,  $N/m^3$

## INTRODUCTION AND BACKGROUND

Hydraulic suspension systems used in moving massive, heavy structures are fairly recent developments in Europe. Most applications are confined to the slow-speed transport of such items as ship hulls, massive generators or heavy oil field equipment over short distances. This paper presents some ideas, conceived on the MX program, for application to high-speed transporters; in particular, a heavy duty trailer or a self-propelled vehicle for commercial transport on the interstate Highway network of the USA. This application might never have been possible under present weight per axle limitations until the development of multiple wheeled hydraulic suspension.

Typically, hydraulic suspensions take the form of pendulum axles supporting interconnected hydraulic struts at each set of bogies. Examples are shown in Figs. (1), (2) and (3). Accumulators are often, but not always, used in the hydraulic circuit to control transmissibility of input forces at the road/tire interface. At very slow speeds the forces on all tires are uniformly distributed regardless of irregularities in the road surface. At moderate and high speeds, the interaction between fluid, structure and tires quickly becomes a dominant factor in the "ride" transmitted to the payload.

Finite element models of structure have been around for many years. On the other hand, finite element models of fluid have not been as extensively used as continuous fluid models because structural interaction is rarely designed into a fluid system. Most familiar examples of interaction have resulted from accidental design whether it be water hammer, cooling water flow in a nuclear power plant, or POGO instability in a liquid fueled rocket. The spectacular POGO phenomenon has driven engineers to study fluid/structure coupling in great detail. In particular, White and Berry, Ref. (1), formulated a method based on classical fluid dynamic theory for coupling finite elements of fluid with structure which is consistent with state-of-the-art methods used in structural dynamic analysis. This method was successfully applied to a liquid-fueled Titan III launch vehicle in preparation for the Viking launches in the mid-1970's. The method was verified by excellent agreement with test data.

Transporters with hydraulic suspension may seem only remotely related to the Titan III vehicle. They are, in fact, similar in all respects except for closed-system plumbing of the hydraulic fluid as opposed to the open-system flow of the Titan III propellant. In other words, the transporter fluid system is oscillatory but non-flowing whereas the Titan III fluid system consists of oscillatory flow superposed on steady state flow. This is an important distinction for it allows the damping of the hydraulic fluid in the transporter to be accurately described by constant coefficients rather than by the more complex energy losses in a flowing system. As a consequence, system performance can be studied on the basis of linear analysis.

## METHOD OF APPROACH

The equations of motion of the fluid elements are first written as finite elements possessing inertance, resistance and compliance analogous to mass, damping and stiffness respectively of a structural system. After imposing continuity at all finite fluid degrees of freedom, the fluid system is coupled to the structural system by Rayleigh-Ritz assumed modes which satisfy the boundary conditions.

Modes and frequencies of the undamped coupled system are calculated by standard eigenproblem routines.

Damping in the combined system is built up from discrete constant coefficients at each tire/axle differential displacement; from laminar flow resistance in each fluid element; and from modal damping expressed as a percentage of critical damping in the structure.

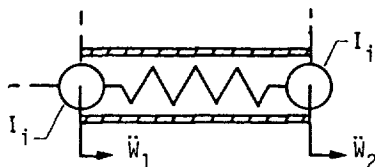
The response of the system to input disturbances at the roadway surface are expressed as accelerations or loads, shears and moments by standard load transformation methods commonly in use. The input disturbances can take the form of discrete time functions or random acceleration spectra at the road/tire interface.

The fidelity of the analytical model is demonstrated by comparison with test data.

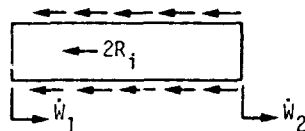
## FINITE ELEMENTS OF THE FLUID MODEL

Fluid elements possess the fundamental properties of mass, damping and stiffness and can be modelled in a manner identical to structural elements, requiring only the preservation of continuity,  $\rho AV = \text{constant}$ , from one section to another. However, it is much easier to work in flow units instead of displacements as in the case of structural elements; in flow rates, instead of velocities and in flow rates per second, instead of accelerations. For this reason, it is customary to express fluid mass as inertance; fluid damping as resistance and fluid stiffness as compliance.

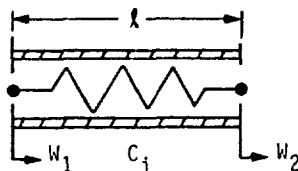
Consider, then, these properties in a finite elastic fluid element flowing in an elastic pipe.



As in the case of a structural element, the total mass of the fluid is divided into two equal inertances at each end of a spring. The degrees of freedom are denoted by flows  $W_1$  and  $W_2$ .



Similarly, the total resistance to flow of the fluid element relative to the pipe wall is divided into two equal coefficients of flow rates  $W_1$  and  $W_2$ .



Compliance of the element reflects the elastic properties of both the fluid and the pipe. An effective bulk modulus is used for this purpose; namely, the well known expression

$$E_{\text{eff}} = \left( \frac{1}{E_b} + \frac{D}{Et} \right)^{-1} \quad (1)$$

The effect of longitudinal elasticity in the pipe is ignored in this expression which contains only the effect of circumferential pipe strain. Comparing the two elements:

### Structural Element

$$\text{mass: } m = \frac{\rho A_i l}{2g}$$

$$\text{damping: } c \text{ or } \zeta = c/c_c$$

$$\text{stiffness: } k = \frac{A_i E}{l}$$

### Fluid Element

$$\text{inertance: } I_i = \frac{l}{2\rho A_i g}$$

$$\text{resistance: } R_i = \frac{64\nu \left( \frac{l}{D} \right)}{\pi \rho g D^3} \quad (\text{laminar flow})$$

$$\text{compliance: } C_i = \frac{E_{\text{eff}}}{\rho^2 A_i l}$$

For a typical hydraulic suspension system the finite elements follow a repeating pattern at each bogie. One loop of this pattern is shown in Fig. (4), where four finite fluid elements are arranged to show their relation to the hydraulic cylinder containing a piston driven by the axle. Also shown is a grounded accumulator. The loop shares a common line with all other loops. For simplicity, accumulator mass and damping are neglected. A half model of the fluid system is shown in Fig. (5) for the 5-axle semitrailer shown in Fig. (2).

## FLOW CONTINUITY

Before imposing continuity on the finite elements of fluid it is necessary to condition the compliance of the element by a strain matrix defined as.

$$\psi = \begin{bmatrix} 1, -1, \\ , 1, -1 \end{bmatrix} \quad (2)$$

Thus, for one element and compliance,  $C$ , having degrees of freedom at each end of the element

$$\left[ \psi^T C_i \psi \right] = \begin{bmatrix} C_i & -C_i \\ -C_i & C_i \end{bmatrix} \quad (3)$$

and 
$$R_i = \begin{bmatrix} R_i \\ R_i \end{bmatrix} \quad (4)$$

The compatible arrangement of inertia, resistance and compliance matrices for one loop of three finite elements with six elemental degrees of freedom plus a grounded accumulator,  $C_4$ , would take the form

$$I_i = \begin{bmatrix} I_1 & & & & & \\ & I_1 & & & & \\ & & I_2 & & & \\ & & & I_2 & & \\ & & & & I_3 & \\ & & & & & I_3 & 0 \end{bmatrix} \quad (5)$$

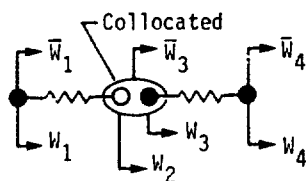
$$R_i = \begin{bmatrix} R_1 & & & & & \\ & R_1 & & & & \\ & & R_2 & & & \\ & & & R_2 & & \\ & & & & R_3 & \\ & & & & & R_3 & 0 \end{bmatrix} \quad (6)$$

$$\psi^T C_i \psi = \begin{bmatrix} C_1 & -C_1 & & & & \\ -C_1 & C_1 & & & & \\ & & C_2 & -C_2 & & \\ & & -C_2 & C_2 & & \\ & & & & C_3 & -C_3 \\ & & & & -C_3 & C_3 & C_4 \end{bmatrix} \quad (7)$$

The fluid equation becomes

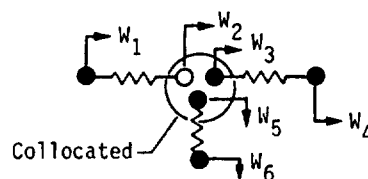
$$I_i \{\ddot{W}_i\} + R_i \{\dot{W}_i\} + \psi^T C_i \psi \{W_i\} = \{p_i\} \quad (8)$$

Flow continuity requires the imposition of Kirchoff's law at every junction between fluid elements. That is,  $\sum W_i = 0$  at each junction. For the two-element junction the flows  $W_2 - W_3 = 0$  or  $W_2 = W_3$



$$\begin{Bmatrix} W_1 \\ W_2 \\ W_3 \\ W_4 \end{Bmatrix} = \begin{bmatrix} 1 & & & \\ & 1 & & \\ & & 1 & \\ & & & 1 \end{bmatrix} \begin{Bmatrix} \bar{W}_1 \\ \bar{W}_3 \\ \bar{W}_3 \\ \bar{W}_4 \end{Bmatrix}$$

Similarly, for a 3-element junction



$$\begin{Bmatrix} W_1 \\ W_2 \\ W_3 \\ W_4 \\ W_5 \\ W_6 \end{Bmatrix} = \begin{bmatrix} 1 & & & & & \\ & 1 & & & & \\ & & 1 & & & \\ & & & 1 & & \\ & & & & 1 & \\ & & & & & 1 \end{bmatrix} \begin{Bmatrix} \bar{W}_1 \\ \bar{W}_3 \\ \bar{W}_3 \\ \bar{W}_4 \\ \bar{W}_5 \\ \bar{W}_6 \end{Bmatrix}$$

By performing these operations at every junction in the system, we arrive at the relation

$$\{W_i\} = [\text{CONT}] \{\bar{W}\}$$

where: [CONT] = Continuity matrix (9)

$\{\bar{W}\}$  = Independent absolute flow coordinate

The fluid equation of motion now becomes

$$[\text{CONT}]^T I_i [\text{CONT}] \{\ddot{\bar{W}}\} + [\text{CONT}]^T R_i [\text{CONT}] \{\dot{\bar{W}}\} + [\text{CONT}]^T [\psi^T C_i \psi] [\text{CONT}] \{\bar{W}\} = [\text{CONT}]^T \{p_i\} \quad (10)$$

$$\text{or } I_f \{\ddot{\bar{W}}\} + R_f \{\dot{\bar{W}}\} + C_f \{\bar{W}\} = \{\bar{p}\}$$

#### FLUID/STRUCTURE COUPLING

Writing the two systems of equations in isolation:

$$m \{\ddot{x}\} + c \{\dot{x}\} + k \{x\} = -\{mg\} \quad (11)$$

$$I_f \{\ddot{\bar{W}}\} + R_f \{\dot{\bar{W}}\} + C_f \{\bar{W}\} = \{\bar{p}\}$$

The structural equations include the axles and tires of the transporter. The tires are represented by grounded springs. Since the structural system is isolated from the fluid system, the axles and tires will not even support the weight,  $-(mg)$ , imposed by the transporter on the free pendulum axles until the fluid is coupled.

The  $\bar{W}$  coordinate represents absolute fluid flow.

$$\text{Let: } \{\bar{W}\} = T_F \{x\} + \{\tilde{W}\} \quad (12)$$

Where:  $T_F \{x\}$  = Flow induced by structural motion.

$\{\tilde{W}\}$  = Flow relative to structure.

The flow,  $\bar{W}$ , produced by motion of the hydraulic pistons shown for example in Fig. 5, can be determined from the static fluid equations where  $\{\bar{W}\}$  and  $\{\tilde{W}\} = 0$ . Thus, at rest

$$C_F \{\bar{W}\} = \begin{bmatrix} C_{fpp} & C_{fpo} \\ C_{fop} & C_{foo} \end{bmatrix} \begin{Bmatrix} \bar{W}_p \\ \bar{W}_o \end{Bmatrix} = \begin{Bmatrix} \bar{p} \\ 0 \end{Bmatrix} \quad (13)$$

Where:  $\{\bar{W}_p\}$  = Flow out of hydraulic cylinders due to piston displacement

$\{\bar{W}_o\}$  = All other remaining flows.

Successive unit flows out of each cylinder; namely,  $\bar{W}_A, \bar{W}_E, \bar{W}_J, \bar{W}_O, \bar{W}_T$  (referring to Fig.

5) will yield five static modes of flow.

$$\begin{Bmatrix} \bar{W}_p \\ \bar{W}_o \end{Bmatrix} = \begin{bmatrix} I & \\ -C_{foo} & C_{fop} \end{bmatrix} \begin{Bmatrix} \bar{W}_p \\ \bar{W}_o \end{Bmatrix} \quad (14)$$

Eq. (14) is a familiar operation to structural dynamicists. It is a static; i.e. Guyan reduction of the fluid to the flows  $\{\bar{W}_p\}$

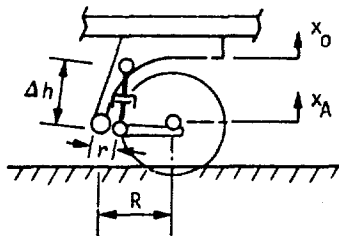
$\{\bar{W}_p\}$  is related to piston displacement by

$$\{\bar{W}_p\} = -(\delta A_p) \{\Delta h\} \quad (15)$$

The minus sign is consistent with the positive sign of  $\Delta h$  shown in Fig. 6.

$$\text{But, } \{\Delta h\} = \left(\frac{r}{R}\right) \begin{bmatrix} I & \\ -I & \end{bmatrix} \begin{Bmatrix} x_o \\ x_A \end{Bmatrix} \quad (16)$$

indicated in the sketch below.



Substituting Eq. (15) and (16) into (14) and then substituting (14) into (12)

$$\{W\} = \underbrace{\begin{bmatrix} I & \\ -C_{foo} & C_{fop} \end{bmatrix} \delta A_p \frac{r}{R} \begin{bmatrix} I & \\ -I & \end{bmatrix}}_{\text{Static Modes} = T_F} \begin{Bmatrix} x_o \\ x_A \end{Bmatrix} + \underbrace{\begin{bmatrix} I & \end{bmatrix}}_{\text{Dynamic Modes}} \{\tilde{W}\} \quad (17)$$

Further simplification is obtained by noting that relative flow at the piston and cylinder head = 0. That is,

$\{\tilde{W}_p\} = 0$  and may be discarded

$$\text{Therefore: } \{\bar{W}\} = \begin{Bmatrix} \bar{W}_p \\ \bar{W}_o \end{Bmatrix} = T_F \{x\} + \begin{bmatrix} I & \end{bmatrix} \{\tilde{W}\}$$

$$\text{or } \{\bar{W}\} = \begin{bmatrix} T_F & \\ I & \end{bmatrix} \begin{Bmatrix} x \\ \tilde{W} \end{Bmatrix} \quad (18)$$

where:  $\begin{bmatrix} I & \end{bmatrix}$  = Relative coordinate transformation

$$\begin{Bmatrix} \tilde{W}_p \\ \tilde{W}_o \end{Bmatrix} = \begin{bmatrix} I & \end{bmatrix} \begin{Bmatrix} \tilde{W}_o \end{Bmatrix}$$

or simply  $\begin{Bmatrix} \tilde{W}_p \\ \tilde{W}_o \end{Bmatrix} = \begin{bmatrix} I & \end{bmatrix} \{\tilde{W}\}$ , dropping the subscript o on  $\tilde{W}_o$ .

Returning to the original equations of motion in isolation, Eq. 11, we substitute the Rayleigh-Ritz transformation

$$\begin{Bmatrix} x \\ \tilde{W} \end{Bmatrix} = \begin{bmatrix} I & \\ T_F & \end{bmatrix} \begin{Bmatrix} x \\ \tilde{W} \end{Bmatrix} \quad (19)$$

and impose the principle of Virtual Work. Setting the right-hand side to zero and neglecting damping, the modes of the coupled system are determined from

$$\left[ \begin{array}{c|c} m + T_F^T I_f T_f & T_F^T I_f \tilde{I} \\ \hline I^T I_f T_f & I^T I_f \tilde{I} \end{array} \right] \begin{Bmatrix} \ddot{x} \\ \ddot{w} \end{Bmatrix}$$

$$+ \left[ \begin{array}{c|c} k + T_F^T C_f T_f & 0 \\ \hline 0 & \tilde{I}^T C_f \tilde{I} \end{array} \right] \begin{Bmatrix} x \\ w \end{Bmatrix} = 0 \quad (20)$$

where modes are defined by:  $\begin{Bmatrix} x \\ w \end{Bmatrix} = \phi \{q\}$  (21)

It is shown in Ref. (1) that stiffness coupling between  $x$  and  $w$  cannot exist. This accounts for the zeroes in Eq. (20).

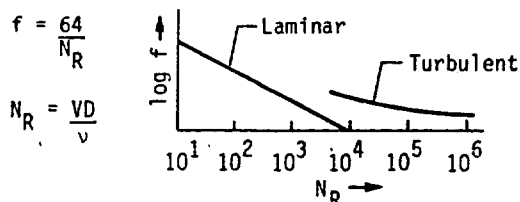
#### FLUID DAMPING

Fluid damping is assumed to be consistent with laminar flow in the hydraulic lines due to non-flowing oscillatory motion. This implies Reynolds numbers are less than about 10,000. Under such conditions, the pressure head drop is

$$\Delta P = f \left( \frac{\ell}{D} \right) \left( \frac{V^2}{2g} \right) \quad (22)$$

where:  $f$  = friction factor  
 $\ell$  = pipe length  
 $D$  = pipe diameter  
 $V$  = mean flow velocity

From the Hagen-Poiseuille Law for laminar flow



Consequently  $\Delta p = f \left( \frac{\ell}{D} \right) \left( \frac{V^2}{2g} \right) = \frac{64}{2g} \left( \frac{V}{D} \right) \left( \frac{\ell}{D} \right) V = 2R_i \dot{w}_i$

Substituting  $\bar{p} A_i V = \dot{w}_i$ ,

$$2R_i = \frac{64}{2g} \left( \frac{V}{D} \right) \left( \frac{\ell}{D} \right) \left( \frac{1}{\bar{p} A_i} \right) \quad (23)$$

Eq. (23) represents elemental resistance and must be conditioned by the continuity matrix, [CONT] to form

$$R_f = [\text{CONT}]^T R_i [\text{CONT}]$$

in the fluid system equations, Eq. (11).

#### SYSTEM RESPONSE

The response of the system to excitation at the road/tire interface is a straightforward application of base-drive techniques. It should be noted that when the Rayleigh-Ritz transformation, Eq. (19), is applied to the right-hand side of Eq. (11):

$$\left[ \begin{array}{c|c} I^T & T_F^T \tilde{I} \\ \hline 0 & \tilde{I}^T \tilde{I} \end{array} \right] \begin{Bmatrix} -mg \\ p_0 \end{Bmatrix} = \begin{Bmatrix} -(mg) + T_F^T \{p_0\} \\ \tilde{I}^T \{p_0\} \end{Bmatrix} \quad (24)$$

$$= \begin{Bmatrix} 0 \\ \tilde{I}^T \{p_0\} \end{Bmatrix}$$

where  $p_0$  = static equilibrium pressure

If, now, the tire contact points are introduced as the base drive degrees of freedom  $x_t$ , the perturbation equations about static equilibrium pressure will take the form

$$\begin{bmatrix} M_{tt} & M_{ts} \\ M_{st} & I \end{bmatrix} \begin{Bmatrix} \ddot{x}_t \\ \ddot{q} \end{Bmatrix} + \begin{bmatrix} C_{tt} & \\ & [2\zeta\omega] \end{bmatrix} \begin{Bmatrix} \dot{x}_t \\ \dot{q} \end{Bmatrix} + \begin{bmatrix} K_{tt} & \\ & [\omega^2] \end{bmatrix} \begin{Bmatrix} x_t \\ q \end{Bmatrix} = \begin{Bmatrix} F(t) \\ 0 \end{Bmatrix} \quad (25)$$

$$M_{st} = \phi^T M T$$

$\phi$  = modes, Eq. (21)

$M$  = mass matrix of Eq. (20)

$T$  = static modes of stiffness matrix, Eq. (20) reduced to unit displacements  $x_t$

$$[2\zeta\omega] = \phi^T \tilde{I}^T [2\zeta_s \omega R_f] \tilde{I} \phi$$

$2\zeta_s \omega$  = structural damping

The lower set of equations in Eq. (25) can be rearranged to give

$$[I] \{\ddot{q}\} + [2\zeta\omega] \{\dot{q}\} + [\omega^2] \{q\} = -[\phi^T M T] \{\ddot{x}_t\} \quad (26)$$

An example of an input displacement function is shown in Fig. (6) for a tire rolling over a finite step. The step is represented by an equivalent cam. Acceleration of the cam follower is then used in Eq. (26) to calculate response. Load transformation matrices are used to calculate accelerations or loads, shears and bending moments at any point on the transporter or payload.

When the input is random, it is usually expressed in the form of displacement spectra as shown in Fig. (7). From Ref. (2), data gathered from roughness measurements on many types of roads were placed in one of two broad categories: Primary Roads and Secondary Roads. The plots shown are intended to envelope the two types of data. For any given speed, Fig. (7) is converted to acceleration power spectral density vs. frequency, shown in Fig. (8) and (9). In this form, the RMS value of response is readily calculated by methods of Ref. (3).

For example, an approximate solution for RMS response is defined by

$$\ddot{x}^2 = \sum_{r=1}^n \phi_r^2 \frac{\pi}{2} Q f_r S_u(f_r) r_r^2 \quad (27)$$

where:  $Q = \frac{1}{2\zeta}$

$$\{\phi_r\} = [\phi_r^T M T] [I] \frac{\downarrow}{\uparrow} \frac{\text{No. of input drivers}}{\text{modal participation factor for uncorrelated base drive.}}$$

Matrix multiplication must be preserved before squaring  $r_r$ .

#### COMPARISON OF CALCULATED RESPONSE WITH TEST DATA

A limited amount of test data has become available for direct comparison with predicted response. A tractor/semitrailer test vehicle developed by Goodyear Aerospace Corp. similar to Fig. (2), was driven at various speeds over a single step input consisting of a board of rectangular 1x8 inch cross-section anchored to the roadway surface. The vehicle was driven in a direction perpendicular to the length of the board so as to produce a symmetric disturbance to the vehicle. Accelerations at a number of points were recorded by isolated equipment carried in a chase van. The recording equipment was connected to instrumentation located on the semitrailer by hard line umbilical. The speed of the test vehicle was varied between 5 and 16 mph. The load on the semitrailer was a water tank filled to a level simulating the payload weight.

The entire vehicle was modelled mathematically. Structural elements are shown in Fig. (10). Hydraulic suspension elements are shown in Fig. (4) and (5) including the accumulators precharged to 300 psi. The base drive input at eight axles was simulated by the cam-follower arrangement of Fig. (6). Viscosity of the hydraulic fluid was taken as 18.5 centipoise at an assumed test condition of 100°F. All system modes were retained up to 40 hz for calculating response.

Accelerations calculated on the semitrailer bed at the forward and aft supporting points of the water tank payload are shown in

Fig. (11) and (12). Actual test measurements are also shown. Similar plots of accelerations measured at the front and rear semitrailer axles are shown in Fig. (13) and (14).

An analysis of errors in the test measurements indicates a root-sum-square error of about ±30%. Although the amount of test data available is limited, good agreement was obtained with the analytical model.

#### CONCLUSIONS

Good agreement between test and analysis leads to the following conclusions:

- (1) The finite element method, applied to the fluid elements of a hydraulic suspension system, is compatible with state-of-the-art finite element methods used in structural dynamics.
- (2) The method of analysis outlined here is capable of providing a precise design tool for evaluating performance and stability of a high speed transporter.
- (3) Fluid/structural interaction will be a feature of many new transporters which will be in general commercial use on the Interstate Highway network of the USA.

#### REFERENCES

- (1) C. W. White and R. L. Berry, "The Dynamic Interaction of Combined Fluid/Structural Systems" Report No. R-75-48628-002, Task No. D-28R, Denver Division of Martin Marietta, Corp., October 1975.
- (2) J. R. Harvey and R. A. Wursche, "Roughness Measurement and System Response Evaluation for Highway Environment." Shock and Vibration Bulletin No. 35, Part 5, Feb. 1966.
- (3) W. C. Hurty and M. F. Rubenstein, "Dynamics of Structures," Prentice-Hall, Inc., 5th ed. pp 404-405, 1964.

#### DISCUSSION

Mr. Sutherland (Wyle Labs): Did you integrate the hydraulic finite element into a structural finite element on a combined system?

Mr. Woods: Yes.

Mr. Sutherland: With how many elements roughly?

Mr. Woods: We had 120 degrees of freedom for the structure, and about 43 degrees of freedom for the fluid.



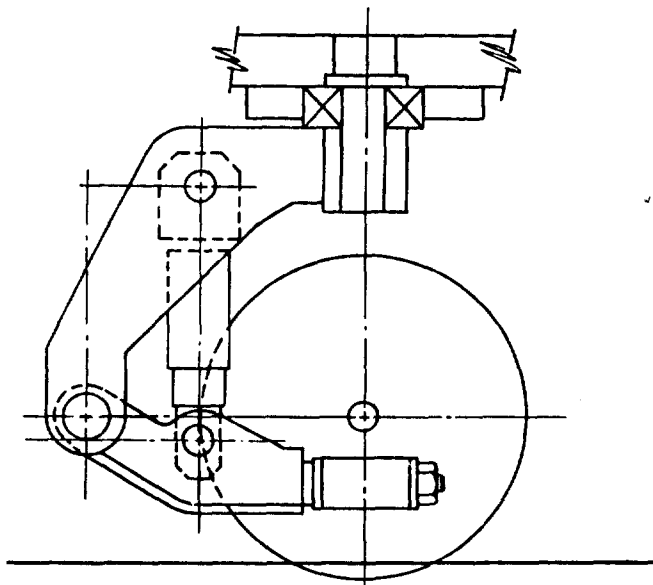


Figure 1 Side View of Bogie Assembly

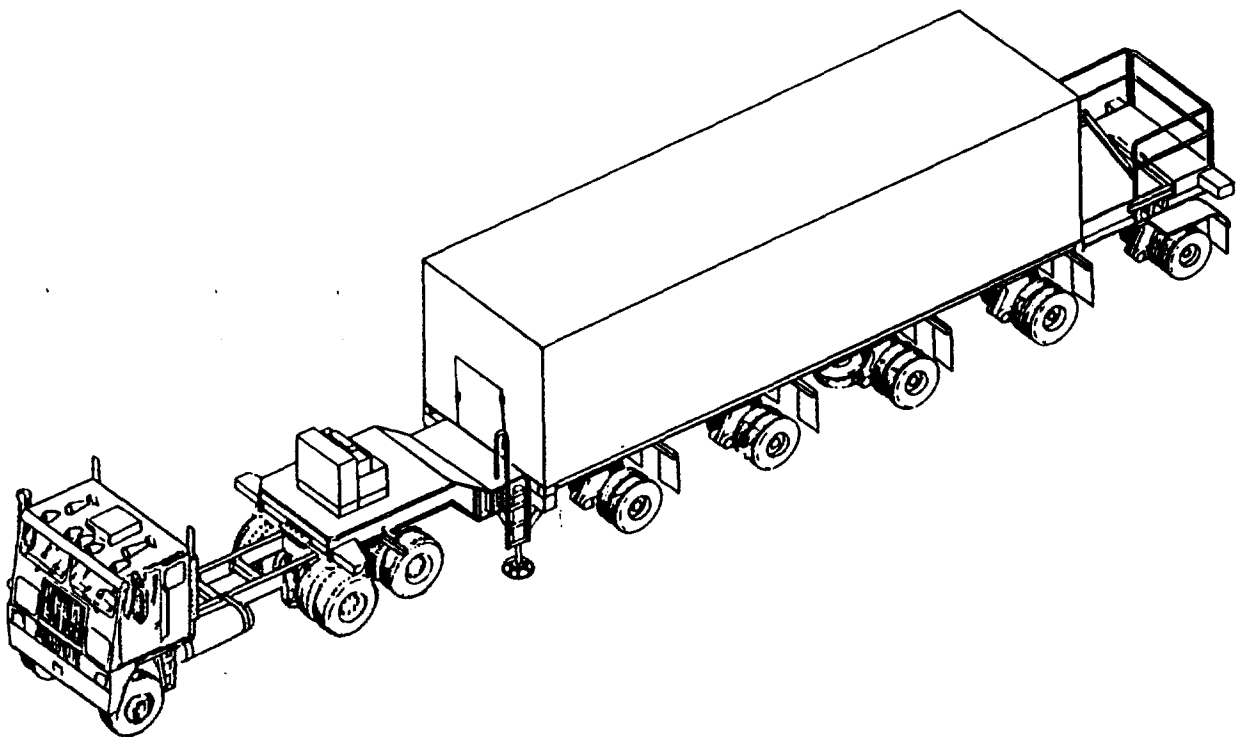


Figure 2 Tractor/Semitrailer Transporter

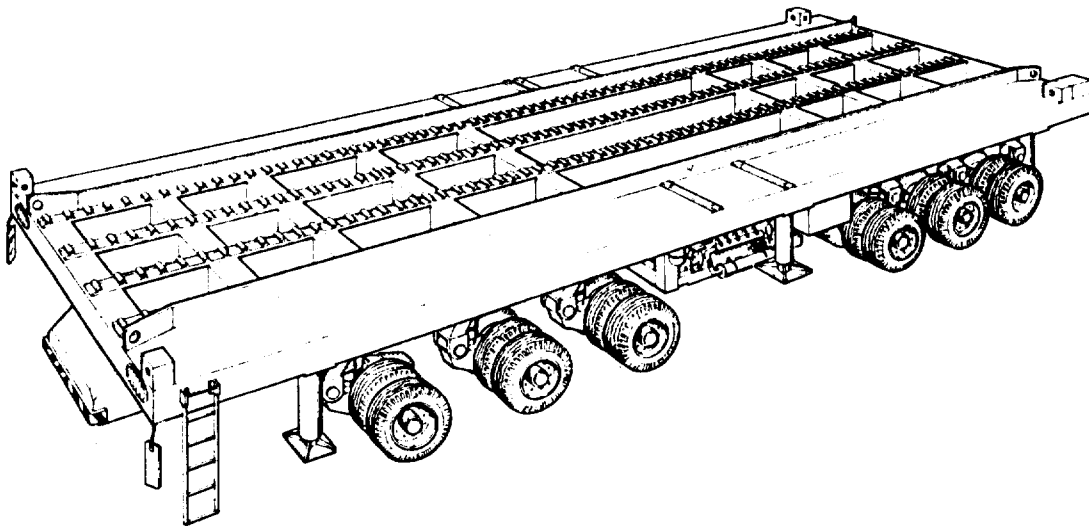


Figure 3 Self-Propelled Transporter

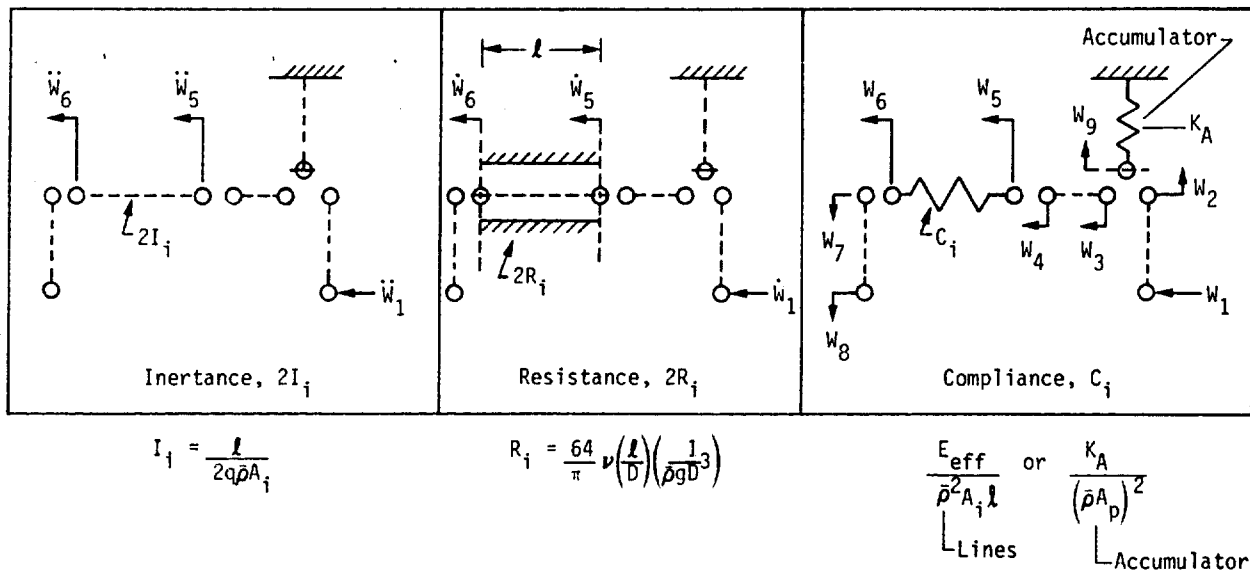


Figure 4 Typical Repeating Pattern of Fluid Elements in a Hydraulic Suspension System

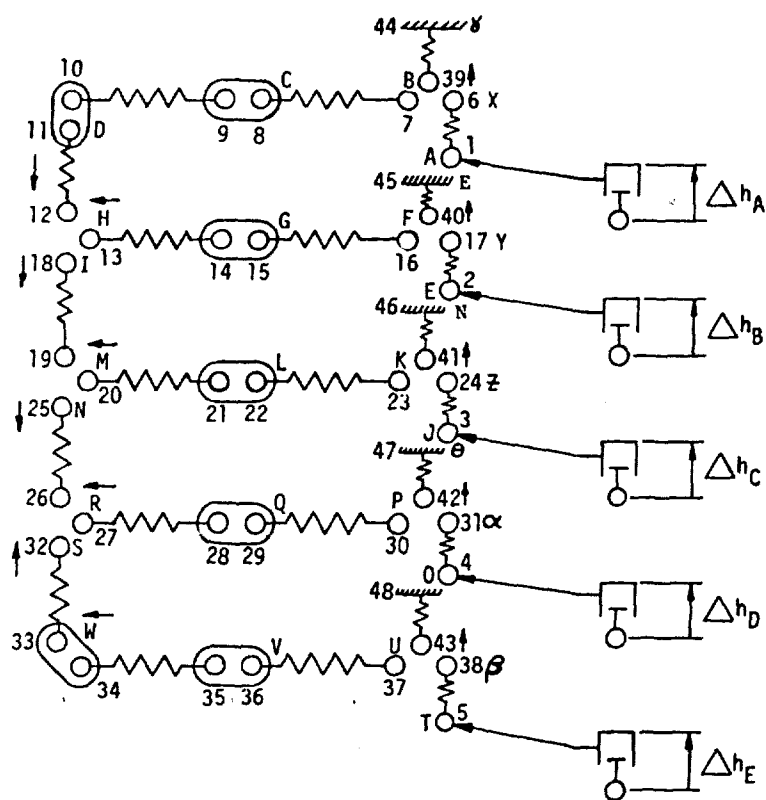


Figure 5 Half-Model Schematic of Fluid System Elements

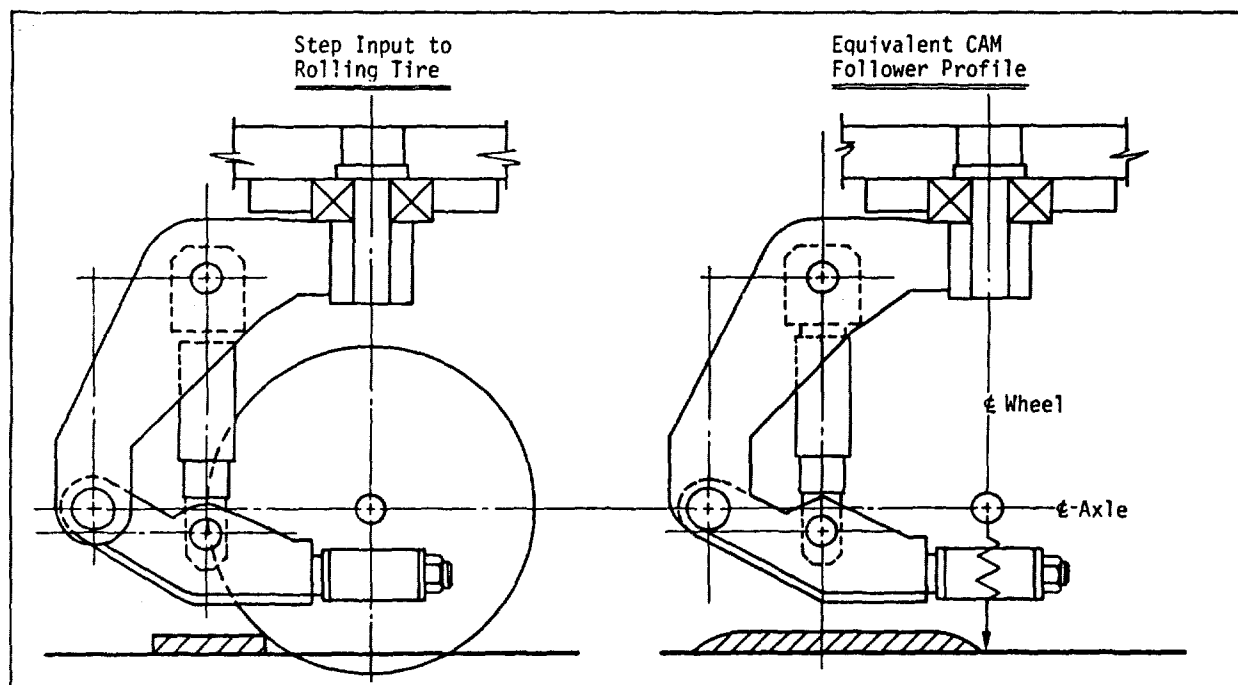


Figure 6 Step Input to a Rolling Tire and Equivalent CAM/CAM-Follower

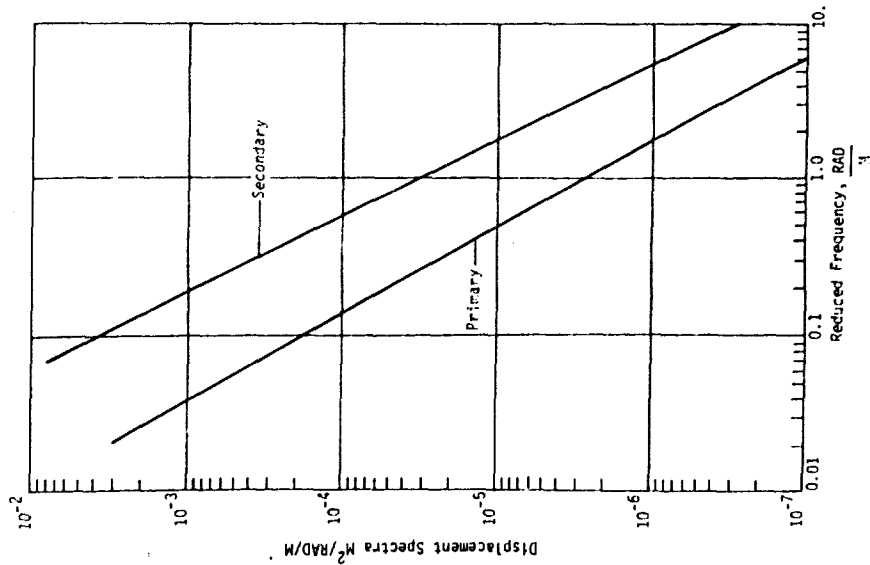


Figure 7 PSD Profiles: Primary and Secondary Roads

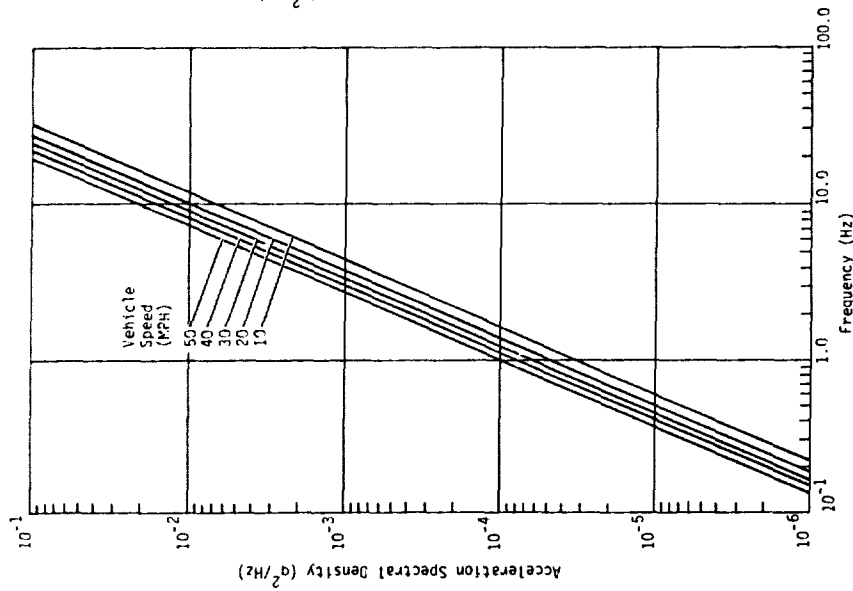


Figure 8 Random Vibration Input at Road/Tire Interface for Vehicle Traveling on Primary Roads

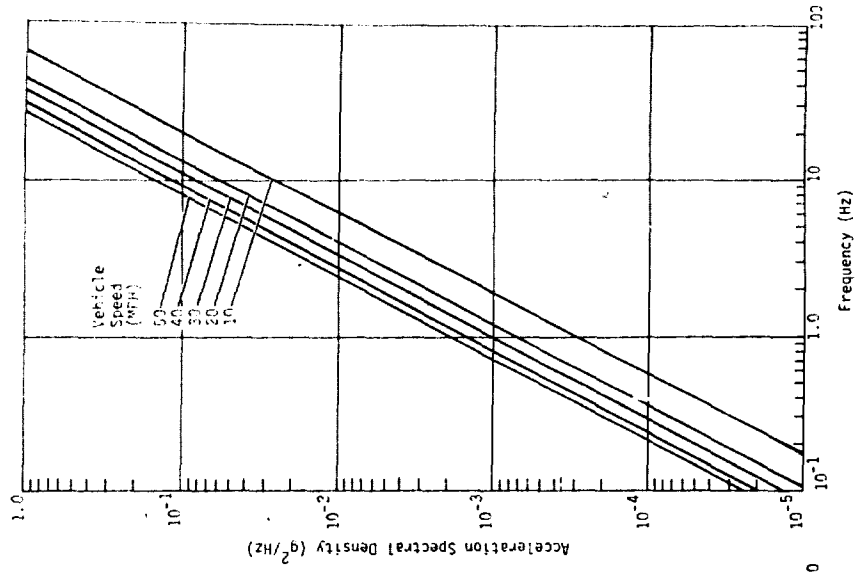


Figure 9 Random Vibration Input at Road/Tire Interface for Vehicle Traveling on Secondary Roads

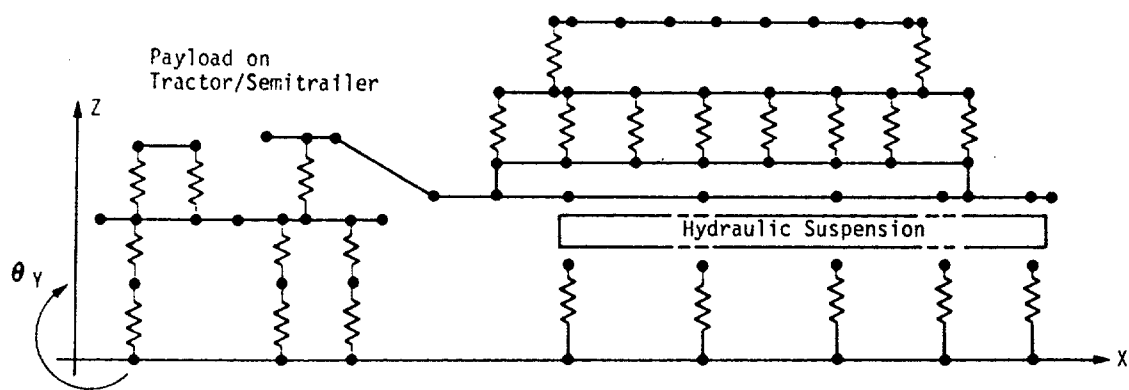


Figure 10 Structural Elements of Tractor/Semitrailer with Payload

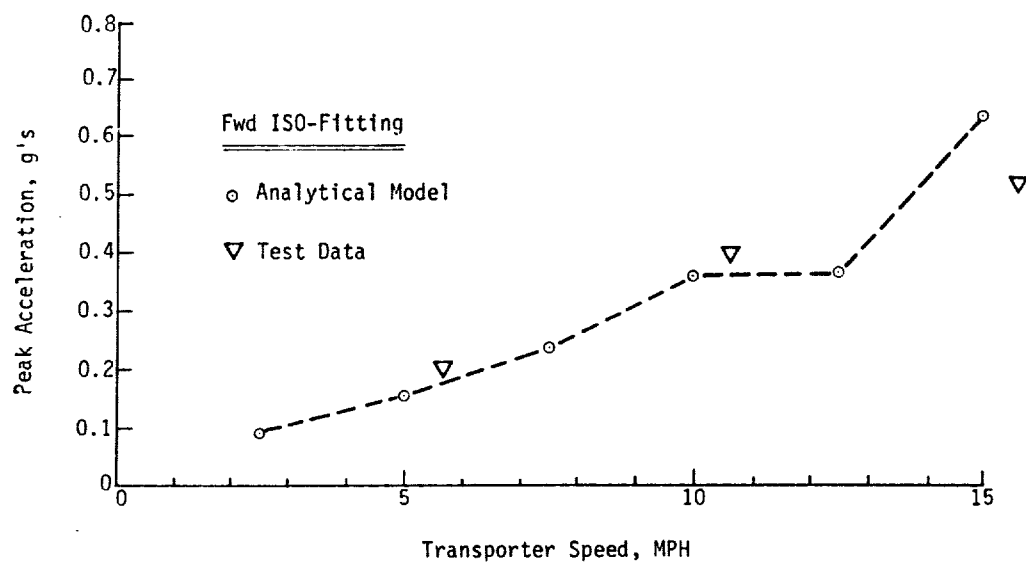


Figure 11 Analysis VS Test: Peak Vertical Acceleration at Forward ISO-Fitting

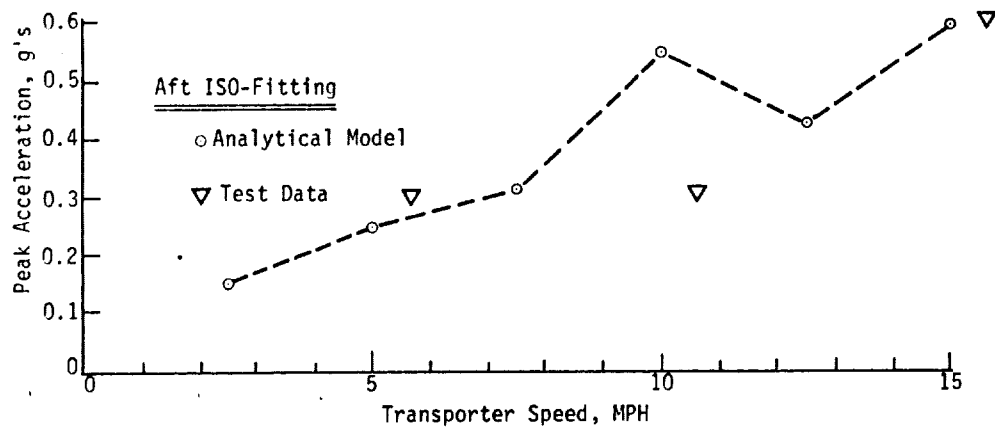


Figure 12 Analysis VS Test: Peak Vertical Acceleration at Aft ISO-Fitting.

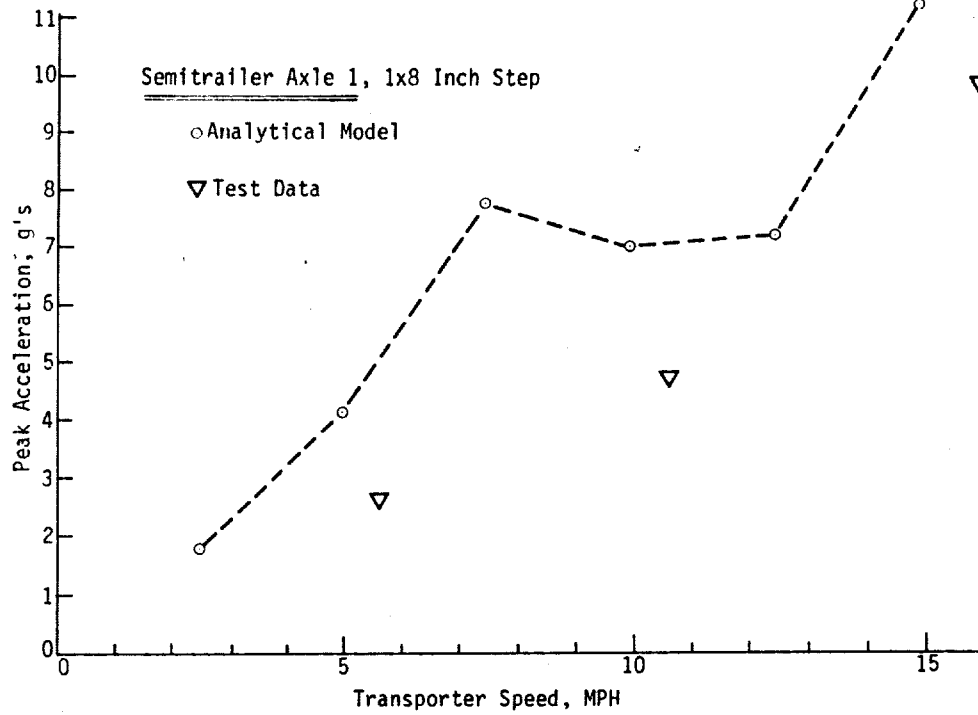


Figure 13 Analysis VS Test: Peak Vertical Acceleration at Semitrailer Axle 1.

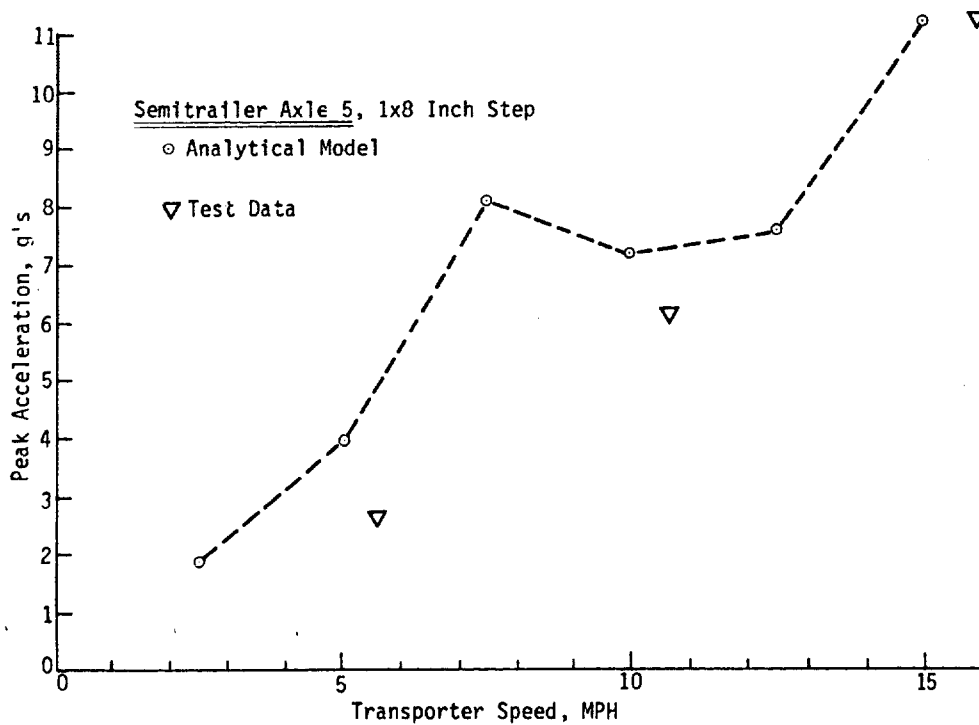


Figure 14 Analysis VS Test: Peak Vertical Acceleration at Semitrailer Axle 5

## NONLINEAR ANALYSIS OF PNEUMATIC GENERATORS USED FOR VIBRATION CONTROL

S. Sankar  
Associate Professor  
Concordia University, Montreal, PQ

R.R. Guntur  
Associate Professor  
Union College, Schenectady, N.Y.

And

S.G. Kalambur  
Electronics Associates Incorporated  
West Long Branch, New Jersey, USA

This paper deals with pneumatic isolators using passive and active force generators. Through non-linear analysis, realistic digital simulation programmes have been developed for investigating the transmissibility characteristics of active and passive pneumatic systems. It is shown that active system offers greater flexibility to the designer than the passive system. Based on the results of the study of the active system, guide lines for selecting various feedback gains are presented.

### INTRODUCTION

For isolating a mechanical system from vibrations produced by the environment within which it operates, a vibration control system is employed. In the past, only passive vibration control systems were considered by designers because active vibration control systems were very expensive. However, passive systems have many drawbacks and a designer has no choice but to accept a compromise solution when designing a passive vibration control system. In situations where the performance limitations of passive systems that are imposed by the lack of flexibility in designing cannot be accepted, and the high cost of active control systems is justifiable in view of their flexibility, active vibration control systems are potential alternatives. The scope of the present investigation is limited to passive and active pneumatic isolation systems.

Some of the basic aspects of pneumatic isolation systems were discussed in references [1,2]. Pneumatic suspension systems were described in references [3,4,5]. Cavanaugh [6], Kunica [7] and Esmailzadeh [8] studied servo-controlled pneumatic isolator systems. Klinger and Calzado [9] proposed an active pneumatic suspension system for a passenger rail car. Karnopp, Crosby and Harwood [10] used the concept of control force and described a means by

which the desired performance of a vibration control system could be obtained with the aid of semiactive force generators. Sankar and Guntur [11] studied the transmissibility characteristics of active vibration control system that used pneumatic force generators; however, this analysis of the performance of an active system was based on a linearized model.

In this paper, transmissibility characteristics of an active pneumatic vibration control system will be studied using a non-linear model. The objective of this investigation is to determine the effect of the various feedback gains on the transmissibility characteristics. The performance of the active system is compared with that of a passive pneumatic vibration control system that uses a fixed size orifice as a means to provide the required amount of damping. Based on the results of this paper, general guide lines for selecting various feedback gains are outlined.

### PASSIVE SYSTEM

A schematic diagram of a passive isolator is shown in Figure 1. The mass is supported by the force generated across the piston of the actuator and the mechanical spring. A damping force is produced whenever there is a flow of air through the orifice area. Thus, the effec-

tive damping coefficient is dependent on the orifice area.

The non-dimensionalized equations for the rate of change of pressure chambers can be written as follows:

$$\dot{p}_1 = \gamma \left[ \dot{M}^* \frac{t_1}{(1-x_2+x_1)} - \frac{p_1}{(1-x_2+x_1)} (-\dot{x}_2 + \dot{x}_1) \right] \quad (1)$$

$$\dot{p}_2 = \gamma \left[ -\dot{M}^* \frac{t_2}{A_r(1+x_2-x_1)} - \frac{p_2}{(1+x_2-x_1)} (\dot{x}_2 - \dot{x}_1) \right] \quad (2)$$

The mass flow is given by,

$$\dot{M}^* = - \frac{p_1 a \beta N}{t_1^{1/2}} \quad \text{if } p_2 > 0.5283 p_1 \quad (3)$$

where

$$N_{12} = \left[ \frac{(p_1/p_2)^{2/\gamma} - (p_1/p_2)^{(\gamma+1)/\gamma}}{(\frac{\gamma-1}{2}) (\frac{2}{\gamma+1})^{\gamma+1/\gamma-1}} \right]^{1/2} \quad (4)$$

and

$$\dot{M}^* = \frac{p_2 a \beta N}{t_2^{1/2}} \quad p_2 \leq 0.5283 p_1 \quad (5)$$

where

$$N_{21} = \left[ \frac{(p_1/p_2)^{2/\gamma} - (p_1/p_2)^{(\gamma+1)/\gamma}}{(\frac{\gamma-1}{2}) (\frac{2}{\gamma+1})^{\gamma+1/\gamma-1}} \right]^{1/2} \quad (6)$$

The equation of motion is as follows:

$$\ddot{x}_1 = c_1 p_1 - c_2 p_2 + c_3 (x_3 + x_2 - x_1) - c_4 \quad (7)$$

For the performance analysis of the passive system, a simple sinusoidal input excitation given by the following relation is employed:

$$x_2 = x_0 \sin \omega t \quad (8)$$

The equations (1-8) are employed in a digital simulation program and the results are presented in the form of absolute displacement transmissibility and absolute acceleration transmissibility characteristics in Figures 2 and 3. The values of various variables used in the simulation program are given in Table 1.

#### PERFORMANCE ANALYSIS OF THE PASSIVE SYSTEM

The absolute displacement transmissibility (TADR) vs frequency (F:rad/s) curves for  $x_3 = 0.50$  (=AL) are shown in Figure 2. The absolute acceleration transmissibility (AR) vs frequency (F:rad/s) curves for  $x_3 = 0.50$  (=AL) are shown in Fig. 3. The results in Fig. 2 indicate that when the normalized area of the orifice is very small 0.00018, the peak value of the absolute displacement transmissi-

bility is very high. By employing optimization techniques, the area 'a' for which the peak value of the absolute displacement transmissibility is the minimum is determined and it is found to be 0.00045. As 'a' is increased above this optimum value, the peak absolute displacement transmissibility increases as shown in Fig. 2. It should be noted that even though the optimum orifice area of 0.00045 minimizes, the peak value of the displacement transmissibility, with this orifice area of 0.00045 the displacement transmissibility is higher than that with an orifice area of 0.00018 in the frequency range of 5 to 19 rad/s.

Similar qualitative aspects have been exhibited by the absolute acceleration transmissibility characteristics shown in Fig. 3. The results in Figs. 2 and 3 show the deficiencies of a passive system. One of these deficiencies is that the absolute displacement or acceleration transmissibility will not be lower than 1.0 at near zero frequencies. It is also noted that when an attempt is made to minimize the peak displacement transmissibility, the displacement at either the low frequency end or at the high frequency end will be adversely affected.

#### ACTIVE SYSTEM

An active pneumatic vibration control system offers considerable design flexibility. Sankar et al [11] investigated the effect of various feedback terms on the performance of a vibration control system that employs a pneumatic force generator with the help of a lineanised model. Present study will take into account non-linearities and will be useful in comparing the results of planned experimental work in this area.

A schematic diagram of an active isolator using a servo-controlled pneumatic force generator is shown in Fig. 4. The piston of the pneumatic actuator forms a wall between the two chambers of the actuator. The lower chamber is sealed and the upper chamber is connected to an electro-pneumatic servo-valve. This servo-valve regulates the flow in and out of chamber 1. The output displacement ( $x'_1$ ), output velocity ( $\dot{x}'_1$ ) and output acceleration ( $\ddot{x}'_1$ ) are used as feedback signals with respective feedback gains  $k_3$ ,  $k_2$  and  $k_1$  in controlling the mass flow and thus the control force.

The non-dimensionalized equations for rates of change of pressure with respect to time are as follows:

$$\dot{p} = \gamma \left[ \dot{M}^* \frac{t_1}{(1-x_2+x_1)} - \frac{p_1}{(1-x_2+x_1)} (-\dot{x}_2 + \dot{x}_1) \right] \quad (9)$$

$$\dot{p}_2 = \gamma \left[ -\frac{p_2}{(1+x_2-x_1)} (\dot{x}_2 - \dot{x}_1) \right] \quad (10)$$



The non-dimensionalized equations of flow are as follows:

$$\ddot{m}_1^* = - \frac{a_{s1} \beta p_1}{t_1^{\frac{1}{2}}} \quad (11)$$

If  $k_1 \ddot{x}_1 + k_2 \dot{x}_1 + k_3 x_1 \geq 0$ , and if  $p_a < 0.5283 p_1$

where

$$a_{s1}^* = (a_{s1} - a_{s1}^*) \frac{\alpha}{\tau_V} \quad (12)$$

and  $a_{s1}$  is given by the following relation

$$a_{s1} = (a_{s1})_{\max} \text{ if } |k_1 \ddot{x}_1 + k_2 \dot{x}_1 + k_3 x_1| \geq (a_{s1})_{\max} \quad (13)$$

Otherwise,

$$a_{s1} = k_1 \ddot{x}_1 + k_2 \dot{x}_1 + k_3 x_1 \quad (14)$$

If  $k_1 \ddot{x}_1 + k_2 \dot{x}_1 + k_3 x_1 \geq 0$ , and if  $p_a > 0.5283 p_1$

$$\ddot{m}_1^* = - \frac{a_{s1}^* \beta p_1 N_{e1}}{t_1^{\frac{1}{2}}} \quad (15)$$

Equations (12) to (14) define other variables and  $N_{e1}$  is given by

$$N_{e1} = \left[ \left( \frac{p_a}{p_1} \right)^{2/\gamma} - \left( \frac{p_a}{p_1} \right)^{\frac{\gamma+1}{\gamma}} \right]^{\gamma_2} \quad (16)$$

If  $k_1 \ddot{x}_1 + k_2 \dot{x}_1 + k_3 x_1 < 0$ , and if  $p_1 < 0.5283 p_s$

$$m^* = - \frac{a_{s1}^* \beta p_s}{t_s^{\frac{1}{2}}} \quad (17)$$

where  $a_{s1}^* = (a_{s1} - a_{s1}^*) \frac{\alpha}{\tau_V}$  (18)

$$a_{s1} = -(a_{s1})_{\max} \text{ if } |k_1 \ddot{x}_1 + k_2 \dot{x}_1 + k_3 x_1| \geq (a_{s1})_{\max} \quad (19)$$

and

$$a_s = k_1 \ddot{x}_1 + k_2 \dot{x}_1 + k_3 x_1 \quad (20)$$

if  $k_1 \ddot{x}_1 + k_2 \dot{x}_1 + k_3 x_1 < 0$ , and if  $p_1 > 0.5283 p_s$

$$\ddot{m}_1^* = - \frac{a_{s1}^* \beta p_s N_{s1}}{t_s^{\frac{1}{2}}} \quad (21)$$

Equations (18) to (20) define other variables and  $N_{s1}$  is given by,

$$N_{s1} = \left[ \left( \frac{p_1}{p_s} \right)^{2/\gamma} - \left( \frac{p_1}{p_s} \right)^{\frac{\gamma+1}{\gamma}} \right]^{\frac{1}{2}} \quad (22)$$

To obtain the absolute displacement transmissibility of the active vibration control system, equation 11-22 are solved using a digital computer. Data for the active system are given in Table 2.

#### PERFORMANCE OF THE ACTIVE PNEUMATIC VIBRATION CONTROL SYSTEM

The variations of the absolute displacement transmissibility at a frequency of 2.5 rad/s with  $k_2$  for various values of  $k_1$  and  $k_3$  are shown in Fig. 5. There are five bands (1 to 5) in which the values of the absolute displacement transmissibility fall for five different values of  $k_3$ , namely, 1, 2, 3, 4 and 5. In all these cases,  $k_1$  varies from 0.04 to 0.14. Evidently, as  $k_3$  is increased, the absolute displacement transmissibility at a frequency of 2.5 rad/s decreases for a given set of values of  $k_1$  and  $k_2$ . For a given set of values of  $k_1$  and  $k_3$ , the absolute displacement transmissibility decreases as  $k_2$  is increased. It is also observed from the results (not shown in Fig. 5) that when  $k_1$  is lower than 0.04, the absolute displacement transmissibility is higher than 1.0 indicating that a part of the control force produced by the force generator should depend on the acceleration. However, if  $k_1$  is higher than 0.14, the absolute displacement transmissibility will be higher than 1.0 indicating that very high gains for the acceleration feedback term are not suitable. Previous linear analysis [8,11] did not reveal the fact that the gain for the acceleration feedback term should have a small positive value.

The absolute displacement transmissibility characteristics for four different values of  $k_2$  (0.5, 1.0, 1.5 and 2.0) when  $k_1 = 0.04$  and  $k_3 = 1.0$  are given in Fig. 6. The results in Fig. 6 indicate that the peak value of the absolute displacement transmissibility for any of the four values of  $k_2$  used in the simulation is very high. It is also noted that as  $k_2$  is increased, the frequency at which the absolute displacement transmissibility peaks (resonance frequency) is also increased. The reason for this can be explained from the fact that an increase in the velocity feedback gain  $k_2$  increases the effective stiffness of the system and thus increases the natural frequency of the system.

Figure 7 shows the absolute transmissibility displacement characteristics for four values of  $k_2$ , namely 0.5, 1.0, 1.5 and 2.0, when  $k_1 = 0.06$  and  $k_3 = 1.0$ . By comparing the results in Fig. 7 with those in Fig. 6, it is observed that as  $k_1$  is increased, the peak value of the absolute displacement transmissibility is decreased for a given set of values of  $k_2$  and  $k_3$ . It is also noted from the results in Fig. 7 that as  $k_2$  is increased, the frequency at which the absolute displacement transmissibility reaches its maximum value also increases.

Figure 8 presents the absolute displacement transmissibility characteristics for four values of  $k_2$  (0.5, 1.0, 1.5 and 2.0) if  $k_1 = 0.04$  and  $k_3 = 5.0$ . The results in Fig. 8 indicate that for any value of  $k_2$  considered the peak value of the absolute displacement transmissibility is very high. It is also noted that as  $k_2$  is increased, the resonance frequency is also increased. In Figure 8, it can also be seen that an increase in the velocity feedback gain for given values of the displacement and acceleration feedback gain, decreases the peak value of the absolute displacement transmissibility.

By comparing the results in Fig. 6 with those in Fig. 8, one can determine the effect of  $k_3$  on the absolute displacement transmissibility for a given set of values of  $k_1$  and  $k_2$ . It is noted from Figs. 6 and 8 that for a given set of values of  $k_1$  and  $k_2$ , an increase in the value of  $k_3$  decreases the value of the absolute displacement transmissibility at a frequency of 2.5 rad/s; however, an increase in the value of  $k_3$  also increases the peak value of the absolute displacement transmissibility.

In Fig. 9 are presented the absolute displacement transmissibility characteristics for four values of  $k_2$  (0.5, 1.0, 1.5, 2.0) when  $k_1 = 0.06$  and  $k_3 = 5.00$ . The results in Fig. 9 show that as  $k_2$  is increased, the resonance frequency is increased. By comparing the results in Fig. 9 with those in Fig. 8, it is gathered that as  $k_3$  is increased, the peak value of the absolute displacement transmissibility is decreased for a given set of values of  $k_1$  and  $k_2$ . By comparing the results in Fig. 9 with those in Fig. 7, the effect of  $k_3$  can be determined for a given set of values of  $k_1$  and  $k_2$ . An increase in  $k_3$  decreases the absolute displacement transmissibility at a frequency of 2.5 rad/s. An increase in  $k_3$  also results in an increase in the peak value of the absolute displacement transmissibility for a given set of values of  $k_1$  and  $k_2$ . Comparing the results in Figs. 6, 7, 8 and 9 with those in Fig. 2, one can easily note the flexibility offered by the active system.

#### CONCLUSION

Based on the discussion of the results presented above, the following conclusions can be drawn:

The active system offers greater flexibility to the designer than the passive system.

A small amount of the total control force generated by the active components of the system should depend on the acceleration of the mass of the system. The value of the acceleration feedback should be in the range of 0.04 - 0.14 for the system under consideration. As  $k_1$  is increased, the peak value of the absolute displacement transmissibility is decreased for a given set of values of  $k_2$  and  $k_3$ .

An increase in the value of the velocity feedback gain  $k_2$  will result in an increase in the resonance frequency.

An increase in the value of the displacement feedback gain  $k_3$  also increases the peak values of the absolute displacement transmissibility for a given set of values of  $k_1$  and  $k_2$ .

It is hoped that the above guidelines for selecting various feedback gains will be useful in designing active pneumatic isolators.

#### ACKNOWLEDGEMENT

This investigation was supported through grants from the Natural Sciences and Engineering Research Council of Canada.

#### REFERENCES

1. Hirtreiter, A.B., "Air Springs", Machine Design, April 1965.
2. Sainsbury, J.H., "Air suspension for Road Vehicles", Proc. Inst. Mech. Engrs. (A.D.), No. 3 1957-58.
3. Nicholas, K.E., "New trends in using air suspensions", Engineering Materials and Design, July 1959.
4. O'Shea, C.F., "The Ford approach to air suspension", S.A.E. Transactions, Vol. 66, 1958.
5. Berry, W.S., "The air-coil spring", S.A.E. Transactions, Vol. 66, 1958.
6. Cavanaugh, R.D., "Air suspension and servo-controlled isolation systems", Shock and Vibration Handbook (Edited by C.M. Harris and C.E. Crede), Vol. 2, McGraw-Hill, 1961.
7. Kunica, S., "Servo controlled pneumatic isolators", Design News, September 15, 1965.
8. Esmailzadeh, E., "Servo-valve controlled Pneumatic suspensions", Journal of Mechanical Engineering Science, Vol. 21, 1979.
9. Klinger, D.L., and Calzado, A.J., "A pneumatic on-off vehicle suspension system", Journal of Dynamic Systems, Measurement and Control, Vol. 99, Series G, 1977.
10. Karnopp, D.C., Crosby, M.J., and Harwood, R.A., "Vibration control using active force generators", Journal of Engineering for Industry, Vol. 96, Series B, No. 2, May 1974.
11. Sankar, S., and Guntur, R.R., "Pneumatic vibration control using active force generators" The Shock and Vibration Bulletin 51, Part I, May 1981.

TABLE 1: DATA FOR THE PASSIVE SYSTEM

Variable	Value Used in the Simulation
$A_1$	$1.14 \times 10^{-3} \text{ m}^2$
$A_2$	$1.069 \times 10^{-3} \text{ m}$
$k$	$2.635 \times 10^3 \text{ N/m}$
$L$	$7.62 \times 10^{-2} \text{ m}$
$mg$	$4.45 \times 10^2 \text{ N}$
$\gamma$	1.4
$P_0$	$5.52 \times 10^5 \text{ N/m}^2$
$T_0$	295°k
$V_0$	$8.6868 \times 10^{-5} \text{ m}^3$
$x_3^i$	$2.06 \times 10^{-2} \text{ m}$

TABLE 2: DATA FOR THE ACTIVE SYSTEM

Variable	Value Used in the Simulation
$A_1$	$1.14 \times 10^{-3} \text{ m}^2$
$A_2$	$1.069 \times 10^{-3} \text{ m}$
$k$	$2.635 \times 10^3 \text{ N/m}$
$L$	$7.62 \times 10^{-2} \text{ m}$
$mg$	$4.45 \times 10^2 \text{ N}$
$\gamma$	1.4
$P_0$	$5.52 \times 10^5 \text{ N/m}^2$
$P_s$	$8.3 \times 10^5 \text{ N/m}^2$
$T_0$	295°k
$V_0$	$8.6868 \times 10^{-5} \text{ m}$
$x_3^i$	$2.06 \times 10^{-2} \text{ m}$
$\tau_v$	0.01 sec

# NOMENCLATURE

$A_{12}$	Area of the orifice between the two chambers (passive system).	$P_a$	$P_a/P_0$
$A_1$	Head side area of the piston	$P_s$	$P_s/P_0$
$A_2$	Rod side area of the piston	$P_1$	$P_1/P_0$
$AL$	$x_3$	$P_2$	$P_2/P_0$
$A_r$	$A_2/A_1$	$R$	Gas constant
$A_{s1}$	Area of the orifice created by the movement of the spool in the servo-valve of the active system.	$T_0$	Reference temperature
$A_0$	Reference area	$T_1$	Temperature in chamber 1
$a$	$A_{12}/A_0$	$T_2$	Temperature in chamber 2
$A_{s1}^*$	$A_{s1}/A_0$	$T_s$	Temperature of the air being supplied
$c_1$	$\frac{A_1 \alpha^2 P_0}{L m}$	$t$	time
$c_2$	$\frac{A_2 \alpha^2 P_0}{L m}$	$t_s$	$T_s/T_0$
$c_3$	$\frac{k \alpha^2}{m}$	$t_1$	$T_1/T_0$
$c_4$	$\frac{g \alpha^2}{L} + \frac{P_a \alpha^2}{L m} (A_1 - A_2)$	$t_2$	$T_2/T_0$
$k$	Mechanical spring stiffness	$V_0$	Reference volume $A_1 L$
$k_1$	Acceleration feedback gain	$x_1'$	Output displacement
$k_2$	Velocity feedback gain	$x_2'$	Input displacement
$k_3$	Displacement feedback gain	$x_3'$	Initial compression of the spring
$L$	Reference length	$x_0$	Input amplitude
$M_0$	Reference mass - $(\frac{P_0 V_0}{RT_0})$	$x_1$	$x_1'/L$
$m$	Mass of the system to be isolated	$x_2$	$x_2'/L$
$\dot{M}_1^*$	Dimensionless mass flow rate into chamber 1 of the passive system	$x_3$	$x_3'/L = AL$
$\dot{M}_2^*$	Dimensionless mass flow rate into chamber 2 of the passive system.	$\alpha$	Reference time
$\dot{m}_1^*$	Dimensionless mass flow rate into chamber 1 of the active system.	$\beta_1, \beta_2$	Dimensionless constants
$P_a$	Atmospheric pressure	$\gamma$	$(c_p/c_v)$ the ratio of specific heats of air
$P_0$	Reference pressure	$\tau$	$t/\alpha$
$P_s$	Supply pressure	$\tau_v$	Valve time delay
$P_1$	Pressure in chamber 1	$(\cdot)$	Denotes derivative with respect to $\tau$
$P_2$	Pressure in chamber 2		

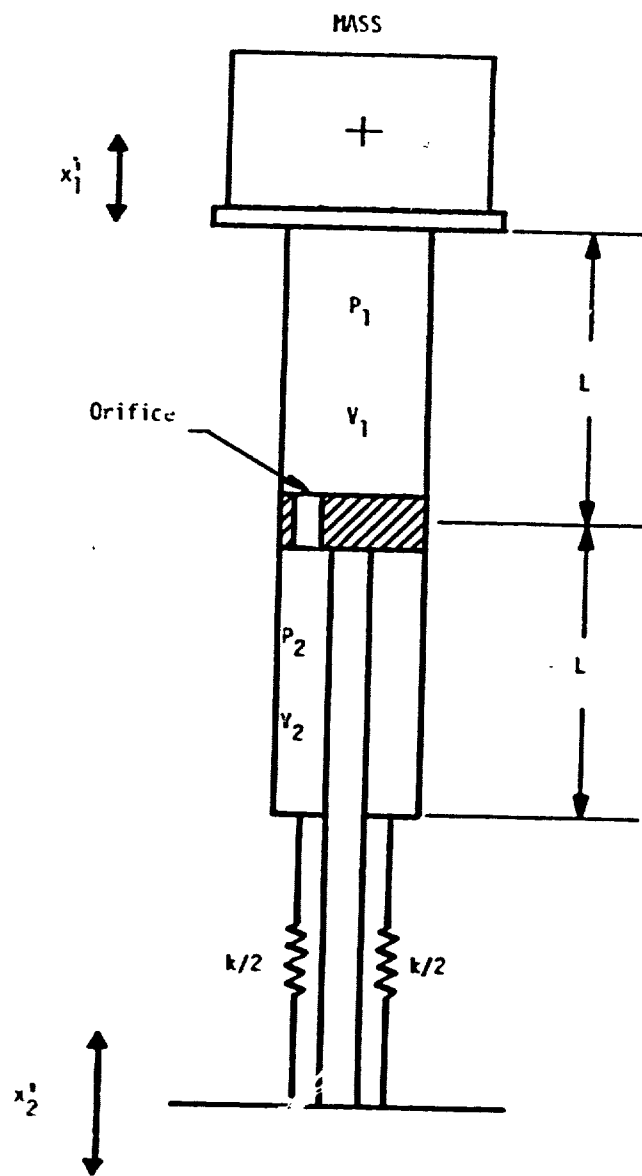


FIGURE 1: Schematic Diagram of the Passive Pneumatic System

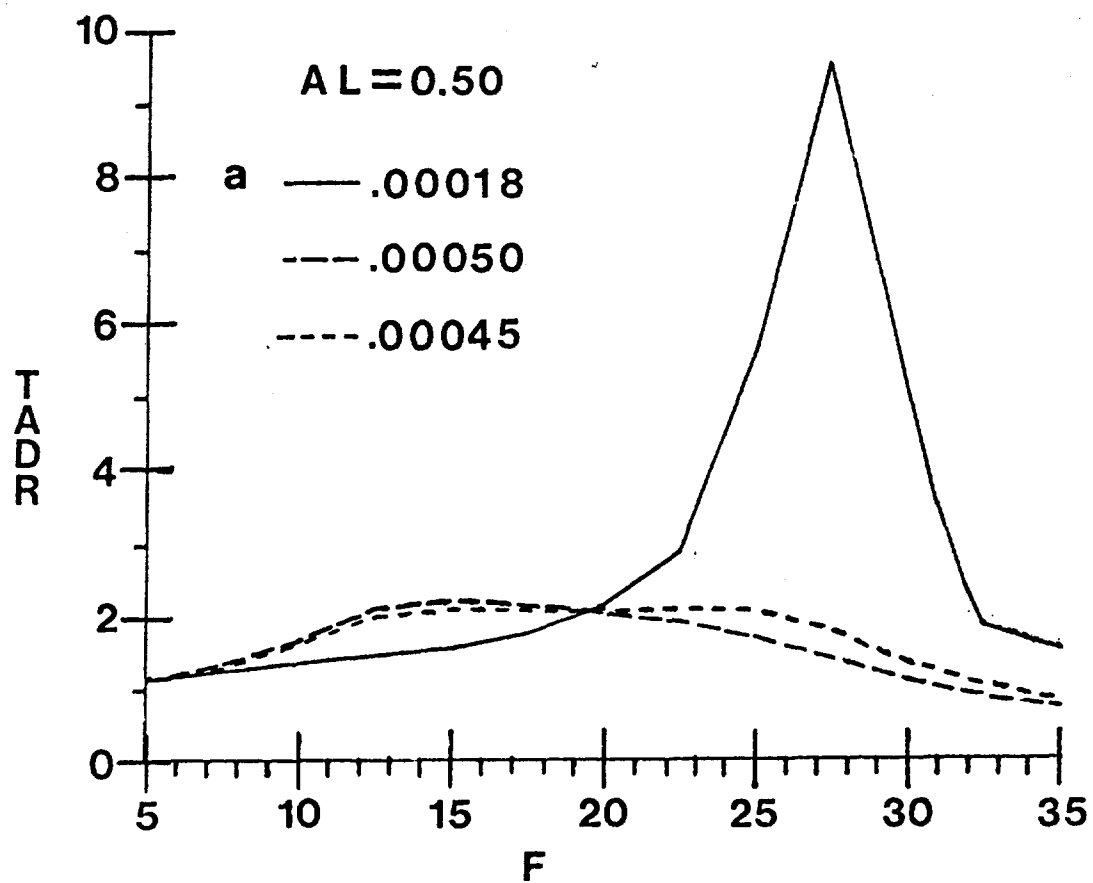


FIGURE 2: Absolute Displacement Transmissibility (TADR) vs Frequency (F: rad/s) Curves for the Passive System for Three Different Normalized Orifice Areas, 0.00018, 0.00050 and .00045.

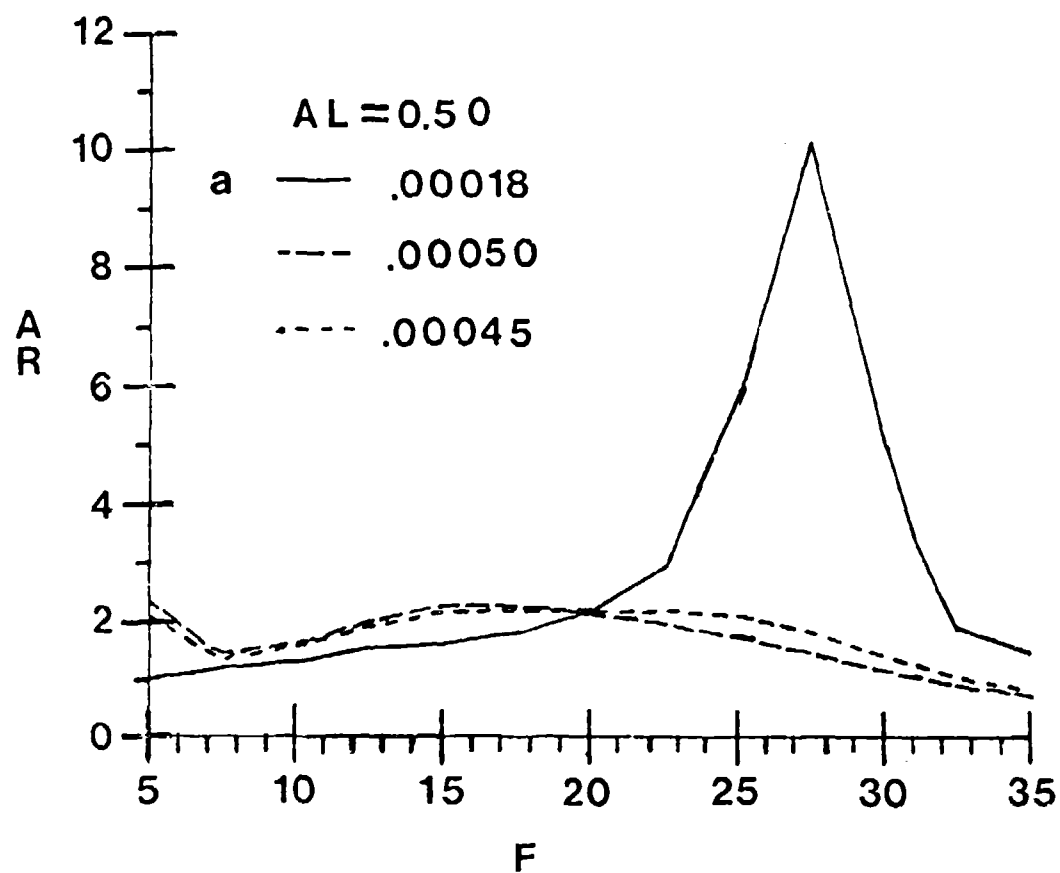


FIGURE 3: Absolute Acceleration Transmissibility (AR) vs Frequency (F: rad/s)  
 Curves for the Passive System for Three Different Normalized Orifice  
 Areas 0.00018, 0.00050 and 0.00045.

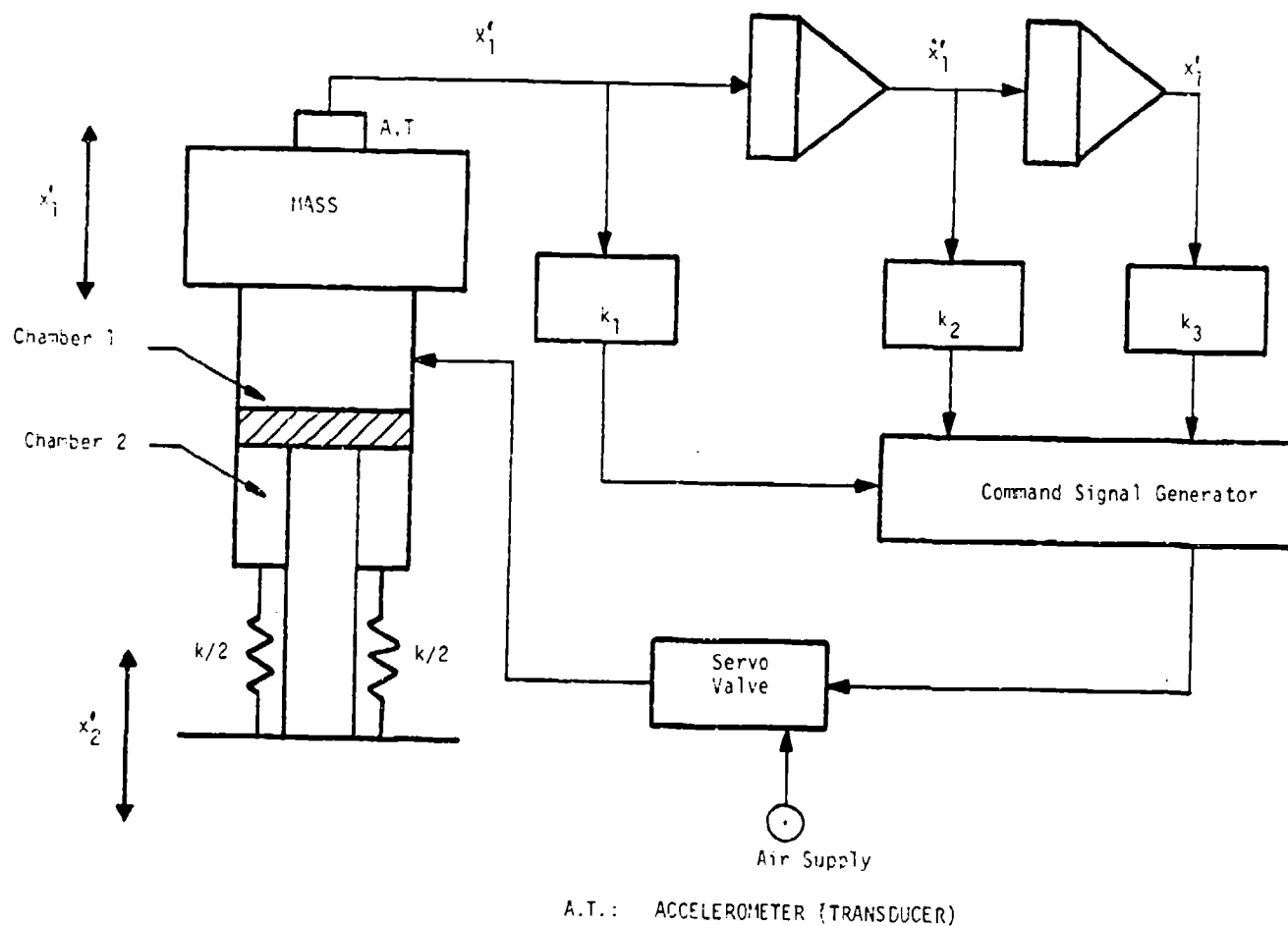


FIGURE 4: Schematic Diagram of the Active Pneumatic System



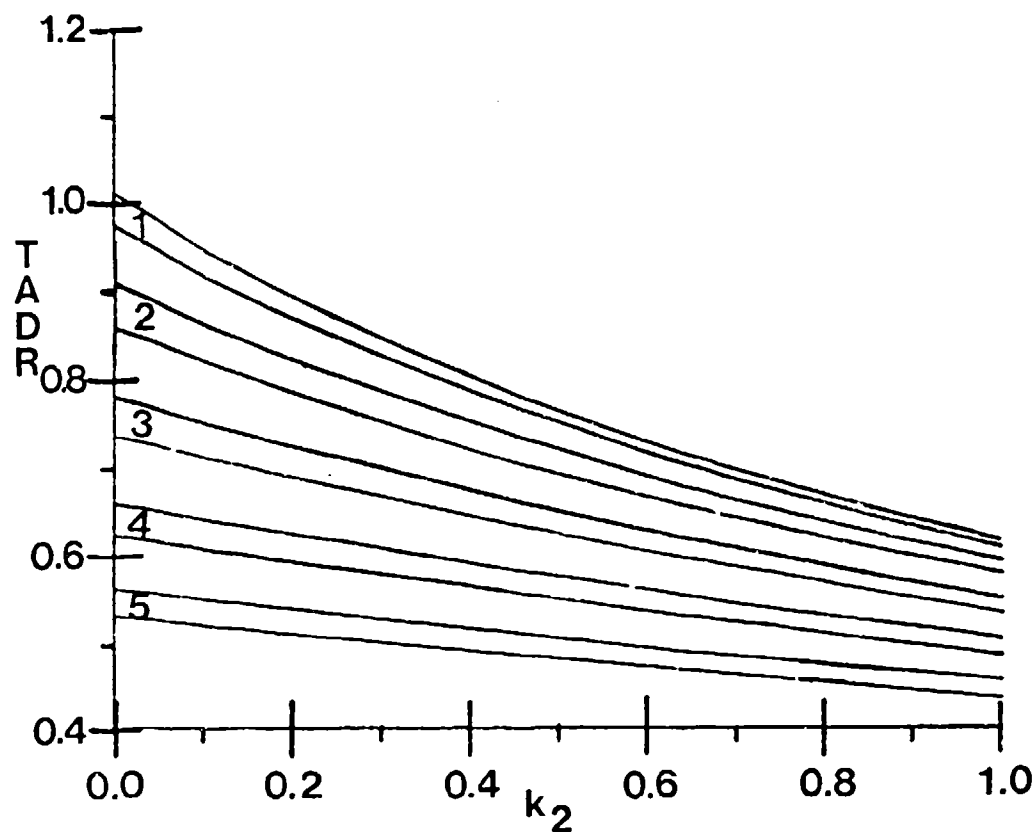


FIGURE 5: Absolute Displacement Transmissibility at a Frequency of 2.5 rad/s vs Feedback gain  $k_2$ .

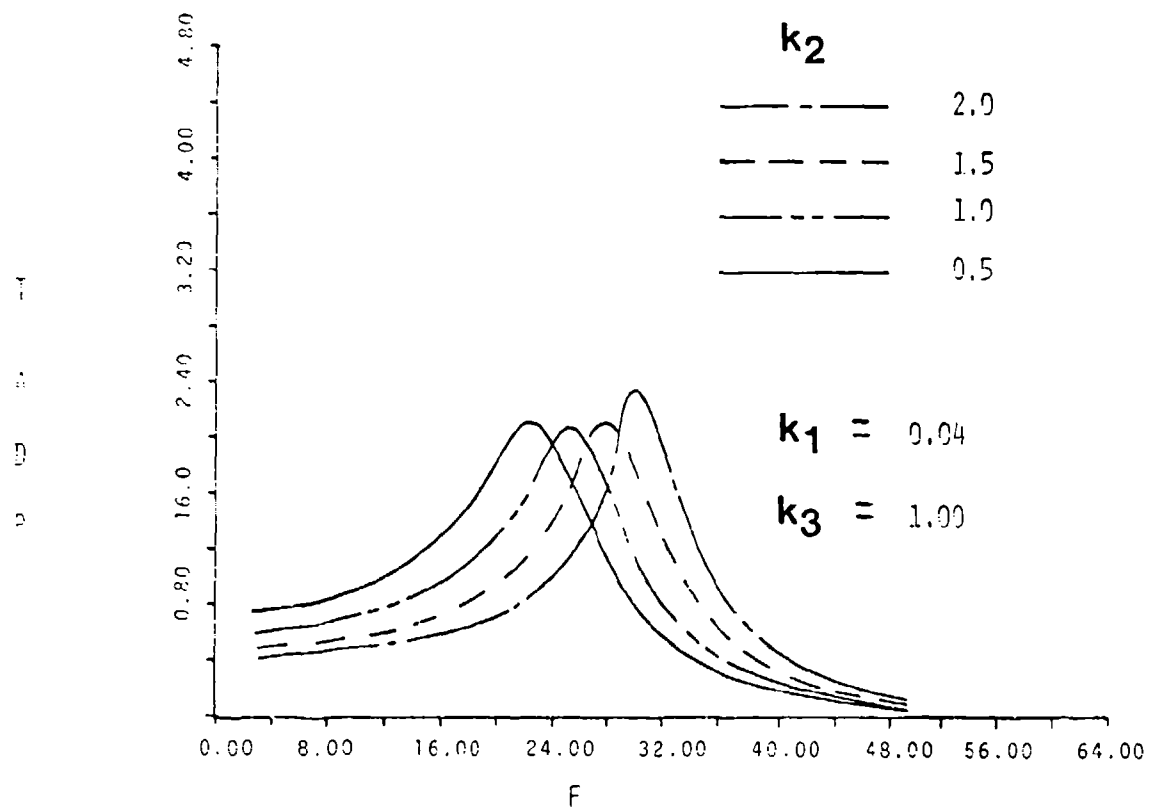


FIGURE 6: Absolute Displacement Transmissibility (TADR) vs Frequency (F) for Four Values of  $k_2$  (0.5, 1.0, 1.5 and 2.0) when  $k_1 = 0.04$  and  $k_3 = 1.00$

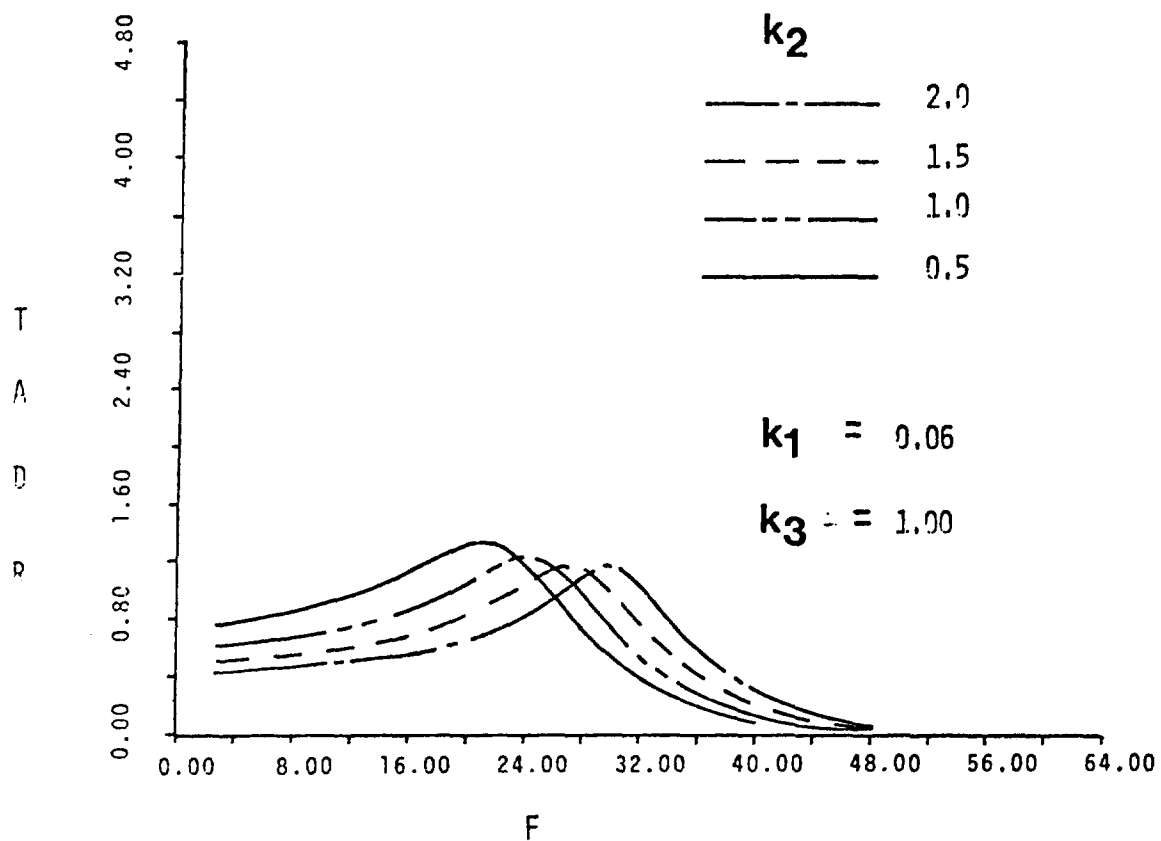


FIGURE 7: Absolute Displacement Transmissibility (TADR) vs Frequency (F) for Four Values of  $k_2$  (0.5, 1.0, 1.5 and 2.0) when  $k_1 = 0.06$  and  $k_3 = 1.00$ .

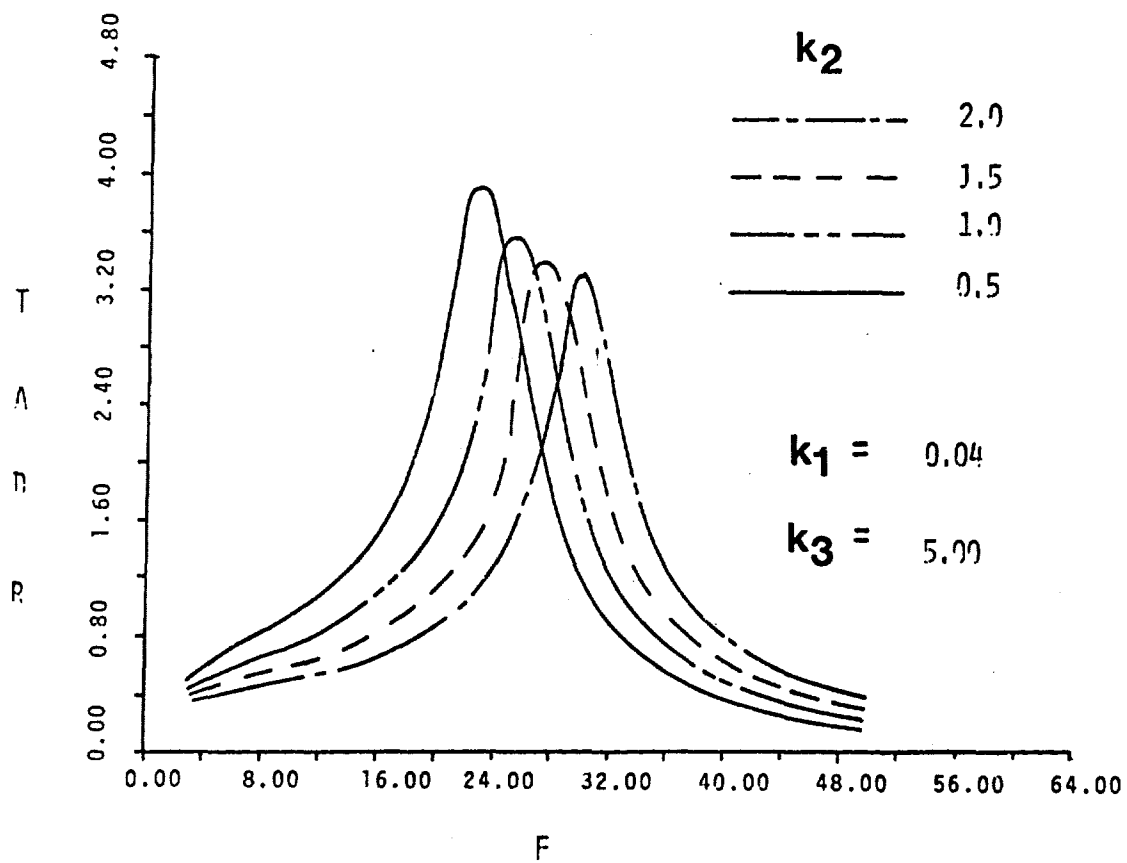


FIGURE 8: Absolute Displacement Transmissibility (TADR) vs Frequency (F) for Four Values of  $k_2$  (0.5, 1.0, 1.5 and 2.0) when  $k_1 = 0.04$  and  $k_3 = 5.00$

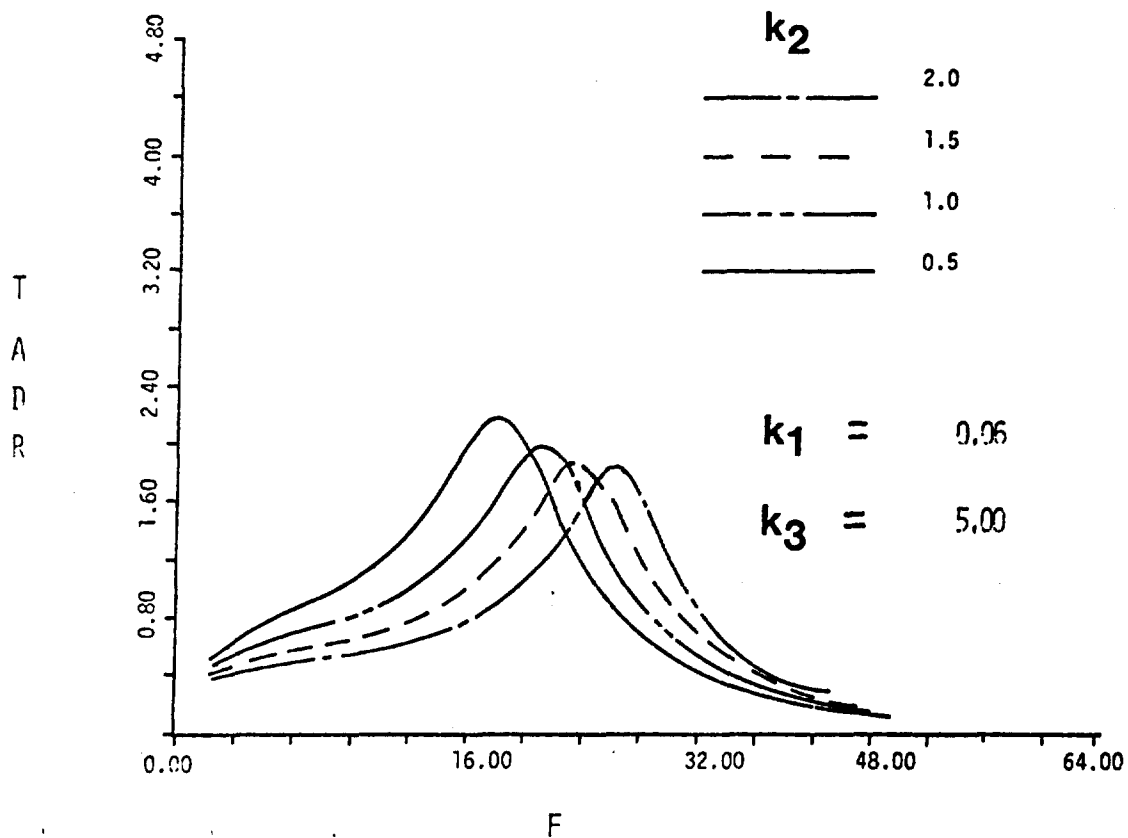


FIGURE 9: Absolute Displacement Transmissibility (TADR) vs Frequency (F)  
for Four Values of  $k_1$  (0.5, 1.0, 1.5 and 2.0) when  $k_2 = 0.06$  and  $k_3 = 5.00$

## REDUCTION OF HYDRAULIC LINE OSCILLATING PRESSURES INDUCED BY PUMP CAVITATION

By George Druhak, Paul Marino, and Murray Bernstein  
Grumman Aerospace Corp.  
Bethpage, New York

A Helmholtz resonator cavitation attenuator was developed to reduce oscillating pressure and resulting vibration induced stresses. Its development, the magnitude of reduction it effected in hydraulic line and bracket stresses, and the analytic procedure to calculate the standing pressure wave induced stresses in hydraulic lines are described.

### INTRODUCTION

Piston pump induced cavitation is an inherent problem in all current aircraft, and its severity increases with higher energy systems. When an aircraft loses hydraulic fluid, the normal ripple pulses caused by the engine driven hydraulic pump are increased significantly, resulting in highly fluctuating pressures that can induce appreciable vibratory motion in critical locations.

The aircraft described in this report has two main hydraulic systems. One is the Combined hydraulic system, which powers the flight control actuators and all the aircraft utilities; and the other is the Flight hydraulic system, which powers only the flight control actuators. Each is a completely independent, closed system powered by a variable volume engine driven pump that can supply 85 gpm at 3000 psi when operating at 5550 RPM. Between the pump and the filter module, each system contains a section of approximately 15 ft of hydraulic line in which the effects of bracket and hydraulic line failures caused by cavitation generally occur. Elements downstream of this section are less severely affected because the filter module acts as an attenuator.

The highly affected sections in each system differ considerably in geometry as well as response to cavitation. In the Combined system (Fig. 1), the affected section shows a violent line response resulting in both line and

bracket failure. The Flight system (Fig. 2) exhibits a low level line response and high bracket stresses.

This paper describes the steps taken at Grumman Aerospace Corporation to reduce the catastrophic effects of cavitation and the analytical studies developed to improve the understanding of the behavior of the two systems during cavitation.

### BACKGROUND

The loss of hydraulic fluid in one of the two self-contained systems, although infrequent, has occurred often enough to be considered a problem. Tests on a hydraulic system simulator have demonstrated that at some point in the loss of hydraulic fluid the pump starts to cavitate. When cavitation occurs, the normal ripple pressure imposed by each piston increases markedly, often by more than an order of magnitude. The fundamental exciting frequency is still at piston frequency, although higher harmonics are present. In our case, the pump had nine pistons operating over a speed range of 3300 RPM to 5550 RPM, thus producing a fundamental exciting frequency of 495-825 Hz. In some instances during the simulation, cavitation of 10 to 20 sec duration was enough to cause failures in the line support brackets. Redesigning the brackets, their support structure, and the adjacent structural areas in order to avoid these failures would require an increase in fatigue life of about  $10^4$ . The necessary redesign would require rework

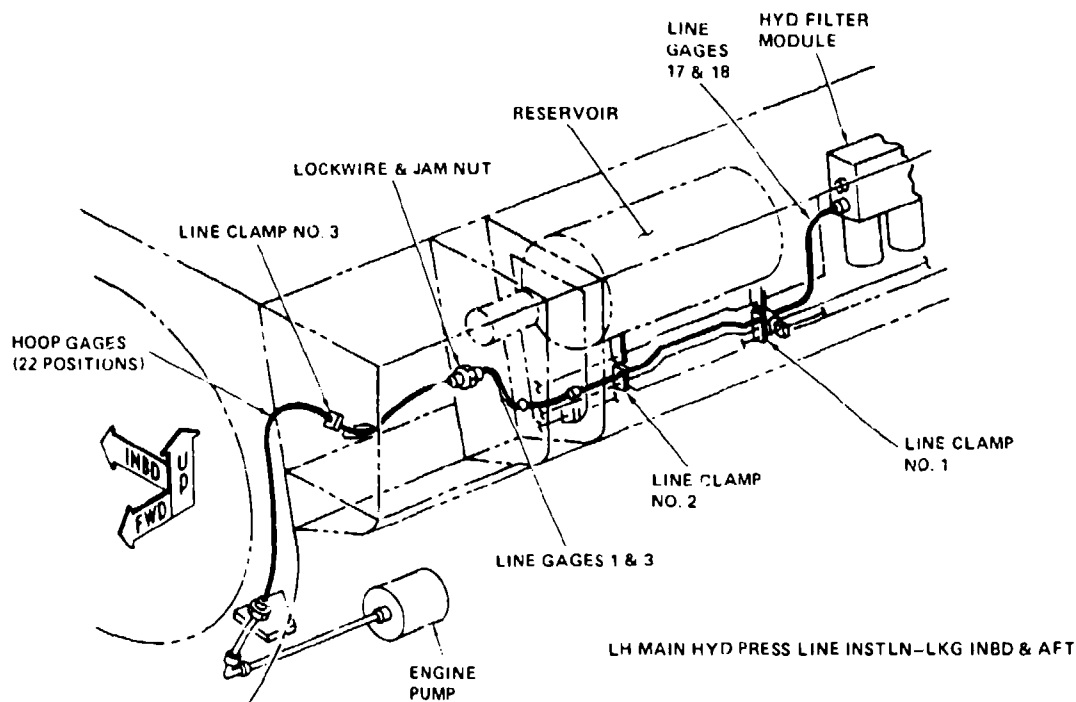


Fig. 1 - Portion of Combined hydraulic system

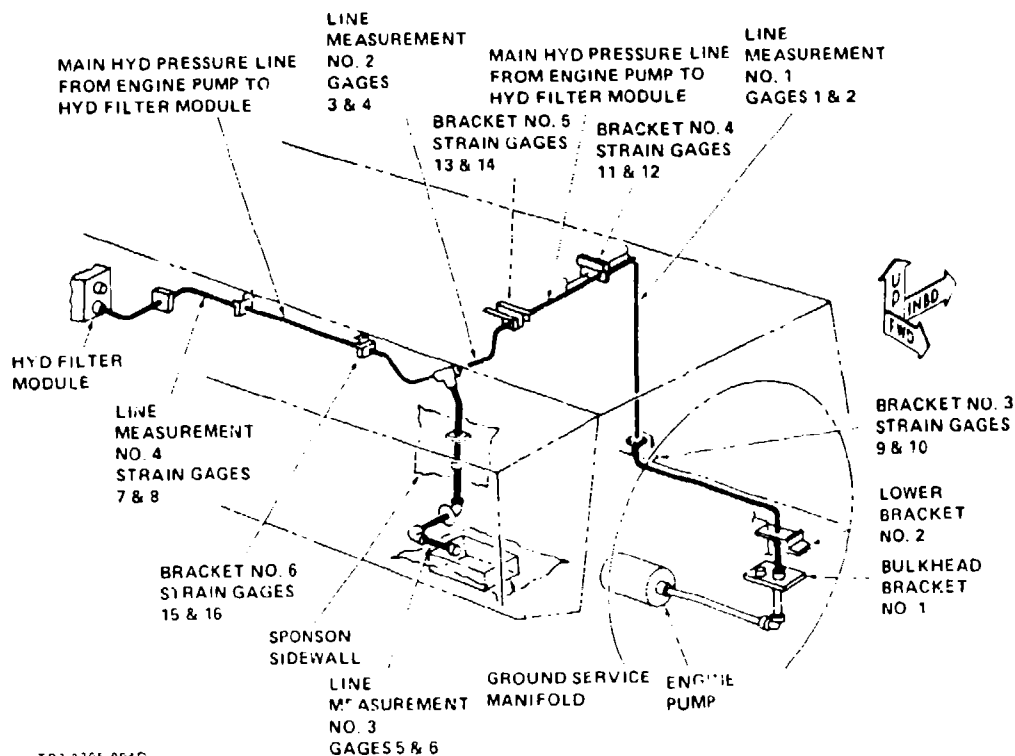


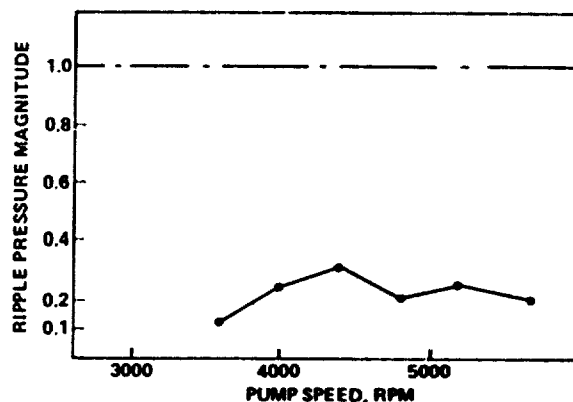
Fig. 2 - Portion of Flight hydraulic system

and then the retrofitting of all aircraft, both very costly. In addition, because in many locations the structural areas are difficult to access, reworking would require substantial time, keeping aircraft out of service for long periods. Therefore, Grumman decided to look for other alternatives to correct the problem.

Grumman previously had done work to reduce the pressure pulsations due to ripple. A commercially available ripple attenuator was installed in both the hydraulic system simulator and in an actual aircraft for ground tests. Stresses were measured at locations considered critical in the pressure line. The effect on stress levels, shown in Fig. 3, included reductions of up to .5; but over the lower portion of the frequency range, the levels actually were slightly higher. In addition, the unit was too large to install in the areas where it was required, and there were difficulties in achieving the required operational integrity. There also was some uncertainty as to the unit's effectiveness under cavitation induced pressure oscillation.

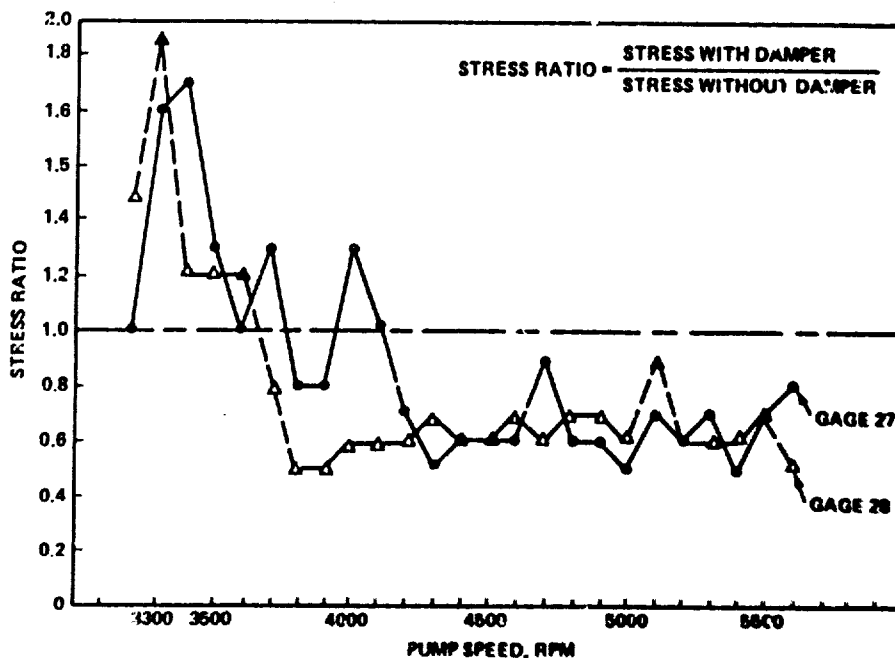
Later, an expansion chamber type of attenuation was investigated on the hydraulic system simulator. A configuration was developed that reduced the pressure ripple mag-

nitudes by as much as a factor of 5 (0.2 of ripple pressure without attenuator), as shown in Fig. 4. This unit also attenuated system response during cavitation. However, the size of the chamber was excessive for the available space. In addition during cavitation the unit interacted adversely with the pump pressure compensation system. Failures occurred in pump compensator springs during some of the tests.



T82-0205-006D

Fig. 4 - Effect of expansion chamber on ripple pressures in Combined system



T82-0205-005D

Fig. 3 - Effect of commercial damper on line stress at input to filter module in Combined system



## ATTENUATOR SELECTION

An analytical study was undertaken at this point to define the most suitable type of attenuator. The information obtained from Ref. 6 was a useful starting point. The analysis was complicated because, unlike conventional ripple attenuators that operate in a homogenous fluid, the cavitation attenuator had to function in a non-homogeneous fluid-air mixture. Important considerations in the attenuator selection process included achieving minimum effect on steady line pressure and flow, high structural integrity, no significant effect on pump service life, and high effectiveness under both normal and cavitating conditions.

Various devices were analytically studied to determine whether they provided a suitable means of attenuating normal ripple and cavitation pulsations. A broad frequency range was adopted as a design requirement in order to provide attenuation during cavitation and ripple throughout the entire speed range of the engine-driven hydraulic pump.

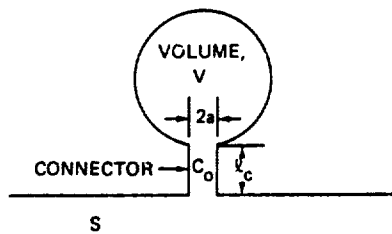
An expansion chamber could provide high attenuation over a large frequency range

during cavitation, but a computer analysis indicated that this installation would have an adverse effect on pump stability. A tuned standpipe could generate high attenuation but only over a very narrow frequency range. An in-line filter provided some attenuation during normal ripple and cavitation modes of operation over a large frequency range. The attenuation was not as large as that provided by the expansion chamber. The drawback of the in-line filter, as well as the other devices discussed, was the difficulty in installing the unit in an existing aircraft system and the effect on line pressure and system flow.

After a review of available devices, a Helmholtz resonator was selected as the most feasible attenuating device. The Helmholtz resonator is normally employed as a narrow frequency band device; but by suitably selecting the characteristic features, it appeared possible to cover an adequately wide frequency range for both normal ripple and cavitating conditions. The design parameters for the attenuator are shown in Fig. 5. The size of the Helmholtz resonator permitted it to be installed at the outlet port of the hydraulic pump. This location is considered the optimum since it provides for attenuation of pump pulsations immediately exiting the pump.

### ATTENUATOR - BRANCH TYPE

#### GENERAL CONFIGURATION & CRITICAL PARAMETERS

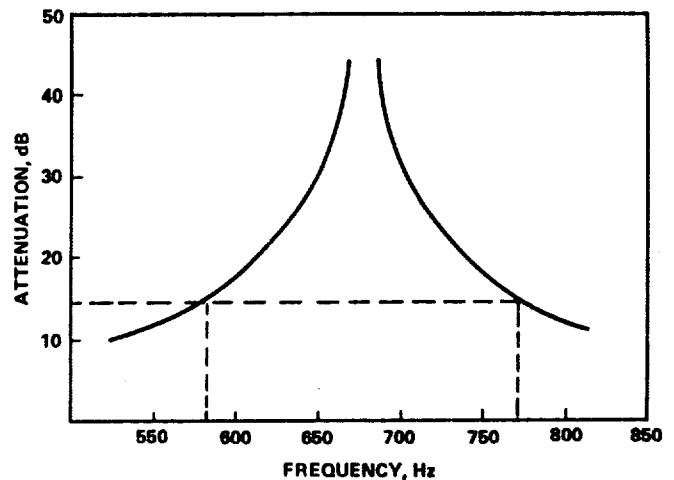


- V = VOLUME OF RESONANT CHAMBER
- a = RADIUS OF CONNECTOR
- $l_c$  = LENGTH OF CONNECTOR
- S = CROSS-SECTIONAL AREA
- $C_o$  = CONDUCTIVITY OF CONNECTOR
- $\beta_a$  = EMIRICAL CONSTANT (BETWEEN  $\frac{\pi}{2}$  AND  $\frac{\pi}{4}$ )

#### GENERAL EQUATIONS

$$\text{ATTENUATION} = 10 \log_{10} \left[ 1 + \left( \frac{C_o V}{2S} \frac{f - f_r}{f_r f} \right)^2 \right]$$

T82-0205-007D



(REFERENCE: NACA RPT 1192, 1952, REF 6)

$$C_o = \frac{\pi a^2}{l_c + \beta_a}$$

$$f_r = \frac{C}{2\pi} \sqrt{\frac{C_o}{V}}$$

- $f_r$  = RESONANT FREQUENCY
- $f$  = FREQUENCY
- C = VELOCITY OF SOUND

Fig. 5 - Design parameters for Helmholtz resonator

## ATTENUATOR TESTING

Initially there was an uncertainty about the applicability of the attenuator design formulas, which are based upon air as the fluid medium, to hydraulic line operation under normal and cavitating conditions. Therefore, the attenuator was fabricated with inserts to permit varying the tuning by modifying the connection geometry, and several configuration variables were tested during the program.

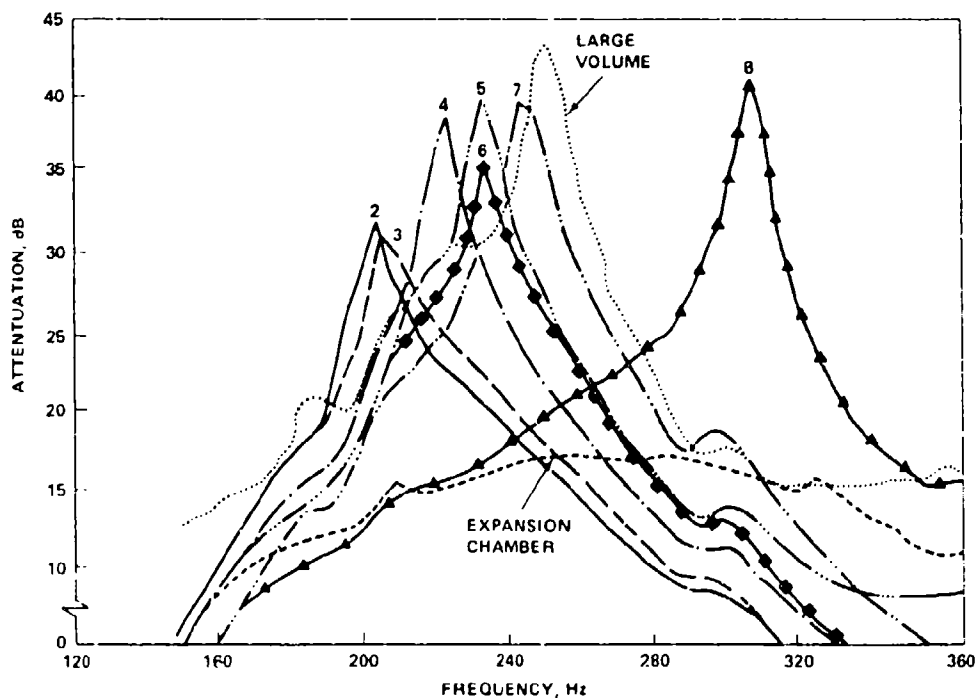
Prior to the installation of the attenuators in the hydraulic system simulator, acoustical characteristics of each configuration were measured in air and compared to the calculated values. The testing was conducted on a modified acoustical standing wave apparatus consisting of two straight tubes with a speaker that was located at one end and that generated a constant frequency noise signal. The attenuator was placed between the tubes. A microphone was used to record the peak noise measurement in the tubes on either side of the resonator. A fiberglass termination was utilized to minimize reflected waves. Typical measured attenuation curves for various designs, including an expansion chamber, are shown in Fig. 6.

The significant geometry for these attenuators is shown in Table 1. The attenuator design is sensitive to the dimension of the connection, which is part of a manifold having instrumentation ports; so determining the effective geometry is difficult except by test.

An available aircraft hydraulic simulator was adopted for the test as shown in Fig. 7. The hydraulic line runs and supporting brackets duplicated the aircraft installation from the pump to the filter module. Pump pressures, line accelerations and strains, and bracket

TABLE 1  
Attenuator Geometry

Config- uration	Volume m <sup>3</sup>	Throat Diameter m	Throat Length 4	Frequency Of Peak Hz
2	.00044	.0139	.0139	205
3	.00044	.0144	.0139	205
4	.00044	.0158	.0155	225
5	.00044	.0158	.0155	235
6	.00044	.0165	.0102	235
7	.00044	.0158	.0102	245
8	.00044	.0165	.0191	310
Large Volume	.00069	.0208	.0191	245



YB2-0205-0086

Fig. 6 - Comparison of resonator attenuations in air

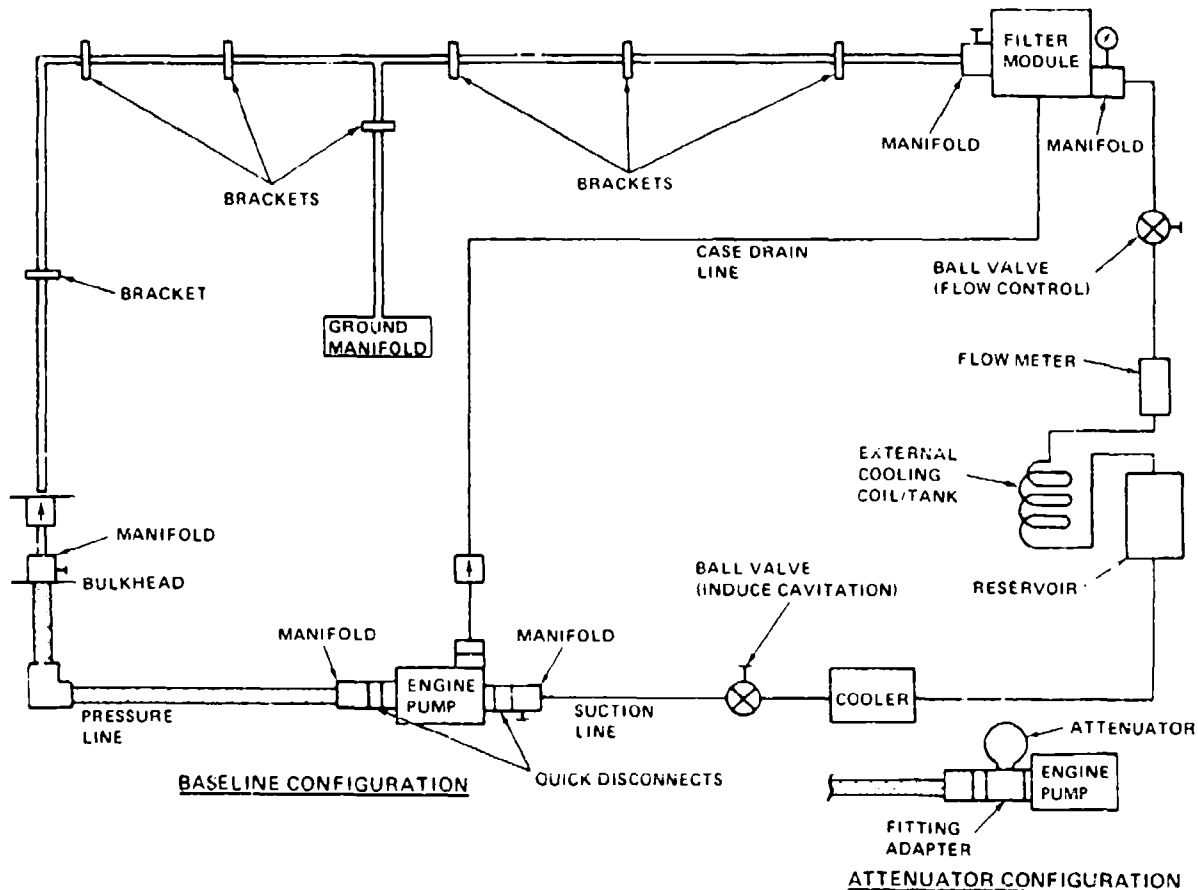


Fig. 7 - Flight system test setup

strains were measured in order to determine the effectiveness of the resonator throughout the frequency range. Pressure, temperature and flow parameters were monitored in an effort to provide a method of verifying capability over the entire speed range of the engine-driven hydraulic pump. Manual flow control valves were utilized to induce the cavitation mode of operation, rather than an actual depletion of the hydraulic system during each test run. A series of baseline runs was made to determine the pump speeds that generated the highest peak stresses during normal system operation. Five critical pump speeds were selected on the basis of producing the highest system response. These speeds were then used when cavitation was induced to determine the performance of the attenuator.

The first series of cavitation runs was performed to determine the tuning of an optimum attenuator that would provide the greatest reduction of destruction energy over the entire speed range. The pump was

stabilized at a selected RPM and the ball valve in the suction line was gradually closed until cavitation occurred. This condition was maintained while stress readings were obtained from the various gages.

During the course of these investigations, it was noted that the Flight system stress variation with attenuator configurations was appreciable at a pump speed of 5550 RPM but did not change significantly at 3850 RPM. The magnitude of the system response at the lower RPM imposed higher-than-desirable stresses at several bracket locations.

It was decided to increase the peak attenuation in order to reduce the stresses at the lower frequency by increasing the spherical volume of the attenuator. Acoustical tests in air of the larger volume attenuator showed a broadening of the characteristic attenuation curve but not a large increase in the peak attenuation. Figure 8 shows a comparison between the theoretical frequency band cal-

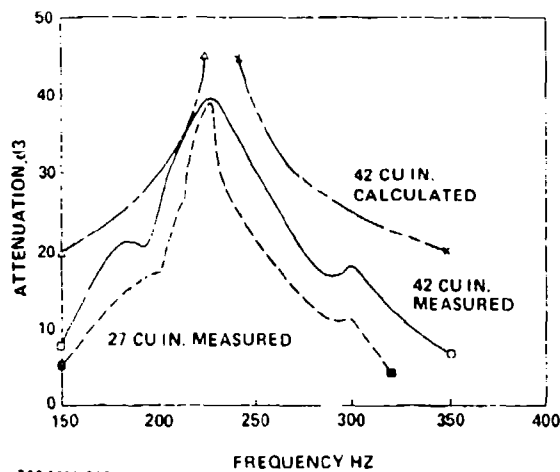


Fig. 8 - Comparison of calculated & measured attenuation in air

culated for the 42-cu.-in.-volume attenuator and the measured values for the 27-cu.-in.- and 42-cu.-in.-volume attenuators. The plot shows the increase in attenuation gained at the low end of the frequency range by increasing the volume. At a frequency of 190 Hz the level of attenuation for the new volume was 22 dB level compared to 16 dB level for the old volume. This type of improvement was typical over the entire frequency band. The attenuator was also designed to provide a connection for external hydraulic power during ground maintenance. This is most likely the cause of the non-linearities in the measured values.

Simulator results using this attenuator showed a general reduction in system stress levels at all pump speeds, with the smallest reduction occurring at 3850 RPM. A review of the hydraulic line geometry indicated that the segment leading to the dead-ended manifold used during ground servicing could be the source of a hydraulic resonance close to the pump ripple value at 3850 RPM. In an effort to move the line frequency out of the low range, a 1-in.-dia by 10-in.-long pipe was added to the ground manifold pressure port. The stresses as generated from this test run showed an increase in bracket stresses at 3850 RPM and a decrease at 4450 RPM. The assumption made was that the internal passages in the ground manifold were distorting the results. There is a mechanical connection in the ground service line 12 in. from the tee to the main line. The ground service line and the manifold were removed and replaced by a 1-in.-dia by 24-in.-long pipe that yielded the same overall length to the ground service line

as adding the 10-in. pipe to the manifold. The stresses recorded from this test run showed approximately a 35% reduction in bracket stresses at 3850 RPM. In order to establish whether removal of the ground service line would reduce the stresses, the 24-in pipe was removed and the 12-in. length of pipe teed off the main pressure line was capped. The stresses recorded during this test run showed no reduction over the original configuration with the ground service line and manifold installed.

The results of some of the testing performed are shown in Fig. 9 and 10 for the Combined hydraulic system and in Fig. 11 for the Flight hydraulic system. The curves illustrate the impact that the attenuator has on reducing the oscillating pressure stresses in the bracket supports and the hydraulic lines in the two systems during cavitation. Hoop stresses were measured as a convenient method of determining pressures over a line segment.

#### DATA ANALYSIS

One problem encountered during the analysis was that the maximum response at the various locations occurred at different pump frequencies. Furthermore, the highly unsteady nature of cavitation produced a large scatter in the data. This problem is illustrated in Fig. 12, which shows the measured stress as a function of pump frequencies at two bracket locations. This condition was compounded by the additional measurements made at other line and bracket locations. These variations in frequency response and large data scatter made it difficult to determine the tuning and effectiveness of the attenuator configurations under test.

Since we desired to reduce the stresses in the entire system, we reasoned that a mean system stress would be indicative of an attenuator's performance at a given frequency.

To obtain the mean system stress, we repeated the cavitation conditions six times at each of five different pump speeds and measured the stresses at various bracket and line locations. Next we calculated and tabulated the mean stress at each location as shown in Table 2. The mean system stress was obtained from the summation of the individual line and bracket mean stresses at each frequency. These mean system stresses were plotted as a function of pump RPM for the various attenuator configurations. The

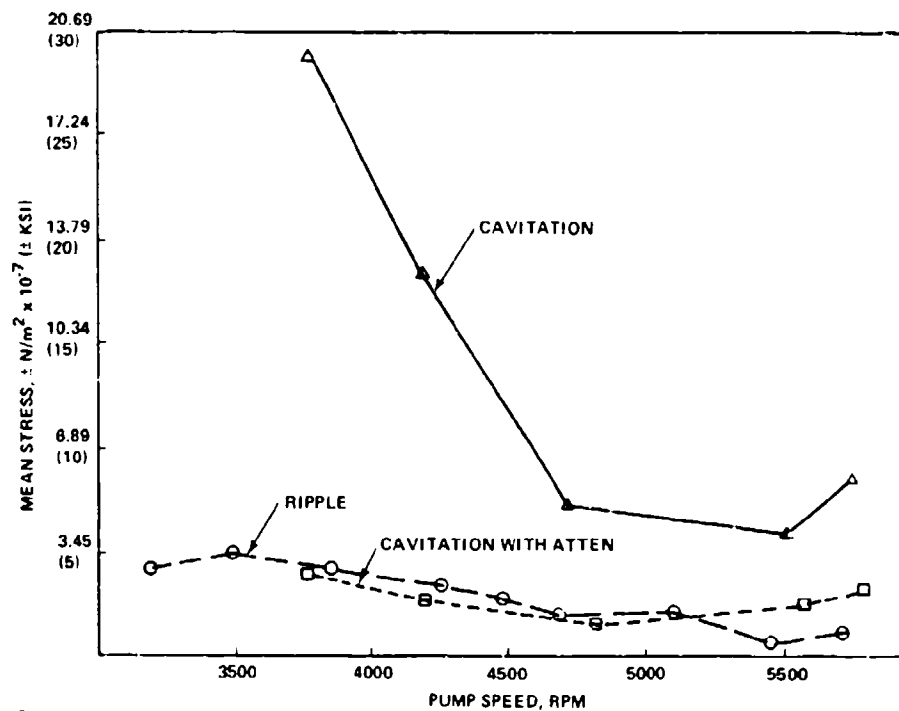


Fig. 9 - Comparison of maximum line stress. Combined system

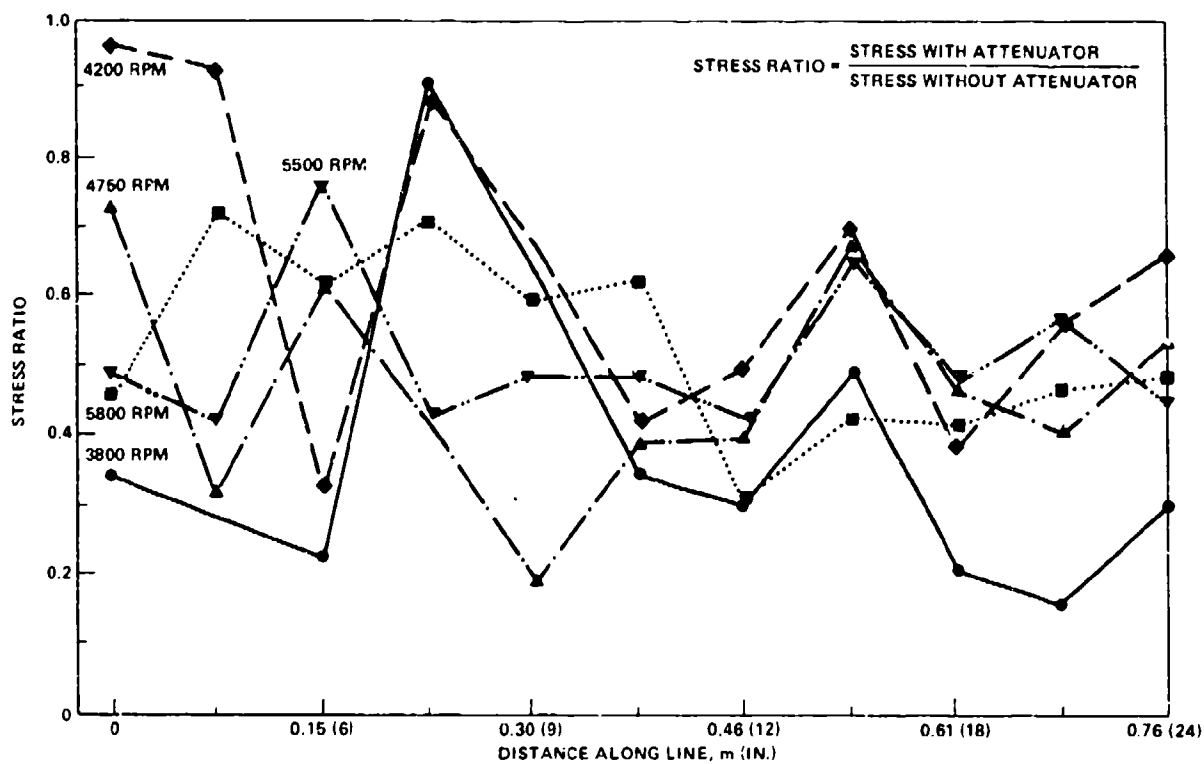


Fig. 10 - Reduction of hoop stress along line by attenuator No. 2. cavitation, Combined system

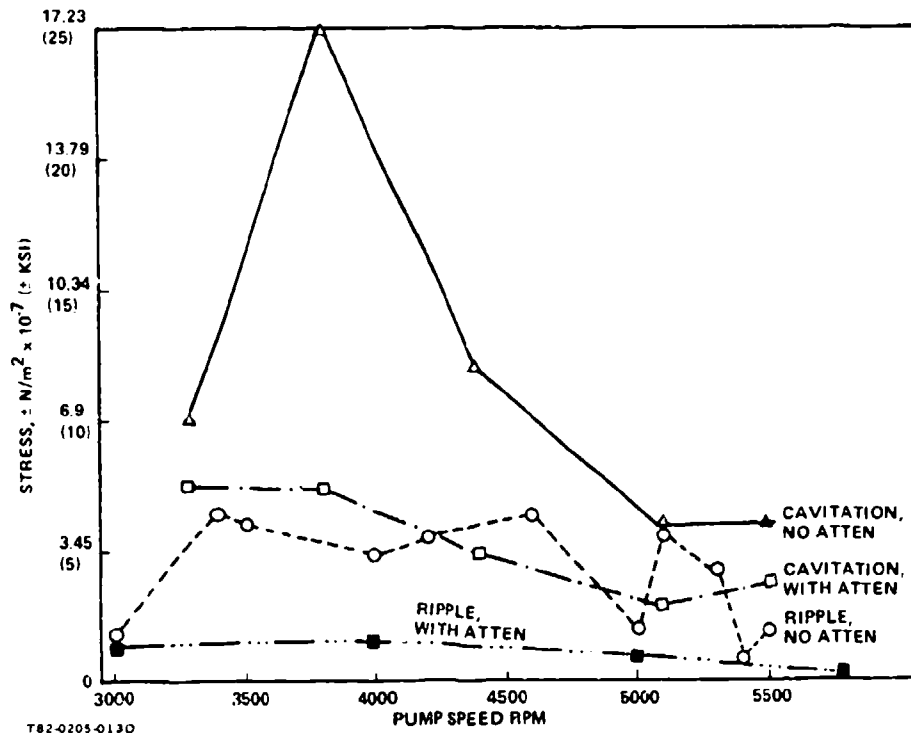


Fig. 11 - Bracket No. 3 stress reduction, Flight system

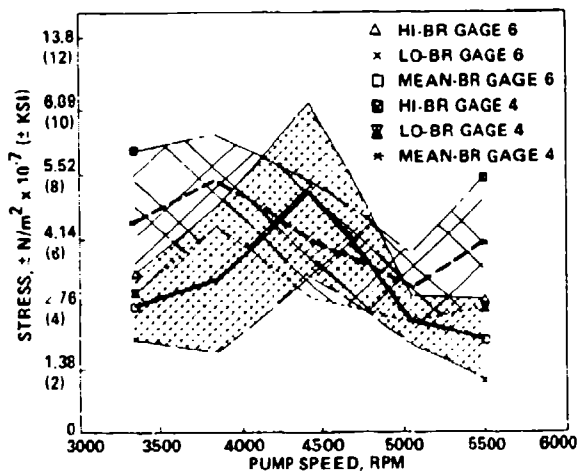


Fig. 12 - Bracket stress at two locations vs pump RPM, Flight system, cavitation with attenuator

attenuators are identified by their resonant frequency in air. Figure 13 shows the mean system stress for the Flight hydraulic system.

In addition to determining the behavior of each attenuator as a function of pump frequency, we wanted to determine the attenuator configuration that would provide the most

effective stress reduction over the entire operating range of pump speeds.

For this purpose we developed the "grand mean." This grand mean was obtained from the summation of the system means at the five test frequencies.

Figure 14 shows the grand mean for the Flight system as a function of attenuator resonant frequency in air. The data indicates that the optimum frequency was 280 Hz for the Flight system and 208 Hz for the Combined system.

#### ATTENUATOR TEST RESULTS

After the selection of the optimum attenuator, the final phase of testing was undertaken. This involved running the entire hydraulic system and cavitating for prolonged periods of time. The first series of tests had determined the optimum attenuator tuning for each system. Installation considerations indicated a common attenuator for both systems. Thus, a compromise resonator with a resonant frequency of 245 Hz was fabricated and used during the second series of tests.

The goal of this second test series was to survive 4 hr of cumulative cavitation and maintain the system intact.

TABLE 2  
Flight System Stress With Attenuator

Gage Location	3350 RPM		3850 RPM		4450 RPM		5050 RPM		5500 RPM	
	Mean	STD Dev	Mean	STD Dev	Mean	STD Dev	Mean	STD Dev	Mean	STD Dev
LINE 1 1	11017	2506	11721	2482	4302	717	5377	958	6150	1158
LINE 2 1	11817	3847	8714	2751	6646	1916	12210	5819	9942	2371
LINE 2 2	8197	1647	7563	1771	8921	2254	7818	1537	15292	2985
LINE 3 1	10978	503	14154	2999	6770	1744	7563	1771	10438	1999
LINE 3 2	8078	2992	10762	3337	4847	1144	11272	2235	8970	3371
LINE 4 1	11121	2261	13106	2309	10473	889	13299	2309	16195	3523
LINE 4 2	17802	5343	11700	1882	8866	1061	11438	3171	9893	310
BRKT 4 1	14844	4550	16299	1634	9638	958	9563	1627	12775	1275
BRKT 4 2	45112	7577	54027	4367	41403	6191	31067	3640	40789	6805
BRKT 5 1	18367	2578	12700	2220	10866	1144	14306	979	15533	2433
BRKT 5 2	23649	6012	14003	1978	12320	1516	17678	2509	14003	2316
BRKT 6 1	27089	3433	32932	7680	51275	9590	24255	2502	20125	4240
BRKT 6 2	49821	11279	50738	12045	29612	1985	20049	3378	26400	3488
System Mean	19837		19871		15842		14300		15885	
Grand Mean 17147.										

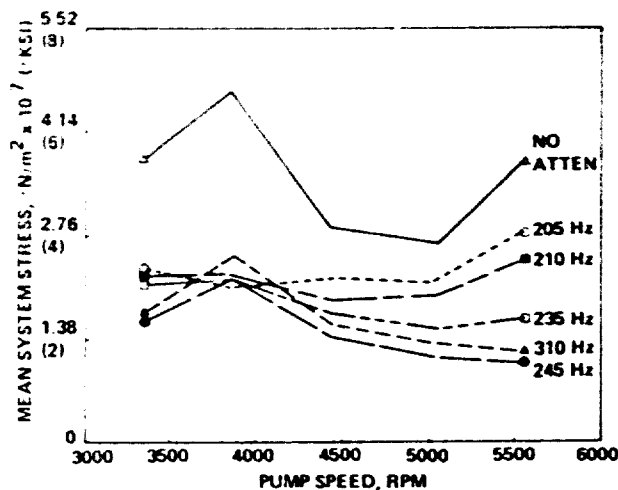


Fig. 13 - Flight system mean stress (all gages) vs pump RPM

The testing established the feasibility of utilizing an attenuator in a hydraulic system in order to attenuate cavitation pulsations. The hydraulic line and bracket stresses recorded throughout the testing consistently verified the reduction in stress levels when using the attenuator. In addition, throughout the testing visual evidence confirmed the effectiveness of the attenuators. During the test runs, without the attenuator installed, jam nuts on bulkhead fittings loosened, line clamp screws sheared, hydraulic line brackets cracked, and plastic hydraulic line support blocks melted. These conditions occurred after less than 20 sec of cavitation.

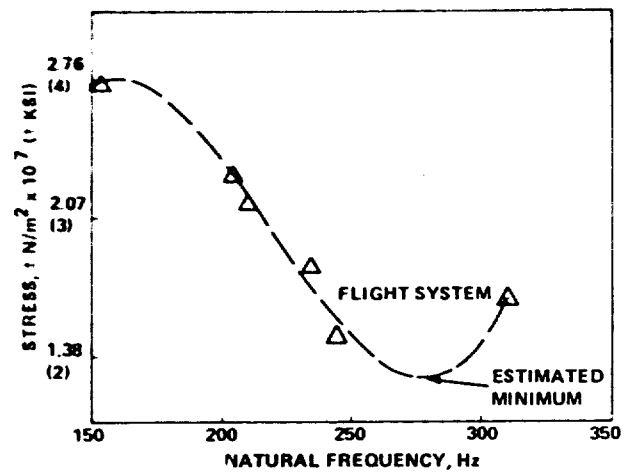


Fig. 14 - Grand mean stress vs attenuator natural frequency

The Combined hydraulic system successfully completed 4 hr of cavitation with the attenuator installed without damage to lines, brackets, and line support blocks. The Flight hydraulic system completed 4 hr of cavitation without damage to lines and line support blocks. However, at 3850 rpm, bracket No. 4 (Fig. 2) cracked several times during the testing. A material change was instituted for this bracket and an additional 2 1/2 hr of cavitation was run without failure.

The addition of the attenuator established a means of reducing the damaging pulsations generated during cavitation at the pump outlet without compromising the hydraulic system.

## LOADS PREDICTION PROGRAM

Concurrently with the development of the attenuator, an analytical procedure was developed to calculate line and bracket loads caused by standing hydraulic pressure waves. The results of this analysis were intended to provide the design engineer with criteria to be used during the routing of hydraulic lines and the location of line supports to minimize system stresses.

The attenuator development program using an aircraft hydraulic system simulator afforded an opportunity to obtain data to verify analytical results. The concepts used in the program are described below.

## LOAD CALCULATION

Pressure standing waves in hydraulic lines can be determined from impedance analyses as described in Ref. 1 and 2. These induce radial forces at the location of bends. The forces on the fluid include the reaction of the pipe bend as shown in Fig. 15 (Ref. 3).

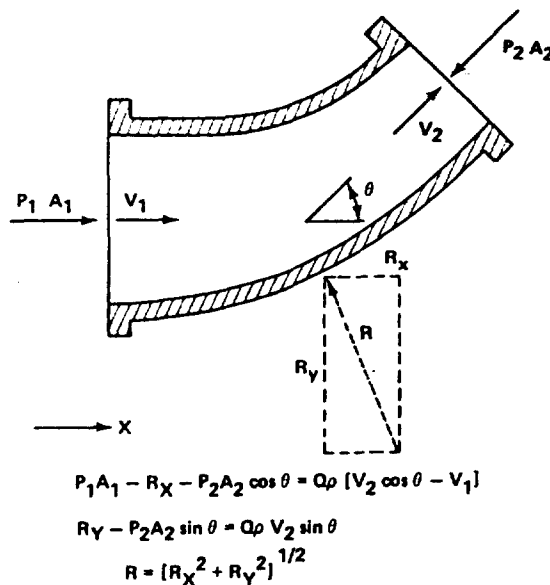
Considering any bend in a pipe of constant cross-sectional area, the radial component of fluid pressure variation and flow velocity is reacted by the pipe bend, while the tangential component is reacted principally by the changes in fluid momentum and does not result in loads on the pipe. The procedure for calculating the fluid induced loads therefore, is based upon determining the radial

component for each hydraulic line segment from the geometry. In aircraft hydraulic lines, this geometry is often quite complex, so that a description of the pipe bends is most readily obtained from detailed finite element grid point locations. Every set of three successive grid points can be considered as describing a bend in the line. The three points are assumed to define the geometry, the first two being the direction of the fluid entering the bend and the second and third the direction of the fluid leaving the bend. Since these three points lie in a plane, and the change in direction of the fluid flow in that plane is required, the coordinate transformation from the global geometry of the grid point system to a local coordinate system in the plane of the bend is determined.

## CALCULATED VIBRATORY RESPONSE OF HYDRAULIC LINES TO PRESSURE STANDING WAVE

After the coordinates are transformed into a single plane, a radial component of the load assumed to act at the middle grid point is calculated as follows:

- The angle between the radial input and output directions is calculated as shown in Fig. 16
- The radial force components due to the standing wave pressures at the first and third grid points are calculated and resolved into orthogonal forces



### LEGEND

P	=	PRESSURE
A	=	FLUID AREA
$V_1, V_2$	=	FLUID VELOCITY
$\rho$	=	FLUID DENSITY
Q	=	FLUID VOLUME VELOCITY
R	=	REACTION FORCE OF PIPE ON FLUID

T82-0205-017D

Fig. 15 - Forces on fluid in pipe (from Ref. 3)



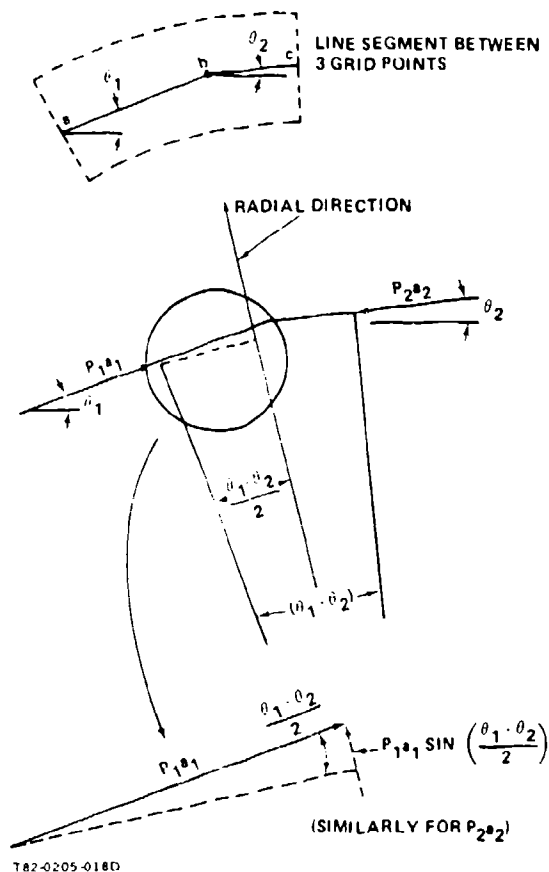


Fig. 16 - Radial component of fluid pressure on pipe bend

- The forces are translated back into the global coordinate system using the inverse of the transformation previously determined.

This procedure for calculating loads at each grid point in the global coordinate system is the algorithm used in a FORTRAN program that generates input cards for the NASTRAN finite element model loads analysis.

#### APPLICATION TO A 90 DEGREE BEND

In an effort to evaluate this procedure on a relatively simple structure, it was applied to a 52-in.-long segment of a 1-in. OD by .051-in.-thick wall titanium pipe bent into a 90° elbow, for which experimental data had been reported in Ref. 4. The pressure standing wave distribution assumed in this analysis is shown on Fig. 17 for comparison with measured values. The difference is due to the simple sinusoidal expression used in the computer algorithm for load calculation. The applied loads calculated are shown on Fig. 18. As anticipated, loads occur only at the bends in the plane of the bend. The calculated mode shapes for a NASTRAN finite element model of the configuration with ends fixed are shown on Fig. 19. It is apparent that the in-plane and out-of-plane modes alternate. These two types of motions are not coupled if all the grid points lie in a single plane. However, the accelerations for this configuration reported in Ref. 4 contain both in-plane and out-of-

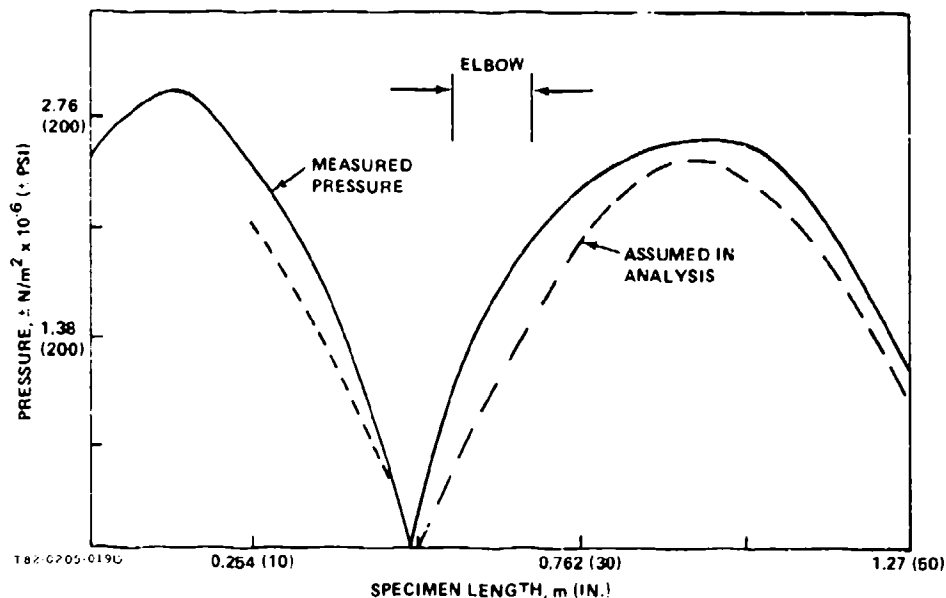
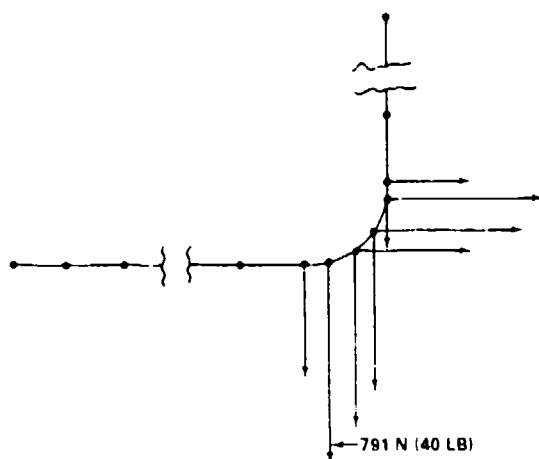


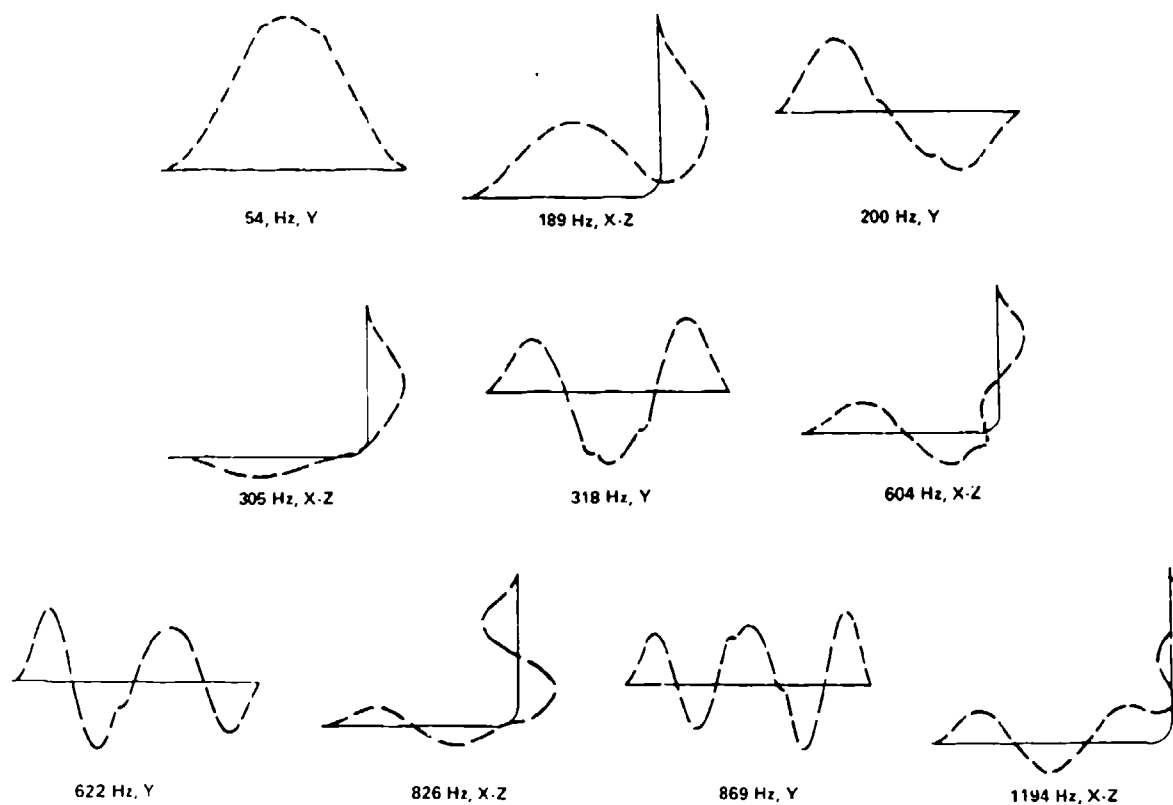
Fig. 17 Pressure standing wave in 90 deg bend



T82-205-0200

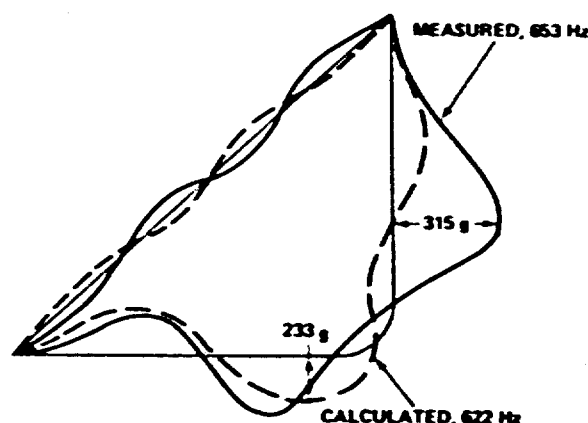
Fig. 18 - Loads due to pressure standing wave, 90 deg bend line finite element model

plane motion. When the finite element geometry is varied by introducing a slight, gradually varying, out-of-plane position to the grid points (.25 in. at the elbow), some coupling of the motion in the two directions occurs. The measured responses from pressure standing waves (from Ref. 4) are compared with those calculated for modes with similar characteristics (Fig. 20). The measured deformation at 653 Hz is similar to the calculated acceleration pattern at 622 Hz, which is also shown. The calculated pattern is more symmetrical since both legs of the elbow have a central node unlike the measured response, where only one leg has a point of no vibratory motion. The out-of-plane motion for both measured and calculated motions have 3 node points each, but those in the measured data are unevenly spaced. The calculated maximum acceleration for an assumed damping ratio of .05 of critical was 250 g compared to 315 g measured.



T82-205-0210

Fig. 19 - Mode shapes for 90 deg bend pipe. Y = out-of-plane, X-Z = in-plane motion



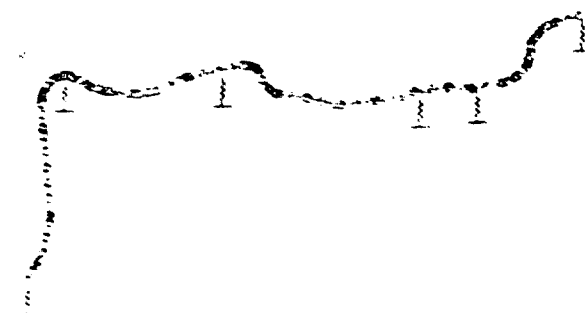
T82-0205-0220

Fig. 20 - Comparison of calculated and measured response for line with 90 deg bend

A major discrepancy between analysis and measurement is the difference in calculated modes for the line. Several attempts were made to vary the support stiffness at one end of the line in order to try to improve the match, but no significant increase in the correlation was noted. A review of the results showed that improvement would be required in the finite element model representation, but the method of calculating the loads appeared to result in responses that gave a moderately good approximation to measured values.

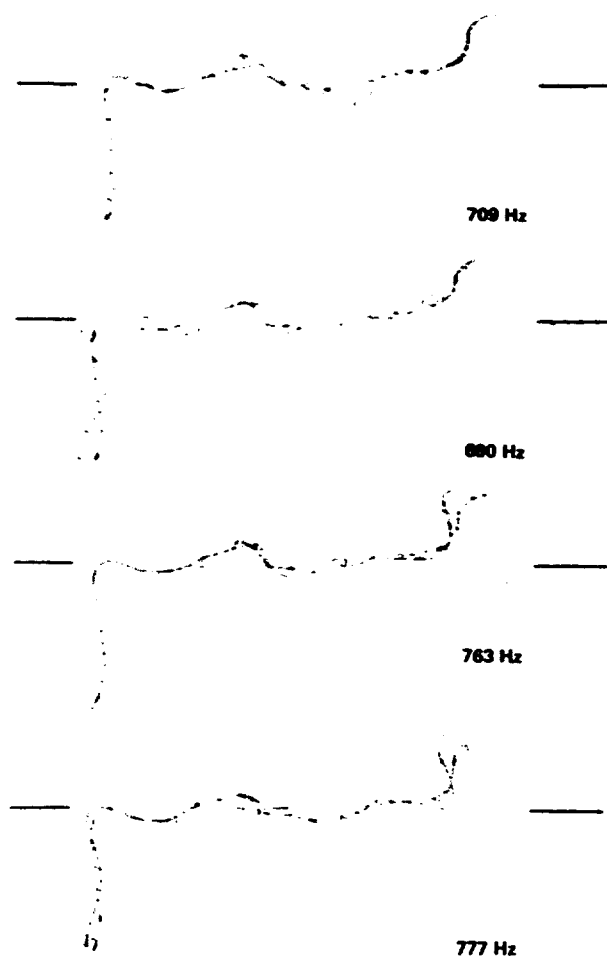
#### APPLICATION TO AIRCRAFT HYDRAULIC LINES

The basic reason for developing the standing pressure wave loads analysis described previously was to calculate the vibratory response of aircraft hydraulic lines. Figure 21 shows the Combined hydraulic system's finite element model of the titanium line between the pump end flex hose and the filter module (about 120 in. downstream of the flex hose). The location of supporting brackets are shown as springs. The right end representing filter module attachment was assumed fixed. The flexibilities of the 5 remaining brackets were calculated from simplified structural models. The calculated resonant frequencies ranged upward from 113 Hz. The frequency range of interest lies between 495 and 825 Hz, corresponding to 3300 to 5500 pump rpm. There were 11 elastic modes below this range and 8 elastic modes within it. The mode shapes become relatively complex. Several are shown on Fig. 22. An attempt was made to measure some of the modes and reconcile



T82-0205-0230

Fig. 21 - Finite element model, Combined system



T82-0205-0240

Fig. 22 - Combined system mode shapes

the measured and calculated values by varying the bracket stiffnesses. However, this was not very successful. We could make one mode match well, but others would not correspond. More work is required on this aspect of the problem.

The standing waves of pressure on the line segment due to pump ripple were calculated for the three hydraulic resonances using a modification of Ref. 1. Typical standing wave magnitude pressure patterns are shown on Fig. 23. They represent an effective acoustical velocity of about 3800 ft/sec. The pressure values for the lowest two frequencies are lower for the first portion of the line because of the influence of the flex hose. The pressure at zero location is at a peak and represents the pump output. The pressure at the 152-in. station is a minimum because the filter module is considered as representing a low acoustical impedance. The calculated magnitudes for ripple pressure were much higher than the values measured at the pump output, and the peak frequencies were slightly different, as

shown in Fig. 24. It was decided to adopt the pressure distribution as calculated but limit the amplitudes and frequencies to the measured values. The calculated relative distribution of maximum stress along the line is shown on Fig. 25. The relative stresses at one of the highest stress locations in the line, as a function of the pump frequency, is shown in Fig. 26, along with the measured stress levels at a similar location. The absolute values of the measured levels are considerably below the calculated values even though a relatively high (.3) value of damping was used. Although the agreement between measured and calculated values requires improvement, the variation of stress along the line length appears reasonable. During several instances when cavitation induced very high stresses, the failures occurred in the line close to the location where the calculated value was the highest.

A finite element model of the Flight hydraulic system between the pump flex hose and filter module, shown in Fig. 27, was also

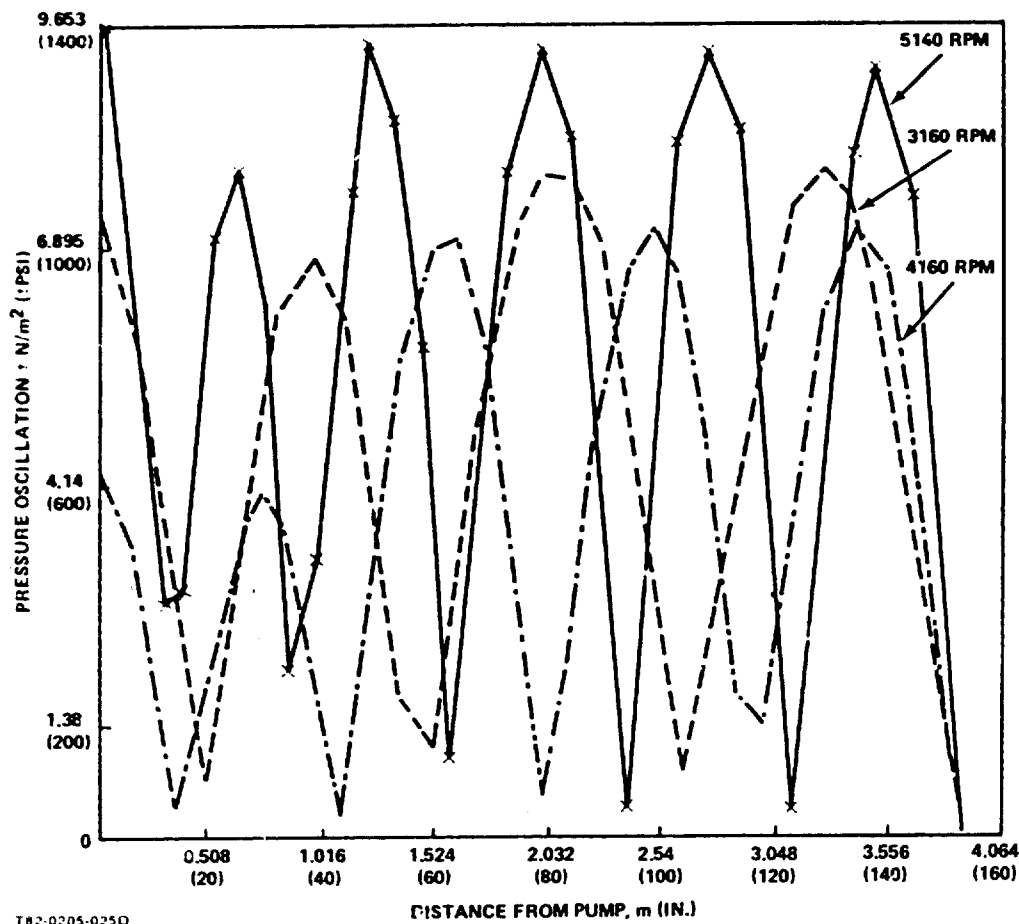
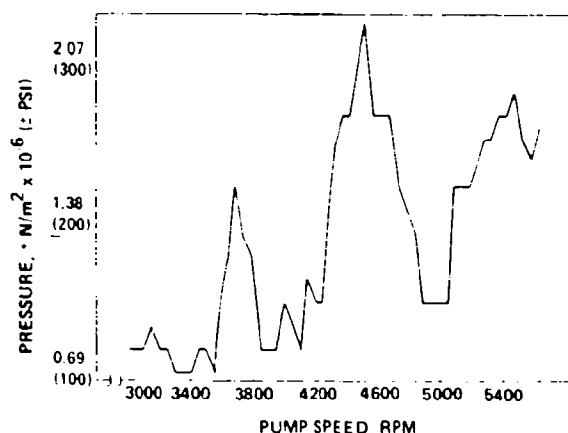
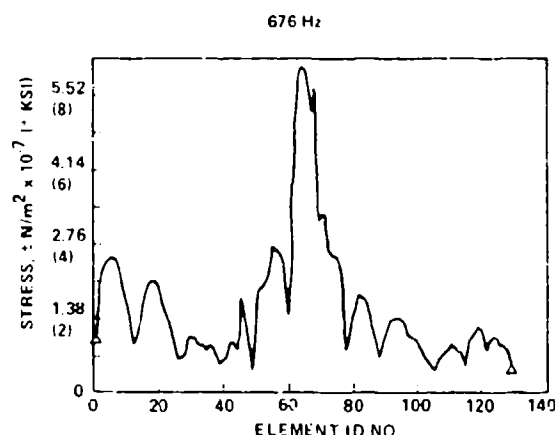
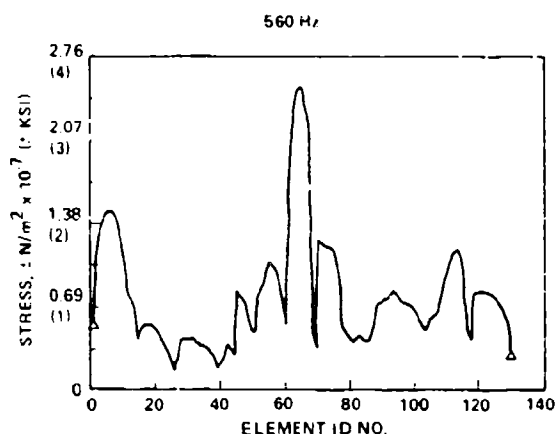


Fig. 23 - Pressure standing wave, Combined system



162-0205-02-00

Fig. 24 - Measured ripple pressure at Combined system pump output



162-0205-02-00

Fig. 25 - F-14 Combined system stress distribution (Note: Line free in rotation at filter module for this calculation)

assembled and analyzed in the same manner to assist in guiding test results. The comparison between calculated and measured stress shown in Fig. 28 for one location checked was considered good both in distribution and in magnitude.

The effect of temperature on calculated stress can be determined from the variation in calculated standing pressure waves shown in Fig. 29. A rise in temperature of 100° F (from 80 to 180° F) resulted in an increase in maximum pressure of 1.5 and a drop in resonant frequency to .91. The effect on the standing wave pattern was not very significant nor was the shift in resonant frequency, considering the limited accuracy in measurements; but the change in amplitudes was significant. Temperature readings were therefore taken during all test runs to allow corrections when required.

## SUMMARY

The testing accomplished to date has shown that it is highly beneficial to have a hydraulic system simulator that faithfully duplicates aircraft line runs and line supports in that section of run between the pump and the filter module. Aircraft problem areas are duplicated on the simulator and can be tested more expeditiously and economically on the simulator.

These same tests have shown that it is possible to develop a cavitation attenuator to reduce system stress. System non-linearities and the non-uniform nature of cavitation make it difficult to assess the tuned frequency response of an attenuator so that maximum performance can be obtained.

The analytical program satisfactorily predicts the locations of the maximum line loads; however, additional effort is required before the load magnitude can be predicted.

## FUTURE EFFORT

The work described is part of an on-going effort to better understand and survive a cavitating system environment. Additional testing is currently scheduled on an aircraft to verify the attenuator performance obtained on the simulator.

It is planned to continue the development of the analytical program to obtain improved load prediction and improved prediction of mechanical resonances. Modifications are also planned to the internal flow program to correct the excessive peak pressures in standing waves and to improve our pump cavitation model.

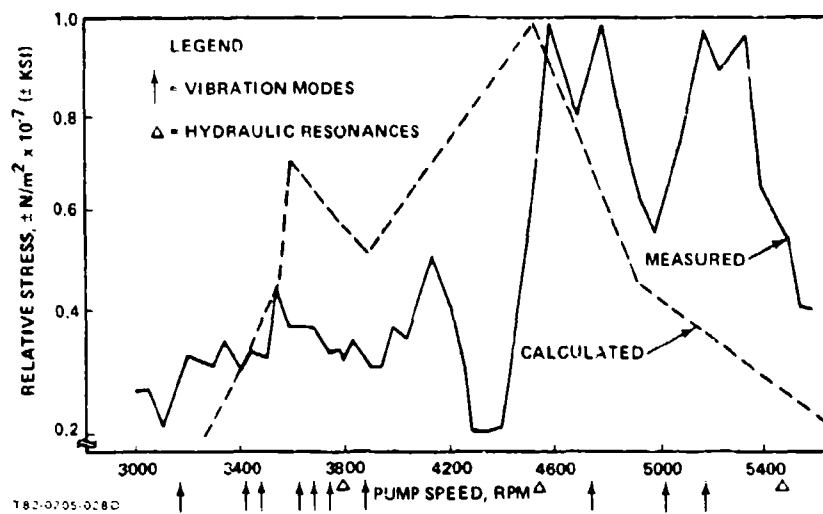
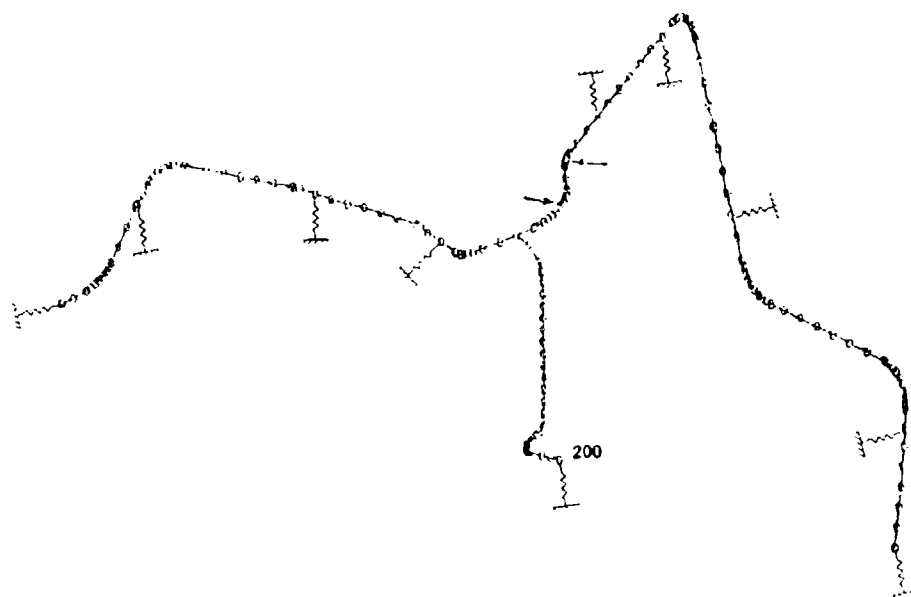


Fig. 26 - Measured & calculated relative stress for Combined system



182-0705-0290

Fig. 27 Finite element model, Flight system

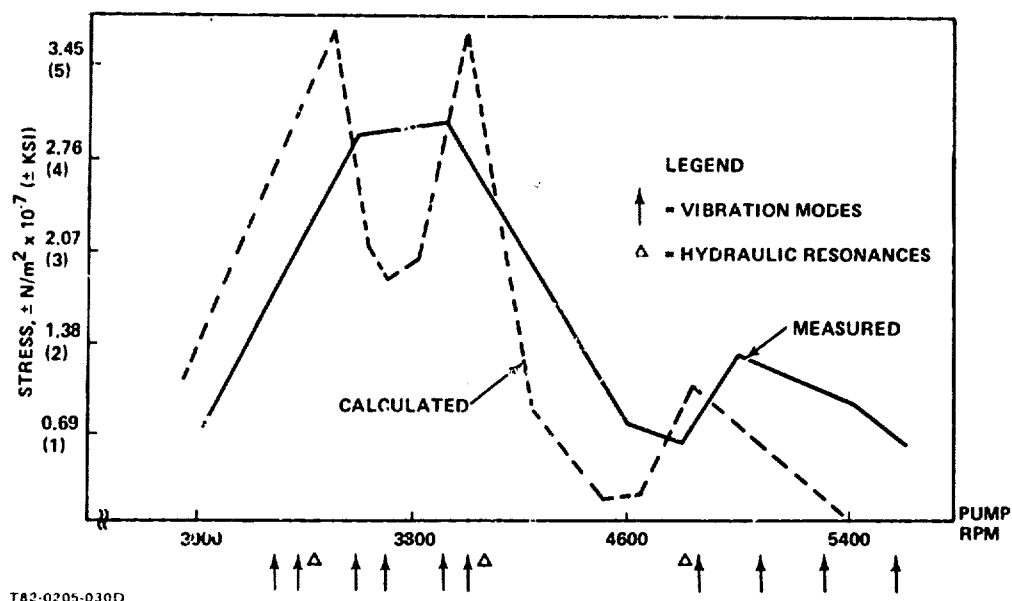


Fig. 28 - Measured & calculated stress, Flight system

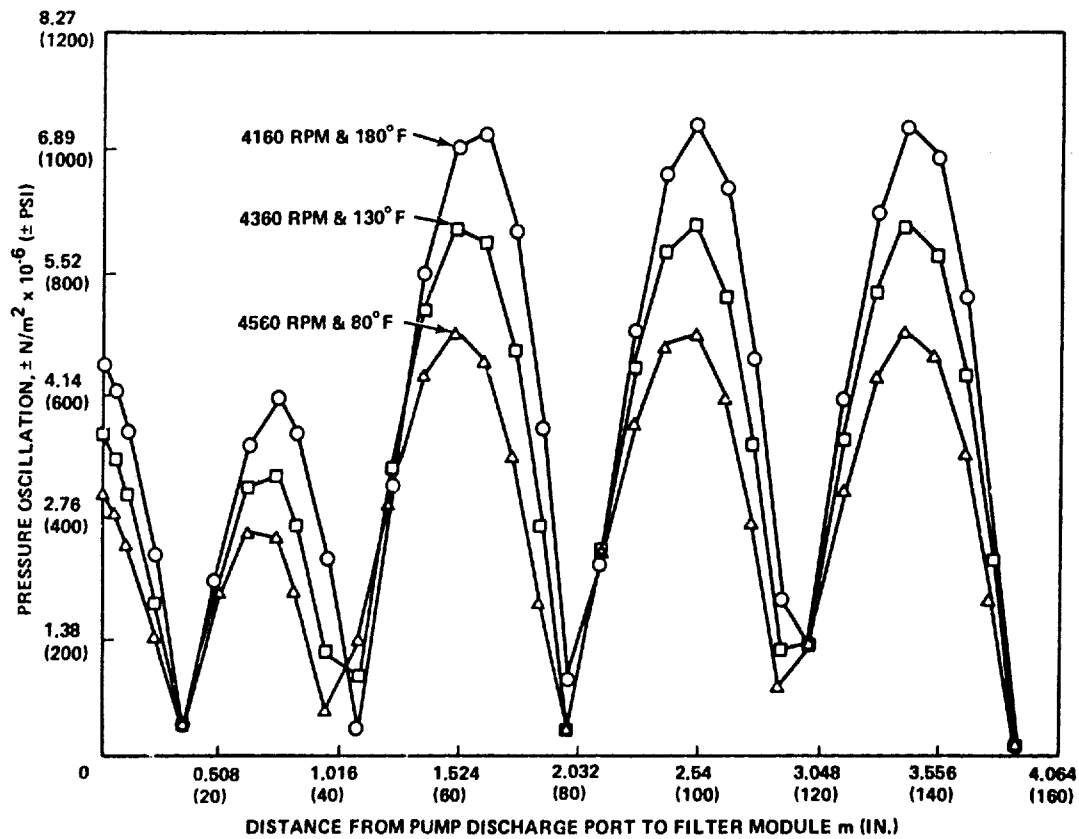


Fig. 29 - Oil temperature effect on Combined system hydraulic resonance standing wave distribution

The overall objective of this effort is the development of an analytical tool for determining line installation criteria for the hydraulic design engineer.

#### ACKNOWLEDGEMENTS

The authors would like to thank the many Grumman personnel whose efforts have contributed to this paper. Among those are:

- Ronald E. Boyland, who developed the original expansion chamber
- Walter R. Belt, who performed the trade-off analysis on the various attenuator configurations
- Frank J. Delaney, who performed the internal flow calculations
- Noc Arcas, who developed and performed the acoustical tests on the attenuators.

A portion of this work was conducted for NAVAIR under Contract Number N-0019-77-A-0202, Order No. 027, and is described in NAVAIR Report No. 7811-9N-V, June 1981.

#### REFERENCES

1. McDonnell Douglas Aircraft Corp., USAF Tech Report AFAPL-TR-76-43, Hydraulic Systems Dynamic Analyses, Volume IV.
2. Streeter, V. L., and Wylie, E. B., "Hydraulic Transients," McGraw Hill 1967.
3. Binder, R. C., "Fluid Mechanics," Prentice Hall, 1946.
4. McDonnell Aircraft Corp., HLMR Final Report, USAF Contract P33616-74-C 20168A P00007.
5. NAVAIR Report No. 78119N-U, "Hydraulic Cavitation Attenuation Study and Test," June 1981.
6. NACA Langley Aeronautical Laboratory Report 1192, "Theoretical and Experimental Investigation of Mufflers (With Comments on Engine Exhaust Muffler Design)," October 6, 1952.



## RUBBER ISOLATORS FOR THE ADATS MISSILE

Jean-Pierre Frottier, Oerlikon-Buehrle Werkzeugmaschinenfabrik, Zurich, CH  
and  
Clifford S. O Hearne, Martin Marietta Orlando Aerospace, Orlando, FL

### ABSTRACT

Ordinarily, rubber isolators are not used in high performance missiles. The leading reasons for this are the dearth of rattle space and the difficulties in determining, and hence designing for, the effects of high, steady acceleration. The present case is exceptional: a lightweight item is suspended on a 1000 Hz isolation system. The item is a missile fin-tip mounted photodetector which receives uplink information on a laser beam carrier. The purpose of isolating the detector is to decrease microphonic noise in its output signal. In the development of this system, a piezoelectric shaker operating to 20 KHz was used to measure the isolation. Excitation in a tactical environmental simulation was provided at the Martin Marietta Ramburner Materials and Propulsion Test Facility and during rocket motor static firings. The ramburner firing produces an acoustical source similar to the ADATS rocket motor plume. Results obtained in an early flight test are also reported.

Rubber mounts are used in the ADATS missile to isolate optical receivers from structural vibration. The optical receivers detect a modulated laser beam which contains uplink guidance information, and the purpose of isolation mounting is reduction of microphonic noise in the receiver output to the signal processor. The frequency band of interest is 1-19 KHz, which includes the laser beam modulation frequencies. Thus, the general need for isolating devices was known, but since the optical receiver and the missile were in concurrent development, and both the vibration environment and the microphonic characteristics of the receiver had low predictability, the isolator design had to be worked in advance of a well-defined requirement. Selected isolator design experimental evaluation is described in this paper.

#### The ADATS System

A brief description of the ADATS system will place the problem in context. ADATS, acronym for Air Defense Anti-Tank System, is a completely self-contained mobile missile system intended to engage aircraft and armor at intermediate ranges. It consists in part of a

sleuable launcher carrying eight solid rocket missiles in canisters and an electro-optical target acquisition and tracking unit supplemented by separate radar and optical target detectors and designators. The missile is guided by a spatially coded laser beam. The system may be mobilized on many military vehicles, and an early development is the M113 type vehicle installation illustrated in Figure 1. ADATS is being developed by Martin Marietta Orlando Aerospace for Oerlikon-Buehrle, Ltd., Zurich, Switzerland.

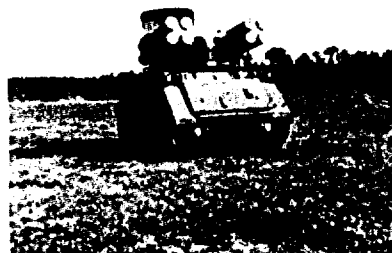


Figure 1. ADATS on the M113

The laser beam signal is detected by optical receivers located in pods at the tips of the horizontal pair of fins, which are in a cruciform arrangement. The pods are visible in Figure 2, which shows a missile just emerged from its canister. The placement of the receivers at the tip of the fin favors reception of the laser-carried signal in the presence of the optically noisy rocket motor plume.

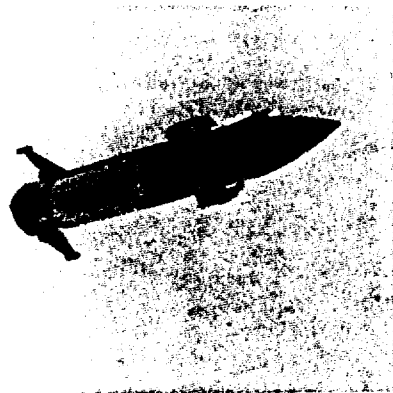


Figure 2. Receivers on Missile Fin Tips

#### The Receivers and Their Mounts

The receiver is composed of a tubular metal dewar closed by an optical window at the after end. Figure 3 shows a dynamically similar facsimile, called a Vibration Test Unit (VTU) used in vibration testing. From a metal forward bulkhead, not visible in the photo, is cantilevered a long slender thin-walled tube which intrudes into the dewar. This tube, known as the coldwell, has a cryostat installed at assembly. The detecting surface chip is supported within the dewar on the interior end of the coldwell. Signal leads from the detector exit the dewar at the forward bulkhead and immediately enter a preamplifier unit attached there. Preamplifier output leads are directed through the missile fins, and the signal is further amplified and processed within the missile. A cooling gas line leading to the cryostat is also embedded in the fin.

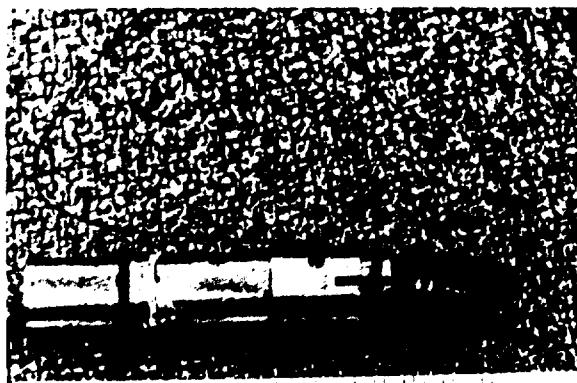


Figure 3. Vibration Test Unit (Receiver Facsimile)

The dewar detector is manufactured in the Martin Marietta Orlando Aerospace Microelectronics Center, and the receiver preamplifier assembly is subsequently fabricated in the Production Division at Orlando. This assembly is supported in the fin tip pod on two 80-durometer silicone rubber rings. The rings are custom made by Minnesota Rubber Company in their Quad-Ring cross section pattern. This type ring is ordinarily used as a hydraulic system seal. It was selected because the lobular corners of the ring's cross section permit a shearing deformation under loads, resulting in a desirable amount of transverse compliance of the mount. This compliance is not too sensitive to variations in initial compression (squeeze) caused by in-tolerance dimensional variations of the pod ID and receiver OD. Figure 4 shows the installation in profile.

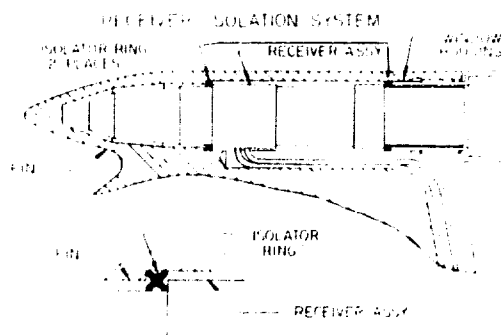


Figure 4. Receiver Isolation System

The VTU of Figure 3 is constructed of rejected parts and is thus dynamically similar to an actual receiver. In the preamplifier section of the VTU in the photograph may be seen embedded an Endevco Picomin 22 accelerometer. This accelerometer has a flat response to 10 KHz. The preamplifier is a PCB potted in epoxy. The accelerometer cable issues from a hole in the steel collar that joins the dewar and preamplifier. In similar fashion, the preamplifier leads and the cold gas line are directed out of an actual receiver. The rubber isolators, the quad rings, are seen adjacent to the seats through which they resist longitudinal loading. On installation, the rings are made snug longitudinally with a small setup load. The rings have survived, in good condition, postflight ground impact loads estimated at 25,000 Gs, and postflight heat loads which globuled the solder at structural joints of the dewar.

#### The Need for Isolation

An indication of the need for detector isolation from its vibration environment appeared early in the program during static firings of test rocket motors. Measurements of laser signal transmissibility through the plume of the development rocket motor were being made using commercially available dewar detectors. The detectors were mounted, windows facing the

plume, close to the exit plane of the nozzle at locations in the soundfield at which SPLs above 160 db could be expected. Although these units, made of glass, not metal incidentally, were supported within a half-inch thick aluminum walled box and were potted in RTV, some were so microphonic as to saturate their signal channels. The immediate problem was solved by placing a half inch sheath of lead on the box exterior and further isolating the dewar detectors on quad rings.

Support of the ADATS receivers on rubber rings had been contemplated for structural integrity reasons. However, protection from folding fin opening shock and the intense vibration environment within the canister during launch became a diminishing concern as early production units were found to be extremely rugged, failing to crack or deform at test levels many times above specification levels.

We had experience with microphonic photodetectors on another program where imaging detectors were much more susceptible to vibration than the ADATS detectors. In that instance, potting in a specially formulated, very dissipative silicone rubber compound and the use of structural components with high material damping in propagation paths had yielded desired results. The specific purpose of damping in that case was to shield the detector from gimbal-bearing noise! The system also had an optical alignment requirement which would have made effective use of isolation techniques difficult. However, application of dissipative materials alone was inappropriate for the ADATS problem where the noise energy is relatively very high. As will be seen below, it appeared that a combination of both isolation and damping (as discussed by Maidenak in his article on the Principle of Supplementarity of Isolation and Dissipation, Reference 1) would offer greater attenuation. We did not add dissipative mechanisms only because it appeared the additional attenuation was not needed.

It is interesting to note that rubber isolation, applied either at the base of the tube or at the base of the chassis, was the traditional method of reducing microphonics caused by vibration of vacuum tube elements in the times in which these Symposia were first convened, and earlier.

#### First Tests of Isolation Concept

Our initial problem was to test the performance of the isolators in the frequency band of interest. To provide a suitable broad band environment in our laboratory - even were one well defined - did not appear practical at that time. We reasoned that the pod tip environment, in the higher frequency bands at least, would be characterized by aerodynamic and aeroacoustical noise inputs and that the environment of the static motor firings would be a near-worst case. A test of the isolation

principle at or near actual tactical environmental levels was desirable, but one does not burn an expensive rocket motor grain just to test the properties of rubber rings. We had a suitable alternative in the Martin Marietta Ramburner Materials and Propulsion Test Facility in which a jet similar to the rocket motor exhaust could be produced, and we proceeded to exploit this resource.

Two pod fins were mounted on the ramburner exhaust tube in appropriate geometric positions relative to the nozzle, as illustrated in Figure 5. The pods contained instrumented metal slugs simulating the receivers (the VTUs did not yet exist). The slugs were supported within pods on standard quad rings of the same ID but forty percent larger cross section than the custom size selected for the missile (the custom rings were not then available). In some runs, the fins were brought to their low temperature extremes before the run commenced by metering evaporated liquid nitrogen into styrofoam containers covering the fins. The styrofoam was removed by lanyard as each run began.

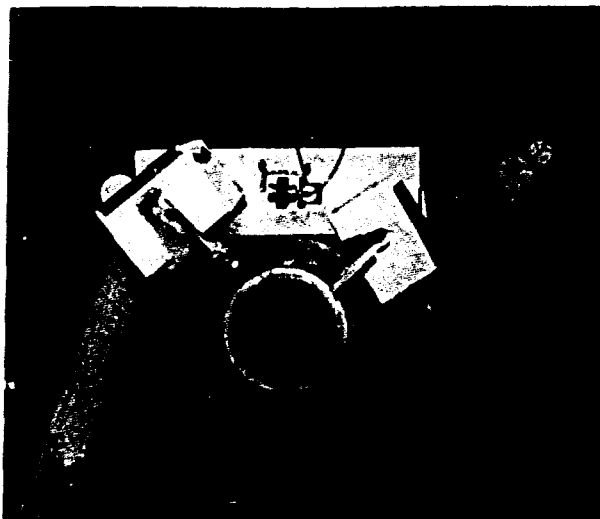


Figure 5. Isolation Test on Ramburner, with Cooling

The pod exterior and the slugs were instrumented with Picomin 22 miniature accelerometers. Treating the pod acceleration as input and the slug lateral acceleration as output in a transfer function analysis produced a typical isolation curve with attenuation beginning at 2 KHz.

However, a resonance appeared at 9,200 Hz, rising from the attenuation level by 20 db over a band of 500 Hz. Because applying damping tape to the center one third of the slug had little effect on the resonance, we attributed it at first to motion other than a slug bending mode; but we were puzzled. The frequency, 9,200 Hz, appeared to be too high for a rigid body pitch of the slug and too low for standing waves in the rubber. We found a partial answer later in the laboratory when the freely suspended slug was found to ring predominantly at the same frequency when struck. The mode of motion was

not identified. This incidental event is mentioned because we have had similar experience with the VTUs at 7,300 Hz. Again, a cigar band wrap of damping tape, actually just electrician's tape this time, had little effect, but a complete longitudinal covering with a tape strip had a profound damping effect. We have some clues to indicate the mode of motion involved here, but as mentioned, we have not explored the possibility of damping treatment in the belief that improvement will not be needed. It remains a potential application of the Principle of Supplementarity.

Our judgement of the degree of isolation attained was based on a comparison of the pod exterior acceleration power spectrum with the receiver acceleration power spectra. The former was directed laterally; that is, normal to the fin plane. The latter two, the accelerometers on the slug, were laterally and longitudinally directed. We also calculated a transfer function from exterior lateral to interior lateral to aid in this judgement. This was an inexact measure because there was not strictly an input-output relation. The two signals were, however, at least semi-coherent. We have omitted presentation of these plots in favor of later results which are more representative of design values.

Our experience in the ramburner facility was very helpful. It showed the workability of the isolation concept and established a test level for design specification which has prevailed through the accumulation of more definitive data. It also gave us a needed preliminary indication that the silicone rubber would perform at the low temperature extreme, -40C. While we were confident, on the basis of material data, that rubber properties would vary little with temperature, we felt it necessary to demonstrate the dynamic properties in the ten kilohertz range.

#### Testing on a Piezoelectric Shake Table

Testing in the ramburner facility was fruitful, but prodigal of manpower and horsepower. We desired to move testing to the laboratory where temperature extremes and steady acceleration loads could be applied more practically, where the tests could be conducted adjacent to the frequency analyzer, an HP 5451B, where scheduling was far easier, and where Florida weather was not a consideration. We also knew we would soon need vibration exciters for quality assurance testing. To this end, we ordered a Wilcoxon D60H Shake Table. We also procured supporting transducer instrumentation, a power supply and a balancing unit. This was all a very modest investment incidentally. When we put the piezoelectric shaker into operation, we were able to control inputs to the receivers from 1.5 KHz to the top of the band of interest. Automatic control was obtained using the HP 5451B.

A preliminary setup is shown in Figures 6 and 7. The shaker table is featured in Figure 6 and is in the foreground of Figure 7. The rubber feet with which it is delivered have been removed and the flat bottom placed in intimate contact with an aluminum block using a low viscosity grease interface. The black ring is a large O-ring used to semi-retain the flowing grease. Sitting on the top of the shaker table in Figure 6 is a short adapter section used to correct a mismatch of table and fixture bolt hole patterns. The rectangular block section is one of the two fixtures used to hold VTUs. The one pictured is used for lateral excitation, the other, not portrayed, is used for longitudinal. The holes in the center of the top and side are used to apply steady loads to the receiver by use of string traction devices. These steady loads were intended to simulate steady acceleration loads. The control accelerometer is a Wilcoxon 111. The two black boxes behind the shaker in Figure 7 are, top to bottom, a Wilcoxon N60H Matching Network and a Wilcoxon PA7CM Power Amplifier. Also seen just to the right is an Endevco 2735 Charge Amplifier and a portion of the HP 5451B chassis. On the left is a stainless steel tube which is the retainer of the aft ring. Also present is a 454 gram (1.0 pound) weight used to set up the longitudinal preload on the retainer tube.

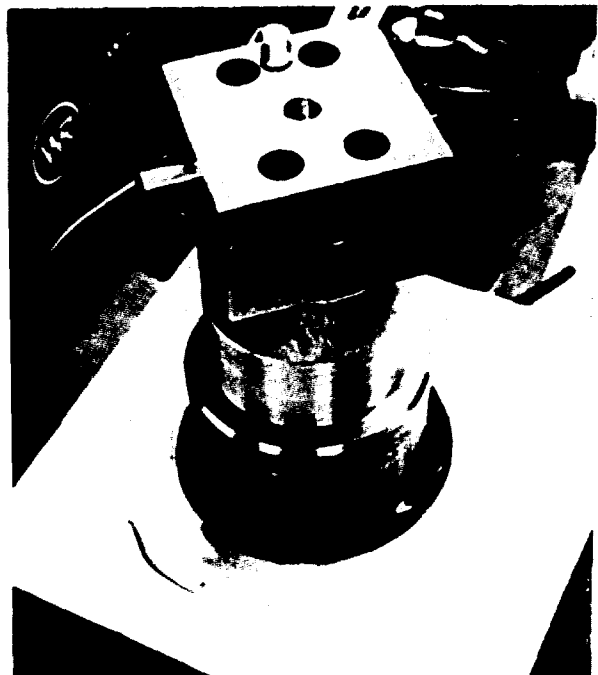


Figure 6. Early Shake Table Arrangement

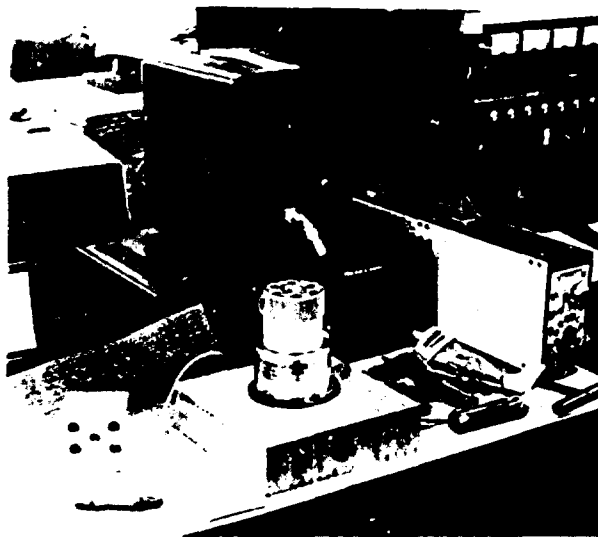


Figure 7. Shake Table and Supporting Units

Figure 8 is a photo of a similar setup, with the shaker now clamped to its base plate to react the string draw loads applied using pulleys mounted on a framework. (The square-edged VTU holding fixture of Figure 6 has been cut down to a circular cylinder.) A 2.7 kilogram (6.0 pound) lead weight, representing 3-sigma longitudinal acceleration, may be seen drawing longitudinally on the VTU. The rig stands on a styrofoam pad because it is removed from a temperature chamber just before excitation is begun.

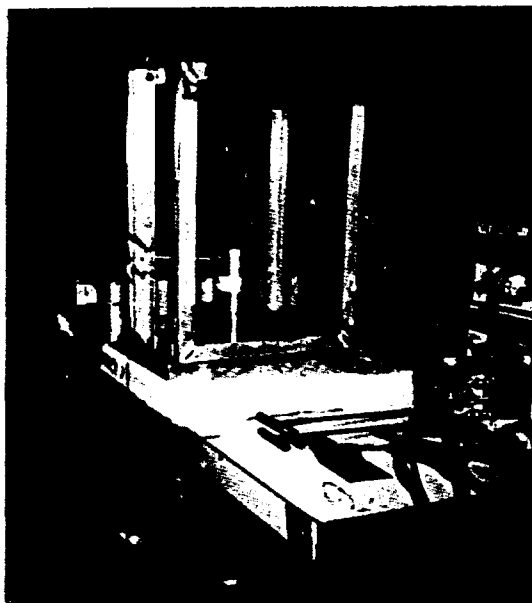


Figure 8. Shake Table with Steady Load Rig

Sample results of the laboratory tests are shown in Figures 9 through 12. They are, in order, an input power spectrum, an output power spectrum (lateral), a magnitude transfer function, and a coherence function. The coherence is approximately twice that found in ramburner and rocket motor tests where the assumption of an input-output relationship was less appropriate. The aforementioned high frequency resonance is evident. These plots correspond to room temperature, zero steady load conditions. Temperature extreme and steady load testing did not drastically change results. Low temperature did reduce attenuation 3 to 5 db in the band up to 5 KHz. The steady loading technique was not wholly representative of a steady acceleration field; however, the steady loads tests did show a lack of dramatic change in attenuation, and this was heuristically helpful.

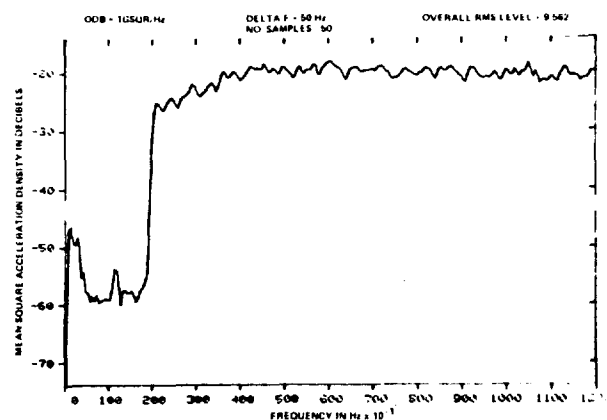


Figure 9. VTU Shake Table Test -  
Input Power Spectral Density

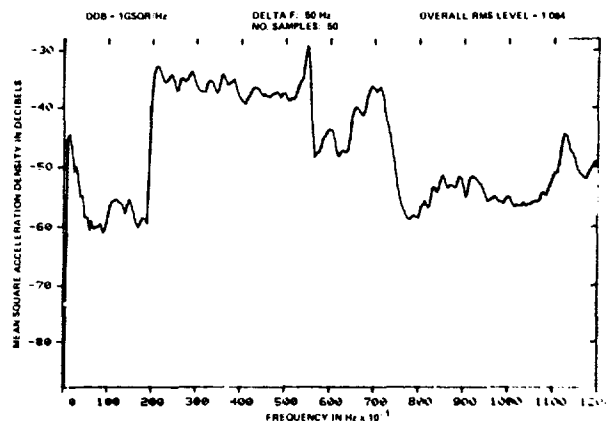


Figure 10. VTU Shake Table Test -  
Output Power Spectral Density

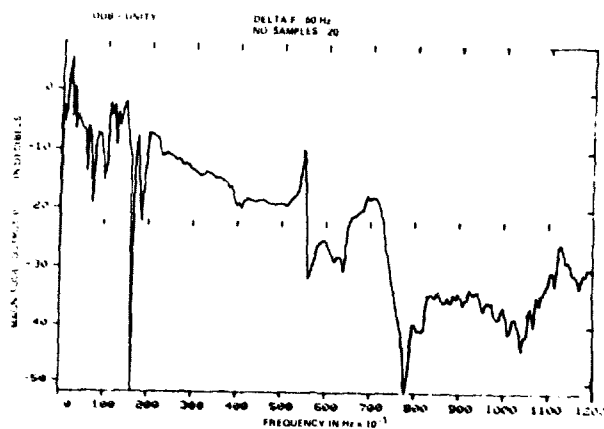


Figure 11. VTU Shake Table Test - Transfer Function

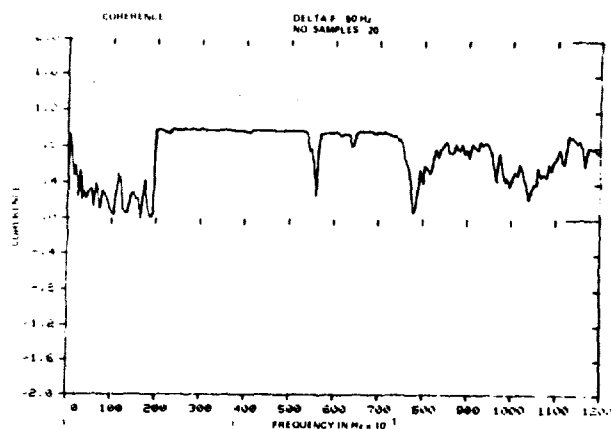


Figure 12. VTU Shake Table Test - Coherence Function

#### Rocket Motor Static Firings and Flight Test

In contrast to results obtained using the shaker table, we show in Figures 13 through 16 the corresponding results obtained for a VTU in a rocket motor static firing. These plots are comparable to the ramburner facility measurements described earlier. Finally, a flight test measurement, from a mid-flight interval, for the receiver lateral acceleration is shown in Figure 17. There is no input-output type result here because of the impossibility of instrumenting the pod in flight. These results appear different from ground results because most of the measurement is in the noise level. The resonance peaks do pop out about 10 db above the noise. We had to suffer greater noise in flight testing not only because the data channels were longer, but because we had to set the accelerometer calibrations higher to accommodate the high levels in the in-canister period and during fin deployment. We found in flight testing that the overall rms level above 2 KHz did not vary widely throughout the entire flight, nor did the spectral distribution. Exceptions to the foregoing statement were the

in-canister and fin deploying periods, in which severe oscillations occurred, but these time intervals are irrelevant to microphonics.

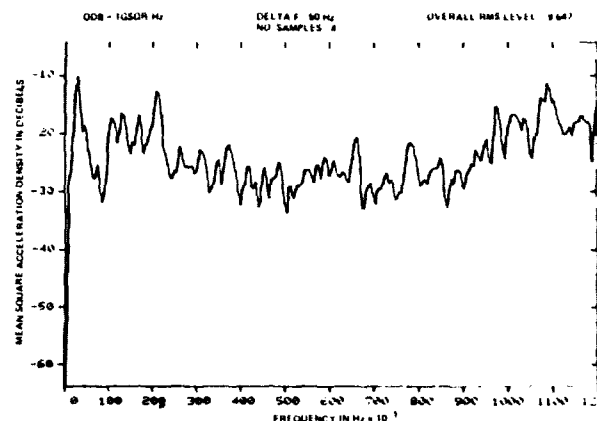


Figure 13. Rocket Motor Firing -  
Input Power Spectral Density (POD)

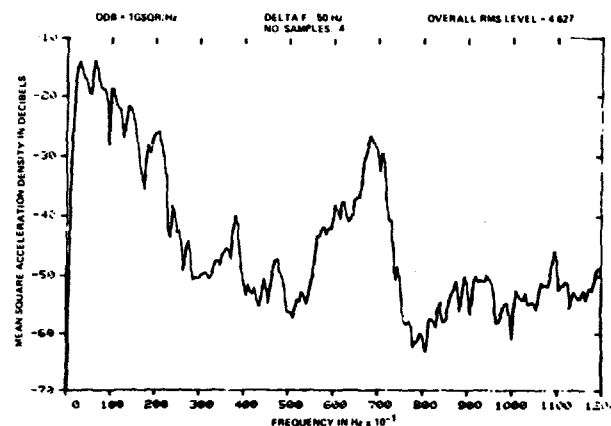


Figure 14. Rocket Motor Firing -  
Output Power Spectral Density (VTU)

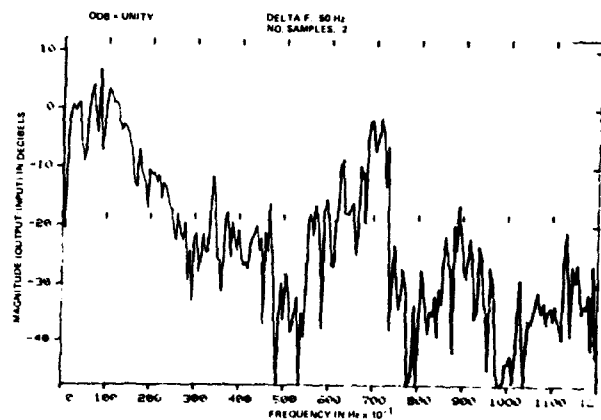


Figure 15. Rocket Motor Firing -  
Transfer Function (VTU)/(POD)

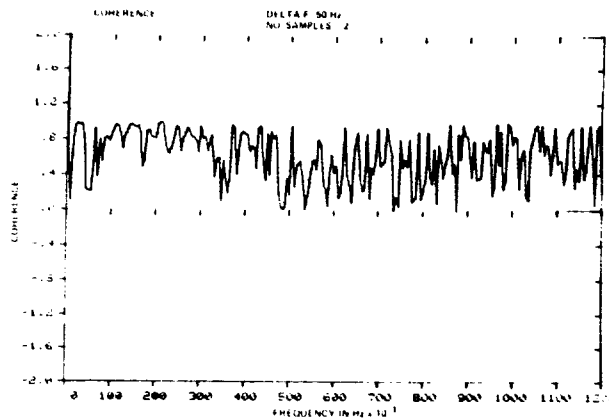


Figure 16. Rocket Motor Firing -  
Coherence Function (VTU & POD)

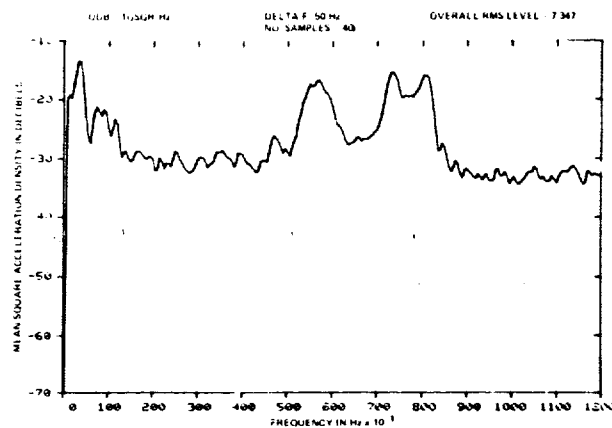


Figure 17. Flight Test -  
VTU Lateral Acceleration

#### Quality Assurance Testing

A microphonic test is applied to each unit manufactured. It was decided to vibrate the complete receiver assembly on its rubber isolation rings and apply the pod environmental level to the fixture. The maximum allowable microphonic noise was specified as a ratio of rms noise with and without excitation in the 1-19 KHz band. Since the fin-traversing section of the gas line is an integral part of the receiver assembly, it was necessary to support the unit in a fixture which has a long dimension relative to the shake table diameter to prevent handling damage to the metal tube. The dimensional disparity was accommodated by the flaring magnesium adapter shown in Figure 18. When the receiver noise measurement proved sensitive to the high voltage on the shake table, the quartz phenolic block shown was inserted, the black boxes on the bench

were moved about 2 meters away, and all grounding and shielding precautions were effected. Then the shaker-on noise increase was reduced to pure microphonics as indicated by coherence function.

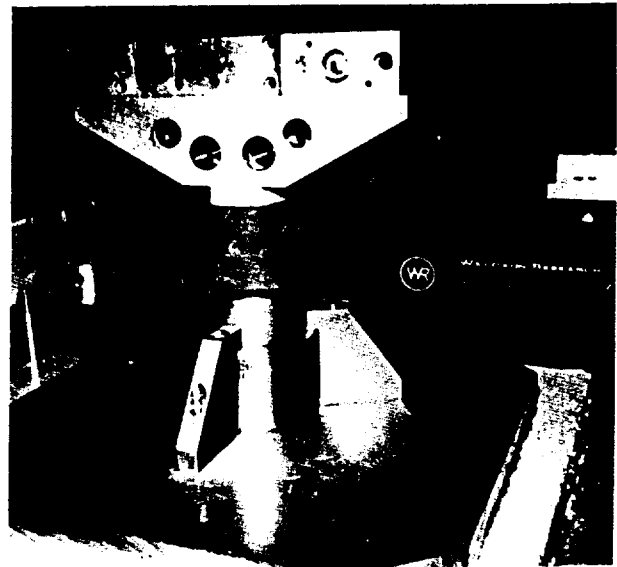


Figure 18.

#### Vibration Test Setup for Receiver Assemblies

Use of coherence functions relating the control accelerometer signal and receiver output has been useful in distinguishing microphonic noise from other sources, especially from extraneous laboratory sources. Figures 19 through 22 show "input" and "output" power spectra, and corresponding transfer and coherence functions. These results varied from unit to unit, but almost all units fell within specification. The test selected for illustration is one that has a correspondence with the resonance spectrum as measured on the VTUs. Not all receivers showed this spectral correspondence and some were practically a-microphonic. We have no precise explanation of these varied phenomena because we have not determined the precise mechanism of the microphonics. And unless specification requirements become more restrictive, we will not investigate such questions.

The preliminary quality test setup described here has been superseded. A Spectral Dynamics controller and analyzer was modified by the manufacturer specifically for the test. Fixturing was reduced in mass and geometry. The control accelerometer is now monitored by a twin to detect failures, and both are of the stud mounted type to eliminate both the variances in behavior and the potential for damage when the cemented type is removed.

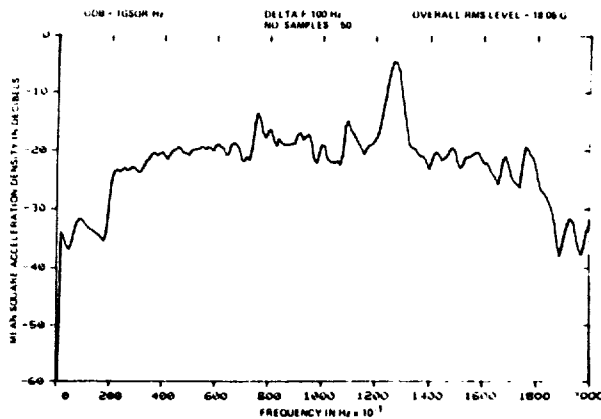


Figure 19. Receiver Shake Table Test - Input  
(Equalization was a problem at this time)

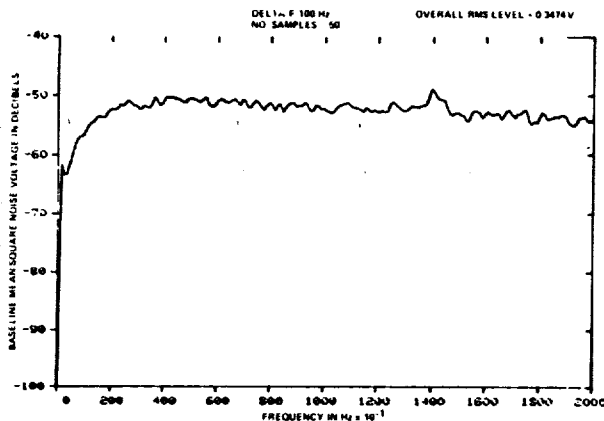


Figure 20A. Receiver Shake Table Test  
Receiver Noise Spectrum--Shaker Off

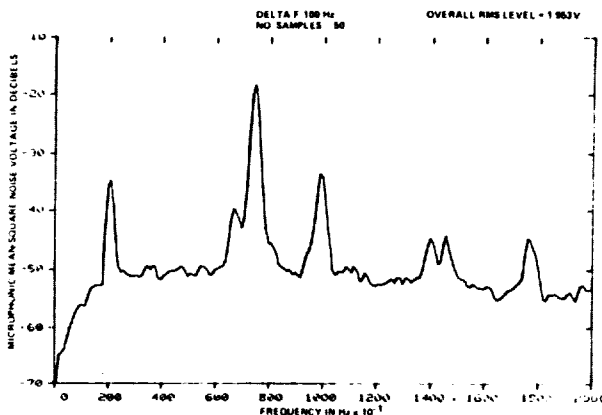


Figure 20B. Receiver Shake Table Test  
Receiver Noise Spectrum--Shaker On

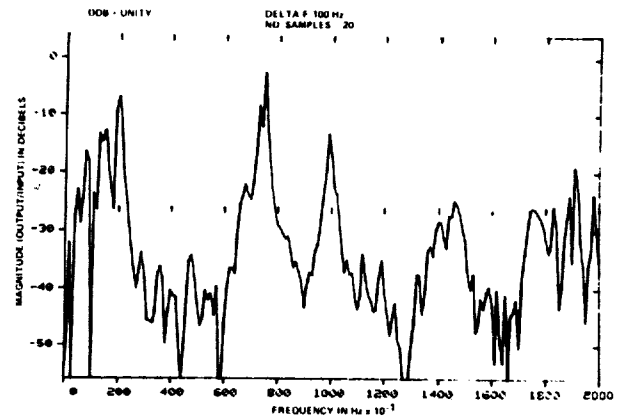


Figure 21. Receiver Shake Table Test - Transfer

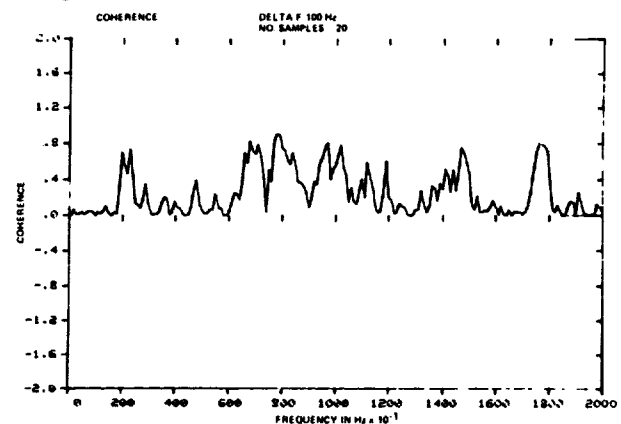


Figure 22. Receiver Shake Table Test - Coherence

#### Conclusion

We do not expect to use rubber isolators in high performance missiles in the usual MIL-STD-810 test frequency band, but use of isolation is feasible when the isolation band is to be well above 1.0 KHz. Rubber isolators were, by inference, the solution to the problem of reducing the microphonic noise in photodetectors in the ADATS missile. The system is still in development at this writing, but the expectation is that the isolators will remain a sufficient solution.

Supplementation of isolation with damping in the configuration would advance the objective of reducing microphonics. It is a resort in case of need.

Use of random vibration to 20.0 KHz on piezo-electric shake tables for engineering development and quality assurance testing of a small component has been found feasible and useful.

#### References:

1. G. Maidanik, "Principle of Supplemantarity of Damping and Isolation in Noise Control," Journal of Sound and Vibration, 77(2), 1981.



## TIME AND TEMPERATURE EFFECTS ON CUSHIONS

Gordon S. Mustin  
Naval Sea Systems Command  
Washington, DC

Dynamic behavior of cushions can be modeled by exponential equations describing the time and temperature dependent loci of the nadirs of logarithmic parabolas in the acceleration-static stress plane and of the lengths of the latus recta of these parabolas. A set of nine empirical constants is sufficient to describe this dynamic behavior over a wide range of drop heights and thicknesses at temperatures ranging from slightly above the glass temperature of the polymer to 344°K. Recommendations are offered for future work exploiting this finding.

### INTRODUCTION

A popular method of presenting data concerning the shock reduction properties of non-linear isolators with distributed mass and elasticity -- i. e. cushions -- is by means of acceleration-static stress curves, generated from data collected in a prescribed fashion [1, 2]. Fig. 1, from Humbert and Hanlon [3], illustrates typical results. A Military Handbook [4] contains over 850 curves of the same general shape; often referred to by the sobriquet "limp spaghetti". All of these 850 curves cover performance only at nominal room temperature conditions, 296°K and 50% relative humidity.

This inquiry was undertaken to ascertain whether the principle of time and temperature superposition, well known in modern rheology and going back to at least 1954 [5], could be used as a tool to present data more compactly, particularly when considering performance at temperatures significantly different from room conditions.

### THEORETICAL CONSIDERATIONS

It is a given that time and temperature affect the response characteristics of viscoelastic materials such as plastic foam cushions. Acceleration is one form of measuring such response under velocity shock conditions. Hence,

$$G = f(\sigma_s, h, T, \theta, t), \quad (1)$$

where

$G$  = acceleration ratio, the dimensionless multiple of the acceleration of gravity,

$\sigma_s$  = static stress in suitable units of weight force per unit area,

$h$  = height of drop, in length units,

$T$  = cushion thickness, in length units,

$\theta$  = absolute temperature, and

$t$  = time,

defines the relationship to be explored here.

Soper and Dove [6] showed that time entered the relationship as strain rate, or impact velocity divided by thickness, with the dimension of inverse seconds. Since velocity at impact is in one-to-one correspondence with height of drop, Eq. (1) can be simplified to read

$$G = f(\sigma_s, h/T, \theta), \quad (2)$$

thus leaving only three variables to be considered.

McDaniel [7] has developed a generalized viscoelastic constitutive model relating the

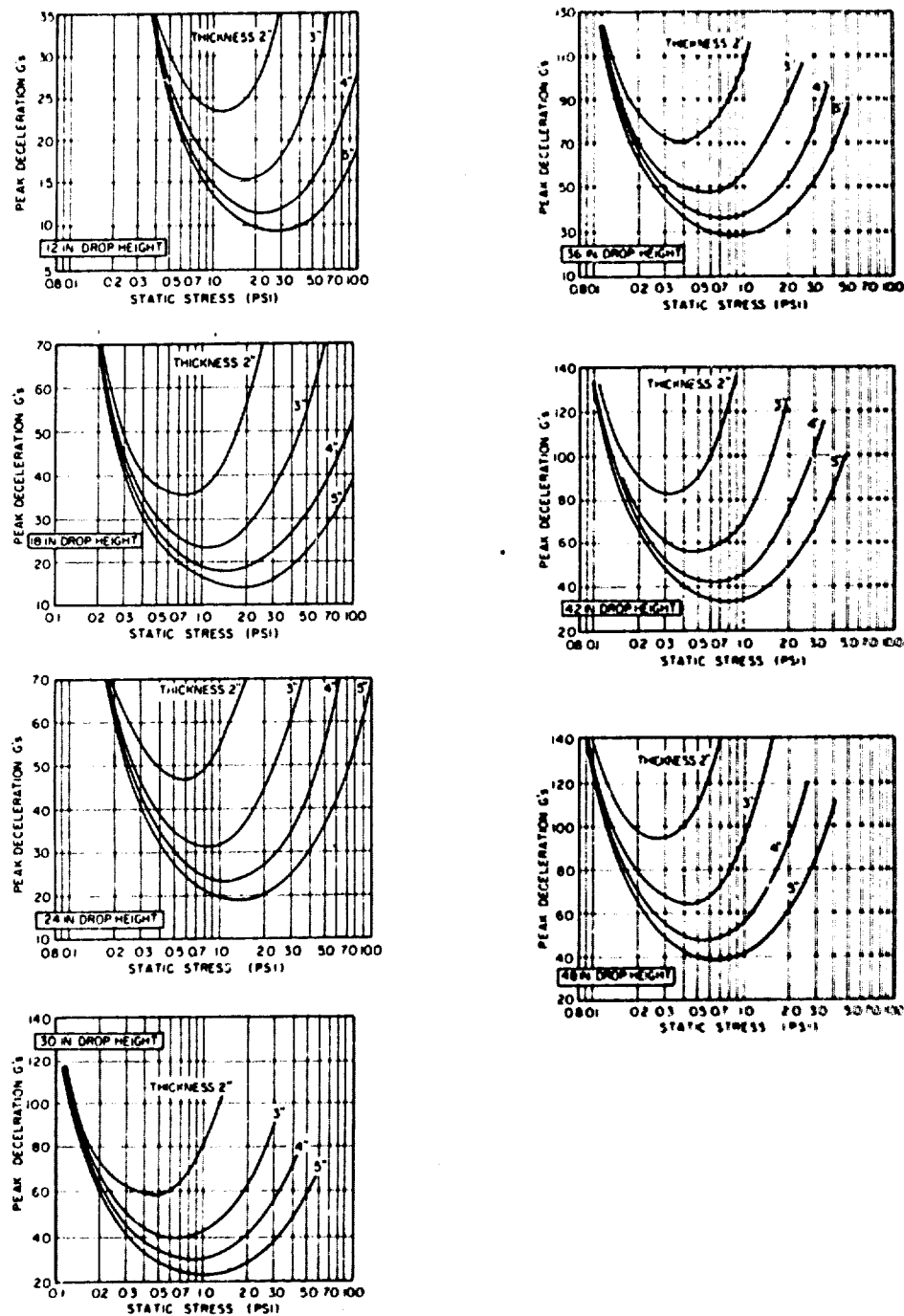


Fig. 1 - Humbert and Hanlon's Data [3] on Behavior of a Polyethylene Foam at Room Temperature Conditions

variables of Eq. (1). The model is accurate but requires determination of such a large number of empirical constants for a given material that sophisticated computer programs are required, and the working hardware needs significant storage capacity. Intuitively, this situation seemed undesirably complicated, at least for preliminary design, and a simpler solution was sought.

Wyskida and co-workers [8-12] demonstrated with statistical rigor that performance at a single thickness, single drop height, and specific temperature, could be modeled by an equation of the form

$$G = a_0 - a_1 x + a_2 x^2, \quad (3)$$

where

$$\begin{aligned} a_1 &= \text{empirical constants determined} \\ &\quad \text{from the data, and} \\ x &= \ln b \sigma_s. \end{aligned}$$

The constant,  $b$ , is chosen to insure that the sign of the logarithm is always positive. Since the workers cited above were working in English units of pounds per square inch, their value of  $b$  was 100. If other stress units are used and it is still desired to retain their  $a_i$ , suitable adjustment in the value of  $b$  must be made.

A total of 520 sets of  $a_i$  were developed for such diverse materials as rubberized hair, polyethylene foam, polyurethane foam, and polypropylene foam. This sample is large enough to conclude that behavior of any cushion exhibiting a curve similar to those in Fig. 1, can be acceptably modeled as a second degree polynomial.

Since Eq. (3) is the quadratic form of the equation of a parabola, it may also be written

$$(x - x_0)^2 = a_2^{-1}(G - G_0), \quad (4)$$

where

$$\begin{aligned} x_0 &= 1/2 a_1 a_2^{-1}, \text{ and} \\ G_0 &= a_0 - 1/2 a_1 x_0. \end{aligned}$$

The quantities  $G_0$  and  $x_0$  are readily recognizable as the optimum acceleration and a transform of the optimum static stress. The concepts of an optimum acceleration and of an optimum static stress corresponding thereto

are well documented (see, for example, Shock and Vibration Monograph SYM-2 [13]).

Geometrically, the quantities  $G_0$  and  $x_0$  are the coordinates of the nadir of a parabola in the  $G$ - $x$  plane while  $1/a_2$  is its latus rectum.

The solution of Eq. (4),

$$x = x_0 \pm [a_2^{-1}(G - G_0)]^{1/2}, \quad G \geq G_0, \quad (5)$$

gives the limits of a range of  $x$  producing acceleration ratios equal to or less than a preselected value of  $G$ .

Table 1 gives the design constants for one material at three different temperatures, four different drop heights, and three thicknesses. The compactness of data presentation, compared to 36 curves, is manifest. Problems arise, however, when the designer wishes to interpolate at temperatures, drop heights, or thicknesses other than those recorded. The main thrust of this effort may, therefore, be described as an attempt to find, from the data available, whether one can substitute numbers into the three relationships:

$$G_0, x_0, a_2 = f(h/T, \epsilon), \quad (6)$$

One should consider what form the functional relation should take. In this connection many investigators, most notably Tobolsky [14], show that the temperature shift factor,  $a(\theta)$ , for a thermorheologically simple polymeric material can usually be expressed in the form

$$a(\theta) = C_i \exp [-C_{i+1}(\theta - \theta_0)], \quad (7)$$

where

$$\begin{aligned} C_i &= \text{empirically determined constants, and} \\ \theta_0 &= \text{a reference temperature, arbitrarily chosen in this paper to be } 294.3^\circ\text{K.} \end{aligned}$$

Eq. (7) is not expected to hold near to or below the glass temperature of the polymer, which may or may not be a practical problem.

It has been demonstrated [15] that optimum static stress of seventeen materials with U-shaped acceleration-static stress curves varies exponentially with the ratio  $h/T$ . In the same paper,  $G_0$  was matched linearly with  $h/T$ . Since the logarithms of

TABLE 1  
Design Constants\* for Hercules Minicel, Density .032 g/cm<sup>3</sup> (2#/ft<sup>3</sup>)

HT. INS.	THICK NESS, INS.	AT 21.1°C (70°F)					AT 71.1°C (160°F)					AT -53.9°C (-65°F)				
		a <sub>2</sub>	a <sub>1</sub>	a <sub>0</sub>	G <sub>0</sub>	x <sub>0</sub>	a <sub>2</sub>	a <sub>1</sub>	a <sub>0</sub>	G <sub>0</sub>	x <sub>0</sub>	a <sub>2</sub>	a <sub>1</sub>	a <sub>0</sub>	G <sub>0</sub>	x <sub>0</sub>
12	1	14.44	118.34	278.24	35.78	4.098	11.27	84.21	197.11	39.81	3.736	14.78	142.48	377.74	34.84	4.813
	2	8.34	78.34	201.97	18.00	4.697	6.31	55.43	142.03	20.30	4.302	12.22	131.51	367.89	14.07	5.381
	3	5.77	58.41	159.93	12.01	5.062	3.73	36.66	105.43	15.35	4.914	10.86	118.13	329.67	8.43	5.439
18	1	25.60	191.85	408.33	48.89	3.747	18.34	120.80	254.30	55.38	3.293	23.67	208.39	510.33	51.67	4.402
	2	13.60	115.32	270.78	26.32	4.240	9.18	70.87	168.61	31.83	3.860	18.32	183.06	480.27	22.97	4.996
	3	9.31	85.07	209.99	15.66	4.569	5.45	47.13	124.13	22.24	4.324	10.78	117.46	336.55	16.59	5.448
24	1	27.86	193.48	403.76	67.84	3.472	23.96	141.90	280.51	70.41	2.961	36.16	301.76	621.02	61.46	4.173
	2	18.71	150.03	333.50	34.74	4.009	13.17	93.58	202.97	36.74	3.553	21.69	210.69	544.94	33.30	4.857
	3	13.98	123.01	289.25	18.66	4.400	9.21	73.58	170.46	23.50	3.995	18.94	194.42	517.16	18.23	5.133
30	1	36.71	233.31	451.82	81.12	3.178	36.04	202.81	368.93	83.61	2.814	42.40	341.36	761.96	74.89	4.026
	2	21.28	164.16	357.55	40.96	3.857	17.08	116.49	238.88	43.65	3.381	31.73	296.01	724.58	34.21	4.665
	3	14.95	127.76	298.20	25.25	4.273	9.61	74.17	173.20	30.09	3.859	22.03	221.35	578.84	22.83	5.024

\*Values of a<sub>0</sub>, a<sub>1</sub> and a<sub>2</sub> taken from Ref. [9]. G<sub>0</sub> and x<sub>0</sub> computed therefrom.

equals are equal, G<sub>0</sub> can also be matched exponentially. These two features having been demonstrated in the past, one is permitted to hope that a<sub>2</sub> varies similarly.

The principle of time and temperature superposition teaches that one can combine the time relations and the temperature shift relations into a single empirical equation. As a result, one seeks a set of constants that satisfy relations of the form

$$\exp [x_0], G_0, a_2 = C_i (h/T)^{C_i+1} \exp [-C_{i+2} (\theta - \theta_0)], \quad (8)$$

where the constants, C<sub>i</sub>, are determined by standard least square techniques.

## RESULTS

Table 2 contains the C<sub>i</sub> for four separate temperature sensitive materials. Compare the nine entries for Minicel in this table, covering the entire range of temperatures from 219.3°K to 344.3°K with the minimum of 108 entries of Table 1 required to describe performance at only three temperatures in this range.

Fig. 2 compares original curves for Minicel at two different temperatures with curves based on the Table 2 constants. Lateral separation at higher accelerations is primarily due to sensitivity to small variations in value of the latus rectum (1/a<sub>2</sub>).

The data analyzed were selected so that the lowest temperature would be above the expected glass temperature of the principal

polymer in the cushion. For this reason, any available data for rubberized hair or for polyurethane foam at 219°K were not used. Table 3 contains a summary of the temperature limits and h/T limits beyond which extrapolation, with all its uncertainties, becomes necessary.

It should be noted that the basic logarithmic parabola, and dependence on strain rate, is not necessarily lost below the glass temperature. Table 4 illustrates this point for rubberized hair at 219.3°K. Note the marked changes in the values for the y-intercept and the slope as compared to Table 2. Behavior is simply different in the glassy region from that in the transition zone. Table 5 contains further evidence that strain rate is a valid variable independent of the glass temperature. This table is a recomputation of the findings of an earlier paper [15]. Note, in particular, that thermoplastic polystyrene is in this table, as are a glass fiber material and several cellulosic products.

It should also be noted that, at least as early as 1963, a British paper [16] implicitly recognized that equal values of h/T produced equal results. Wyskida et. al. confirmed the h/T hypothesis for Minicel foam [17]. The case for the influence of strain rate, as measured by h/T, is considered proven beyond reasonable doubt.

## DESIGN EXAMPLES

Two problems are used to illustrate the potential utility of the principles found herein.

TABLE 2  
Multiple Temperature Design Constants for Four Materials

	$C_1$	$C_2$	$C_3$	STD. DEV.
Minicel, .032g/cm <sup>3</sup>				
Exp [ $x_0$ ]	554.599	-.896	.00892	1.101
$G_0$	3.034	.971	.000977	2.575
$a_2$	1.746	.888	.00449	3.220
Rubberized Hair, Type V				
Exp [ $x_0$ ]	38.872	-.506	.00705	3.599
$G_0$	2.805	.774	.00394	2.537
$a_2$	1.663	1.123	-.00651	3.387
Polyether Urethane, .048g/cm <sup>3</sup>				
Exp [ $x_0$ ]	60.530	-.535	.00826	1.427
$G_0$	2.237	.920	.00583	3.799
$a_2$	2.708	.661	-.00248	2.032
Ethafoam, .032g/cm <sup>3</sup>				
Exp [ $x_0$ ]	433.967	-.727	.00912	1.163
$G_0$	1.922	.997	-.00199	3.272
$a_2$	3.270	.644	.00601	3.718

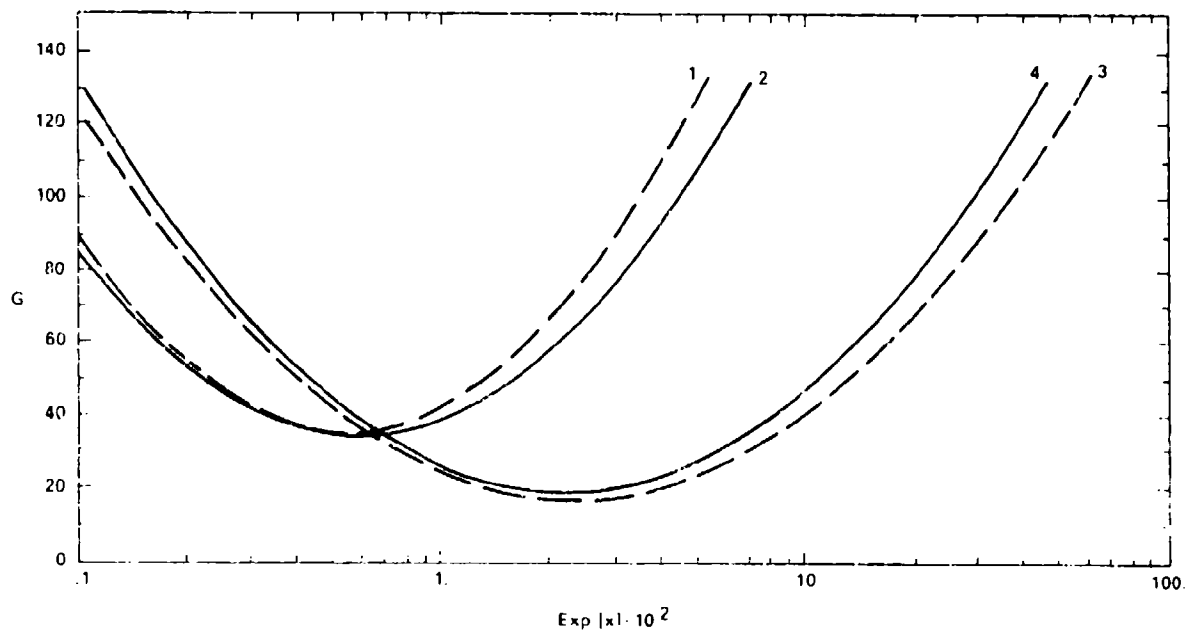


Fig. 2 - Comparison of two original curves and two predicted curves for Minicel foam. Curves 1 and 2 are for  $h/T=12$  at 21.1 degrees Celsius. Curves 3 and 4 are for  $h/T=6$  at -53.9 degrees Celsius. Curves 1 and 3 are based on Table 1 while curves 2 and 4 are based on Table 2.

TABLE 3  
Temperature and Impact Velocity Ranges for Constants of Table 2

MATERIAL	TEMPERATURE, °K		h/T*		DATA SOURCE
	MIN.	MAX.	MIN.	MAX.	
Minicel, .032g/cm <sup>3</sup>	327.1	344.3	4	30	9
Rubberized Hair, Type V	302.1	344.3	4	15	12
Polyether Urethane, .048g/cm <sup>3</sup>	302.1	344.3	3	30	10
Ethafoam, .032g/cm <sup>3</sup>	327.1	344.3	3	30	11

\*These are the limits of the data available for analysis in the data sources indicated.

TABLE 4  
Design Constants for Rubberized Hair,  
Type V, at 219.3°K

PROPERTY	C <sub>1</sub>	C <sub>2</sub>	STD. DEV.
Exp [x <sub>0</sub> ]	199.95	-.86	1.13
G <sub>0</sub>	3.99	.80	1.42
a <sub>2</sub>	1.14	1.07	2.01

Problem No. 1. An 18 kg (40 lb) object is to be subjected to a 0.61m (24 in) drop test. Allowable maximum acceleration is 25g and environmental temperatures are -25°C, 21°C and 60°C. Assume that the organization has opted for 32 kg/m<sup>3</sup> (2 lb/ft<sup>3</sup>) density Minicel as the preferred material.

Solution. The first step is to compute the minimum thickness which can possibly be used from

$$T_{\min} = h(G_m/C_1)^{-1/C_2} \exp [-C_3(\theta - \theta_0)/C_2], \quad (9)$$

A whole number value of T above T<sub>min</sub> is then selected in order to compute, in turn, the values of G<sub>0</sub>, a<sub>2</sub>, the radical from Eq. (5), x<sub>0</sub>, x<sub>max</sub>, and x<sub>min</sub>. The results are given in Table 6. A pad 8 cm thick and with x ranging from 4.50 to 4.82 will give the desired results. A pad 13 cm x 21 cm will produce an x of 4.67. Computed accelerations for this configuration at each temperature are also shown in Table 6.

Problem No. 2. An existing design for a 60 kg item uses a 30 cm by 30 cm pad 2.54

cm thick. Some damage has occurred in shipment and reappraisal of shock sensitivity indicates 50g is the maximum allowable in a 0.46 m drop. Temperature range is -23°C to 52°C. Could drop heights of this magnitude be the cause of damage? If so, by how much must the cushion thickness be increased to bring accelerations to an acceptable level? It is not desired to change the area of the pad and, again, 32 kg/m<sup>3</sup> Minicel is the preferred material.

Solution. Results are in Table 7. As before, T<sub>min</sub> is found and is very close to the thickness of this pad. When, however, expected performance at h/T = 18.1 and x = 4.552 are computed, the answer to the first question must be in the affirmative. A thickness increase of not quite 1 cm would produce safe performance at all temperatures.

Attention is particularly directed to the fact, as shown in Table 7, that accelerations at a given value of x can be higher at elevated temperatures than at low or room temperature conditions. It is unwise to assume that room temperature data can be extrapolated safely to the high or low temperatures normally expected in military distribution systems.

The two problems were deliberately chosen so that one or more features, such as temperature or thickness, were not covered by previously developed design curves or regression equations. The constants of Table 2 permit generating curve equations for any set of circumstances, within the limits stated in Table 3.

#### DISCUSSION

This paper uses data collected by others. The author cannot, therefore, guarantee that

TABLE 5  
Constants for  $G_o$  and  $\text{Exp}[x_o]$  as a Function of  $h/T$  at 295.9°K

MATERIAL	$G_o$		$\text{Exp}[x_o]$	
	$C_1$	$C_2$	$C_1$	$C_2$
Polyester Urethane, .064g/cm <sup>3</sup>	3.18	1.03	61.29	-.47
Rubberized Hair, .022g/cm <sup>3</sup>	3.31	.96	21.43	-.80
Rubberized Hair, .024g/cm <sup>3</sup>	3.39	.97	15.29	-.51
Polystyrene Foam, .006 0.024g/cm <sup>3</sup>	4.66	.97	367.90	-.79
Polyester Urethane, .040g/cm <sup>3</sup>	2.31	1.06	33.18	-.27
Polyether Urethane, .024g/cm <sup>3</sup>	3.04	1.09	35.89	-.25
Wood Fiber Felt, .029g/cm <sup>3</sup>	3.54	.95	8.76	-.35
Wood Fiber Felt, .038g/cm <sup>3</sup>	5.12	.94	13.74	-.45
Rubberized Hair, .032g/cm <sup>3</sup>	3.72	1.00	40.91	-.86
Polyethylene Foam, .032g/cm <sup>3</sup>	4.00	1.00	609.85	-.96
Wood Fiber Felt, .024g/cm <sup>3</sup>	3.25	.94	7.63	-.29
Cellulose Wadding	6.03	.87	4.99	-.34
Bound Fiberglass, .018g/cm <sup>3</sup>	4.41	.93	18.17	-.70

TABLE 6  
Solution to Problem No. 1

PROPERTY	TEMPERATURE, °C		
	21	-25	60
$T_{\min}$	6.95	7.28	6.68
$T = 8, h T = 7.625$			
$G_o$	21.8	22.8	21.0
$a_2$	10.6	13.0	8.9
Radical	.55	.41	.67
$x_o$	4.50	4.91	4.15
$x_{\max.}$	5.05	5.32	4.82
$x_{\min.}$	3.95	4.50	3.48
Set $x = 4.67$			
G	22.1	23.6	23.4

TABLE 7  
Solution to Problem No. 2  
(60 Kg Item, 50g Max., Pad Area 30 x 30,  
Drop Ht. 46cm, Minicel Cushion)

THICKNESS, cm	ACCELERATION, G		
	-23°C	21°C	52°C
2.54 (1 inch)*	58	66	73
2.68**	55	61	68
3.00	47	52	57
3.25	43	47	51
3.30	42	46	50
3.40	41	44	48
3.50	39	42	46
3.81 (1-1/2 inch)	36	38	41
5.08 (2 inch)	27	26	28

\*Original thickness

\*\*Theoretical minimum thickness, pad area free to vary.

the constants of Table 2 are as accurate as may be desirable for design use. The data used are, however, internally consistent and usable to demonstrate the essential point that time and temperature effects are predictable and can be modeled.

It should be noted that not every cushion structure necessarily exhibits behavior which can be modeled by a logarithmic parabola. The Military Handbook contains a few curves for two plastic films, formed to enclose bubbles of air, which do not. The structure of these cushions forecasts complex behavior involving not only air compression but also tensile effects in a plastic film, complicated by non-linear geometry. Nonetheless, even these curves are regular and could be modeled by suitable polynomials, and seem to be influenced in regular fashion by  $h/T$  ratio.

It is evident that pages 217 through 282 of MIL-HDBK-304 [4] are essentially redundant. It has been demonstrated that these 66 pages can be reduced to a few master curves and that the room temperature constants showing variation of the coordinates of the nadir and the variation of the latus rectum of the logarithmic parabola with respect to  $h/T$  can be tabulated. The effort is not very difficult, since the values of the constants can be estimated from the existing curves. The improvement therein can be determined by least squares techniques. The corrections are linear.

If the original data have been retained, they can be used to even better effect. While so doing, statistically valid rejection criteria for outliers must be enforced. Wyskida and his co-workers did use such criteria to good effect. One of their reports [17] contains a devastating critique of the "rejection by eyeball" technique apparently used by the contractor performing the test work backing up the curves in the Military Handbook. This handbook will have to be revised at some time in the near future, anyhow, since it is Department of Defense policy to convert to metric. All the data in the handbook are in English units.

It has been shown that effects of time and temperature on cushions can be modeled and can have marked effects on the behavior of the cushion, effects which a designer should consider. This leads to the inevitable conclusion that data must be accumulated concerning performance at other than room temperature. This, however, raises a fundamental question

concerning test procedures and data analysis. There is a systematic difference in the results obtained by Wyskida and his co-workers and the results in the Military Handbook for basically identical materials. Wyskida's curves exhibit lower accelerations for similar conditions at room temperature than do the curves published in the Military Handbook. It is difficult to hold material temperature constant if successive drops are to be made at extreme temperatures and Wyskida [17] advances the argument that performing five successive drops within a fairly short time is unrealistic and should be avoided.

The test procedures used in generating the Military Handbook did require five successive drops at a given height and static stress at not less than 1 minute intervals. The first reading was automatically discarded and the remaining four were simply averaged. When this is done, the true thickness may not be the original thickness, simply because material recovery times are relatively slow. As an example, a nominal 5.1 cm (2 in) sample of Minicel could be only 4.52 cm (1-25/32 in) thick when measured 3 minutes after impact from a height of 0.61 m (24 in). This does not seem like much of a loss in thickness, but it represents an 11 percent change in  $h/T$  and produces comparable changes in  $G_0$ ,  $x_0$  and  $a_2$ . Notably,  $G_0$  would, using the constants of Table 2, rise from 33.9 to 37.9.

Resolution of these differences is left to those who follow. With all test and data reduction procedures, however, the need for standardization and reproducibility soon outweighs the need for simulating the "real" world. Accordingly, this investigator sees no long range harm in, effectively, using first drop data, as was done by Wyskida and his co-workers. The design data are never completely definitive and should always be backed by tests of the actual package.

The foregoing statement does not apply to testing and recording data concerning semi-rigid foams. Here the designer is interested in the performance he might reasonably expect after a series of drops, since little or no recovery is reasonably to be expected. Publishing data after, say, the fifth drop using the original thickness as the base-line is laudable. Drysdale et. al. [16] did this for expanded polystyrene foam in 1963. More recently, Chatman [18] has done likewise, as does much of the manufacturers' literature. Unfortunately, the Military Handbook is silent on this point.



Not too long ago, computations as complex as those indicated by Eqs. (8) and (9) would be intractable for routine use. Any individual with a pocket scientific computer can now solve them readily and does not need tables of logarithms or a slide rule.

#### CONCLUSIONS

The conclusions which can be drawn from the foregoing are relatively few in number, but basic:

1. Performance of key elements of cushions depend upon the  $h/T$  ratio at all temperatures of possible interest.

2. The existing data in MIL-HDBK-304 can be readily converted to show the effects of the  $h/T$  ratio at room temperature.

3. Temperature effects above the glass temperature can be modeled by a simple exponential function.

4. Major changes in test methods, data collection procedures and reporting methods are required to take advantage of all of the foregoing.

5. It is possible to bring package cushion design data into some semblance of conformity with what polymer scientists have been teaching for years. This paper shows a simple way of doing so. It is hoped that someone will accept the challenge.

# LITERATURE CITED

1. ASTM D1596, Method of Test for Dynamic Properties of Package Cushioning Materials.
2. MIL-C-26861, Cushioning Material, Resilient Type, General.
3. W. G. Humbert and R. G. Hanlon, Package Engineering, April 1962.
4. MIL-HDBK-304B, Package Cushioning Design, 31 October 1978.
5. A. W. Nolle, J. Polymer Sci., 5 (1), 1, 1950.
6. W. G. Soper and R. C. Dove, Data Presentation for Cushioning Materials, 17th Annual Tech. Conf., Soc. Plastics Engs, Paper 27-4, January 1961.
7. D. McDaniel, Modeling the Impact Response of Bulk Cushioning Materials, US Army Missile Command Technical Rept. RD-75-16, 9 May 1975.
8. R. M. Wyskida and D. McDaniel, Modeling of Cushioning Systems, Gordon and Breach Science Publishers, New York, NY, 1980.
9. R. M. Wyskida and M. R. Wilhelm, Temperature Sensitive Dynamic Cushion Function Development and Validation for Hercules Minicel Thermoplastic Foam, The University of Alabama in Huntsville, Huntsville, AL, UAH Rept. No. 159 (MICOM Rept. No. RL-CR-75-1), Vol. I, September 1974.
10. R. M. Wyskida, M. R. Wilhelm and J. D. Bynum, Temperature Sensitive Dynamic Cushioning Function Development for Polyester and Polyether Type Polyurethane Foam, UAH Rept. No. 159 (MICOM Rept. No. RL-CR-75), Vol. III, December 1974.
11. R. M. Wyskida, M. R. Wilhelm and J. D. Bynum, Temperature Sensitive Dynamic Cushioning Function Development and Validation for Dow Ethafoam Polyethylene Foam, UAH Rept. No. 172 (MICOM Rept. No. RL-CR-75-4), Vol. I, July 1975.
12. R. M. Wyskida, M. R. Wilhelm and J. D. Bynum, Temperature Sensitive Dynamic Cushioning Function Development and Validation for Blocksom Rubberized Hair, UAH Rept. No. 172 (MICOM Rept. No. RL-CR-75-4) Vol. III, July 1975.
13. G. S. Mustin, Theory and Practice of Cushion Design, the Shock and Vibration Information Center, United States Department of Defense, 1968.
14. A. V. Tobolsky, "Stress Relaxation Studies of the Viscoelastic Properties of Polymers," Rheology, Theory and Applications, Vol. 2 (F. R. Eirich, ed.), Academic Press, New York, NY, 1958.
15. G. S. Mustin, A New Approach to Package Cushioning Design, The Shock and Vibration Information Bulletin No. 35, Part 5, 193, February 1966.
16. J. Drysdale, G. A. Gordon, E. E. Wheeler and P. D. Marsden, Packaging, 34, March, June and July 1963. Their curves may also be found as Figure 4.62 of reference 13.
17. R. M. Wyskida, M. R. Wilhelm, J. D. Bynum and J. D. Johannes, Development and Application of Confidence Intervals and Prediction Limits on Dynamic Cushioning Functions for Selected Temperature Sensitive Cushioning Materials, UAH Rept. No. 180 (MICOM Rept. No. RL-CR-76-3), October 1975.
18. R. L. Chatman, Package Engineering, 26, No. 8, 56-60, July 1981.

## EXTRANEOUS EFFECTS IN DAMPING MEASUREMENT

Robert J. Hooker  
Department of Mechanical Engineering  
University of Queensland  
St. Lucia  
Queensland 4067, Australia

and

S. Prasertsan  
Prince of Songkla University  
Hat-yai, Thailand

It is shown that for some material damping measurements the assumption that extraneous effects may be ignored on the basis of tests with a low damping specimen is not necessarily valid. Analytical and experimental investigations are reported for a common torsional damping apparatus arrangement in which load is applied to the specimen through end shanks. The experimental results indicate much greater errors associated with end effects than are expected from analytical considerations

### INTRODUCTION

In experimental investigations of the damping properties of materials great care is taken to ensure absence of extraneous losses. The development of an apparatus requires as a first step the reduction of extraneous effects and demonstration that either such effects are insignificant or that appropriate corrections can be made. An almost universal technique for assessing (the absence of) extraneous losses is to conduct tests, in the particular apparatus, with a specimen of material having inherent energy dissipation very much lower than that of the materials proposed for subsequent testing. The apparatus is developed to the extent that energy dissipated as measured with the low damping specimen is small compared with the proposed range of measurement. It is then assumed that extraneous effects may be neglected.

A comprehensive study was undertaken by Cottell, Entwistle and Thompson [1] with the aim of developing apparatus design details which ensure minimum unwanted losses. They reported

a loss factor of the order of 0.000003 (specific damping capacity 0.002%) for an aluminum alloy. This was at the time the lowest value of damping ever measured.

For some apparatus configurations, the assumption that extraneous effects may be neglected on the basis of tests with a low damping specimen is not necessarily valid. Consider an apparatus in which loading is applied to the specimen through some form of clamp. Typically the specimen has a "working section" and end "shanks" which are held in the clamps. Between working section and shank there is a "transition region", commonly a fillet. Sources of extraneous loss in the clamping region are:

- (1) Friction effects due to slip at clamp-specimen shank interface.
- (2) Inherent loss in the material of the clamp.
- (3) Inherent loss in the material of the specimen shank and transition region.

Sources (1) and (2) are tested adequately by the "low damping specimen" approach. In the case of source (3), the test with low damping specimen of necessity is one with low damping shanks. Shank losses are therefore low and are not assessed adequately. When a "high" damping specimen is tested, losses in the shank and transition region are taken to be associated with the working section. Normally, shank and clamp geometry are arranged to minimize losses of source (1) type, for example by the use of square cross-section in the shank, vee-clamps and a high clamping pressure. Thus substantial stress concentrations may occur in the shank and transition region. Since energy dissipation is stress dependent to the power 2 or more then the extraneous end effects may be significant.

An investigation of the significance of end effects has been carried out for a torsional apparatus. The stress distribution throughout working section, transition region and shank was determined by finite element analysis and the relative contributions of these regions to energy dissipation calculated. Experimental assessment was performed by tests on a range of specimens in which the end size, geometry and loading were kept constant but the volume of material in the working section varied.

#### PHYSICAL ARRANGEMENT

The study is based on an apparatus described by Hooker and Mead [2] and illustrated in principle in Figure 1. The specimens have a cylindrical working section and square end shanks, with a plain fillet providing transition between working section and end shank. They are excited in torsional vibration about the axis AB and experiments may be conducted with either one or two specimens in the apparatus. Operation is at steady state forced resonance, with vibratory torque applied to the inertia bar I by electrodynamic (permanent magnet and moving coil) exciters. Energy dissipated in the specimen is obtained by determining the energy supplied to the exciters.

Absence of extraneous losses other than those under investigation was verified by tests with low damping material (aluminum alloy, 5.0-6.0% Cu, 0.4% Si, 0.7% Fe, 0.3% Zn, 0.2-0.6% Pb). The high damping material tested was a manganese copper alloy ("Sonoston", 53% Mn, 37.5% Cu, 5% Al, 3% Fe, 1.5% Ni).

Specimen dimensions for both materials are given in Table I. The basis for specification of specimen dimensions was that three different lengths of working section be chosen and that all specimens in any particular material have the same torsional stiffness. Thus all tests for one configuration and one material would be conducted at the same frequency thereby eliminating any frequency dependent effects.

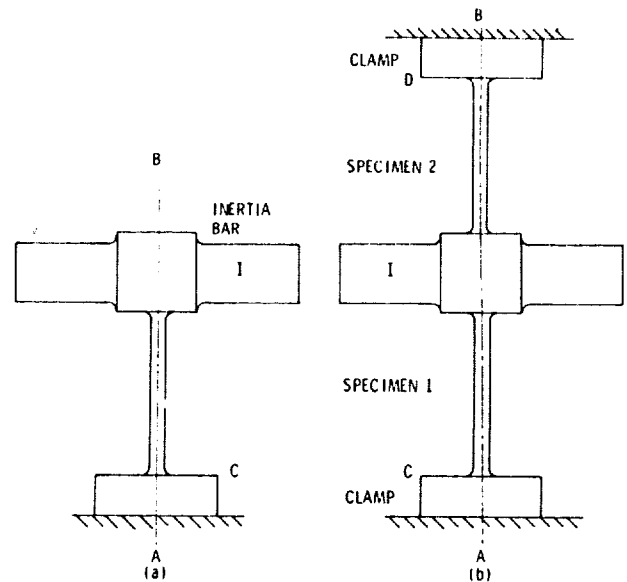


Figure 1. Apparatus configurations  
(a) One specimen arrangement,  
(b) Two specimen arrangement

TABLE I. SPECIMEN DETAILS

Cylindrical working section  
Square end shanks, 12.7 mm x 25.4 mm long  
Transition fillets, 3 mm radius

Specimen Type No. Working Section	1	2	3	4
Length mm	101.60	101.60	127.00	152.40
Outer Dia. mm	10.60	8.16	8.65	9.06*
Inner Dia. mm	9.53			

\*Specimen 4 in MnCu, outer dia. = 8.74

#### ANALYTICAL STUDY

An indication of the order of magnitude of any effect due to the fillet can be obtained from a stress concentration factor. From Petersen [3], a typical stress concentration factor for the type 2 specimen is 1.1 and the fillet region occupies one-fifteenth of the working section volume. The proportion of energy dissipation associated with the fillet therefore amounts to  $(1.1)^n/15$ , where  $n = 2.33$  (see Section 4.2), i.e., 8.3%. This result is an overestimate of the effect of the fillet since the maximum stress concentration factor applies to portion only of the fillet region.

Stress distribution in working section, fillet and end shank was determined by a finite element analysis. The loading considered was torsion and stresses produced by initial clamping pressure were ignored since steady mean stresses have only a small effect on energy dissipation for "Sonoston" alloy [2]. Element mesh details

are shown in Figure 2. As usual the fineness of

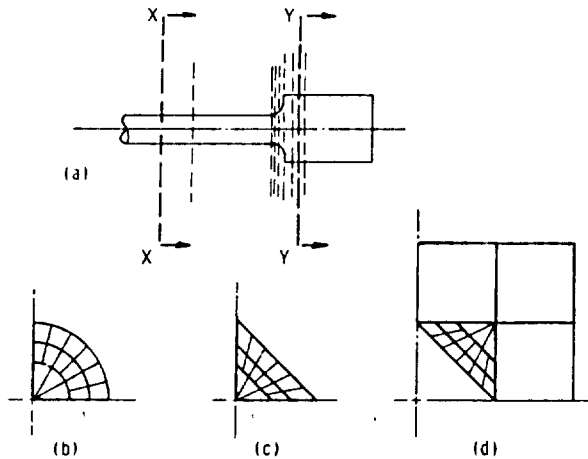


Figure 2. Element mesh details  
(a) Transverse dividing planes  
(b) Section XX  
(c) Section YY  
(d) Section through clamp at YY

mesh is a compromise with computational capability. Results were verified by comparison with the known stress distribution in the cylindrical working section.

In the specimen working section the stress state is pure shear, but in the square shank, especially near the edges, a combined direct/shear stress state exists. Prediction of damping therefore requires knowledge of the nature of material behaviour under combined stress loading, i.e., of the way in which energy dissipation depends on the relative magnitudes of direct and shear stress amplitudes. Two common bases for assessing material behavior, which may be considered as limiting conditions, are:

- (1) Energy dissipation dependent on total strain energy, or
- (2) Energy dissipation dependent on distortional strain energy.

Calculations for energy dissipation have been carried through for both cases, with the contributions of working section, fillet and shank determined separately. A damping exponent  $n = 2.33$  was used (see Section 4.2).

For case (1) and specimen type 1, the contributions to total energy dissipation of fillet and shank regions were 3.8% and 0.3% respectively, giving a total predicted extraneous effect of 4.2%. The corresponding results for case (2) are 3.8, 1.2 and 5.0%. As will be seen later, these results are low. It is therefore relevant to note here that the finite element analysis, even though it was performed with 117 elements on one-eighth of the specimen (utilizing symmetries), did not produce stress concentration effects in

the fillet. It may be that a very much finer mesh is required.

#### 4. EXPERIMENTAL STUDY

##### 4.1 Low Damping Specimens

A series of tests was conducted with the low damping specimens to establish the performance capability of the apparatus and hence ensure absence of extraneous losses associated with the apparatus itself. Results are shown in Figure 3, in which energy dissipated is plotted against rotational amplitude  $\theta_0$  of the inertia bar for six test configurations. For the cases of one specimen installed, all tests are at the same frequency (24 Hz) and one particular value of  $\theta_0$  implies also for all specimens equal amplitudes of rotational velocity, energy stored and torsional moment. However, surface strain amplitude differs in each case. It is seen from Figure 3 that results for all one-specimen cases collapse to the one power law line,  $\Delta U = 0.40 \theta_0^{2.16}$ .

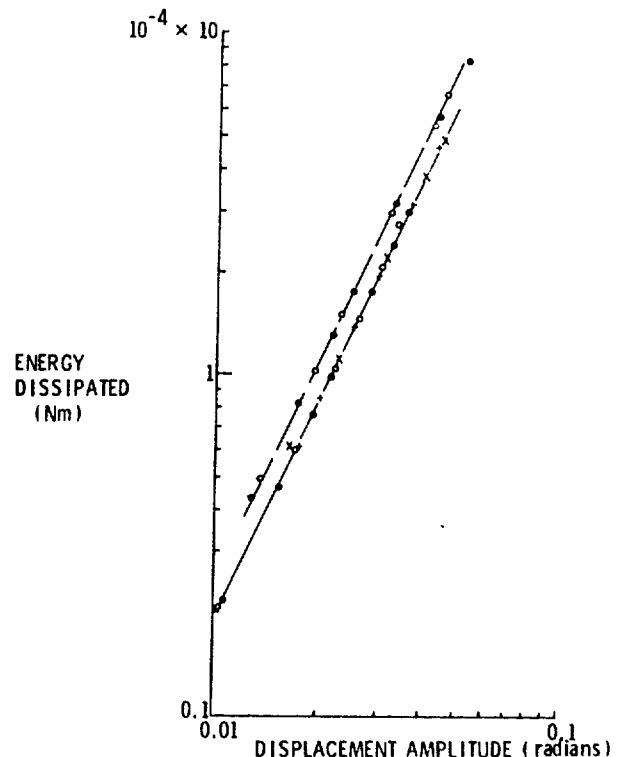


Figure 3. Energy dissipated per cycle, aluminium alloy.  
o specimen type 1,  
• type 2, + type 3, x type 4  
-- -- one specimen,  
— — two specimens

For specimen geometries 1 and 2, further tests were conducted with two specimens installed in the apparatus, giving a test frequency  $24\sqrt{2} = 34$  Hz. Results from these tests are also shown in Figure 3, from which it can be seen that the increase in frequency has resulted in an increase in energy dissipated. It can be anticipated that air damping effects will be significant and will be velocity dependent. Velocity dependence from Figure 3, follows the relation  $\dot{\theta}^{2.16}$ , in which case the double specimen tests would be expected to give energy dissipation 2.11 times that for the single specimen case, whereas the ratio found experimentally is 1.32. Hence losses may be considered partly displacement dependent and partly velocity dependent, i.e.

$$\Delta U = a \dot{\theta}_0^{2.16} + b \dot{\theta}_0^{2.16} \quad (1)$$

$$= a \dot{\theta}_0^{2.16} + b (\omega \theta_0)^{2.16} \quad (2)$$

Solving on this basis gives  $a = 0.285$  and  $b = 2.19 \times 10^{-6}$  (in S.I. units). For the one-specimen configuration, the velocity dependent loss is 28% of the total loss.

The total energy dissipation at maximum vibrational amplitude, for the one-specimen low damping material case, corresponds to a specimen loss factor of 0.0008. This compares with values greater than 0.025 for the high damping material tests. Hence extraneous effects in the apparatus account for less than 4% of the losses measured.

#### 4.2 High Damping Specimens

End effects were examined by tests with high damping solid specimens types 2, 3 and 4, of nominal lengths 100, 125 and 150 mm but identical end shank and transition geometry. Again the diameters were selected to produce equal natural frequencies. Results are shown in Figure 4, plotted as energy dissipated  $\Delta U$  versus surface shear strain amplitude  $\gamma_m$ . The results follow a power law and can be represented as

$$(\Delta U)_i = J_i \gamma^n \quad i = 2, 3, 4 \quad (3)$$

where  $n = 2.33$ ,  $J_2 = 4.83 \times 10^4$ ,  $J_3 = 6.11 \times 10^4$ ,  $J_4 = 6.58 \times 10^4$  (Nm). At  $\gamma_m = 0.001$ , the loss factors are  $\eta_2 = 0.0266$ ,  $\eta_3 = 0.0238$  and  $\eta_4 = 0.0210$ .

For the same surface shear strain amplitude,  $\Delta U$  increases with increase of specimen volume, but the increase is less than in proportion to volume. The results therefore suggest that total energy dissipated is the sum of a volume-independent (end effect) component and a volume-dependent (working

section) component. Hence it is postulated that

$$\Delta U = (c + dV) \gamma_m^{2.33} \quad (4)$$

$$\text{i.e. } J_i = c + dV_i \quad (5)$$

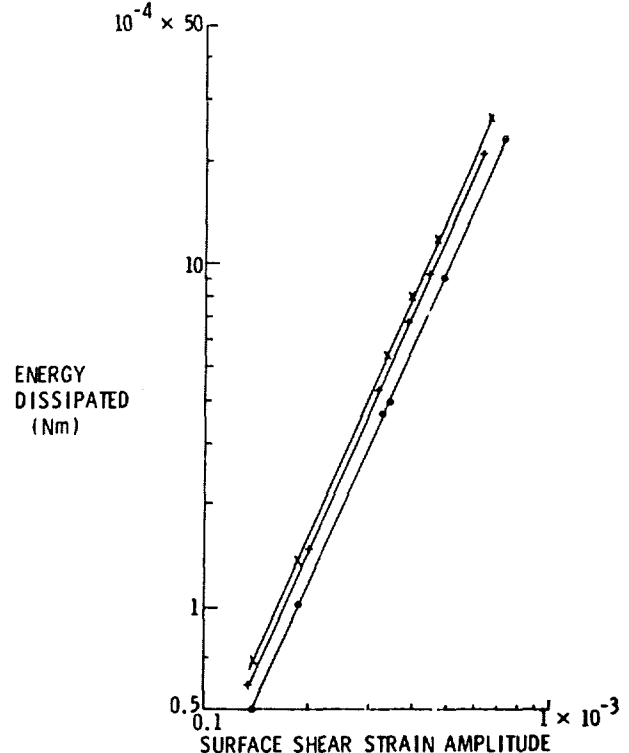


Figure 4. Energy dissipated per cycle, manganese-copper.  
● specimen type 2, + type 3,  
x type 4

The best fit straight line to the three experimental points available gives  $c = 2.50 \times 10^4$  Nm,  $d = 4.80 \times 10^9$  Nm<sup>-2</sup>, with a root mean square error which is 2.5% of the mean  $J$  value. The energy dissipated in the whole specimen is therefore

$$\Delta U = (2.50 \times 10^4 + 4.80 \times 10^9 V) \gamma_m^{2.33} \quad (6)$$

The significance of this result is that for the three specimens tested (types 2, 3, and 4), the losses associated with end effects, as a percentage of the total loss measured, are respectively 51%, 42%, and 37%. For example, the experimental loss factor for specimen 2 at  $\gamma_m = 0.001$  is  $\eta = 0.0266$ , but the true specimen loss factor is 0.0132. This corresponds to a material (i.e. uniform stress distribution situation) loss factor of  $0.0132 \times (n + 2) / 4 = 0.0143$ , see [4]. Material loss factor as determined in this way is the same for all three specimens and is shown in Figure 5.

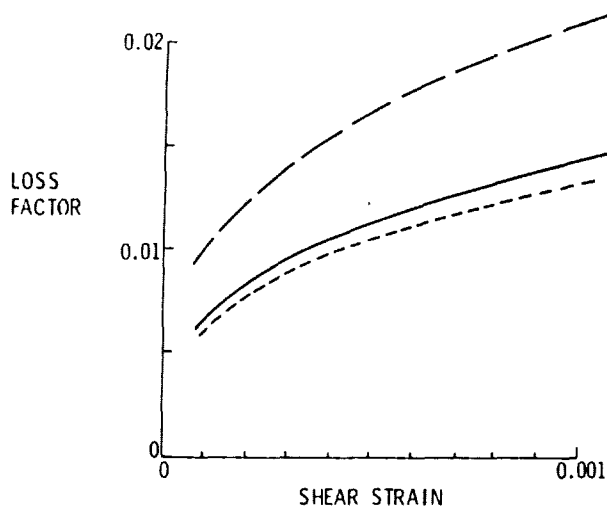


Figure 5. Loss factor.

— — — — — entire specimen, type 4  
 - - - - - working section,  
 - . - . - material

Tests were also performed in one-specimen configuration using specimen type 1 and in the two-specimen configuration with specimens type 1 and with specimens type 2. With two specimens installed, the total energy dissipation was doubled, i.e. both working section and end effect losses were doubled and the results per specimen are unchanged.

With hollow specimens, the stress distribution in the working section is almost uniform (inner diameter/outer diameter = 0.90), so that for the same strain energy a greater proportion of the material is highly stressed and higher values of energy dissipated are expected. The same power law was observed ( $n = 2.33$ ), with energy dissipated greater than for solid specimens in the ratio 2.0. By calculation [4], for  $n = 2.33$  and diameter ratio 0.90, the anticipated ratio is 1.81. These values may be considered reasonably consistent, since the specimen end geometries (solid and hollow) are different.

## 5. CONCLUSION

It has been shown in principle that tests with a low damping specimen do not necessarily prove the absence of extraneous end effects in damping measurement. However, a substantial discrepancy exists between the magnitudes of such effects as predicted analytically and as determined experimentally. For the particular situations considered, the analysis predicts extraneous effects amounting to 5% and the experiments indicate effects up to 50%. Investigation of this discrepancy, preferably by alternative approaches, is necessary.

## NOTATION

a, b, c, d constants  
 $n$  damping law exponent  
 $J$  damping law constant  
 $U$  energy stored  
 $\Delta U$  energy dissipated per cycle =  $J\gamma_m^n$   
 $\gamma_m$  surface shear strain amplitude  
 $\theta_o$  rotational displacement amplitude  
 $\dot{\theta}_o$  rotational velocity amplitude  
 $\eta$  loss factor =  $\Delta U/2\pi U$

## Subscript

i specimen type number,  $i=1,2,3,4$

## REFERENCES

- [1] Cottell, G.A., Entwistle, K.M. and Thompson, F.C., 1948. The Measurement of the Damping Capacity of Metals in Torsional Vibration. Journal Inst. Metals 74, 373-424.
- [2] Hooker, R.J. and Mead, D.J., 1981. An Apparatus for Determination of the Effect of Mean Strain on Damping. Journal Phys. E: Sci. Instrum. 14, 202-207.
- [3] Peterson, R.E., 1974. Stress Concentration Factors. Wiley, NY.
- [4] Harris, C.M. and Crede, C.E., 1976. Shock and Vibration Handbook. McGraw-Hill, NY, 2nd Edition, Chapter 36.

#### DISCUSSION

Mr. Henderson (AFWAL): Did you consider the nonlinear effects in your finite element analysis?

Mr. Hooker: The finite element analysis was an elastic analysis, and then the dissipated energy was calculated on the basis of the  $J$  sigma to the  $N$  law on both an equivalent stress basis, Von Neiser's stress, and a total strain energy basis; this gives a band within which the results would be expected.



DYNAMIC ANALYSIS OF  
A LARGE STRUCTURE WITH ARTIFICIAL DAMPING

Q.L.Tian, D.K.Liu\*, Y.P.Li, and D.W.Wang  
Institute of Mechanics, the Chinese Academy of Sciences,  
Beijing, China.

A complex modal synthesis method is presented in this paper to analyse the dynamic response of a large structure with artificial damping. Firstly, the whole structure is dis-integrated into several substructures, then the complex redundant force vector is applied to represent the reaction between the interfaces of substructures, the reaction between the absorbers and the substructures. The locally modified stiffness matrix is applied to represent the local constrained layer damping treatment. The motion equation of the assembled structure is deduced by the fixed interface mode synthesis method, as a result a complex matrix in the form of localized modification of the original undamped matrix, is obtained. Owing to the modal truncation and the behavior of localized modification, the size of this new matrix is small enough to be solved by a complex eigenvalue program with low cost. The transfer function of the assembled system was calculated by the complex modal superposition method, so that the dynamic response could be calculated when the structure is subjected to a forced vibration, no matter it is harmonic or random.

#### INTRODUCTION

There are many effective methods for suppressing the vibration level of a structure, for example, adding viscoelastic layers on some flexible members(1), adding absorbers on antinodal points(2), inserting some viscoelastic links between antinodal parts of two parallel elements(3), using a part of a structure as an auxiliary mass which is supported on another parts by means of some viscoelastic materials (4), changing some rigid joints into viscoelastic ones so as to increase damping(5), etc., a proper combination of above techniques can be used to obtain a considerably improvement of vibration performances of some structure with a low cost.

One of the keys to extend the use of damping technology is the ability to analyze the effect on dynamic response of structure by these damping treatments. Local damping treatment will lead to a non-proportional damping matrix, its dynamic analysis has been found to be rather difficult. Modal Strain Energy Method was firstly incorporated with the analysis

of damped structure by NASTRAN Program(6), which found to be the most attractive method, but a significant error would be introduced, when it is applied to a structure with heavy discrete damping. A complex modal synthesis method was presented to solve this kind of problem. Unlike usual method, it is unnecessary to double the size of the matrix and replace the second order differential equations by first order equations, the complex eigenvalue and eigenvector of the complex matrix will be directly calculated by a complex eigensolution program. On the substructure level, the eigenproblem are solved by SAPIV. Then the Ritz vectors of the superstructure are synthesized from the substructural modes. Owing to the modal truncation, the degree of freedoms of superstructure after being synthesized is reduced considerably, so it can be calculated by a complex eigensolution with low cost.

The transfer function of the assembled system was calculated by the complex modal superposition method, but it is unstable in the domain of negative frequencies, so it is impossible to analyze the random response. To solve this problem, the actual solution is expressed by the sum of a pair of conjugate values, as suggested by Y.Tsushima in ref(7).

\* Space Science and Technology Center,  
The Chinese Academy of Sciences.

The formulation of variance for moment of a cantilever structure is derived, when its foundation exerted by a random excitation.

#### THE MOTION EQUATION OF SUBSTRUCTURE

The whole structure is dis-integrated into several substructures, among which two substructures "s" and "s+1" are shown in fig.1.

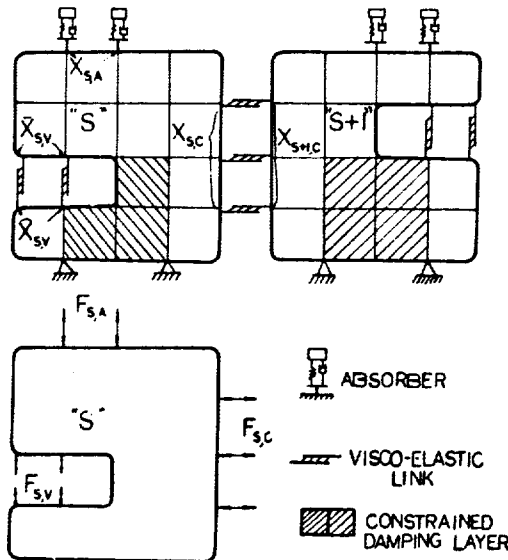


FIG. 1: The Damping treatments and its reactions on Substructure

1. A series of viscoelastic links are inserted between some nodes of the common interface. Let the general coordinate vector of the whole system be designated by  $X$ , an  $N \times 1$  vector.

$$X = [\dots, X_s^T, X_{s+1}^T, Y_s^T, Y_{s+1}^T, \dots]$$

where superscript  $T$  represents transpose,  $X_s$  is the general coordinate vector of the substructure  $s$ , which is an  $N_s \times 1$  vector.  $Y_s$  is the general coordinate vector of the absorbers on the substructure  $s$ , which is an  $N_{s,a} \times 1$  vector.  $N_s$  and  $N_{s,a}$  are the number of D.O.F. of the substructure  $s$  and absorbers attached on it respectively. The vector  $X_s$  is related to  $X$  through a project matrix  $A_s$ ,  $X_s = A_s X$ , where  $A_s = [\dots, 0, I, 0, \dots]$  is an  $N \times N$  matrix, its elements are zero everywhere, except at the location corresponding to  $X_s$  in  $X$ , where the submatrix is an unit matrix. These links give a couple of force (or torque) vectors which having same value but in the opposite directions, acting on the interface between the substructure "s" and "s+1".

$$F_{s,c} = T_{s,c} \{X_{s,v} - X_{s+1,v}\} = T_{s,c} P_{s,c} X \quad (1)$$

where  $T_{s,c}$  is an  $N_{s,c} \times N_{s,c}$  complex diagonal matrix, its elements are the complex rigidity of these links,  $N_{s,c}$  is the number of links between the interfaces, and

$P_{s,c} = [0, 0, \dots, 0, I, 0, 0, -I, 0, \dots]$  is an  $N_{s,c} \times N$  matrix, its elements are zero everywhere, except two opposite unit matrices located at the positions corresponding to  $X_{s,c}$  and  $X_{s+1,c}$  in vector  $X$ .

2. Several viscoelastic links are inserted between some antinodal points of parallel elements of substructure  $s$ , resulting in a couple of force (or torque) vectors acting on each of these points.

$$F_{s,v} = T_{s,v} P_{s,v} X \quad (2)$$

where  $P_{s,v} = [0, 0, \dots, 0, I, -I, 0, \dots, 0]$  is an  $N_{s,v} \times N$  matrix, it contains two unit matrices, they have opposite sign, located at the positions corresponding to  $X_{s,v}$  and  $X_{s,v}$  in vector  $X$ , and all other submatrices are zeros, and  $T_{s,v}$  is an  $N_{s,v} \times N_{s,v}$  complex diagonal matrix, its elements are the complex rigidity of these links, which connect the vectors  $X_{s,v}$  and  $X_{s,v}$ ,  $N_{s,v}$  is the number of the links.

3. Adding absorbers on some antinodal points of substructure  $s$  is equivalent to applying a force (or torque) vector to it, i.e.,

$$F_{s,a} = T_{s,a} \{X_{s,a} - Y_s\} = T_{s,a} P_{s,a} X \quad (3)$$

where  $T_{s,a}$  is an  $N_{s,a} \times N_{s,a}$  diagonal matrix, its elements is the complex rigidity of the absorbers,  $N_{s,a}$  is the number of the absorbers on substructure "s" and  $P_{s,a} = [0, \dots, I, 0, 0, \dots, -I, 0, 0, \dots]$  is an  $N_{s,a} \times N$  matrix, it contains two unit matrices, they have opposite sign, located at the positions corresponding to  $X_{s,a}$  and  $Y_s$  in vector  $X$ , and all other submatrices are zeros.

4. Adding constrained damping layer on some members to introduce a local modification of the stiffness matrix, for example, when constrained damping layer is added to a tension-compression member, the member's rigidity will change from  $EF/L$  to  $\frac{2EcFc + EF}{L} (a + ib)$  (8)(9)

where  $E_c F_c/L$  is the axial rigidity of the constraining plate,  $a$  and  $b$  are two constants, which are related to the damping layer and member's geometric parameters. When a simple constrained damping layer is added to a beam, its flexural rigidity will be transformed from

$$EI_0 \text{ to } EI_0 \left(1 + \frac{x}{1+x}\right) y$$

where  $EI_0$  is the uncoupled flexural rigidity,  $x$  and  $y$  are two parameters. (1)

When a complex constrained damping layer is used, or it is added on a complex member, the member's rigidity will be determined by the analysis of finite element method or experiment

After the system is treated by means of constrained damping layer, the local modification of the stiffness matrix will be of form

$$K_{s,l} X_s = K_{s,l} A_s X$$

where  $K_{s,l}$  is an  $N_s \times N_s$  matrix, its elements are determined by the complex rigidity of the localized constrained damping layer, the other elements, which are not related to damping layer, are all zeros. So far four kinds of damping treatments have been mentioned. The first three of them are applied on the boundary of the substructure. The motion equation of the substructure "s" is derived from the summing of all the contributions of four kinds of treatment, that is,

$$A_s^T M_s A_s \ddot{X} + A_s^T K_s A_s X + A_s^T K_{s,l} A_s X + P_{s,a}^T T_{s,a} P_{s,a} X + P_{s,v}^T T_{s,v} P_{s,v} X + P_{s,c}^T T_{s,c} P_{s,c} X = -A_s^T M_s \{1\} \ddot{X}_0 \quad (4)$$

where  $\ddot{X}_0$  is the acceleration of the foundation.

#### MOTION EQUATION OF THE WHOLE SYSTEM

The eq. (4) is the motion equation of the substructure s, in which the coordinates are arranged in order of the global coordinate. All the motion equations of other substructures can be derived similarly, so the motion equation of the whole system can be assembled from them, i.e.

$$M \ddot{X} + K X = -M \{1\} \ddot{X}_0 \quad (5)$$

where

$$M = \begin{bmatrix} M_s & & & \\ & M_{s+1} & & \\ & & R_s & \\ & & & R_{s+1} \end{bmatrix} \quad (6)$$

$M_s$  is the mass matrix of the substructure S.

$R_s$  is an  $N_s \times N_s$  diagonal matrix, its elements are the masses of the absorbers on the substructure S.

$$K = K_1 + K_2 + K_L \quad (7)$$

where  $K_1$  is the stiffness matrix of the original unassembled structure,  $K_1$  and  $K_2$  are the modified stiffness matrices of the damped structure.

$$K_1 = \begin{bmatrix} K_s & & & \\ & K_{s+1} & & \\ & & C & \\ & & & 0 \end{bmatrix} \quad (8)$$

$$K_L X = A_s^T K_{s,l} A_s X \quad (9)$$

$$K_2 X =$$

$$\begin{bmatrix} T_{s,c} & & -T_{s,c} & & -T_{s,a} & & \\ & & & & & & \\ & -T_{s,c} & & T_{s+1} & & & -T_{s+1,a} \\ & & & & & & \\ & -T_{s,a} & & & T_{s,a} & & \\ & & & -T_{s+1,a} & & T_{s+1,a} & \end{bmatrix} \begin{bmatrix} X_{s,b} \\ X_{s,i} \\ X_{s+1,b} \\ X_{s+1,i} \\ Y_s \\ Y_{s+1} \end{bmatrix} \quad (10)$$

$$\text{where } \begin{bmatrix} X_{s,b} \\ X_{s,i} \end{bmatrix} = X_s$$

$X_{s,b}$  are attachment degrees of freedom of the substructure s,  $X_{s,i}$  are internal D.O.F. of substructure s. Successively arranging the D.O.F., that are related to the three kinds of damping treatment on the boundary of substructure, gives

$$T_s X_{s,b} = \begin{bmatrix} T_{s,c} & & & & \\ & T_{s,v} & & -T_{s,v} & \\ & & -T_{s,v} & & T_{s,v} \\ & & & & \\ & & & & T_{s,a} \end{bmatrix} \begin{bmatrix} X_{s,c} \\ X_{s,v} \\ X_{s,v} \\ X_{s,a} \\ X_{s,r} \end{bmatrix} \quad (11)$$

where all matrices are diagonal,  $X_{s,r}$  are the D.O.F. of the nodal points on the boundary, which are unrelated to the first three kinds of damping treatment. The total number of D.O.F. of the whole system is equal to the sum of the number of D.O.F. of all substructures and all absorbers, i.e.,

$$N = \sum N_s + \sum N_{s,a}$$

#### MODAL SYNTHESIS METHOD

For a large structure, N seems too large to solve complex eigenvalue, so the constraint modes and truncated constrained normal modes are superposed to obtain a modal transformation of the physical coordinates,

$$X_s = \begin{bmatrix} X_{s,b} \\ X_{s,i} \end{bmatrix} = \begin{bmatrix} I & 0 \\ U_{s,b} & U_{s,i} \end{bmatrix} \begin{bmatrix} Q_{s,b} \\ Q_{s,i} \end{bmatrix} = W_s Q_s \quad (12)$$

where  $U_{s,b}$  are the constraint modes, and  $U_{s,i}$  are the truncated constrained normal modes. Both  $U_{s,b}$  and  $U_{s,i}$  can be calculated by SAPIV.

$Q_{s,b}$  are attachment D.O.F.  
 $Q_{s,i}$  are modal D.O.F.

$$\text{Let } W = \begin{bmatrix} W_s & & & \\ & W_{s+1} & & \\ & & I & \\ & & & I \end{bmatrix} \quad (13)$$

$$\text{and } Q^T = \begin{bmatrix} \dots & Q_s^T & Q_{s+1}^T & Y_s^T & Y_{s+1}^T & \dots \end{bmatrix} \quad (14)$$

$$\text{then } X = WQ \quad (15)$$

substituting eq. (15) into eq. (5) and pre-multiplying by  $W^T$ , then eq. (5) becomes

$$W^T M \ddot{Q} + W^T K Q = -W^T M \{1\} \ddot{X}_0, \text{ i.e.,} \quad (16)$$

$$m \ddot{Q} + k Q = -W^T M \{1\} \ddot{X}_0$$

where

$$m = \begin{bmatrix} W_s^T M_s W_s & & & \\ & W_{s+1}^T M_{s+1} W_{s+1} & & \\ & & R_s & \\ & & & R_{s+1} \end{bmatrix} \quad (17)$$

$$k = W^T K_1 W + W^T K_2 W + W^T K_3 W \quad (18)$$

$$W^T K_1 W = \begin{bmatrix} W_s^T K_s W_s & & & \\ & W_{s+1}^T K_{s+1} W_{s+1} & & \\ & & 0 & \\ & & & 0 \end{bmatrix} \quad (19)$$

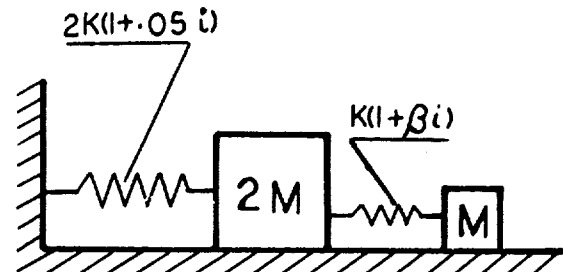
$$W^T K_2 W = \begin{bmatrix} W_s^T K_{s,l} W_s & & & \\ & W_{s+1}^T K_{s+1,l} W_{s+1} & & \\ & & 0 & \\ & & & 0 \end{bmatrix} \quad (20)$$

Since the discrete dampers are located on the boundary only, so  $W^T K_2 W$  has the same form as matrix  $K_2$ , but its dimension is condensed from  $N \times N$  to  $n \times n$ , due to the truncated modal transformation. Through this transformation the dimension of the matrix equation is reduced from  $N \times N$  to  $n \times n$ ,  $n$  is the number of the D.O.F. of  $Q$ .

#### COMPLEX TRANSFER FUNCTION

Eq. (16) is a complex equation, its approximate solution can be obtained with the modal strain energy method, as shown in ref. (6), but if the structure with heavily discreted damping is calculated by this method, a considerable error will be introduced. For exam-

ple, a two-D.O.F. system is shown in fig. 2.



A 2 D.O.F. System with Complex Springs  
 FIG. 2.

The loss factor of the  $r$ 'th mode of this two-D.O.F. system, with different  $\beta$ , is calculated by the modal strain energy method and complex eigenvalue method respectively, its results are shown as follows.

TABLE 1

The Modal Damping of the 2 D.O.F. System

$\eta_r$ $\beta$	0.2	0.4	0.6	1.0
$\eta_1$ exact	0.100	0.150	0.183	0.186
appx.	0.100	0.167	0.233	0.370
$\eta_2$ exact	0.150	0.268	0.433	0.752
appx.	0.167	0.283	0.416	0.683

Note that, if  $\beta = 1.0$  a significant error of  $\eta$  will be introduced, when this problem is calculated by the approximate method - modal strain energy method. To overcome this drawback, the complex eigenvalue  $\lambda_r$  and the corresponding eigenvectors  $V_r$  ( $r=1,2,\dots,n$ ) are founded by the Q.R. Program, directly.

where

$$\lambda_r = -\omega_r^2 (1 + i\eta_r) \quad (21)$$

and  $\eta_r$  is the  $r$ 'th modal damping.

Note that the complex matrix  $k$  is symmetric, so the eigenvectors satisfy the orthogonality condition.

$$V_r^T M V_s = 0, \quad r \neq s \quad (22)$$

when the vector has been scaled to satisfy the normalizing condition

$$V_r^T M V_r = 1$$

$$\text{then } V^T M V = I \quad (23)$$

$$\text{and } V^T K V = -\Lambda \quad (24)$$

where

$$\Lambda = \begin{bmatrix} -\lambda_1 & & \\ & -\lambda_2 & \\ & & \ddots \\ & & & -\lambda_n \end{bmatrix}$$

Returning to equation (16), introducing the change of coordinates

$$Q = VZ$$

pre-multiplying by  $V^T$ , and using eq.(23) and (24), the set of uncoupled equations is obtained as:

$$\ddot{Z}_r(t) + \omega_r^2(1 + i\eta_r)Z_r(t) = -V_r^T W^T M^{-1} \ddot{X}_0(t) \quad (25)$$

$r = 1, 2, \dots, n$

Applying Fourier transformation to eq. (25), then we obtain

$$\bar{Z}_r(\omega) = \bar{H}_r(\omega) \bar{F}_r(\omega) \quad (26)$$

where

$$\bar{H}_r(\omega) = \frac{1}{\omega_r^2(1 + i\eta_r) - \omega^2} \quad (27)$$

and

$$\bar{F}_r(\omega) = -\bar{V}_r^T W^T M^{-1} \ddot{X}_0(\omega) = -\sum V_{r,s} W_{s,j} \ddot{X}_{0,j}(\omega) = D_r \ddot{X}_0(\omega) \quad (28)$$

The denominator of  $\bar{H}_r(\omega)$  has two roots  $\omega_{r,2} = \pm \omega_r(1 + i\eta_r)^{1/2}$ , root  $-\omega_r(1 + i\eta_r)^{1/2}$  is lower than the real axis in the complex plane, so  $\bar{H}_r(\omega)$  is unstable in the domain of negative frequencies. To obtain a stable solution in the whole frequency range the actual solutions are expressed by the sum of a pair of conjugate values, as suggested by reference (7), i.e.,

$$\bar{Z}_r(\omega) = \bar{H}_r(\omega) \bar{F}_r(\omega)|_{\omega > 0} + \hat{H}_r(\omega) \hat{F}_r(\omega)|_{\omega < 0} \quad (29)$$

where  $\bar{H}_r(\omega)$  and  $\bar{F}_r(\omega)$  are obtained from eq.(27) and (28), respectively,  $\hat{H}_r(\omega)$  and  $\hat{F}_r(\omega)$  are the conjugates of  $\bar{H}_r(\omega)$  and  $\bar{F}_r(\omega)$ , respectively. Eq. (29) is the solution of modal coordinate in frequency domain.

Similarly, the displacement vector has the form

$$\bar{X}(\omega) = W[\bar{V} \bar{Z}(\omega)|_{\omega > 0} + \hat{V} \hat{Z}(\omega)|_{\omega < 0}] \quad (30)$$

#### RANDOM VIBRATION

When a cantilever structure exerted by the steady random vibration of a base movement, the maximum bending moment often occurs at its root section. When the fixed interface modal synthesis method is used, the bending moment at the root section can be divided into two parts, one of them is contributed by the attachment D.O.F., i.e.,

$$M_1(\omega) = M_{j,b} \bar{X}_j + M_{j,b} \{\bar{V}_j \bar{Z}|_{\omega > 0} + \hat{V}_j \hat{Z}|_{\omega < 0}\} \quad (31)$$

where subscript "j" represents the j'th attachment D.O.F.,  $M_{j,b}$  is the static bending moment

at the root section, which can be calculated by SAPIV or determined by the experiment, by means of fixing all the attachment D.O.F., except  $X_j = 1$ . The other part is the dynamic bending moment at the root section, contributed by the normal modes, i.e.,

$$M_2(\omega) = \sum \omega_k^2 L^T M_k \{\bar{V}_k \bar{Z}|_{\omega > 0} + \hat{V}_k \hat{Z}|_{\omega < 0}\} \quad (32)$$

where  $L^T$  is a row vector, that consists of the heights of masses, which are above the root section,

$W_k$  is the k'th column of matrix  $W$ ,  $V_k$  is the k'th row of matrix  $V$ .

$$\text{Let } \omega_k^2 L^T M_k = C_k \quad (33)$$

$$\text{and } \sum C_k \bar{V}_{n,k} + \sum M_{j,b} \bar{V}_{n,j} = \bar{B}_n \quad (34)$$

$$\sum C_k \hat{V}_{n,k} + \sum M_{j,b} \hat{V}_{n,j} = \hat{B}_n \quad (35)$$

$$\text{Then } \bar{M}(\omega) = \sum (\bar{B}_n \bar{Z}_n|_{\omega > 0} + \hat{B}_n \hat{Z}_n|_{\omega < 0}) \quad (36)$$

and its conjugate is

$$\hat{M}(\omega) = \sum (\hat{B}_n \hat{Z}_n|_{\omega > 0} + \bar{B}_n \bar{Z}_n|_{\omega < 0}) \quad (37)$$

The spectral density for the base moment is

$$S_{MM}(\omega) = \lim (1/T \bar{M} \hat{M}) = \lim \sum \sum (\bar{B}_n \hat{B}_m \bar{Z}_n \hat{Z}_m|_{\omega > 0} + \hat{B}_n \bar{B}_m \hat{Z}_n \bar{Z}_m|_{\omega < 0}) = \sum \sum (\bar{B}_n \hat{B}_m \bar{D}_n \hat{D}_m \bar{H}_n \hat{H}_m|_{\omega > 0} + \hat{B}_n \bar{B}_m \hat{D}_n \bar{D}_m \bar{H}_n \hat{H}_m|_{\omega < 0}) S_{X_0 X_0}(\omega) \quad (38)$$

Integrating this expression with respect to  $\omega$  from  $-\infty$  to  $+\infty$  gives the variance for the base moment as

$$\sigma_M^2(t) = \frac{1}{2\pi} \int_{-\infty}^{\infty} S_{MM}(\omega) d\omega = \frac{1}{2\pi} \int_{-\infty}^{\infty} \sum \sum (\bar{B}_n \hat{B}_m \bar{D}_n \hat{D}_m \bar{H}_n \hat{H}_m|_{\omega > 0} + \hat{B}_n \bar{B}_m \hat{D}_n \bar{D}_m \bar{H}_n \hat{H}_m|_{\omega < 0}) S_{X_0 X_0}(\omega) d\omega \quad (39)$$

Let

$$\bar{B}_n \hat{B}_m \bar{D}_n \hat{D}_m = A_{m,n} + iB_{m,n} \quad (40)$$

then

$$\hat{B}_n \bar{B}_m \hat{D}_n \bar{D}_m = A_{m,n} - iB_{m,n} \quad (41)$$

when Eq.(41) and (40) are used, eq.(39) becomes

$$\sigma_M^2(t) = \frac{1}{2\pi} \int_{-\infty}^{\infty} \sum \sum \left[ \frac{(A_{m,n} + iB_{m,n}) S_{X_0 X_0}}{[\omega_n^2(1 + i\eta_n) - \omega^2][\omega_m^2(1 + i\eta_m) - \omega^2]} \right]_{\omega > 0} + \left[ \frac{(A_{m,n} - iB_{m,n}) S_{X_0 X_0}}{[\omega_n^2(1 + i\eta_n) - \omega^2][\omega_m^2(1 + i\eta_m) - \omega^2]} \right]_{\omega < 0} d\omega \quad (42)$$

When  $S_{\ddot{x}_0}(\omega)$  varies slowly in the frequency domain interested, eq.(42) can be integrated by the calculus of residues. Since the  $\tilde{H}_m(\omega)$  and  $\tilde{h}_m(\omega)$  have a pair of poles

$$\omega_m \sqrt{1+i\gamma_m} = \omega_m (a_m + ib_m)$$

$$\text{and } -\omega_m \sqrt{1-i\gamma_m} = \omega_m (-a_m + ib_m)$$

at the positive and negative frequency domain, respectively,  
So

$$\begin{aligned} \sigma_M^2(t) = & i \sum \sum [\text{Res}(\omega_{m,1}) S_{\ddot{x}_0}(\omega_{m,1}) (A_{m,n} + iB_{m,n}) \\ & + \text{Res}(\omega_{m,2}) S_{\ddot{x}_0}(\omega_{m,2}) (A_{m,n} - iB_{m,n})] \end{aligned}$$

where  $\text{Res}(\omega_{m,1})$  is the residue at  
 $\omega_{m,1} = \omega_m \sqrt{1+i\gamma_m}$  etc.,

$$\text{If } S_{\ddot{x}_0}(\omega_{m,1}) = S_{\ddot{x}_0}(\omega_{m,2}) = S$$

then

$$\begin{aligned} \sigma_M^2(t) = & i \sum \sum \left[ \frac{(B_{m,n}a_m - A_{m,n}b_m)(\omega_m^2 - \omega_n^2) -}{2\omega_m(a_m^2 + b_m^2)(\omega_m^2(1+\gamma_m^2) + \omega_n^2(1+\gamma_n^2)) -} \right. \\ & \left. \frac{-(\omega_m^2\gamma_m + \omega_n^2\gamma_n)(A_{m,n}a_m + B_{m,n}b_m)}{2\omega_m^2\omega_n^2(1-\gamma_m\gamma_n)} \right] S \end{aligned} \quad (43)$$

$$\text{where } a_m = \frac{1}{\sqrt{2}} \sqrt{1 + \sqrt{1 + \gamma_m^2}}$$

$$\text{and } b_m = \frac{1}{\sqrt{2}} \sqrt{1 + \gamma_m^2} - 1$$

When two nature frequencies  $\omega_m, \omega_n$  are well separated, and  $\gamma_m \approx \gamma_n < 0.1$ , the cross terms in eq.(43) will be very small and can be neglected, it leads to an approximate expression

$$\sigma_M^2(t) \approx \sum \frac{A_{m,n} S}{4\gamma_m \omega_m^3} \quad (47)$$

It agrees well with eq.(2.130) in ref.(10). From eq.(33), (34), (35), (40), (41), it is obvious that  $A_{m,n} \propto \omega_m^4$ , so the component of the high frequencies in eq.(47) seems to dominate, but owing to the inertia forces of each masses being different in phase at high frequencies, the contribution of high modes to is very small. Calculated results show that only a few terms of low frequency modes are enough to account for this practical example.

#### Example

Some practical vibration problems have been treated with presented method, for example, a number of dynamic absorbers was used to suppress some resonance vibration of a cantilever structure, which has some closed resonance peaks in the vicinity of 20Hz, causing a serious bending moment at the root section of this structure. To overcome the drawback of the usual tuned absorbers, that the response depends on the tuning parameters too sensitively, six absorbers are hung on a section of the structure. The stiffness and the damping para-

meters of these absorbers are different from each other, and it makes their tuning frequency range wide enough to cover the resonance frequencies.

The eigensolution of the original structure without dampers was computed by SAPIV and then verified through experiment. Usually the dynamic response of the original structure is contributed mainly by the first few modes and hence the original system can be represented by its truncated modal parameters, the number of D.O.F. of the whole system is suppressed from 60 to 8 through this truncated modal transformation, and the results of the calculated response is accurately enough.

For the sakes of finding the conditions for the minimum bending stress of the structure and studying the effects of the parameters on the dynamic response of it, a lot of response curves at the top of the structure, bearing the harmonic excitation from the base movement, are calculated when the parameters of these absorbers vary in a considerable range, some of the calculated results and the lumped mass model of the structure are shown in fig.3.

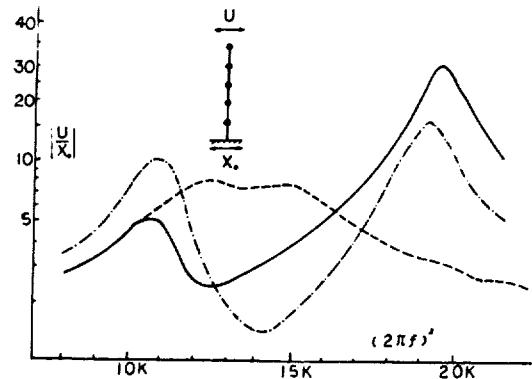


fig.3. The  $H(\omega)$  varies with different parameters of absorbers

#### CONCLUSION

Four kinds of damping treatment are recommended in the presented paper, all its contributions are determined by a complex matrix in the form of localized modification of the original undamped matrix.

We be sure that continuously adjust parameters and locations of these treatments can bring about steady improvement in the dynamic performance of any structure.

#### REFERENCES

1. T.F. Derby, and J.E. Ruzicke, "Loss Factor and Resonant Frequency of Shear-Damped Structure Composites," NASA - CR - 1269, 1969

2. J.C. Snowdon, "Vibration and Shock in Damped Mechanical Systems," John Wiley, New York, 1968.
3. D.C. Johns and A.D. Kashif, "Damping of Structures by Viscoelastic Links," Shock and Vibration Bull. No.36, Part 4, 1P.9- 1966
4. G.E. Hobbs, D.J. Kuypier, and J.J. Brooks, "Response Analysis of A System with Discrete Dampers," Shock and Vibration Bull. No.46, Part 4, 1P.137-152, 1976
5. R.L. Nelson, "Techniques for the Design of Highly Damped Structures," Shock and Vibration Digest V.9. No.7, 1P.3-11 July 1977
6. C.D. Johnson, D.A. Kienholz, L.C. Rogers, "Finite Element Prediction of Damping in Structures with Constrained Viscoelastic Layers," Shock and Vibration Bull. No.51, 1981
7. Y.Tsushima, et.al., "Analysis of Equations of Motion with complex Stiffness Mode Superposition method Applied to System with Many D.O.F." Nuclear Engng and Design Vol.37, No.1, 1P.47 1976
8. T.I.Tian , and C.Y.Zhu, "The Optimal Damping of A Constrained Layer Damping Rods" Strength of Machine, Chinese, No.7, 1P.39-36, 1978
9. L.J. Torvik, "Damping Applications for Vibration Control" A.I.A.A.-Vol 38 A.S.A.E. 1P.85-112, 1980
10. R.B. Workerton, The Dynamical Behaviour of Structures Pergamon Press, PP.102, 1976

# AN EXPERIMENTAL STUDY OF THE NON-LINEAR BEHAVIOUR OF A STRANDED CABLE AND DRY FRICTION DAMPER

C.S. Chang, Professor and  
Qianli Tian, Associate Professor

Institute of Mechanics,  
Chinese Academy of Sciences  
Beijing (Peking),  
China

The non-linear characteristics of a stranded cable and dry friction damper are shown by its hysteresis loop and dynamic response curves. The fundamental resonant frequency is found to be amplitude-dependent. The damper with a standard stranded cable has a high amplification factor at large amplitudes of vibration. This undesirable characteristic is overcome by adding a spring coil to the central portion of the cable. The modified cable damper is shown to suppress the fundamental resonant vibration of a cantilever structure.

## I. INTRODUCTION

An aluminum cantilever structure has a very complicated profile along its length. The amplitudes of vibration at its first two resonant frequencies are extremely large because of the low loss factor (0.0015). The vibration of the structure could be reduced effectively by a classical damped dynamic absorber with a constrained -layer viscoelastic element. Temperature sensitive, viscoelastic material could not be used, however, because the structure will be subjected to large temperature variations. This deficiency leads to the development of a dry-friction type damper which employs a stranded cable as its damped spring element.

## II. THE HYSTERESIS LOOP OF THE STRANDED CABLE

The stranded cable is composed of seven strands, each formed by nineteen wires as shown in Fig.1.

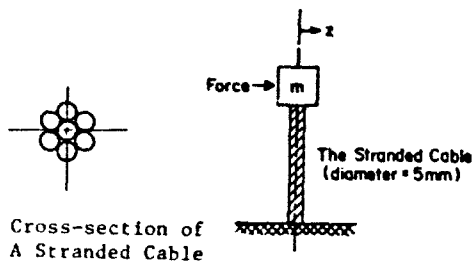


Fig. 1 The cable damper.

When a force is applied to the free end of the stranded cable, the displacement at its free end will follow the path indicated by  $oaA'B'C'D'E'F'A''B''C''D''E''A''$  as the load  $P$  follows sequence  $o-A'-D'-A''-D''-A''$ . It can be seen that the no-load deflection of the stranded cable is path dependent. The zero load deflection can be  $\delta_B$ , or  $\delta_E$ , or  $\delta_D$  or  $\delta_B$  as shown in Fig. 2.

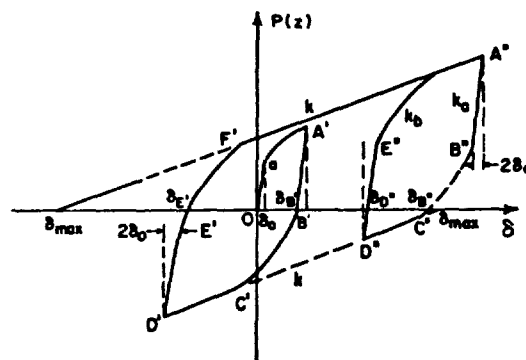


Fig. 2 The hysteretic behaviour of the stranded cable.

When the load is small or just reversed in direction, friction between the strands will hold them together so that the cable behaves like an elastic element. Hence the lines  $oa$ ,  $A'B'$ ,  $D'E'$ ,  $A''B''$  and  $D''E''$  are lines of constant stiffness,  $k_a$ . When the load is increased so that the friction between the strands is



insignificant, the stranded cable behaves again like an elastic element with a stiffness which is the resultant of the stiffnesses of seven separate strands. Hence the lines like  $C'D'$ ,  $F'A''$  and  $C''D''$  are lines of constant stiffness,  $k$ . The stranded cable will behave non-linearly when the load is just large enough to initiate slip. Slip will continue to happen as the load increases further. So that curved paths like  $AA'$ ,  $B'C'$ ,  $E'F'$  and  $B''C''$  occur. Consequently, symmetrical hysteresis loops are obtained experimentally as shown in Fig. 3

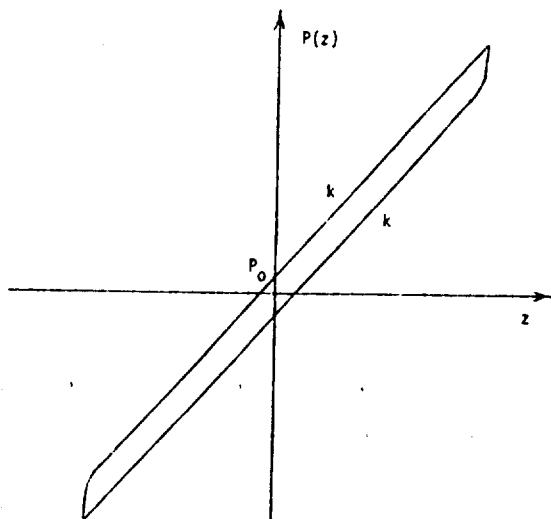


Fig. 3A The hysteresis loop of a standard stranded cable

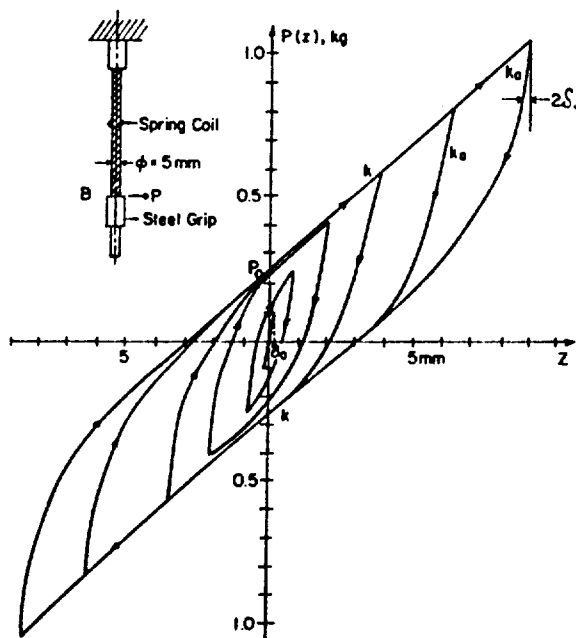


Fig. 3B The hysteresis loop of point B of a stranded cable with a central spring coil.

when the symmetrical load is cycling. A simplified version of a typical loop is shown in Fig. 4.

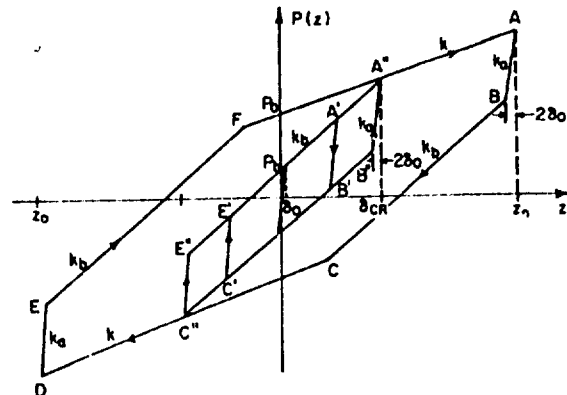


Fig. 4 A simplified version of the hysteresis loop for the stranded cable with a central coil.

It is composed of lines corresponding to  $k_a$ ,  $k_b$  and  $k$ . On the other hand, a loop may be composed of two lines corresponding to  $k_a$  and  $k_b$  if the applied load is less than a critical value. There are a number of publications on bi-linear hysteresis systems [1,2,3,4]. The standard stranded cable has a narrow hysteresis loop (fig. 3A) while the cable with a central spring coil has a much larger area of hysteresis loop (fig. 3B), indicating large frictional effects.

### III DYNAMIC RESPONSE OF A CABLE DAMPER

The damper is excited sinusoidally as shown Fig. 5.

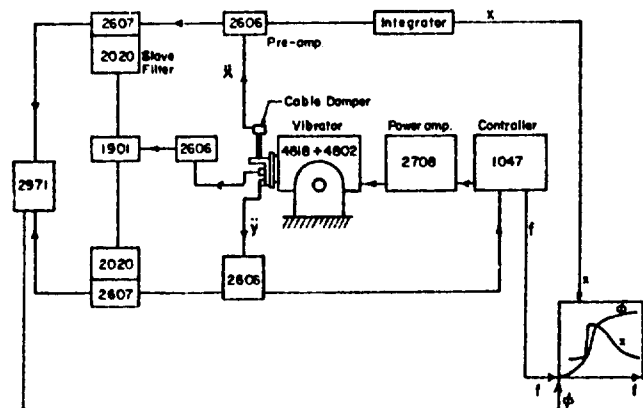


Fig. 5 The experimental set-up for dynamic response of cable damper (The numbers are Bruel & Kjaer's type No.)

The dynamic response curves for the amplitude and phase angle are shown in Fig. 6.

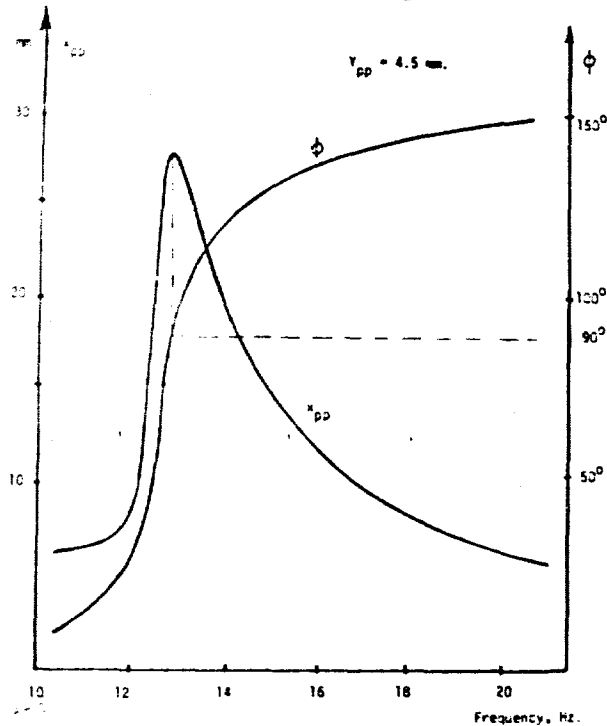


Fig. 6 The response curves for amplitude & phase of a cable damper.

It can be seen that the damper has a non-linear response curve which has peaks at the phase angle of  $90^\circ$ . The resonant frequency of the damper is amplitude-dependent as shown in Fig. 7.

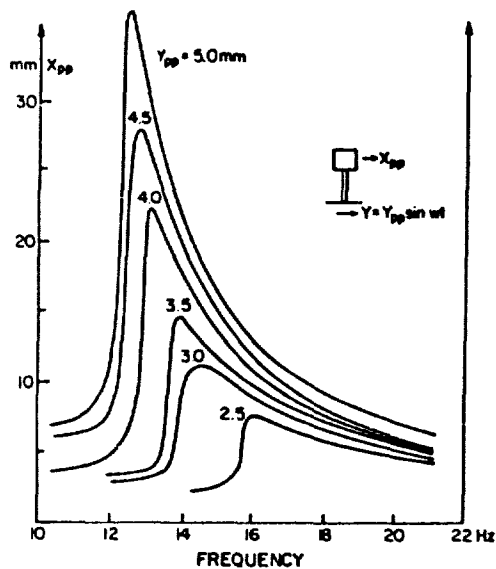


Fig. 7 The effect of input level on the response curve of a cable damper with a standard cable.

The shape of the response curve depends greatly on the magnitude of the friction between the strands (Fig. 8).

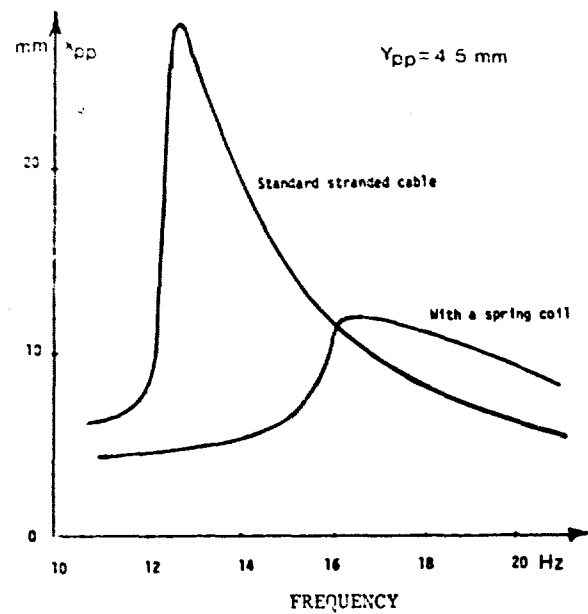


Fig. 8 The effect of the central spring coil on the response of cable damper.

The standard stranded cable has a small friction force and its amplification factor  $Q$ , defined as the ratio of the maximum displacement in the response curve to the input level at the base, grows in with increasing input level at the base in Fig. 9 as shown.

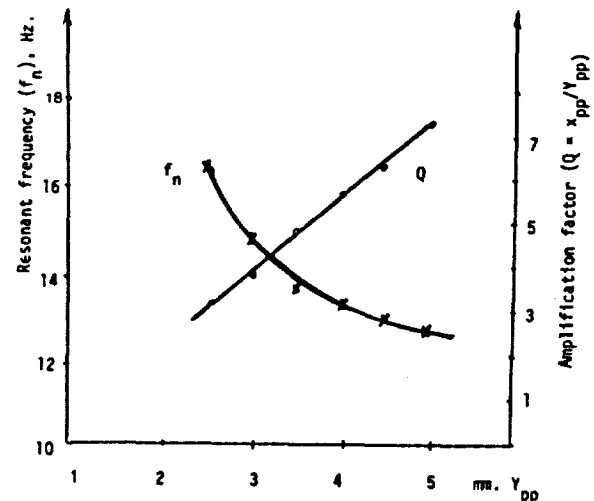


Fig. 9 The resonant frequency and amplification factor of a damper with a standard cable.

The high amplification factor at large amplitudes of vibration made the damper ineffective in controlling the vibration of the primary structure in the early stage of development of the cable damper. For large amplitudes of vibration, the damper with standard cable was observed, with the aid of a stroboscope, to loosen so that the strands separate. To prevent slackening of the normal cable, a simple spring coil is placed around the cable at the central position. The spring coil keeps the strands together when the damper mass of the cable damper is vibrating at a large amplitude. The cable damper with the central spring coil has a much higher resonant frequency, as shown in Fig. 8, and has a practically constant amplification factor of three (Fig. 10).

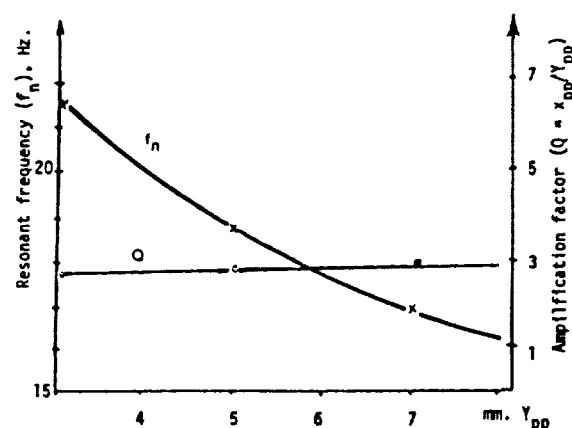


Fig. 10 The resonant frequency and amplification factor of a damper with a central spring coil on its cable.

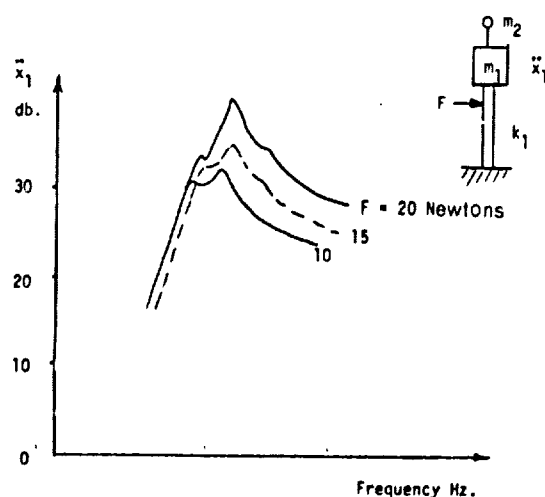


Fig. 11 The effect of force level on the response curve of a cantilever structure with cable dampers.

#### IV THE NON-LINEAR RESPONSE OF THE CANTILEVER STRUCTURE WITH CABLE DAMPER

For a classical linear and optimally tuned dynamic absorber, the shape of its response curve will remain the same as the excitation level is increased.

In the case of a system with the cable dampers, the dampers can be tuned optimally only for a given level of excitation. That is, the shape of the response for this system is amplitude-dependent as shown in Fig. 11.

A large number of response curves were obtained experimentally for different damper masses and various levels of constant base excitation. The maximum value in each response curve is plotted in Fig. 12.

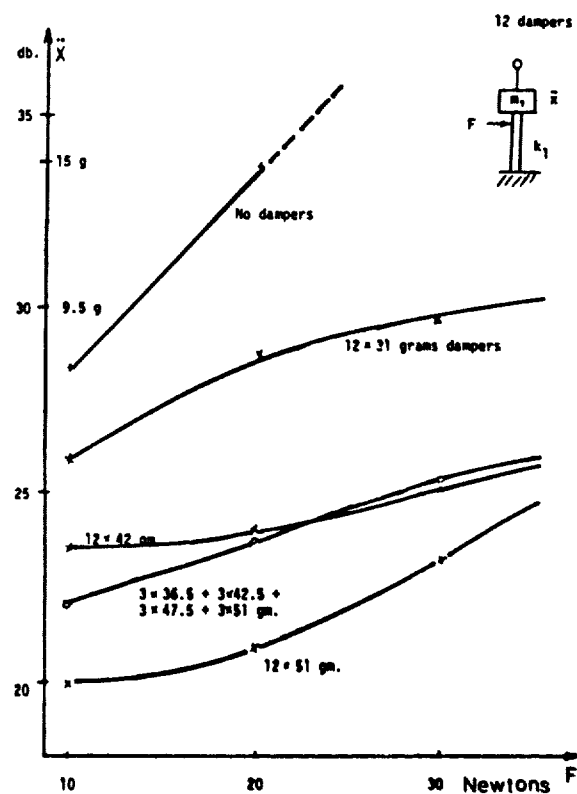


Fig. 12 The effect of damper mass and exciting force on the maximum response of a cantilever structure.

It can be seen that it is better to employ a heavier damper mass but this produces a higher weight penalty. The damper mass has to be divided into twelve equal portions, i.e. twelve cable dampers are employed, because there is a maximum permissible mass for a given cable element. It can be shown that the corresponding permissible acceleration  $A_{\max}$  for each damper is given by

$$A_{\max} = \frac{4 P_0}{\pi m}$$

where  $P_0$  is related to the friction between the strands and  $m$  is the mass of each damper (Fig. 3 or Fig. 4). The cable with a central spring coil has a much larger friction than the standard one.

It is interesting to note that the cable dampers are still effective in vibration control when the natural frequency of the cantilever is changed from 18 Hz. to 24 Hz. as shown in Fig. 13. The insensitivity to the change of natural frequency of the primary structure is a desirable property of a damper in solving a practical problem.

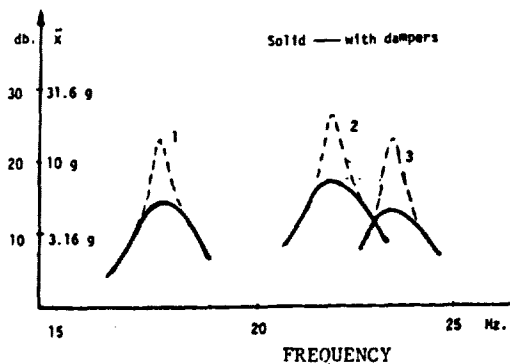


Fig. 13 The effectiveness of dampers for structures of different natural frequencies (tested with the same set of dampers).

## V. COMPARISON TEST

Comparison tests were performed to check the effectiveness of the cable dampers in reducing the vibration of a cantilever structure. These tests were undertaken on a slip table, sweeping from 10 Hz. to 35 Hz. at a constant amplitude of 1 mm. The cantilever structure was tested first in one direction and then in a direction perpendicular to the previous one. The results are given in Fig. 14. They show the appreciable reduction in the vibration of the cantilever structure due to the addition of the cable dampers.

## VI. SUMMARY

The normal stranded cable is a non-linear element with low damping at large amplitudes of vibration. A spring-constrained cable damper has larger friction and effectively reduces the vibration of a cantilever structure.

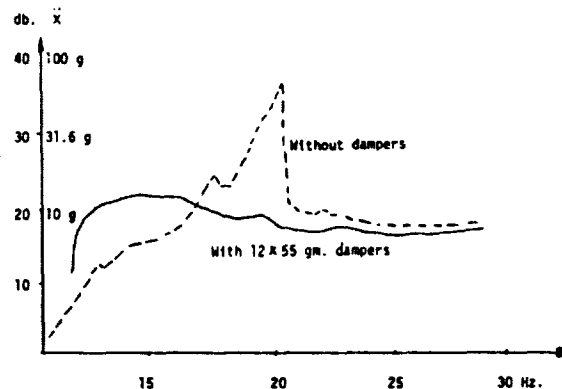


Fig. 14A The effect of cable damper on the response of a cantilever structure.

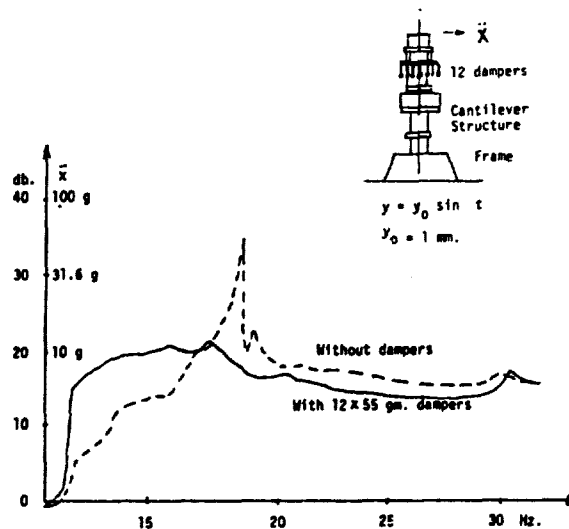


Fig. 14B Same as Fig. 14A except the direction of excitation is changed by 90 degrees.

#### ACKNOWLEDGEMENT

The authors wish to express their warm thanks to Professor Neil Popplewell (University of Manitoba), who read the manuscript and made many suggestions for improvement which we were pleased to incorporate, and to Dr. David I.G. Jones (AFML) for his interesting comments.

#### REFERENCES

1. T.K. Caughey, "Sinusoidal Excitation of a System with Bilinear Hysteresis", J.App.Mech. Vol. 27, 1960, pp. 640-643.
2. W.D. Iwan, "The Dynamic Response of the One Degree of Freedom Bilinear Hysteretic System", Proc. 3rd World Conference on Earthquake Engineering, Vol. II, 1965, pp. 783-796.
3. S.F. Masri, "Forced Vibration of the Damped Bilinear Hysteresis Oscillator" J. Acoust. Soc. Am. Vol. 57, 1975, pp. 106-112.
4. W.D. Iwan, "The Steady-State Response of a Two-Degree-of-Freedom Bilinear Hysteretic System" J. App. Mech. Vol. 32, 1965, pp. 151-156.

## RESPONSE OF PNEUMATIC ISOLATOR TO STANDARD PULSE SHAPES

M. S. Hundal  
The University of Vermont  
Department of Mechanical Engineering  
Burlington, Vermont 05405

Operation of a symmetric passive pneumatic shock isolator is analyzed. The governing equations are put in dimensionless form and solved numerically. A parametric study is made in terms of dimensionless parameters representing mass, stiffness and orifice/piston area ratio. On the basis of a sustained acceleration input the system is found to have optimum response for a certain range of the area ratio. System response is determined for six pulse shapes: rectangular, half-sine, versed sine, rising saw-tooth, falling saw-tooth and triangle.

### INTRODUCTION

Shock isolators are used to mitigate damaging effects on sensitive payloads, of impulsive motion of the base or foundation. A variety of isolator designs exist to satisfy the constraints of different situations. A pneumatic isolator offers the advantages of cleanliness and simplicity of design, but tends to be bulky and "springy". The pneumatic element has found application both as shock isolator as well as an absorber. An optimum isolator is one which minimizes the payload acceleration for a given base input. The relative motion of the payload is also important, as this governs the "rattle space" which must be provided.

A detailed review of literature on pneumatic isolators and absorbers which appeared up to 1980 is given in Reference [1]. Eshleman and Rao [2] investigated shock isolation characteristics of six types of elements, one of which was a pneumatic spring; however no analysis was given. Fox and Steiner [3] analyzed the operation of a pneumatic shock isolator and presented experimental data which correlate well with analytical results. The design of the isolator used by them is different from that of the one presented here. Pneumatic shock absorbers have been investigated by Takahashi [4], and by Hundal [5]. Shock isolators with

linear and quadratic damping have been analyzed and their characteristics compared by Hundal [6].

The system to be analyzed is shown in Figure 1. The isolator consists of a pneumatic damper in parallel with a spring of stiffness  $K$ . The base motion is  $u(t)$  and that of the payload,  $x(t)$ . The response of such a system to pulses of rectangular and half-sine shapes has been described in Reference [7]. In this paper the results are extended to other pulse shapes.

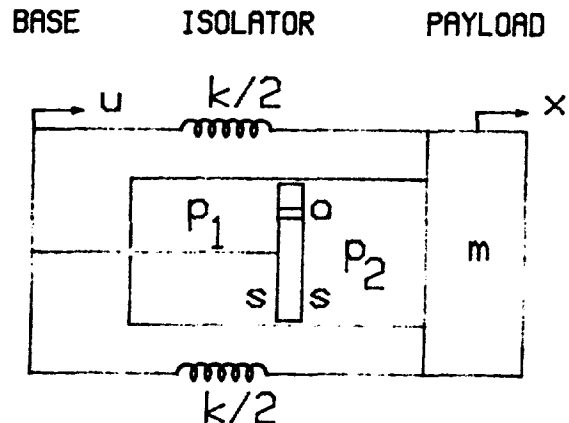


Figure 1. Isolator and Payload System

## SYSTEM ANALYSIS

The analysis from Reference [7] is repeated here for convenience. The equation of motion for the payload of mass  $m$  is

$$m\ddot{x} = k(u-x) + (p_2 - p_1)s \quad (1)$$

where  $p_1$  and  $p_2$  are pressures on either side of the piston and  $s$  is the piston area, assumed to be the same on both sides. Primes represent differentiation with respect to the physical time,  $t$ . Let the relative displacement of mass be  $\delta = u - x$ , substituting which equation (1) becomes

$$m\delta'' + k\delta = m\ddot{u} - (p_2 - p_1)s \quad (2)$$

with initial conditions:  $\delta = \delta' = 0$  and  $p_1 = p_2 = p_0$  at  $t = 0$ . The input pulse  $\ddot{u}$  is of duration  $t_f$  and maximum amplitude  $A$ . The different pulse shapes considered here are described in Table 1. Note that in each case  $\ddot{u} = 0$  for  $t > t_f$ .

TABLE 1

### Input Acceleration Pulse Shapes

No.	Pulse	Description
1	Rectangular	$A, t < t_f$
2	Half-sine	$A \sin(\pi t/t_f), t < t_f$
3	Versed-sine	$(A/2)[1 - \cos(2\pi t/t_f)], t < t_f$
4	Rising Saw-tooth	$At/t_f, t < t_f$
5	Falling Saw-tooth	$A(1-t/t_f), t < t_f$
6	Triangular	$2At/t_f, t < t_f/2$ $2A(1-t/t_f), t_f/2 < t < t_f$

The operation of the pneumatic damper is analyzed by assuming an adiabatic process. The governing equations are given below. The subscript  $i = 1, 2$  refers to the two sides of the piston. The exponent  $n = 1.4$  for air.

Equation of state:

$$m_i = p_i v_i / R\theta_i; i = 1, 2 \quad (3)$$

Adiabatic process:

$$\theta_i / \theta_0 = (p_i / p_0)^{(n-1)/n}; i = 1, 2 \quad (4)$$

Conservation of mass:

$$m_2' = -m_1'$$

In the above equations,  $m_i$  is mass,  $v_i$  is volume,  $\theta_i$  is temperature of air and  $R$  is the gas constant. Subscript 0 denotes initial condition. Upon differentiating equation (3) and substituting (4),

$$m_i' = C_1 (v_i' p_i^{1/n} + v_i p_i^{(1-n)/n} p_i') \quad (6)$$

where  $C_1 = p_0^{(n-1)/n} / R\theta_0$ . Let  $v_{10}$  and  $v_{20}$  be the initial volumes on either side of the piston. Then

$$v_1 = v_{10} + s\delta; v_1' = s\delta' \quad (7a)$$

$$v_2 = v_{20} - s\delta; v_2' = -s\delta' \quad (7b)$$

Upon substituting the above in equation (6), we obtain the flow equations

$$m_1' = C_1 [s\delta' p_1^{1/n} + (v_{10} + s\delta) p_1^{(1-n)/n} p_1'] \quad (8a)$$

$$m_2' = C_1 [-s\delta' p_2^{1/n} + (v_{20} - s\delta) p_2^{(1-n)/n} p_2'] \quad (8b)$$

Mass flow rate through an orifice is given by [8]

$$m_d' = C_0 a C_2 p_u / \sqrt{\theta_u}, \text{ for}$$

$$p_u / p_d > 1.894 \quad (9a)$$

and

$$m_d' = C_0 a C_3 (p_d / p_u)^{1/n} \sqrt{1 - (p_d / p_u)^{(n-1)/n}} \cdot p_u / \sqrt{\theta_u} \quad (9b)$$

where  $a$  is the orifice area,  $C_0$  the orifice coefficient and the subscripts  $d$  and  $u$  refer to downstream and upstream variables, respectively. Thus if  $p_1 > p_2$ ,  $u = 1$  and  $d = 2$ , and vice versa. The coefficients  $C_2$  and  $C_3$  in equation (9) are given by

$$C_2 = \left\{ \frac{n}{R[(n+1)/2]^{(n+1)/(n-1)}} \right\} \quad (10a)$$

$$C_3 = \left\{ \frac{n}{R(n-1)} \right\}^{1/2} \quad (10b)$$

Equations (2), (8) and (9) are the governing equations for the shock

isolator/mass system. Now, in order to cast these into a dimensionless form, we introduce the following variables and parameters: Accelerations,  $\ddot{X} = \ddot{x}''/A$ ,  $\ddot{D} = \ddot{s}''/A$ ;  $\ddot{U} = \ddot{u}''/A$ ; displacements,  $X = x/\ell$ ,  $D = s/\ell$ ; time,  $T = t\sqrt{A/\ell}$ ; pressures,  $P_1 = p_1/p_0$ ,  $P_2 = p_2/p_0$ ; stiffness,  $K = k\ell/p_0s$ ; mass,  $M = mA/p_0s$ ; area,  $S = C_0C_2Ra/s\sqrt{A}$ ; and initial volumes,  $V_{10} = v_{10}/s\ell$ ,  $V_{20} = v_{20}/s\ell = 1 - V_{10}$ . In these expressions  $\ell$  is the cylinder length. Note also that as a consequence of the above  $D = s'/\sqrt{A}$ ,  $\dot{X} = x'\sqrt{A}$ ,  $\dot{P}_1 = p_1'\sqrt{A/p_0}$ , where the dots represent differentiation with respect to  $T$ .

Upon making the above substitutions, the governing equations take the form of equations (11), (12) and (13). These equations contain a parameter  $C_4$  which is defined as

$$C_4 = n \text{ for } p_u/p_d > 1.894$$

and

$$C_4 = 5.41(p_d/p_u)^{1/n} [1 - (p_d/p_u)^{(n-1)/n}]^{1/2} \text{ for } p_u/p_d < 1.894. \quad (10c)$$

Equation of motion:

$$M\ddot{D} + K\ddot{D} = M\ddot{U} + P_1 - P_2 \quad (11)$$

Pressure equations, for  $P_2 > P_1$ :

$$(V_{10} + D)\dot{P}_1 + n\dot{D}P_1 = C_4SP_1^{(n-1)/n} \cdot P_2^{(n+1)/2n} \quad (12a)$$

$$(V_{20} - D)\dot{P}_2 - n\dot{D}P_2 = -C_4SP_2^{(3n-1)/2n} \quad (13a)$$

and for  $P_1 > P_2$ :

$$(V_{10} + D)\dot{P}_1 + n\dot{D}P_1 = -C_4SP_1^{(3n-1)/2n} \cdot P_2^{(n+1)/2n} \quad (12b)$$

$$(V_{20} - D)\dot{P}_2 - n\dot{D}P_2 = C_4SP_1^{(n+1)/2n} \cdot P_2^{(n-1)/n} \quad (13b)$$

The initial conditions are  $D = \dot{D} = 0$ ,  $P_1 = P_2 = 1$  at  $T = 0$ . The absolute mass acceleration is given by

$$\ddot{X} = \ddot{U} - \ddot{D} = (KD + P_2 - P_1)/M \quad (14)$$

The expression for the dimensionless input acceleration  $\ddot{U}$  can easily be found from Table 1 as follows: replace  $A$  by 1,  $t$  by  $T$ , and  $t_f$  by  $T_f$ , where  $T_f = t_f\sqrt{A/\ell}$ .

#### COMPUTATION OF SYSTEM RESPONSE

Equations (11), (12) and (13) are non-linear, they are therefore solved numerically by using fourth-order Runge-Kutta method. The governing equations contain five parameters, viz.,  $K$ ,  $M$ ,  $S$ ,  $V_{10}$  and  $T_f$ . In the absence of the damper the system natural frequency is  $(K/m)^{1/2}$ . We recognize however that for low values of  $S$ , i.e. small orifice area, and large piston displacement, the pneumatic stiffness can be significant. This must be borne in mind when selecting the integration step size. We now consider the effect of each system parameter.

The parameter  $V_{10}$  indicates the initial position of the piston. If it is required that the shock isolator have identical response to input in either direction, the piston must initially be at the middle position. Thus in the following  $V_{10} = V_{20} = 0.5$  has been used.

The effect of pulse duration  $T_f$  has been found to be similar to that in the case of shock isolators with linear or quadratic damping [6]. For a rectangular impulse the maximum mass acceleration increases monotonically with  $T_f$  up to a certain value, and remains constant thereafter. Thus in the results of parametric studies given below the case of sustained acceleration is considered first. The effect on system response of varying pulse shape and  $T_f$  is given later in this section.

We see from equation (11) that for a sustained acceleration input the steady state piston displacement is  $D_{ss} = M/K$ . The maximum displacement can, of course, be greater than this and depends on the damping effect of the orifice. As it is necessary that  $D_{max} < V_{20}$  in order to avoid impact of piston at the end of its stroke, the ratio of  $K$  to  $M$  is governed by the relationship  $M < V_{20}K$ .

In the absence of the damper, equations (11) and (14) can be solved analytically. For a sustained



acceleration, we can show that  $\ddot{x}_{\max} = 2$ . Thus in the following only those parameter values are considered for which  $\ddot{x}_{\max} < 2$ .

We consider next the results of the numerical solution of the governing equations for the case of constant, sustained acceleration. Figure 2 shows the variation of the maximum mass acceleration  $\ddot{x}_{\max}$ , i.e. the shock transmissibility, versus orifice/piston area ratio  $S$ , for the selected values of stiffness and parameters,  $K$  and  $M$ . From these results the following points are worth noting: (a)  $\ddot{x}_{\max}$  is a strong function of  $K$  and  $S$ , but a weak function of  $M$ , (b)  $\ddot{x}_{\max}$  approaches the minimum value of 1 as  $K$  approaches 0, (c) the minimum value of  $\ddot{x}_{\max}$  occurs for  $S$  in the range of 0.4 to 0.5. This is similar to the results obtained by Fox and Steiner [3], although the damper design is different.

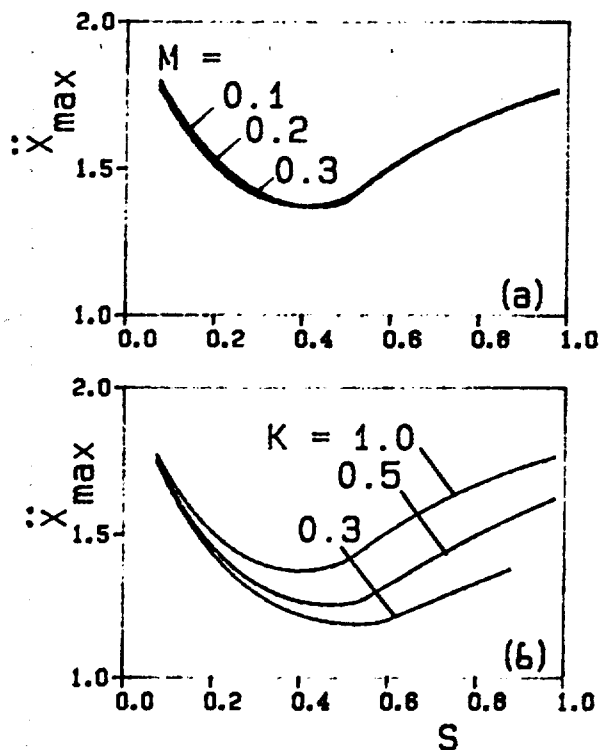


Figure 2. Maximum Mass Acceleration  
(a)  $K = 1$ ; (b)  $M = 0.1$

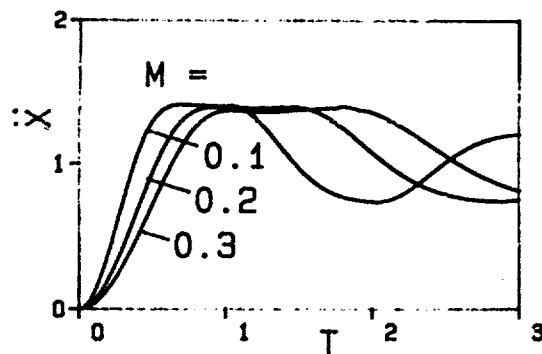


Figure 3. Acceleration Time Response.  
 $K = 1$ ;  $S = 0.5$

Figure 3 shows the time response of the system for different values of  $M$ . We see that  $\ddot{x}_{\max}$  occurs at different values of time, but its magnitude is not significantly different. The minimum values of  $\ddot{x}_{\max}$  can be expressed explicitly as a function of  $K$  by using the least squares fit. This functional relationship, for the range  $0.1 \leq K \leq 5$  has been found to be the following:

$$\min(\ddot{x}_{\max}) = 1.03 + 0.48K - 0.117K^2 + 0.0103K^3 \quad (15)$$

A plot of this equation is shown in Figure 4. We emphasize that this is an approximate representation of the minima from Figure 2(b) for the given range of  $K$ .

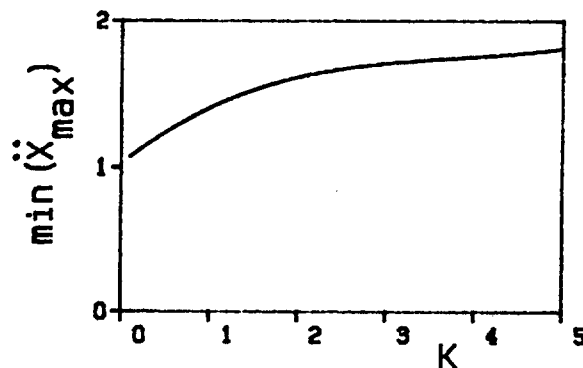


Figure 4. Minimum  $\ddot{x}_{\max}$ , Equation (15)

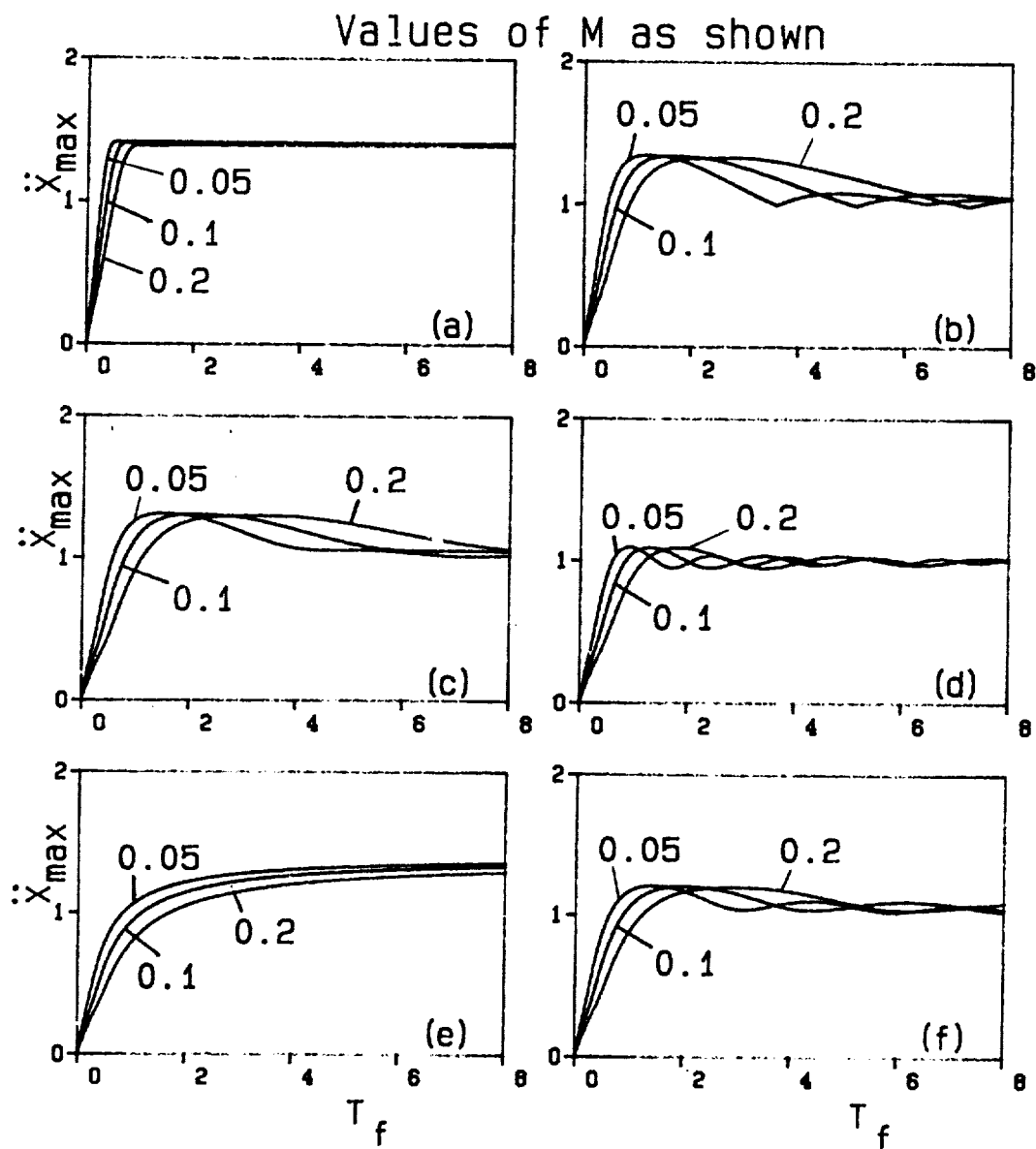


Figure 5. Shock Transmissibility  $X_{\max}$ ;  $K = 1$ ,  $S = 0.5$  for different pulse shapes. (a) rectangular, (b) half-sine, (c) versed-sine, (d) rising saw-tooth, (e) falling saw-tooth, and (f) triangular.

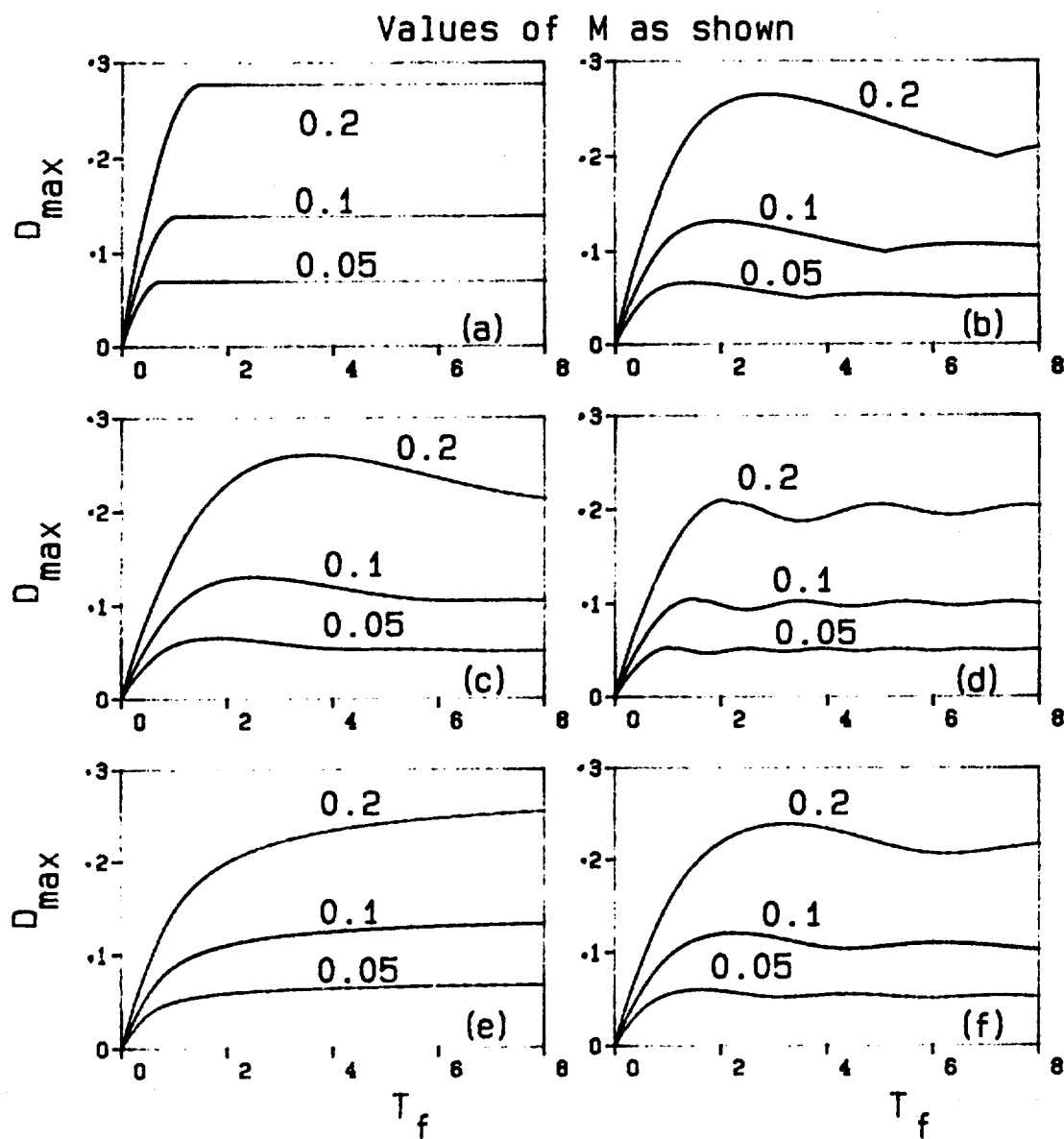


Figure 6. Maximum Relative Displacement  $D_{\max}$ ;  $K = 1$ ,  $S = 0.5$  for different pulse shapes. (a) rectangular, (b) half-sine, (c) versed-sine, (d) rising saw-tooth, (e) falling saw-tooth, and (f) triangular.

Finally, we consider the effects of pulse shape and duration on the system response. Figure 5 shows plots of shock transmissibility  $X_{max}$  for the different pulse shapes. The corresponding plots of relative motion  $D_{max}$  are shown in Figure 6. These plots are qualitatively similar to those for a linear system [9]. For the rectangular and falling saw-tooth pulses, the transmissibility increases monotonically with duration. For the other four pulse shapes we note a succession of maxima and minima.

#### DESIGN EXAMPLES

We noted earlier that in order to restrict the steady state displacement to  $D_{ss} = V_0 = 0.5$  it is necessary that  $M < V_0 K = 0.5 K$ . However since  $D_{max}$  can be greater than  $D_{ss}$ , a lower restriction on  $M$  is necessary. A parametric study was made for the range  $0.1 < K < 5$  and  $S = 0.4$  to  $0.5$ . The results show that to achieve  $D_{max} < 0.5$ , it is necessary that  $M < K/3$ .

We can summarize the design process in the following steps: (a) For a given case  $m$  and  $A$  are known. (b) From constraints on cylinder diameter, piston area  $s$  is known. (c) Find  $M$ . (d) Use  $K > 3M$  and find  $X_{max}$ . If this is higher than desired, use larger  $s$  or  $p_0$ . (e) Find  $k$  from definition of  $K$ . (f) From constraints on cylinder length, find  $k$ . (g) Find the required orifice area  $a$  from definition of  $S$ , for  $S = 0.5$ .

Let us consider an example where  $m = 20$  kg and a sustained acceleration of  $A = 10$  m/s<sup>2</sup> is applied. From Figure 4 it is seen that lower the value of  $K$ , lower is the shock transmissibility  $X_{max}$ . Let us choose  $K = 0.5$ , for which  $X_{max} = 1.25$ , or  $x'_{max} = 12.5$  m/s<sup>2</sup>. Let  $p_0 = 1$  atm. = 0.101 MPa. Try two different damper diameters.

- (a) For diameter 0.2 m,  $s = 0.0314$  m<sup>2</sup>,  $p_{os} = 3185$  N. Since  $K = k\ell/p_{os}$ , we have  $k\ell = 1592$  N. Let  $\ell_{max} = 0.2$  m, then  $k = 7964$  N/m. For this case  $M = mA/p_{os} = 0.063 = 0.126 K$ , i.e.  $M < K/3$ .
- (b) For diameter 0.1 m,  $s = 0.0079$  m<sup>2</sup>,  $p_{os} = 796$  N. For  $K = 0.5$ ,  $k\ell = 398$  N. Thus for  $\ell = 0.2$  m,  $k = 1990$  N/m. For this case  $M = 0.25 = 0.5 K$  which is greater than  $K/3$ , thus

unacceptable.  $M_{max} = 0.5/3 = 0.16$ , and thus  $p_{os} = 1200$ . This gives a minimum diameter of 0.123 m. The corresponding  $k\ell = 600$  N, from which  $k$  and  $\ell$  can be selected.

We note from the foregoing discussion that to obtain a lower value of shock transmissibility, a lower value of parameter  $K$  be used. This means a combination of higher  $p_0$  and  $s$  and smaller  $k$  and  $\ell$ .

#### CONCLUSION

The response of a passive pneumatic shock isolator of the given design has been determined. The results are in terms of dimensionless parameters and are therefore of more general use. The parametric study performed points to the values for an optimum system. It has been shown that shock transmissibility is governed primarily by damper size.

#### REFERENCES

1. Hundal, M.S., "Pneumatic Shock Absorbers and Isolators", Shock and Vibration Digest, Vol. 12, No. 9, 1980, pp. 17-21.
2. Eshleman, R.L., and Rao, P.N., "The Response of Mechanical Shock Isolation Elements to High Rate Input Loading", Shock and Vibration Bulletin, Vol. 40, Pt. 5, 1969, pp. 217-234.
3. Fox, G.L., and Steiner, E., "Transient Response of Passive Pneumatic Isolators", Shock and Vibration Bulletin, Vol. 42, Pt. 4, 1972, pp. 85-91.
4. Takahashi, T., "Air Dashpot Energy Absorption Characteristics", Review of Electronic Communications Laboratory (Japan), Vol. 22, 1974, pp. 71-81.
5. Hundal, M.S., "Analysis of Performance of Pneumatic Impact Absorbers", Journal of Mechanical Design, Transactions of ASME, Vol. 100, 1978, pp. 236-241.
6. Hundal, M.S., "Response of Shock Isolators with Linear and Quadratic Damping", Journal of Sound and Vibration, Vol. 76, 1981, pp. 273-281.

7. Hundal, M.S., "Passive Pneumatic Shock Isolator: Analysis and Design", Journal of Sound and Vibration, Vol. 84, 1982 (in press).
8. Blackburn, J.F., Reethof, G., and Shearer, J.L., Fluid Power Control, MIT Press, Cambridge, Mass., 1960, pp. 215-217.
9. Derby, T.F., and Calcaterra, P.C., "Response and Optimization of an Isolation System with Relaxation Type Damping", NASA, CR-1542, 1970.